Gas sensing and Electrical properties of Metal Oxide Nanostructures

A Thesis submitted in partial fulfillment
of the requirements of the degree of

Doctor of Philosophy

By

Chandra Sekhar Rout

Chemistry and Physics of Materials Unit
Jawaharlal Nehru Centre for Advanced Scientific Research
(Deemed University)
Bangalore – 560 064 (INDIA)

June 2008

To my beloved parents

Declaration

I hereby declare that this thesis entitled **"Gas sensing and Electrical properties of Metal Oxide Nanostructures"** is an authentic record of research work carried out by me under the supervision of Prof. C. N. R. Rao, FRS at the Chemistry and Physics of Materials Unit, Jawaharlal Nehru Centre for Advanced Scientific Research, Bangalore, India.

In keeping with the general practice of reporting scientific observations, due acknowledgement has been made whenever work described here has been based on the findings of other investigators. Any oversight due to error of judgement is regretted.

Chandra Sekhar Rout

Certificate

Certified that the work described in this thesis titled **"Gas sensing and Electrical properties of Metal Oxide Nanostructures"** has been carried out under my supervision at the Chemistry and Physics of Materials Unit, Jawaharlal Nehru Centre for Advanced Scientific Research, Bangalore, India.

Prof. C. N. R. Rao

Acknowledgements

I acknowledge Prof. C.N.R. Rao, FRS for giving me this opportunity to work under his guidance, suggesting the problems and introducing me into different areas of research. I express my deep sincere gratitude to him for his support, guidance and inspiration. My association with him will be always a source of inspiration to me.

I thank Dr. A.R. Raju for setting up the gas-sensing measurement system and for the initial experiments.

I acknowledge Dr. A. Govindaraj for his valuable guidance, which helped me to synthesize the nanomaterials. It has been a tremendous learning experience for me.

I am extremely grateful to Prof. G. U. Kulkarni for introducing me to CAFM measurements and other studies. I thank him for being patient and understanding whenever I approached him with any doubts or queries. The discussions with him have helped me to learn many things.

I thank Dr. M. Eswaramoorthy and Mr. Saikrishna for useful their discussions during the mesoporous carbon related work.

I thank Prof. Timothy Fisher (Purdue Univrsity, USA) for his valuable discussions during the electrical studies of SWNTs.

I thank Mr. Manu Hegde, Mr. Vijay K. Nair, Ms. Tasneem, Ms. Nirmala, Mr. K. Ganesh, Mr. Vinay B.R. and Dr. Girija Shivakumar for their help during experimental measurements.

It is a pleasure to thank all the faculty members of CPMU and TSU, especially Profs. N. Chandrabhas, K.S. Narayan, Shobhna Narshiman, Umesh V. Waghmare, A. Sundersan for various discussions and courses. Also I thank Profs S.B. Kripanidhi, K.B.R. Varma, K. Rajanna, S. Mohan of IISc for their extremely useful and enjoyable courses.

I thank Vijay, Bhuvana, Dr. N.S. John, Dr. A. Angapane and Ved for their help and support during my work with CAFM studies.

I have been fortunate to have excellent labmates in all the labs that I have worked. I thank all my labmates, Vivek, Leela, Bhat, Subramanyam, Neenu, Kanishka, Rakesh, Claudy, Gomathi, Basant, Kalyani, Barun, Sandeep for their help.

My heartiest acknowledgement to Dr. S. K. Swain for his valuable suggestions.

I thank all my seniors, especially Drs. Asish, Behera, M. Seikh for their help and support.

All my friends in JNC, Gopal, Jyoti, Thiru, Shibu, Jaita, Dhritiman, Bhargava, Reji, Kalyan, Dinesh, Gurunath, Raju, Madhu and Sudhansu, Khatei, Rama, Debakanta bhai, Hembram bhai in IISc, Tapan bhai in IIAP, Bibhu in RRI, Manas, Anand, Manisha and … many more…..

The help of Basavaraj with SEM, Usha madam with TEM, Selvi with FESEM, Srinath in designing the electrical measuring set-ups, Anil with XRD, Vasu with UV and PL. I thank Arogyanathan, Sunil and Moorthy for their assistance.

I am thankful to all the office staff in CSIR-COE JNCASR, Mrs. Sashi, Gowda, Xavier and Victor.

It is a pleasure to thank Mrs. Indumati Rao and Sanjay Rao for their hospitality at their residence.

I acknowledge all my teachers with whom I have come across throughout my career.

I would like to express my sincere gratitude to my parents for their support, encouragement and patience without that this study would not have been completed.

Preface

This thesis consists of four parts of which Part-1 gives a brief overview of the synthesis, properties and applications of nanomaterials. Part-2 deals with the synthesis and characterization of different nanostructures of metal oxides and a detailed study of their gas-sensing characteristics. Nanoparticles, nanowires, nanorods and nanotubes of metal oxides such as ZnO, In_2O_3, WO_{3-x}, V_2O_5, TiO_2 and SnO_2 have been prepared by different chemical routes and characterized by transmission electron microscopy, X-ray diffraction, energy dispersive X-ray analysis and Raman spectroscopy. Sensing characteristics of the thick films of oxide nanostructures for H_2, ethanol, aliphatic hydrocarbons, H_2S, NH_3 and nitrogen oxides have been studied. Hydrogen sensing characteristics of single nanowires of ZnO, TiO_2 and $WO_{2.72}$ as well as hydrocarbon sensing characteristics of single $WO_{2.72}$ nanowires have also been investigated by conducting atomic force microscopy. The best sensitivities are found with nanostructures of ZnO (~1720 at 125 °C, H_2), (~2500 at 125 °C, Ethanol), $WO_{2.72}$ (~10^6 at 200 °C, aliphatic hydrocarbon), WO_3 (~ 3300 at 250 °C, H_2S), In_2O_3 (~ 60 at 150 °C, NO, NO_2 and N_2O) and SnO_2 (~ 250 at 300 °C, NH_3).

Part-3 of the thesis contains results of studies on the electrical properties and hydrogen-sensing characteristics of field effect transistors (FETs) based on nanorods of ZnO and $WO_{2.72}$. Electroluminescence and rectifying properties of heterojunction light emitting diodes (LEDs) based on ZnO nanorods have been studied. n-ZnO NR/p-Si and n-ZnO NR/p-PEDOT/PSS heterojunction LEDs have been fabricated with ZnO nanorods (NRs) grown by a low-temperature method as well as by employing pulsed laser deposition.

Part-4 of the thesis deals with the supercapacitive behavior of RuO_2 and IrO_2 functionalized mesoporous carbon. Results of studies on the interaction of single-walled carbon nanotubes (SWNTs) with electron donor and acceptor aromatic molecules are reported based on electrical measurements.

Contents

PART 2

PART 3

Properties of field effect transistors and heterojunction light emitting diodes based on metal oxide nanorods 173

PART 4

Part 1

Nanomaterials: A Brief Survey

1.1 Introduction

In the last few years, a little word has attracted enormous attention, and investigation from all over the world. The word is “nano”. What it presents in terms of science and technology, which are also called nanoscience and nanotechnology, is much more than just a word describing a specific length scale. It has dramatically changed every aspect of the way we think in science and technology and will certainly bring more and more surprises into our daily life as well as into the world of the future [1]. “Nano” means one billionth (10^{-9}), so 1 nanometer refers to 10^{-9} meter and is expressed as 1 nm. 1 nm is so small that things smaller than it can only be molecules, clusters of atoms or particles in the quantum world. Nanometer is a special point in the overall length scale because nanometer scale is the junction where the smallest manufacturable objects meet the largest molecules in nature. The structures, devices and systems having at least one dimension in nanometer scale are not only smaller than anything that we have ever made before, but also possibly the smallest solid materials that we are able to produce. Besides, in nanometer scale, the properties of materials that we are familiar with in our daily life, such as color, melting point, electronic, catalytic or magnetic properties [2], will change dramatically or be replaced by completely novel properties due to what is usually called size effect [3]. Simply saying, nanoscience tells us how to understand the basic theories

and principles of nanoscale structures, devices and systems (1-100 nm); and nanotechnology tells us what to do and how to use these nanoscale materials.

On December 29 1959, Richard P. Feynman described the problems of manipulating and controlling things on a small scale and predicted that there is plenty of room at the bottom [4], which, as the central idea of nanoscience and nanotechnology, has long been the pursuit of scientists worldwide. In the past decades, the development of various chemical or physical methods have enabled us to partly fulfill this goal [5–18], based on which many new and promising fields have been established, including nanofabrication, nanodevices, nanobiology, and nanocatalysis, etc. Among all kinds of nanosystems such as zero- [5], one- [6–7], and two-dimensional [8] systems, one-dimensional (1D) nanostructures are particularly interesting in that they usually have diameters in nanometer scale and lengths in micro- and/or even macroscale, the controlled growth of which involves the breaking of crystal symmetry and are quite different from the general concept of crystal growth [9].

Size effects constitute a fascinating aspect of nanomaterials. Bulk metals possess a partially filled electronic band and their ability to conduct electrons is due to the availability of a continuum of energy levels above the Fermi level, E_F. However when bulk metal is broken down, the continuum of electronic states break down and ultimately, the material becomes insulating. The emerging discreteness of energy levels would not manifest themselves as long as the gap is less than K_BT. For semiconductors, the E_F is in between the filled and the unfilled levels. As the size of the system decreases, the energy levels become discrete, with a similar spacing as in metals. Thus, the band gap of the semiconductor effectively increases.

Similarly, the shape of the nanocrystals plays a crucial parameter in the determination of their properties [14-18]. The shape of the nanocrystals can be classified by their dimensionality. Figure 1.1.1 illustrates the basic geometrical motifs of nanocrystals: zero-dimensional (0D) isotropic spheres, cubes, and polyhedrons; 1D rods and wires; 2D discs, prisms and plates. The most distinct shape effects are observed in the density of energy states (DOS) [19]. The DOS (ρ (E)) of nanocrystals simultaneously

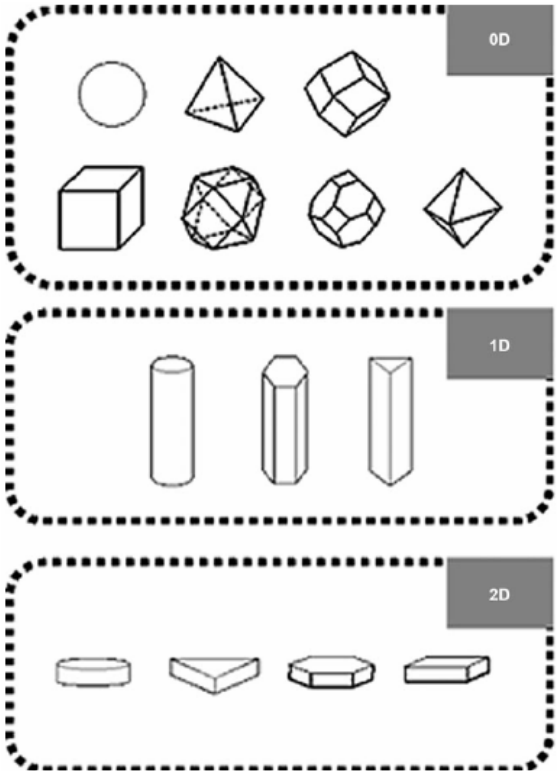

Figure 1.1.1: Basic motifs of nanocrystals: 0D spheres, cubes, and polyhedrons; 1D rods and wires; 2D discs, prisms and plates [20].

evolves from continuous levels into discrete states as the dimensionality is decreased from 3D to 0D as described by the relation $\rho(E) \sim E^{n/2\ -1}$(where n=dimensionality; Figure 1.1.2). In 3D crystals, ρ (E) is a smooth square-root function of energy. The 2D crystals confined along a specific direction (e.g. z-axis) and 1D crystals confined along two directions (e.g. x, y direction) show staircase and saw-tooth like DOS states, respectively, while 0D crystals show δ-function like DOS.

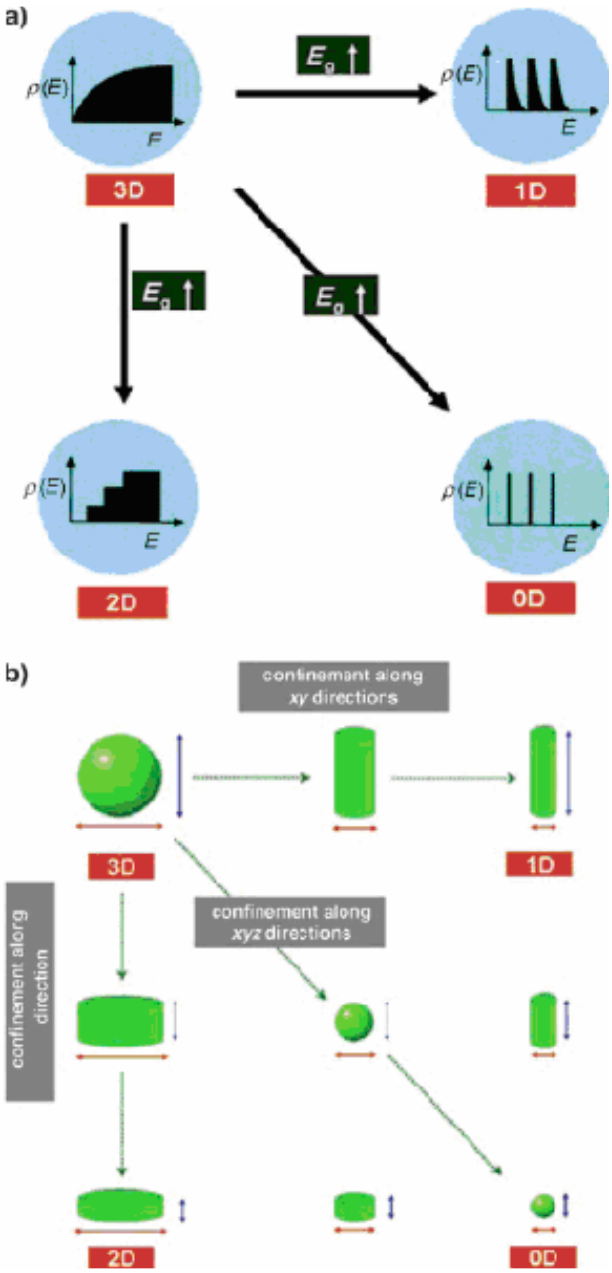

Figure 1.1.2: Shape evolution of crystals and their shape dependent properties. (a) The plot of density of states (DOS) versus energy for 3D, 2D, 1D and 0D crystals. (b) Confinement of 3D crystals along one- (z), two- (xy), and three (xyz) directions results in 2D, 1D and 0D nanocrystals [20].

The band-gap energy (E_g) of nanocrystals is also influenced by their shape. The band-gap energy diagram of CdSe nanocrystals with various diameters and lengths,

depicted in figure 1.1.3 (a), clearly exhibits shape effects [21]. Strong quantum confinement effects are observed as a function of the diameter reduction, while weaker quantum confinement effects are observed as a function of the length reduction. CdSe emission gradually changes from circular to linearly polarized as the nanocrystal shape evolves from spherical to rod like {Figure 1.1.3 (b)}[22].

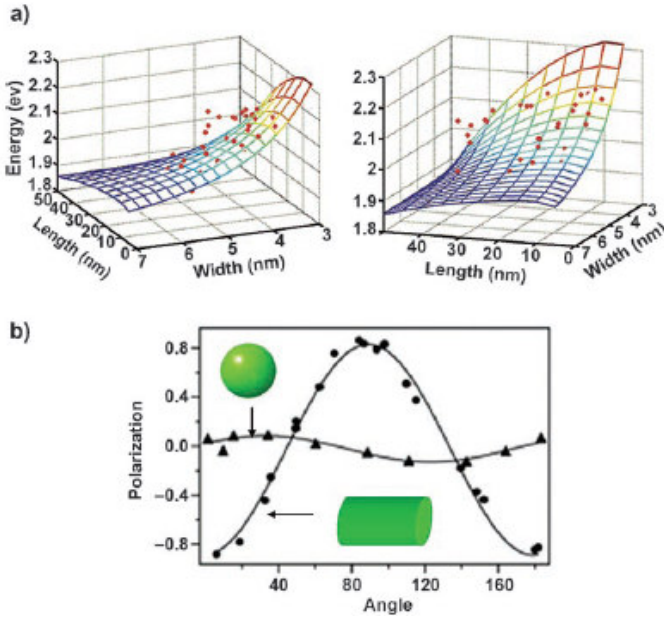

Figure 1.1.3: (a) Band-gap energy diagram of CdSe nanorods [21] and (b) shape-dependent polarized emission properties of CdSe [22]. CdSe nanorods have linearly polarized emission properties, while circularly polarized emission is observed from spherical CdSe nanoparticles.

1.2. Synthetic strategies

Modern materials science is characterized by a close interplay between physics and chemistry. This is especially true for nanomaterials. On the one hand, are the top-down methods which rely on continuous breakup of a piece of bulk matter while on the other are the bottom-up methods that build up nanomaterials from their constituent atoms. The top-down and bottom-up approaches can also be considered to be physical and chemical methods, respectively.

1.2.1 Physical methods

Most physical methods involve the evaporation of a solid material to form a supersaturated vapor from which homogenous nucleation of nanoparticles occurs. In these methods, the size of the particles is controlled by temporarily inactivating the source of evaporation, or by slowing the rate by temporarily inactivating the source of evaporation, or by introducing gas molecules to collide with the particles. Some of the physical methods to prepare nanocrystals are arc discharge, ion sputtering, laser ablation, spray pyrolysis, etc [23].

1.2.2 Chemical methods

Chemical methods have emerged to be indispensable for synthesizing nanocrystals of various types of materials. These methods are generally carried out under mild conditions and are relatively straight forward. Any chemical reaction resulting in a sol consists of three steps: seeding, particle growth and growth termination by capping. An important process that occurs during the growth of a colloid is Ostwald ripening. Ostwald ripening is a growth mechanism whereby smaller particles dissolve releasing monomers or ions for consumption by larger particles, the driving force being the lower solubility of large particles. Ostwald ripening limits the ultimate size distribution obtainable to about 15% of the particle diameter when the growth occurs under equilibrium conditions [23].

(a) Metal nanocrystals by reduction

Metal nanocrystals can be obtained by reducing the corresponding soluble metal salts and by terminating the growth with appropriate surfactants or ions. A variety of reducing agents are used to reduce metals salts to get nanocrystals of metals. Some of them are (1) borohydride reduction [24], (2) citrate reduction [25], (3) alcohol reduction [26] and (4)

reduction using alkylaluminates (AlR_3, R=C_1-C_8) [27]. In 17^{th} century Faraday prepared gold nanoparticles in lab by reducing gold salt. He termed them as "divided metal", which giving rise to a brilliant rose color.

(b) Solvothermal Synthesis

The Solvothermal method provides a means of using solvents at temperatures well above their boiling points, by carrying out the reaction in a sealed vessel. The pressure generated in the vessel due to the solvent vapors elevates the boiling point of the solvent. Typically, solvothermal methods make use of solvents such as ethanol, toluene and water. These are widely used to synthesize zeolites, inorganic open-framework structures and other solid materials. Due to the high pressures employed, one often obtains high-pressure phases of the materials. In the past few years, solvothermal synthesis has emerged to become the chosen method to synthesize nanocrystals [28, 29]. Solvothermal methods are ideally suited for the synthesis of nanocrystals of metal chalcogenides and halides, rather than metal nanocrystals.

(c) Photochemical synthesis

Photochemical synthesis of nanoparticles can be carried out by the light induced decomposition of a metal complex or the reduction of metal salts by photogenerated reducing agents such as solvated electrons. The former is called photolysis and the latter radiolysis. The formation of photographic images on AgBr film is a familiar photolysis reaction. Metals such as Au, Cd and Tl have been obtained by photolysis [30, 31].

(d) Arrested precipitation

Nanocrystals can be obtained from solutions that precipitate the bulk matter under conditions unfavorable for the growth of particulates in the precipitate. For example, the

precipitation of metals salts by chalcogens can be arrested by employing a high pH. To prepare nanocrystals of CdS, CdSe, CdTe, HgSe, HgTe and CdHgTe, typically, a solution containing the metal salt (perchlorate) and the capping agent is treated with NaOH to raise the pH, degassed by bubbling inert gas (to prevent the oxidation of chalcogen source) followed by the introduction of the chalcogen in the form of Na_2S, NaHSe, etc under inert conditions [23].

(e) The liquid-liquid interface

Nanocrystals and films of metals, semi-conductors and oxides can be produced by reactions taking place at the interface of two liquids such as toluene and water [23]. In this method, a suitable organic derivative of the metal taken in the organic layer reacts at the interface with the appropriate reagent present in the aqueous layer to yield the desired product. For example, by reacting $Au(PPh_3)Cl$ in toluene with THPC in water, nanocrystals of Au can be obtained at the interface of two liquids.

1.3 Synthesis of nanocrystals

Nanocrystals are zero-dimensional particles and can be prepared by several chemical methods, typical of them being reduction of salts, solvothermal synthesis and decomposition of molecular precursors, of which the first is the most common method used in the case of metal nanocrystals. Metal oxide nanocrystals are generally prepared by the decomposition of precursor compounds such as acetate, acetylacetonate and cuferronates in appropriate solvents, often under solvothermal conditions. Metal chalcogenide or pnictide nanocrystals are obtained by the reaction of metal salts with a chalcogen or pnicogen source or the decomposition of single source precursors under solvothermal or thermolysis conditions. Addition of suitable capping agents such as long-

chain alkane thiols, alkyl amines and trioctylphosphine oxide (TOPO) during the synthesis of nanocrystals enables the control of size and shape. Monodisperse nanocrystals are obtained by post-synthesis size-selective precipitation.

(a) Metals

Reduction of metal salts in the presence of suitable capping agents such as polyvinylpyrrolidine (PVP) is the common method to generate metal nanocrystals. Furthermore, the sealed reaction conditions and presence of organic reagents reduce the possibility of atmospheric oxidation of the nanocrystals [3, 32]. The popular citrate route to colloidal Au, first described by Hauser and Lynn [33], involves the addition of chloroauric acid to a boiling solution of sodium citrate. The average diameter of the nanocrystals can be varied from 10-100 nm range by varying the concentration of reactants. Au nanocrystals with diameters between 1 to 2 nm are obtained by the reduction of $HauCl_4$ with tetrakis (hydroxymethyl)phosphonium chloride (THPC) which also acts as a capping agent [34].

Liz-Marzan and co-workers [35] have prepared nanoscale Ag nanocrystals by using dimethylformamide as both a stabilizing agent and a capping agent. By using tetrabutylammonium borohydride or its mixture with hydrazine, Jana and Peng [36] obtained monodisperse nanocrystals of Au, Cu, Ag and Pt. In this method, $AuCl_3$, $Ag(CH_3COO)$, $Cu(CH_3COO)_2$, $PtCl_4$ were dispersed in toluene with the aid of long-chain quaternary ammonium salts and reduced with tetrabutylammonium borohydride which is toluene-soluble. Ag nanoprisms {Figure 1.3.1 (a)} are produced by irradiating a mixture of sodium citrate and bis(*p*-sulfonatophenyl) phenylphosphine dihydrate dipotassium capped Ag nanocrystals with a fluorescent lamp. In another method, $AgNO_3$ is reduced

with a mixture of borohydride and hydrogen peroxide and this method has been extended to synthesize branched nanocrystals of Au of the type shown in figure 1.3.1 (b) and (c) [37].

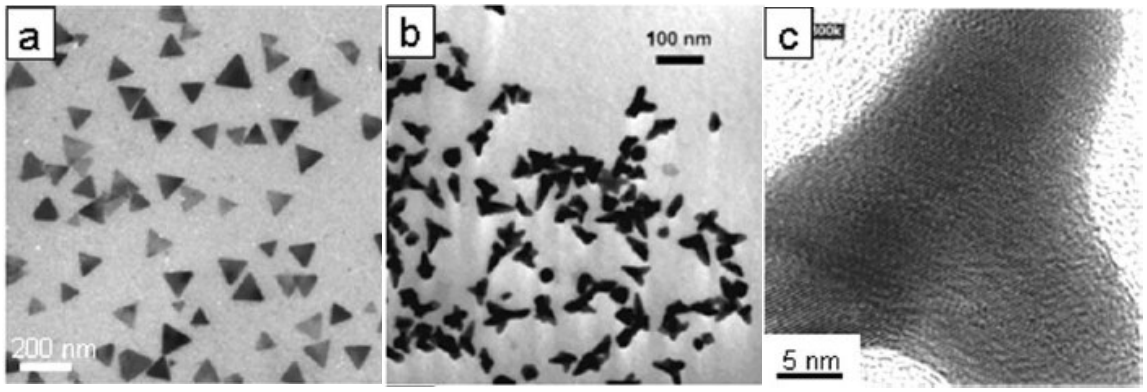

Figure 1.3.1: (a) Ag nanoprisms obtained by controlled irradiation of bis(*p*-sulfonatophenyl) phenylphosphine dihydrate dipotassium capped Ag nanocrystals. (b) Low and (c) high-magnification images of branched Au nanocrystals [37].

(b) Metal oxides

Metal oxide nanocrystals are mainly prepared by the solvothermal decomposition of organometallic precursors. Solvothermal conditions afford high autogenous pressures inside the sealed autoclave that enable low-boiling solvents to be heated to temperatures well above their boiling points. Thus, reactions can be carried out at elevated temperatures and the products obtained are generally crystalline compared to those from other solution-based reactions.

Rockenberger *et al.* [38] described the use of cupferron complexes as precursors to prepare γ-Fe_2O_3, Cu_2O and Mn_3O_4 nanocrystals. CoO nanocrystals with diameters in 4.5–18 nm range have been prepared by the decomposition of cobalt cupferronate in decalin at 543 K under solvothermal conditions [39]. Nanocrystals of MnO and NiO are obtained from cupferronate precursors under solvothermal conditions [40]. Nanocrystals of CdO

and CuO are prepared by the solvothermal decomposition of metal-cupferronate in presence of trioctylphosphine oxide (TOPO) in toluene [41]. ZnO nanocrystals have been synthesized from the cupferron complex by a solvothermal route in toluene solution [42]. γ-Fe_2O_3 and $CoFe_2O_4$ nanocrystals can also be produced by the decomposition of the cupferron complexes [43]. Metallic ReO_3 nanocrystals with diameters in the 8.5 - 2.5 nm range are obtained by the solvothermal decomposition of the Re_2O_7-dioxane complex under solvothermal conditions [44].

Apart from solvothermal methods, thermolysis of precursors in high boiling solvents, the sol–gel method, hydrolysis and use of micelles have been employed to synthesize the metal oxide nanocrystals. Thus, Park *et al.* [45] have used metal-oleates as precursors for the preparation of monodisperse Fe_3O_4, MnO and CoO nanocrystals. 1-Octadecene, octyl ether and trioctylamine have been used as solvents. Hexagonal and cubic CoO nanocrystals can be prepared by the decomposition of cobalt acetylacetonate in oleylamine under kinetic and thermodynamic conditions respectively [46]. Hexagonal pyramid-shaped ZnO nanocrystals have been obtained by the thermolysis of the Zn-oleate complex [47]. ZnO nanocrystals have been prepared from zinc acetate in 2-propanol by the reaction with water [48]. ZnO nanocrystals with cone (Figure 1.3.2), hexagonal cone and rod shapes have been obtained by the non-hydrolytic ester elimination sol–gel reactions [49]. In this reaction, ZnO nanocrystals with various shapes were obtained by the reaction of zinc acetate with 1, 12-dodecanediol in the presence of different surfactants. It has been found that reactions of alcohols such as ethanol and *t*-butanol with Zn powder readily yield ZnO nanocrystals [50].

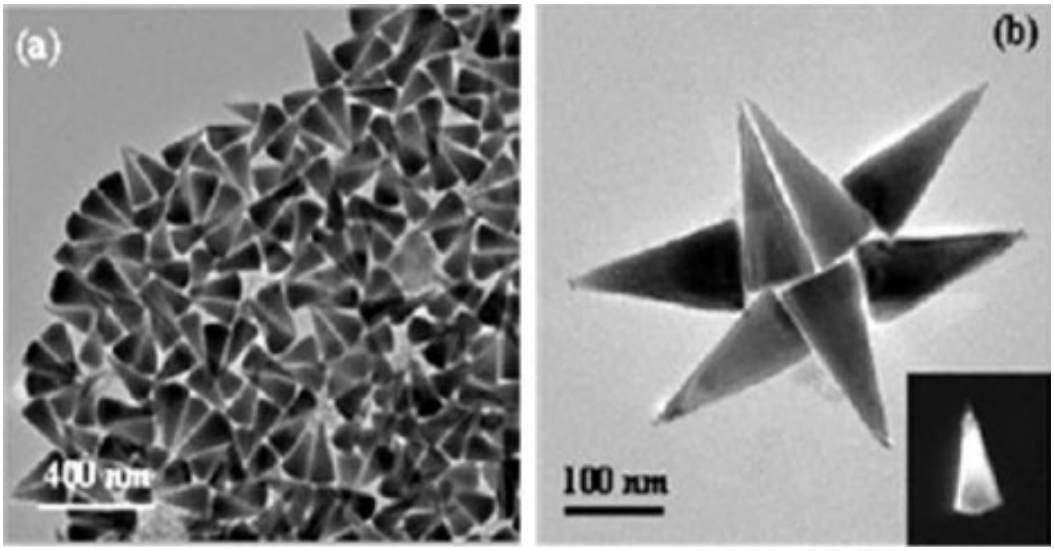

Figure 1.3.2: (a) and (b) TEM images of cone shaped ZnO nanocrystals. Inset in (b) shows a dark field image of a single cone-shaped nanocrystal [49].

Nanocrystals of $BaTiO_3$ are obtained by the thermal decomposition of MOCVD reagents (alkoxides such as $BaTi(O_2CC_7H_{15})[OCH(CH_3)_2]_5$) in diphenyl ether containing oleic acid, followed by the oxidation of the product with H_2O_2 [51]. Thermal decomposition of uranyl acetylacetonate in a mixture solution of oleic acid, oleylamine, and octadecene at 423 K gives uranium oxide nanocrystals [52]. Treatment of metal acetylacetonates under solvothermal conditions produces nanocrystals of metal oxides such as Ga_2O_3, ZnO and cubic In_2O_3 [53]. Nearly monodisperse In_2O_3 nanocrystals have been obtained starting with indium acetate, oleylamine and oleic acid [54]. TiO_2 nanocrystals can be prepared by the low-temperature reaction of low-valent organometallic precursors [55]. Pure anatase TiO_2 nanocrystals have been prepared by the hydrolysis of $TiCl_4$ with ethanol at 273 K followed by calcination at 360 K for 3 days [56]. The growth kinetics and the surface hydration chemistry have also been investigated.

Pileni and co-workers [57, 58] have pioneered the use of oil in water micelles to prepare particles of $CoFe_2O_4$, γ-Fe_2O_3, and Fe_3O_4. The basic reaction involving hydrolysis is now templated by a micellar droplet. The reactants are introduced in the form of a salt of a surfactant such as sodium dodecylsulfate (SDS). Thus, by adding CH_3NH_3OH to a micelle made of calculated quantities of $Fe(SDS)_2$ and $Co(SDS)_2$, nanocrystals of $CoFe_2O_4$ are obtained.

1.4 Synthesis of nanowires, nanorods and nanotubes

There has been considerable interest in the synthesis, characterization and properties of nanowires of various inorganic materials [1, 3]. Nanowires have been prepared using vapour phase methods such as vapour–liquid–solid (VLS) growth, vapour–solid (VS) growth, oxide-assisted growth and the use of carbothermal reactions. A variety of solution methods such as seed-assisted growth, polyol method, and oriented attachment have also been developed for the synthesis of one-dimensional nanostructures.

(a) Metals

Metal nanowires are commonly prepared using templates such as anodic alumina or polycarbonate membranes, carbon nanotubes and mesoporous carbon [59-62]. The nanoscale channels are first impregnated with metal salts and the nanowires obtained by reduction, followed by the dissolution of the template. Nanowires of metals and semiconductors have also been grown electrochemically. This method has been employed to prepare linear Au–Ag nanoparticle chains [63]. Here, sacrificial Ni segments are placed between segments of noble metals (Au, Ag). The template pore diameter fixes the nanowire width, and the length of each metal segment is independently controlled by the amount of current passed before switching to the next plating solution for deposition of

the subsequent segments. Nanowires are released by the dissolution of the template, and subsequently coated with SiO_2. Au nanorods and nanowires have been alternatively prepared by a simple solution based reduction method making use of nanoparticle seeds [64]. Au nanoparticles with ~4 nm diameter react with the metal salt along with the weak reducing agent such as ascorbic acid in the presence of a directing surfactant yielding Au nanorods. This method was extended to prepare dog-bone like nanostructures [65]. The reaction is carried out in two-steps, wherein the first step involves the addition of an insufficient amount of ascorbic acid to the growth solution, leaving some unreacted metal salt after the reaction, which is later deposited on the Au nanorods by the second addition of ascorbic acid. Addition of nitric acid enhances the proportion of Au nanorods with high aspect ratios (~20) in seed-mediated synthesis [66]. The growth of Au nanorods by the seed-assisted method does not appear to follow any reaction limited or diffusion limited growth mechanism [67]. A layer-by-layer deposition approach has been employed to produce polyelectrolyte-coated gold nanorods [68]. Au-nanoparticle modified enzymes act as biocatalytic inks for growing Au or Ag nanowires on Si surfaces by using a patterning technique such as dip-pen-nanolithography [69]. Single-crystalline Au nanorods shortened selectively by mild oxidation using 1 M HCl at 343 K [70]. Aligned Au nanorods can be grown on a silicon substrate by employing a simple chemical amidation reaction on NH_2-functionalized Si substrates [71]. A seed-mediated surfactant method using a cationic surfactant has been developed to obtain pentagonal silver nanorods [72]. A popular method for the synthesis of metal nanowires is the use of the polyol process, [73, 74] wherein the metal salt is reduced in the presence of PVP to yield nanowires of the desired metal. For example, Ag nanowires have been rapidly synthesized

using a microwave-assisted polyol method [75]. CoNi nanowires are obtained by heterogeneous nucleation in liquid polyol [76], while Bi nanowires have been prepared employing $NaBiO_3$ as the bismuth source [77]. Pd nanobars are synthesized by varying the type and concentration of reducing agent as well as reaction temperature [78]. Metal nanowires are obtained in good yields by the nebulized spray pyrolysis of a methanolic solution of metal acetates [79]. This method has been employed for the synthesis of single-crystalline nanowires of zinc, cadmium and lead. The nanowires seem to grow by the vapour–solid mechanism.

(a) Metal oxides

A seed-assisted chemical reaction at 368 K is found to yield uniform, straight, thin single-crystalline ZnO nanorods on a hectogram scale [80]. Zinc oxide nanowires have been synthesized in large quantities using plasma synthesis [81]. Variable-aspect-ratio, single crystalline, 1D nanostructures (nanowires and nanotubes) can be prepared in alcohol/water solutions by reacting Zn^{2+} precursor with an organic base, tetraammonium hydroxide [82]. It has been found recently that reaction of water with zinc metal powder or foils at room temperature gives ZnO nanowires [83]. A multi-component precursor has been used to produce nanoparticles and nanoribbons of ZnO [84]. Porous ZnO nanoribbons are produced by the self-assembly of textured ZnO nanoparticles. Nanobelts of ZnO can be converted into superlattice-structured nanohelices by a rigid lattice rotation or twisting [85]. Well-aligned crystalline ZnO nanorods along with nanotubes can be grown from aqueous solutions on Si wafers, poly(ethylene terephthlate) and sapphire [86]. Atomic layer deposition was first used to grow a uniform ZnO film on the substrate of choice and to serve as a templating seed layer for the subsequent growth of nanorods and

nanotubes. On this ZnO layer, highly oriented two-dimensional (2D) ZnO nanorod arrays were obtained by solution growth using $Zn(NO_3)_2$ and hexamethylenetetramine in aqueous solution. Controlled growth of aligned ZnO nanorod arrays has been accomplished by an aqueous ammonia solution method [87]. In this method, an aqueous ammonia solution of $Zn(NO_3)_2$ is allowed to react with a zinc-coated silicon substrate at a growth temperature of 333–363 K. 3-D interconnected networks of ZnO nanowires and nanorods have been synthesized by a high temperature solid–vapour deposition process [88]. Templated electrosynthesis of ZnO nanorods wherein, electroreduction of hydrogen peroxide or nitrate ions is carried out to alter the local pH within the pores of the membrane, with the subsequent precipitation of the metal oxide within the pores [89]. 1-D ZnO nanostructures have been synthesized by oxygen assisted thermal evaporation of zinc on a quartz surface over a large area [90]. Pattern- and feature-designed growth of ZnO nanowire arrays for vertical devices has been accomplished by following a pre-designed pattern and feature with controlled site, shape, distribution and orientation [91]. In figure 1.4.1 we have shown SEM images of ZnO nanostructures.

The ionic liquid 1-*n*-butyl-3-methylimidazolium tetrafluoroborate has been used to synthesize nanoneedles and nanorods of manganese dioxide (MnO_2) [92]. Crystalline silica nanowires were prepared by Deepak *et al.* [93] by a carbothermal procedure. Crystalline SiO_x nanowires have also been prepared by a low temperature iron assisted hydrothermal procedure [94].

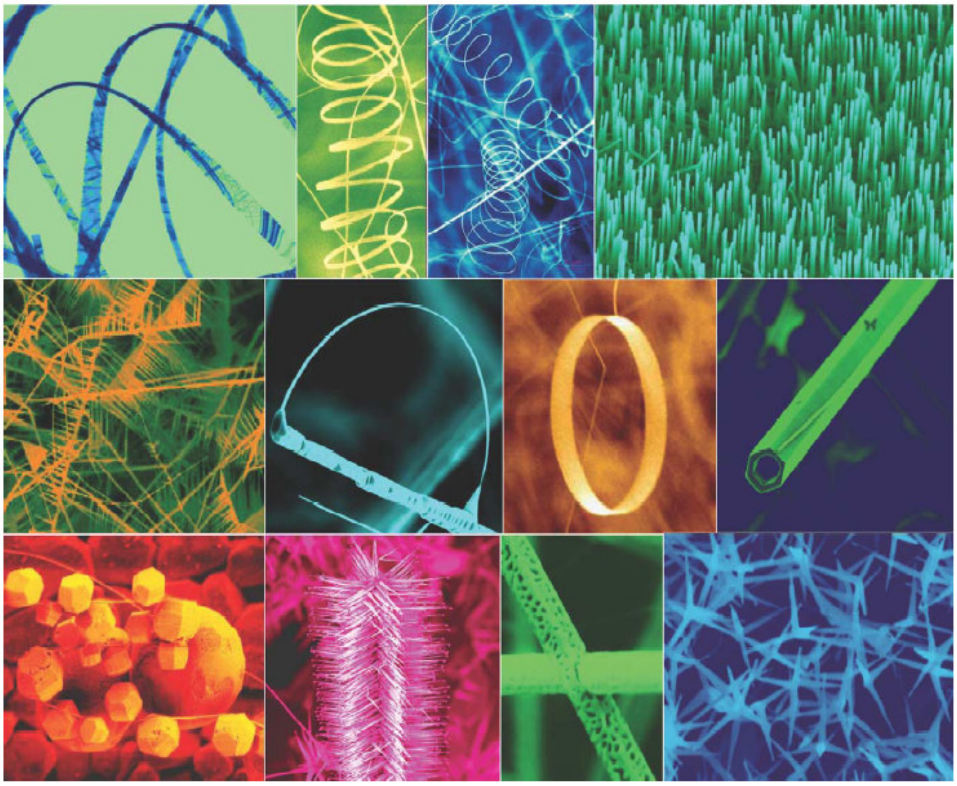

Figure 1.4.1: SEM images of ZnO nanostructures [85].

IrO_2 nanorods can be grown by metal–organic chemical vapour deposition on sapphire substrates consisting of patterned SiO_2 as the non-growth surface [95]. By employing the hydrothermal route, uniform single-crystalline $KNbO_3$ nanowires have been obtained [96]. MgO nanowires and related nanostructures have been produced by carbothermal synthesis, starting with polycrystalline MgO or Mg with or without the use of metal catalysts [97]. This study has been carried out with different sources of carbon, all of them yielding interesting nanostructures such as nanosheets, nanobelts, nanotrees and aligned nanowires. Orthogonally branched single crystalline MgO nanostructures

have been obtained through a simple chemical vapour transport and condensation process in a flowing Ar/O_2 atmosphere [98].

Ga_2O_3 powder reacts with activated charcoal, carbon nanotubes or activated carbon around 1373 K in flowing Ar to give nanowires, nanorods and other novel nanostructures of Ga_2O_3 such as nanobelts and nanosheets [99]. Catalyst-assisted VLS growth of single-crystal Ga_2O_3 nanobelts has been accomplished by graphite-assisted thermal reduction of a mixture of Ga_2O_3 and SnO_2 powders under controlled conditions [100]. Zig-zag and helical one-dimensional nanostructures of α-Ga_2O_3 have been produced by the thermal evaporation of Ga_2O_3 in the presence of GaN [101]. Large scale synthesis of TiO_2 nanorods has been achieved by the non-hydrolytic sol–gel ester elimination reaction, wherein the reaction is carried out between titanium(IV) isopropoxide and oleic acid [102]. Single-crystalline and well facetted VO_2 nanowires with rectangular cross sections have been prepared by the vapour transport method, starting with bulk VO_2 powder [103]. Copious quantities of single-crystalline and optically transparent Sn-doped In_2O_3 (ITO) nanowires have been grown on gold-sputtered Si substrates by carbon-assisted synthesis, starting with a powdered mixture of the metal nitrates or with a citric acid gel formed by the metal nitrates [104]. Vertically aligned and branched ITO nanowire arrays, which are single-crystalline, have been grown on yttrium stabilized zirconia substrates containing thin gold films of 10 nm thickness [105].

Bicrystalline nanowires of hematite (α-Fe_2O_3) have been synthesized by the oxidation of pure Fe [106]. Single-crystalline hexagonal α-Fe_2O_3 nanorods and nanobelts can be prepared by a simple iron–water reaction at 673 K [107]. Mesoporous quasi-single crystalline nanowire arrays of Co_3O_4 have been grown by immersing Si or fluorine doped

SnO_2 substrates in a solution of $Co(NO_3)_2$ and concentrated aqueous ammonia [108]. Networks of WO_{3-x} nanowires are obtained by the thermal evaporation of W powder in the presence of oxygen [109]. A general and highly effective one-pot synthetic protocol for producing one-dimensional nanostructures of transition metal oxides such as$W_{18}O_{49}$, TiO_2, Mn_3O_4 and V_2O_5 through a thermally induced crystal growth process starting from mixtures of metal chlorides and surfactants has been described [110]. Self-coiling nanobelts of $Ag_2V_4O_{11}$ have been obtained by the hydrothermal reaction between $AgNO_3$ and V_2O_5 [111]. Polymer assisted hydrothermal synthesis of single crystalline tetragonal perovskite PZT ($PbZr_{0.52}Ti_{0.48}O_3$) nanowires has been carried out [112]. Nanowires of the type II superconductor $YBa_2Cu_4O_8$ have been synthesized by a biomimetic procedure [113]. The nanowires produced by the calcination of a gel containing the biopolymer chitosan and Y, Ba and Cu salts have mean diameters of 50±5 nm with lengths up to 1 μm. Nanorods of V_2O_5 prepared by the polyol process self-assemble into microspheres [114].

1.5 Synthesis of Carbon nanotubes

Carbon nanotubes, first observed in 1991 [115], occur as multiwalled nanotubes (MWNTs) and single-walled nanotubes (SWNTs) [116]. Primary methods for CNTs synthesis include arc-discharge [115, 117], laser ablation [118], gas-phase catalytic growth from carbon monoxide [119], and chemical vapor deposition (CVD) from hydrocarbons [120–122]. Because impurities in the form of catalyst particles, amorphous carbon, and nontubular fullerenes are also produced during CNTs synthesis, subsequent purification steps are required to separate the tubes. The gas-phase processes tend to

produce nanotubes with fewer impurities and are more amenable to large-scale processing.

The arc-discharge technique generally involves the use of two high purity graphite rods as the anode and cathode. The rods are brought together under a helium atmosphere and a voltage is applied until a stable arc is achieved. The exact process variables depend on the size of the graphite rods. As the anode is consumed, a constant gap between the anode and cathode is maintained by adjusting the position of the anode. The material deposits on the cathode to form a buildup consisting of an outside shell of fused material and a softer fibrous core containing nanotubes and other carbon particles. To create SWNTs, the electrodes are doped with a small amount of catalyst particles [116, 117, 123 – 125].

Initially used for the production of fullerenes, laser ablation technique has, over the years, been improved to allow the production of SWNTs [118, 126, 127]. In this technique, a graphite target held in a controlled atmosphere oven at temperatures near 1200 °C is vaporized by a laser and the vapors condensed over a water-cooled target. To produce SWNTs, the graphite target is doped with a catalyst [118].

Both the arc-discharge and the laser ablation techniques produce a limited volume of sample in relation to the size of the carbon source (the anode in arc-discharge and the target in laser ablation) and require subsequent purification steps to separate the tubes from undesirable byproducts. These limitations have motivated the development of gas-phase techniques, such as chemical vapor deposition (CVD), in which nanotubes are formed by the decomposition of a hydrocarbon or carbon monoxide gas. The gas-phase techniques are amenable to continuous processes since the carbon source is continually

replaced by flowing gas. In addition, the purity of the as-produced nanotubes can be relatively high, minimizing subsequent purification steps. Nikolaev et al. described the gas-phase growth of SWNTs with carbon monoxide as the carbon source [119]. They reported that the highest yields of SWNTs occurred at the high temperature and pressure (1200 °C, 10 atm). Smalley and his co-workers have refined the process to produce large quantities of SWNTs with increased purity. Other gas-phase techniques utilize hydrocarbon gases as the carbon source for production of both single and multi-walled carbon nanotubes [128 – 131]. Figure 1.5.1 shows TEM images of MWNTs, DWNTs and SWNTs.

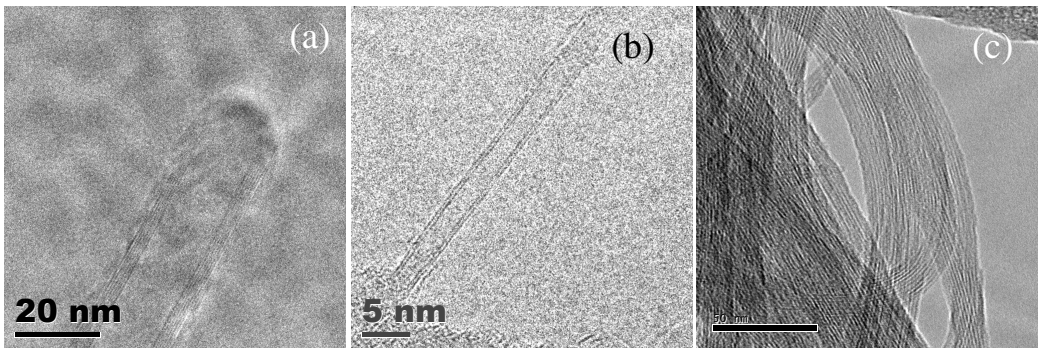

Figure 1.5.1: TEM images of (a) multi-walled, (b) double-walled and (c) single-walled carbon nanotubes.

1.6 Properties and applications

One-dimensional semiconductor nanowires and nanorods have attracted increasing attention due to their physical properties arising from quantum confinement (such as electronic quantum transport and enhanced radiative recombination of carriers). Nanowires have promising potentials in extensive applications and are the fundamental building blocks for fabricating short-wavelength nanolasers, field-effect transistors, solar cells, ultrasensitive nanosized gas sensors, biosensors, nanoresonators, transducers, actuators, nanocantilevers, and field emitters [132-136]. These nanostructures are the

ideal systems for studying transport mechanisms in 1D systems, which are of benefit not only for understanding the fundamental phenomena in low-dimensional systems but also for developing new generation nanodevices with high performance. Many nanowires made of materials such as Si, C, InP, GaAs, CdS, SnO_2, TiO_2, GaN, ZnO, WO_3 and In_2O_3 have been fabricated for different applications using different synthetic methods [136-145]. Among these materials ZnO is considered to be the most prospective one due to its large exciton binding energy (60 meV), high electromechanical coupling constant, and resistivity to harsh environment. Therefore, 1D ZnO structures stimulated so much attention, and a large number of publications have appeared lately reporting nanostructures of various shapes (nanowires, nanobelts, nanorings, nanotubes, nanopropellers, etc.) grown by different methods.

In recent years, carbon nanotubes have been intensively studied due to their importance as building blocks in nanotechnology. The special geometry and unique properties of carbon nanotubes offer great potential applications, including nanoelectronic devices, energy storage, chemical probes and biosensors, field emission displays [146, 147]. Also considerable experimental and theoretical efforts have been devoted to hydrogen storage in nanotube-based materials [148-150].

Graphene, a recently discovered single sheet of graphite, has received considerable attention for its excellent thermal, mechanical and electrical properties [151-154]. The in-plane thermal conductivity and Young's modulus of graphene are ~ 3,000 $Wm^{-1}K^{-1}$ and 1,600 GPa respectively [154]. Being a nearly perfect two-dimensional electron gas, it has mobilities as high as 20, 000 cm^2/V s, which give rise to ballistic transport on the 100 nm scale even at room temperature [155]. Furthermore, the unique "quasi-relativistic" carrier

dynamics in graphene provides new transport phenomena, ready to be explored for novel device applications.

1.6.1 ZnO nanostructures

The crystal structures formed by ZnO are wurtzite, zinc blende and rocksalt. Among these, wurtzite structure (Figure 1.6.1), where each anion (O_2^-) is surrounded by four cations (Zn^{2+}) at the corners of tetrahedron, and vice versa, is thermodynamically more stable phase at ambient conditions. This tetrahedral coordination is typical of sp^3 covalent bonding. But these materials also have a substantial ionic character, which falls at the borderline between covalent and ionic semiconductor.

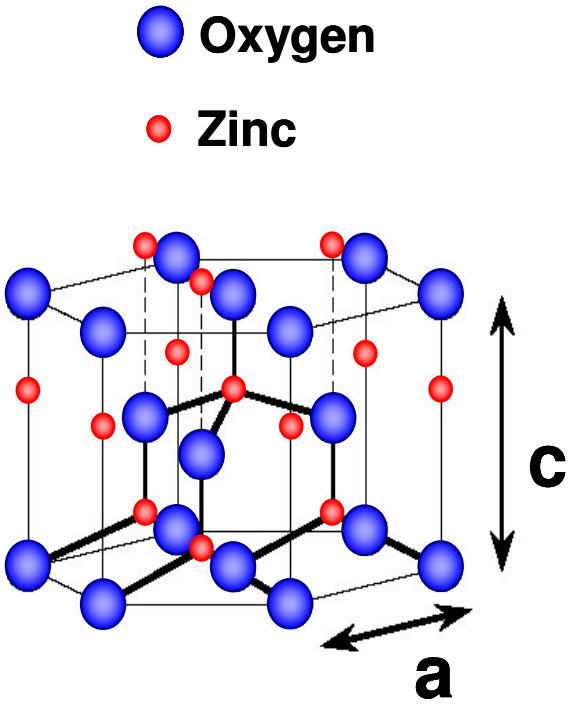

Figure 1.6.1: Wurtzite crystal structure of ZnO [136].

ZnO shows intrinsic n-type conductivity with very high electron density of 10^{21} cm^{-3}, which is due to availability of lot of oxygen vacancies and Zn interstitials. ZnO has a relatively open structure, with a hexagonal close packed lattice where Zn atoms occupy

half of the tetrahedral sites. All the octahedral sites are empty. Hence, there are plenty of sites for ZnO to accommodate intrinsic (namely Zn interstitials) defects and extrinsic dopants. The electronic energy levels of native imperfections in ZnO are illustrated in figure 1.6.2. There are a number of intrinsic defect states within the bandgap of ZnO. The donor defects are: $Zn_i^{\bullet\bullet}$, $Zn_i^{\bullet}$, Zn_i^{x}, $V_o^{\bullet\bullet}$, $V_o^{\bullet}$, V_o and the acceptor defects are: V''_{Zn}, V'_{Zn}. The defect ionization energies vary from –0.05-2.8 eV [156]. Zn interstitials and oxygen vacancies are known to be the predominant ionic defect types. However, which defect dominates in native, undoped ZnO is still a matter of controversy [157].

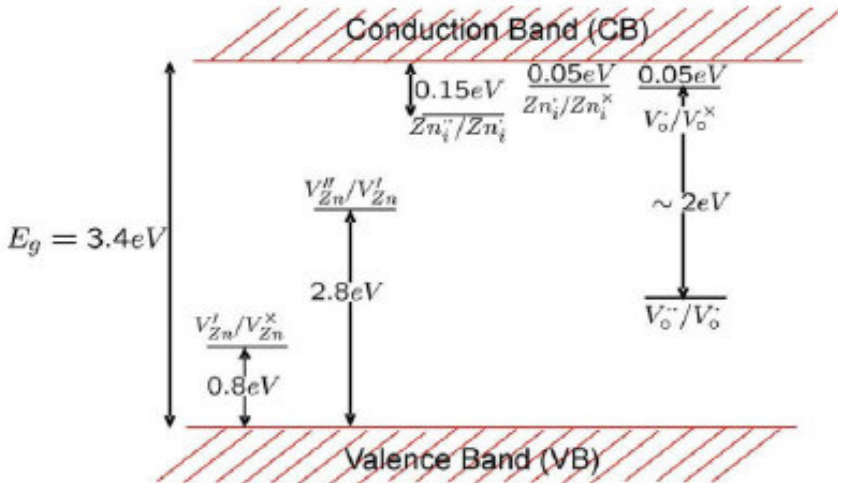

Figure 1.6.2: Energy levels of native defects in ZnO. The donor defects are $Zn_i^{\bullet\bullet}$, $Zn_i^{\bullet}$, Zn_i^{x}, $V_o^{\bullet\bullet}$, $V_o^{\bullet}$, V_o and the acceptor defects are V''_{Zn}, V'_{Zn}.(The Kroger Vink notation is used: i=interstitial sites, Zn=zinc, O=oxygen, V= vacancy. The terms indicate the atomic sites, superscripted terms indicate charges, where a dot indicates a positive charge, a prime indicates a negative charge, and a cross indicates zero charge, with the charges in proportion to the number of symbols [158].

(a) Lasing action

Room temperature PL spectra of ZnO nanowires showed a strong band-edge emission at ~380 nm [132-135]. In addition, a very weak blue band (440-480 nm) and an almost negligible green band (510-580 nm) were observed. These samples were explored

to for possible stimulated emission by measuring the excitation density-dependent emission with excitation from the fourth harmonic of a Nd:yttrium-aluminium-garnet (Nd:YAG) laser. Light emission was collected in the direction normal to the end surface plane (along the c-axis) of the nanowires and lasing was observed in the absence of any fabricated mirrors with increasing pump power as shown in figure 1.6.3.

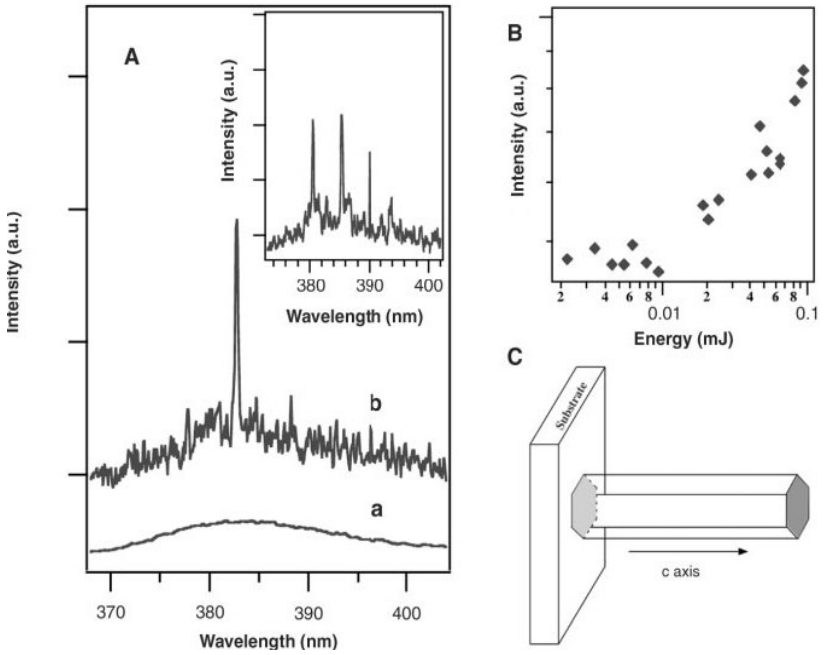

Figure 1.6.3: (A) Emission spectra from nanowire arrays below (line a) and above (line b and inset) the lasing threshold. The pump power for these spectra are 20, 100, and 150 kW/cm^2, respectively. (B) Integrated emission intensity from nanowires as a function of optical pumping energy intensity. (C) Schematic illustration of a nanowire as a resonance cavity [159].

(b) Light emitting diodes (LEDs)

ZnO is considered as a prospective material for fabricating LED structures emitting in the UV region, because of its large exciton binding energy (60 meV). As the growth of reproducible p-type ZnO is not developed yet, different groups have utilized heterojunctions of ZnO nanostructures for the fabrication of LEDs [136]. Yi and coworkers employed p-GaN for the fabrication of n-ZnO/p-GaN nanorod

electroluminescent (EL) devices [160]. p-n heterojunctions based on nanorods of ZnO on p-Si have been studied 161, 162]. Also p-type manganite films [163], strongly p-doped polymers have been employed to fabricate p-n heterojunctions based on ZnO nanostructures [164-167].

(c) Field emission

Field emission properties of the aligned nanorods have been studied [168]. The measurements showed a fairly low turn-on and threshold fields of 2.5 and 4.0 V/mm, respectively. The nanosize perturbations on the nanoneedle tips are assumed to cause such excellent performance. The high emission current density, high stability, and low turn-on field make the ZnO nanorod arrays one of the promising candidates for high brightness field-emission electron source and flat-panel displays.

(d) Field effect transistors (FETs)

ZnO nanorods [169-171], nanowires [172-176] and nanobelts [177] have been successfully utilized for FET fabrication. High performance n-channel FETs with back gate geometry were fabricated using e-beam lithography along with high quality ZnO nanorods prepared by catalyst-free MOVPE [169]. The nanorods were dispersed on SiO_2/Si substrates where the 250 nm thick SiO_2 layer was used as gate dielectric on heavily doped Si and a source-drain electrode of 2-5 μm prepared by e-beam lithography and lift-off method has been employed. The FETs exhibited a transconductance of 140 nS and a mobility of 75 cm^2/V.s. The transconductance of 1.9 μS and electron mobility of 1000 cm^2/V.s have been achieved by coating the nanorod surface with a polyamide thin layer. Noh *et al.* [174] have demonstrated a top-gated ZnO nanowire FET fabricated by ink-jet printing technique, where they have used poly (methyl methacrylate) (PMMA) as

gate dielectric and PEDOT/PSS layer as gate electrode. A transconductace of 513 nS and a mobility of 21.3 cm^2/V.s have been found for a FET with 2 μm channel length. A typical ZnO nanobelt FET showed a gate threshold voltage of –15 V, a peak conductivity of 1.25 $\times 10^{-3}$ $\Omega^{-1}cm^{-1}$ [177]. Single crystalline ZnO nanowires with a circular cross section and omega-shaped gate FET have been utilized to fabricate nanowire devices by bottom gate configuration (Figure 1.6.4) [178, 179]. ZnO nanowire FETs using a self-assembled nanodielectric organic gate insulator have been demonstrated [180, 181]. The field effect behavior of nanocomposite FET containing ZnO nanowires dispersed in a polymer matrix of MEH-PPV has been studied [182].

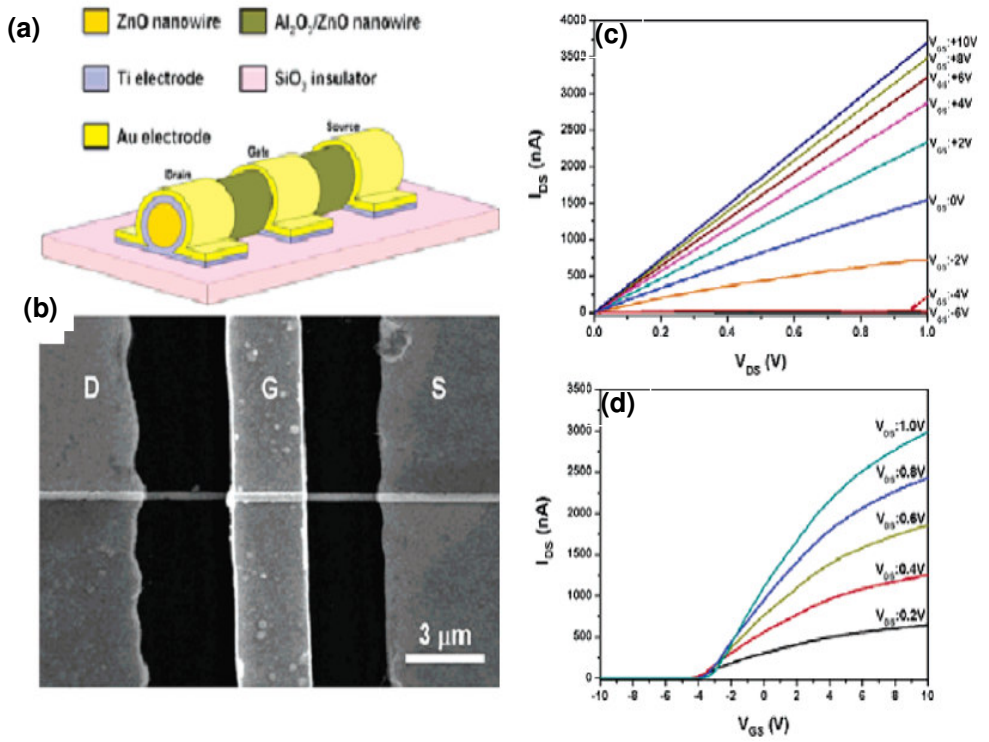

Figure 1.6.4: (a) Schematic and (b) top view SEM image of the Omega-Shaped-Gate FET fabricated by the photolithographic process, typical output and transfer characteristics obtained from the Omega-Shaped-Gate FET: (c) I_{DS} vs V_{DS} characteristics for V_{GS} values ranging from –6 to +10 V; (d) I_{DS} vs V_{GS} characteristics for V_{DS} values ranging from 0.2 to 1 V [179].

(e) Solar cells

Recently, ZnO has been used in dye-sensitized solar cells as an electrode material [183]. Investigations of nanoporous dye-sensitized ZnO films have shown that ultrafast electron injection from the dye into the conduction band of the ZnO nanostructures takes place [184], comparable to the timescale of electron injection into TiO_2 layers, which has been the subject of investigation for a long time [185]. Semiconductors should have a wide bandgap, high charge carrier mobility, and films fabricated from the material need to deliver a high surface area for efficient dye-sensitization and light harvesting, which can only achieved by nanostructured film. Therefore, ZnO seems to be a promising material for this type of solar cell and has the advantage over the metal oxides of easy synthesis of controlled nanostructures.

(f) Nano-generator

A nanowire nanogenerator based on vertically aligned ZnO nanowires have been reported [186], which is driven by an ultrasonic wave to produce continuous direct current output. The nanogenerator was fabricated with vertically aligned zinc oxide nanowire arrays that were placed beneath a zigzag metal electrode with a small gap (Figure 1.6.5). The wave drives the electrode up and down to bend and/or vibrate the nanowires. A piezoelectric semiconducting coupling process converts mechanical energy into electricity. The zigzag electrode acts as an array of parallel-integrated metal tips that simultaneously and continuously create, collect, and output electricity from all of the nanowires. The approach presents an adaptable, mobile, and cost-effective technology for harvesting energy from the environment, and it offers a potential solution for powering nanodevices and nanosystems.

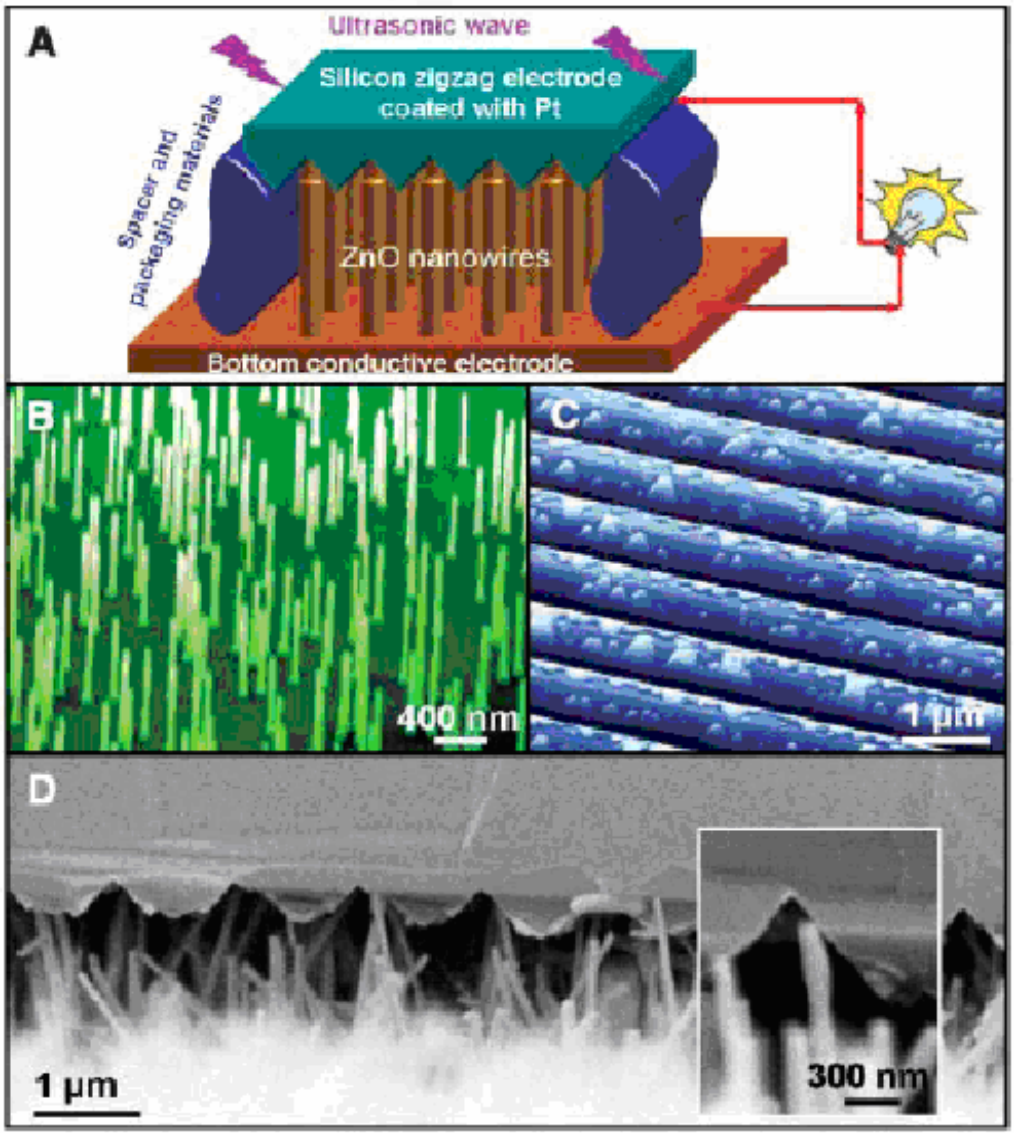

Figure 1.6.5: Nanogenerators driven by an ultrasonic wave. (A) Schematic diagram showing the design and structure of the nanogenerator. Aligned ZnO NWs grown on a solid/polymer substrate are covered by a zigzag electrode. The substrate and the electrode are directly connected to an external load. (B) Aligned ZnO NWs grown on a GaN substrate. The gold catalyst particles used for the growth had been mostly vaporized; thus, the final NWs were purely ZnO with flat top ends. (C) Zigzag trenched electrode fabricated by the standard etching technique after being coated with 200 nm of Pt. The surface features are due to nonuniform etching. (D) Cross-sectional SEM image of the nanogenerator, which is composed of aligned NWs and the zigzag electrode. (Inset) A typical NW that is forced by the electrode to bend [186].

(g) Chemical and bio-sensors

Semiconducting metal oxides have been widely used for sensing various gases and vapors. Among the oxides, ZnO has emerged to become one of the prime material for sensing applications. In the last few years, nanostructures of ZnO have been found to be effective as gas-sensing materials. Due to the interesting properties of the nanostructures, including rods, wires, tubes and belts, it provides many opportunities to study their interesting sensing behavior by making new types of nanosensing structures.

ZnO nanorods synthesized by low temperature chemical solution route [187], solvothermal method [188, 189], solid-state reaction method [190] have been studied for NH_3, H_2S, ethanol and H_2 sensing characteristics. Hydrogen sensing characteristics at room temperature with Pd, Pt coated ZnO nanorods have been investigated [191, 192]. The Pd-coated ZnO nanorods detected H_2 down to < 10 ppm, approximately a factor of 5 larger than without Pd. Pt-coated ZnO nanorods show a current response of approximately a factor of 3 larger at room temperature upon exposure to 500 ppm H_2 in N_2 than the thin films of ZnO. Multipod shaped ZnO nanorods [193] sensor showed higher sensitivity compared to needle like nanorods [194], since at a common junction resulted in a very large surface area and therefore their sensing properties related to the surface reactions could be greatly enhanced. One-dimensional ZnO nanostructures such as nanowires [195], nanonails, nanotrees [196], nanocombs [197] and nanotetrapods [198] have been synthesized by oxygen assisted thermal evaporation of zinc metal and by vapor phase techniques at high temperature, and its H_2S, NO_2, CO, H_2, NH_3, ethanol, acetone, humidity sensing characteristics have been studied. The highest sensitivity is observed in the case of ethanol and acetone. ZnO nanowire sensors have been fabricated with micromechanical system technology and ethanol-sensing characteristics have been

investigated [199, 200]. Optical and conductometric NO_2 sensors have been fabricated using single crystal ZnO nanowires [201]. Vertically aligned nanowire arrays on substrates have been synthesized by thermal evaporation process [202], hydrothermal method [203], and by metal organic chemical vapor deposition method [204] and NO_2, methanol, H_2, NH_3, CO, O_2 sensing characteristics have been studied. Cd-doped ZnO nanowires synthesized by thermal evaporation method, showed a resistance change of more than three orders of magnitude when it was exposed to a pulse of 95% relative humidity [205]. pH sensor [206], Cholesterol sensor [207] and uric acid sensor [208] based on ZnO nanorods have been fabricated.

1.6.2 Carbon nanotubes

Multi-walled nanotubes (MWNTs) can be conceived as multi-layered concentric cylinders of single graphitic (graphene) sheets. The diameter of the inner tube is of the order of a few nanometers while the outermost tubes could be as large as 10-30 nm. Helicity is introduced during the curling of a graphene sheet, which is well established by the electron diffraction studies. This suggests that the growth of the nanotubes occurs as in the spiral growth of crystals. Concentric cylinders in MWNTs are separated by about 3.45 Å, which is close to the separation between the (002) planes of graphite. CNTs being capped by dome-shaped hemispherical fullerene-type units do not have dangling bonds at their tips as is generally expected of the graphitic cylinders. A single-walled (SWNT) is formed by rolling a sheet of graphene into a cylinder along a lattice vector in the graphene plane. Various chiral tubes can be formed with the screw axis along the axis of the tube. The models of the three types of nanotubes: zigzag, armchair and chiral nanotubes are shown in figure 1.6.6.

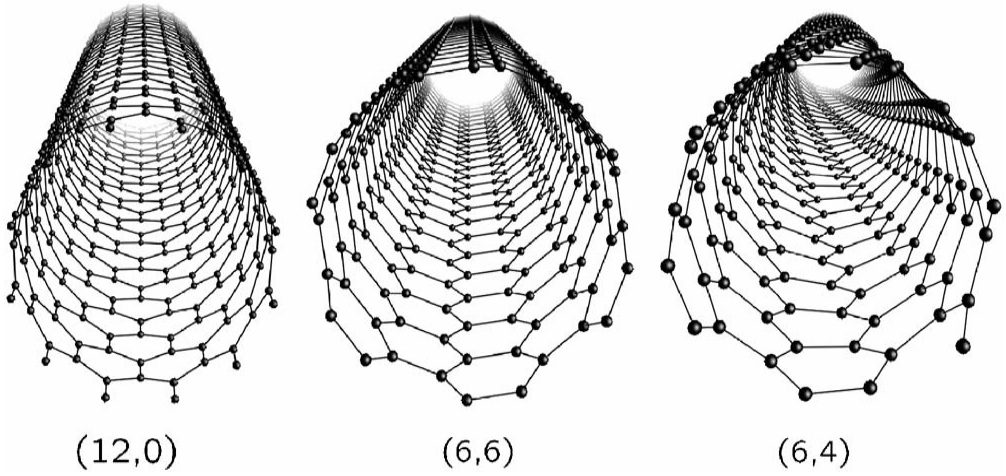

Figure 1.6.6: atomic structures of (12, 0) zigzag, (6, 6) armchair and (6, 4) chiral nanotubes.

Nanotubes can be defined by a chiral angle θ and a chiral vector **C,** given by

$$\mathbf{C} = n\mathbf{a_1}+m\mathbf{a_2} \qquad (1.6.1)$$

The vector **C** connects two crystallographically equivalent sites on a 2D graphene sheet and the chiral angle is the angle it makes with respect to the zigzag direction (Figure 1.6.7). $\mathbf{a_1}$ and $\mathbf{a_2}$ are unit vectors in a 2D graphene lattice and n and m are integers. Several possible chiral vectors can be specified by equation 1.6.1 in terms of pairs of integers (n, m). Many such pairs are shown in figure 1.6.7. The limiting cases are $n = m \neq 0$ (armchair tube) and $n \neq 0$, $m=0$ (zigzag tube). For a nanotube defined by the index (n, m), the diameter, d, and the chiral angle, θ, are given in following equations 1.6.2 and 1.6.3, where $a=1.42\ (3)^{1/2}$ and $0 \leq \theta \leq 30°$.

$$d= a\ (m^2 + mn + n^2)^{1/2}/\pi \qquad (1.6.2)$$

$$\theta = \arctan\ [-(3)^{1/2}\ m]/2n + m \qquad (1.6.3)$$

The (n, m) indices determine the nanotube electronic structure. Armchair SWNTs are metals with n-m=3q, where q is a nonzero integer, are semiconductors with tiny bandgap; and all others are semiconductors with a band gap that inversely depend on nanotube diameter. SWNT for which |n-m|=3q are metallic, and those for which |n-m|=3q±1 are Semiconducting. Thus, we see that 2/3 of the nanotubes correspond to Semiconducting and 1/3 to metallic nanotubes.

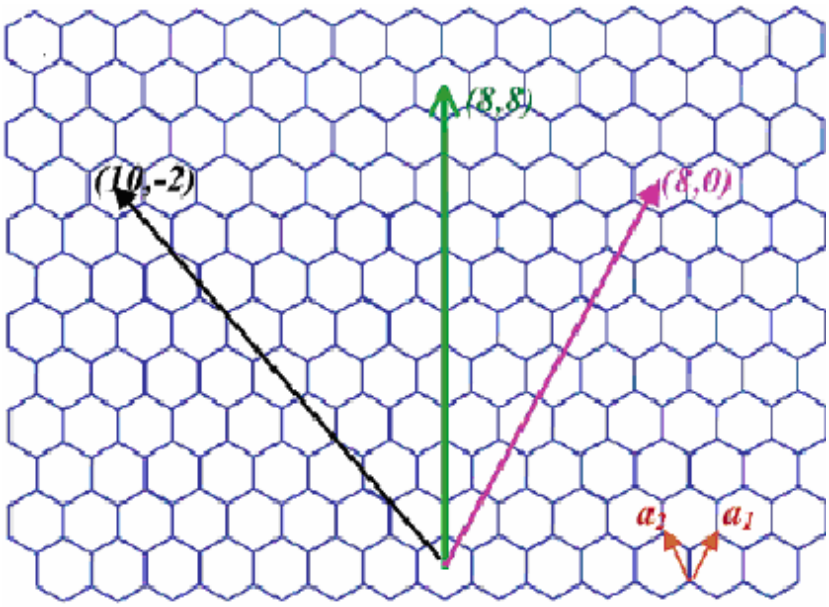

Figure 1.6.7: Schematic honeycomb structure of a graphene sheet. Single-walled carbon nanotubes can be formed by folding the sheet along lattice vectors. The two basis vectors $\mathbf{a}_1$ and $\mathbf{a}_2$ are shown.

Among the various characterization techniques, Raman spectroscopy, electron microscopy, diffraction techniques, UV-Vis spectroscopy are the most extensively used. The XRD pattern of MWNTs shows only the (hk0) and the (001) reflections but no (hkl) reflections [209]. Lot of information regarding the structure of the nanotubes can be (and has already been) acquired from Raman spectroscopy. Using a zone-folding model, Jishi

et al. [210] have calculated the Raman active phonon modes in the nanotubes. The diameter and the chiral angle of the tube determine the frequency of the allowed modes. Rao *et al.* [211] observed the diameter selective resonance behavior of SWNTs. Resonant Raman spectroscopy on isolated nanotubes has been used to determine the index (n, m) of the nanotube [212].

(a) Field emission

CNTs are the best known field emitters of any material [213, 214]. This is understandable, given their high electrical conductivity, and the incredible sharpness of their tip (because the smaller the tip's radius of curvature, the more concentrated will be an electric field, leading to increased field emission; this is the same reason lightning rods are sharp). The sharpness of the tip also means that they emit at especially low voltage, an important fact for building low-power electrical devices that utilize this feature. CNTs can carry an astonishingly high current density, possibly as high as 1013 A/cm^2. Furthermore, the current is extremely stable. An immediate application of this behavior receiving considerable interest is in field emission flat-panel displays.

(b) Supercapacitors and actuators

Because of the high electrochemically accessible surface area of porous nanotube arrays, combined with their electronic conductivity and useful mechanical properties these materials are attractive as electrodes for devices that use electrochemical double-layer charge injection. Examples include supercapacitors, which have giant capacitances in comparison with those of ordinary dielectric based capacitors [215, 216]. These capacitances (typically between ~15 and ~200 Fg^{-1}, depending on the surface area of the carbon nanotube arrays) result in large amounts of charge injection when a few volts are

applied. Nanotube electromechanical actuators function at a few volts, compared with the ~100 V used for piezoelectric stacks and the ~ 1000 V used for electrostrictive actuators.

(c) Field effect transistors and related devices

FETs based on SWNTs have been fabricated [217-221]. In nanotube field effect transistors (NTFETs), gating has been achieved by applying a voltage to a submerged gate beneath a SWNT (Figure 1.6.8), which was contacted at opposite nanotube ends by metal source and drain leads [217]. The transistors were fabricated by lithographically applying electrodes to nanotubes that were either randomly distributed on a silicon substrate or positioned on the substrate with an atomic force microscope [218, 219].

(d) Chemical and biological sensors

Possible chemical sensor applications of nonmetallic nanotubes are interesting, because nanotube electronic transport and thermo power (voltages between junctions caused by interjunction temperature differences) are very sensitive to substances that affect the amount of injected charge [222, 223]. The main advantages are the minute size of the nanotube sensing element and the correspondingly small amount of material required for a response. The analyte-nanotube interaction may have one of two effects. The first effect involves charge transfer from analyte molecule to carbon nanotubes. In the second type of mechanism, the analyte acts as a scattering potential across the carbon nanotube. It is possible to distinguish between mechanisms by taking transistor measurements [224]. If a charge transfer occurs, the threshold voltage will become either more positive (electron withdrawing) or more negative (electron donating). In addition, a scattering mechanism may be observed from an overall drop in conductance. This is because of the scattering effect induced by the target analyte [224].

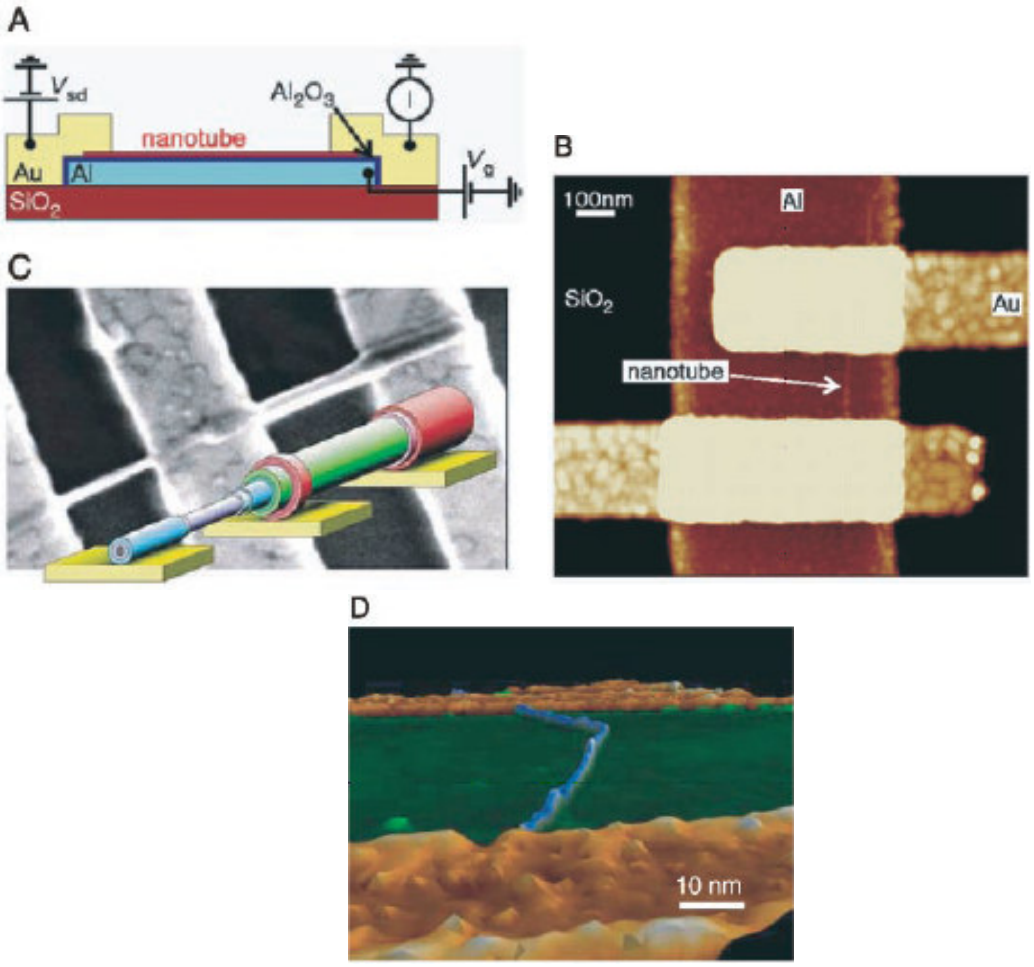

Figure 1.6.8: Nanoelectronic devices. (**A**) Schematic diagram [219] for a carbon NT-FET. The Semiconducting nanotube, which is on top of an insulating aluminum oxide layer, is connected at both ends to gold electrodes. The nanotube is switched by applying a potential to the aluminum gate under the nanotube and aluminum oxide. V_{sd}, source-drain voltage; V_g, gate voltage. (**B**) Scanning tunneling microscope (STM) picture of a SWNT field-effect transistor [219] made using the design of (A). The aluminum strip is over coated with aluminum oxide. (**C**) Image and overlaying schematic representation [221] for the effect of electrical pulses in removing successive layers of a MWNT, so that layers having desired transport properties for devices can be revealed. (**D**) STM image [220] of a nanotube having regions of different helicity on opposite sides of a kink, which functions as a diode; one side of the kink is metallic, and the opposite side is semiconducting. The indicated scale bar is approximate.

1.6.3 Graphene

Graphene is the name given to a flat monolayer of carbon atoms tightly packed into a 2D honeycomb lattice, and is basic building block for graphitic materials of all other dimensionalities [Figure 1.6.9]. It can be wrapped up into 0D fullerenes, rolled into 1D nanotubes or stacked into 3D graphite.

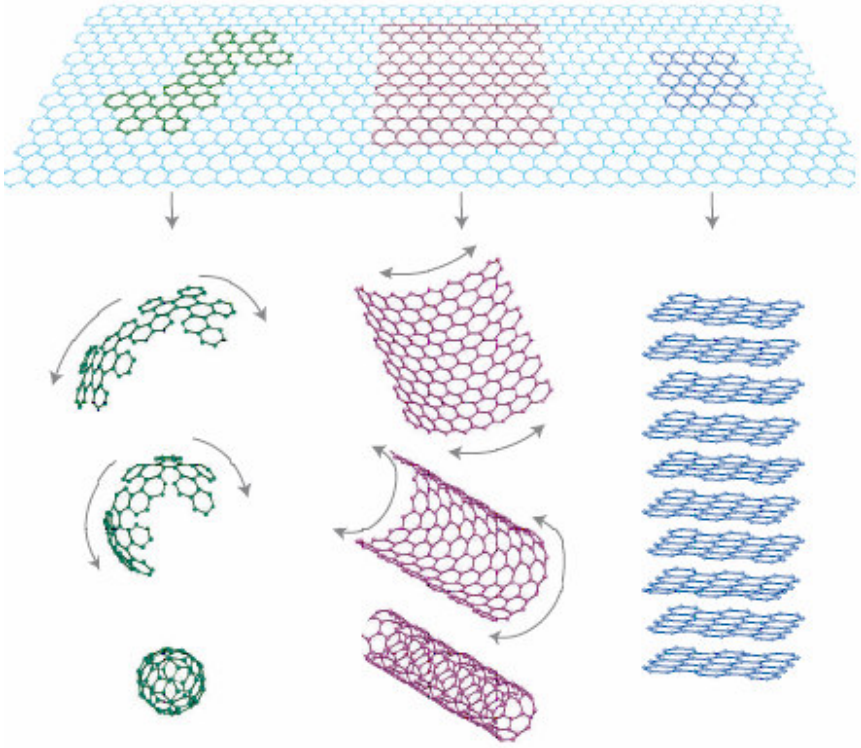

Figure 1.6.9: Mother of all graphitic forms. Graphene is a 2D building material for carbon materials of all other dimensionalities. It can be wrapped up into 0D buckyballs, rolled into 1D nanotubes or stacked into 3D graphite [155].

Top- and bottom-gated, single or few-layer graphene field effect transistors (FETs) have been fabricated [225]. SiO_2 layer is used as the gate dielectric and the measured electron and hole mobilities on these fabricated graphene FETs are as high as ~5400 cm^2/V s.

Graphene based gas sensors allow the ultimate sensitivity such that the adsorption of individual gas molecules could be detected [226, 227]. NH_3, CO and NO_2 sensors based on graphene have been fabricated [226]. Nano-graphene has been investigated as a sensing material using a highly sensitive potentiometric detection technique. Functionalised graphene could detect NO_2 down to 60 ppb in ambient condition with much shorter response time [227].

The room temperature values of the thermal conductivity in the range ~4.84×10^3 to 5.3×10^3 W/mK were extracted for a single-layer graphene from the dependence of the Raman G peak frequency on the excitation laser power and independently measured G peak temperature coefficient [228]. The extremely high value of the thermal conductivity suggests that graphene can outperform carbon nanotubes in heat conduction.

Transparent, conductive, and ultrathin graphene films have been employed as the electrode for solid-state dye-sensitized solar cells [229]. The obtained films exhibit a high conductivity of 550 S/cm and a transparency of more than 70% over 1000-3000 nm. Furthermore, they show high chemical and thermal stabilities as well as ultrasmooth surface with tunable wettability. This work suggests that graphene can be used as electrodes for the development of next generation optoelectronic devices.

1.7 Concluding remarks

From the above discussion, it can be seen readily that nanostructures have many interesting properties, different from their bulk counterparts. Metal oxide nanostructures can be used as key components for different electronic devices. Properties of carbon nanotubes and graphene suggest great promise in different device applications.

References

[1] See, for example, (a) *Handbook of Nanostructure Materials and Nanotechnology*, (Ed. H.S. Nalwa) Academic Press, New York, (2000); (b) *Nanotubes and Nanowires,* C.N.R. Rao, A. Govindaraj, RSC Publishing, (2005); (c) *Nanomaterials: Synthesis, Properties and Applications,* (Ed. A.S. Edelstein, R.C. Cammarata), Institute of Physics, Philadephia, PA, (1996).

[2] See for example, (a) A special issue on nanoscale materials, *Acc. Chem. Res*., 32, **(1999)**; (b) Special issue on nanostructures materials, *Chem. Mater.* 8, 1569 **(1996)**; (c) G.A. Ozin, *Adv. Mater*. 4, 612 **(1992)**.

[3] C. N. R. Rao, A. Mueller, A. K. Cheetham, *The Chemistry of Nanomaterials: Synthesis, Properties and Applications*, Vol.1, Wiley-VCH, Weinheim, **(2004)**.

[4] http://www.zyvex.com/nanotech/feynman.html

[5] A. P. Alivisatos, *Science* 271, 933 **(1996)**.

[6] X. G. Peng, *Adv. Mater*. 15, 459 **(2003)**.

[7] J. T. Hu, T. W. Odom, C. M. Lieber, *Acc. Chem. Res*. 32, 435 **(1999)**.

[8] S. R. Forrest, *Chem. Rev*. 97 (6), 1793 **(1997)**.

[9] Y. N. Xia, P. D. Yang, Y. G. Sun, Y. Wu, B. Mayers, B. Gates, Y. Yin, F. Kim, H. Yan, *Adv. Mater*. 15, 353 **(2003)**.

[10] X. Duan, Y. Huang, Y. Cui, J. Wang, C. M. Lieber, *Nature* 409, 66 **(2001)**.

[11] Y. Cui and C. M. Lieber, *Science* 291, 851 **(2001)**.

[12] Y. Huang, X. Duan, Y. Cui, L. Lauhon, K. Kim, C. M. Lieber, *Science* 294, 1313 **(2001)**.

[13] J. Goldberger, R. He, Y. Zhang, S. Lee, H. Yan, H.-J. Choi, P. Yang, *Nature* 422, 599 **(2003)**.

[14] Z. W. Pan, Z. R. Dai, Z. L. Wang, *Science* 291, 1947 **(2001)**.

[15] X. Y. Kong, Y. Ding, R. Yang, Z. L. Wang, *Science* 303, 1348 **(2004)**.

[16] T. J. Trentler, K. M. Hickman, S. C. Goel, A. M. Viano, P. C. Gibbons, W. E. Buhro, *Science* 270, 1791 **(1995)**.

[17] Y. G. Sun, B. Gates, B. Mayers, Y. Xia, *Nano. Lett.* 2, 165 **(2002)**.

[18] G. Sun, Y. N. Xia, *Science* 298, 2176 **(2002)**.

[19] S.V. Goponenko, *Optical properties of Semiconductor Nanocrystals, Cambridge University Press, New York,* p-23, **(1998)**.

[20] Y.-W. Jun, J. Choi, J. Cheon, *Angew. Chem. Int. Ed.* 45, 3414 **(2006)**.

[21] L.-S. Li, J. Hu, W. Yang, A.P. Alivisatos, *Nano Lett.* 1, 349 **(2001)**.

[22] J. Hu, L.-s. Li, W. Yang, L. Manna, L.-w. Wang, A.P. Alivisatos, *Science* 292, 2060 **(2001)**.

[23] G. U. Kulkarni, P. J. Thomas, and C. N. R. Rao in The Chemistry of Nanomaterials, p. 51, Wiley-VCH, Weinheim, (**2004)**.

[24] R. G. Nuzzo, D. L. Allara, *J. Am. Cherm. Soc*. 1054481 **(1983)**.

[25] A. Harriman *et al., J. Phys. Chem*. *92*, 1286 **(1988)**.

[26] D. Mandler, L. Vlilner, *J. Phys. Chem*. *91*, 3600 **(1987)**.

[27] K. L. Tsai, J. L. Dai, *Chem. Mater*. *5*, 540 **(1993)**.

[28] S. H. Yu *et al., J. Mater. Chem*. *9* 1283 (**1999**).

[29] X. Chen, R Fan, *Chem. Mater*.13802 **(2001)**.

[30] M. Y. Han *et al., Chern. Phys. Lett*. *287*, 47 **(1998)**.

[31] M. Marandi, N. Taghavinia, A. 1. Zad et al *Nanotechnolgy 16*, 334 **(2005)**.

[32] C.N.R. Rao, P.J. Thomas, G.U. Kulkarni, Nanocrystals: *Synthesis, Properties and Applications*, Springer series on materials science, 95, **(2007)**.

[33] E.A. Hauser, J.E. Lynn, *Experiments in colloidal chemistry*, p. 18 (McGraw-Hill: New York 1940).

[34] D.G. Duff, A. Baiker, P.P. Edwards, *Langmuir* 9, 2301 **(1993)**.

[35] I. Pastoriza-Santos, L.M. Liz-Marzan, *Langmuir* 18, 2888 **(2002)**.

[36] N.R. Jana, X. Peng, *J. Am. Chem. Soc.* 125, 14280 **(2003)**.

[37] (a) R. Jin, Y. Cao, C.A. Mirkin, *Science* 294, 1901 **(2001)**; (b) R. Jin, Y. Cao, E. Hao, G.S. Metraux, G.C. Schatz, C.A. Mirkin, *Nature* 425, 487 **(2003)**; (c) G.S. Metraux, C.A. Mirkin, *Adv. Mater.* 17, 412 **(2005)**; (d) E. Hao, R.C. Bailey, G.C. Schatz, *Nano Lett.* 4, 327 **(2004)**.

[38] J. Rockenberger, E. C. Scher, A. P. Alivisatos, *J. Am. Chem. Soc.* 121, 11595 **(1999)**.

[39] M. Ghosh, E. V. Sampathkumaran, C. N. R. Rao, *Chem. Mater.* 17, 2348 **(2005)**.

[40] M. Ghosh, K. Biswas, A. Sundaresan, C. N. R. Rao, *J. Mater. Chem.* 16, 106 **(2006)**.

[41] M. Ghosh, C. N. R. Rao, *Chem. Phys. Lett.* 393, 493 **(2004)**.

[42] M. Ghosh, R. Seshadri, C. N. R. Rao, *J. Nanosci. Nanotechnol.* 4, 136 **(2004)**.

[43] S. Thimmaiah, M. Rajamathi, N. Singh, P. Bera, F. C. Meldrum, N. Chandrasekhar, R. Seshadri, *J. Mater. Chem.* 11, 3215 **(2001)**.

[44] K. Biswas, C. N. R. Rao, *J. Phys. Chem. B* 110, 842 **(2006)**.

[45] J. Park, K. An, Y. Hwang, J. G. Park, H. J. Noh, J. Y. Kim, J. H. Park, N. M. Hwang, T. Hyeon, *Nat. Mater.* 3, 891 **(2004)**.

[46] W. S. Seo, J. H. Shim, S. J. Oh, E. K. Lee, N. H. Hur, J. T. Park, *J. Am. Chem. Soc.* 127, 6188 **(2005)**.

[47] S-H Choi, E-G Kim, J. Park, K. An, N. Lee, A. C. Kim, T. Hyeon, *J. Phys. Chem. B*, 109, 14792 **(2005)**.

[48] Z. Hu,D. J. E.Ramirez, B. E. H. Cervera,G. Oskam and P.C. Searson, *J. Phys. Chem. B* 109, 11209 **(2005)**.

[49] J. Joo, S. G. Kwon, J. H. Yu, T. Hyeon, *Adv. Mater.* 17, 1873 **(2005)**.

[50] L. S. Panchakarla, A. Govindaraj, C. N. R. Rao, *J. Cluster Sci.* 18, 660 **(2007)**.

[51] S. O'Brien, L. Brus, C. B. Murray, *J. Am. Chem. Soc.* 123,12085 **(2001)**.

[52] H. Wu, Y. Yang, Y. C. Cao, *J. Am. Chem. Soc.* 128, 16522 **(2006)**.

[53] N. Pinna, G. Garweitner,M. Antonietti, M. Niederberger, *J. Am. Chem. Soc.* 127, 5608 **(2005)**.

[54] Q. Liu, W. Lu, A. Ma, J. Tang, J. Lin, J. Fang, *J. Am. Chem. Soc.* 127, 5267 **(2005)**.

[55] J. Tang, F. Redl, Y. Zhu, T. Siegrist, L. E. Brus, M. L. Steigerwald, *Nano Lett.* 5, 543 **(2005)**.

[56] G. Li, L. Li, J. B. Goated, B. F. Woodfield, *J. Am. Chem. Soc.* 127, 8659 **(2005)**.

[57] N. Moumen, M.-P. Pileni, *J. Phys. Chem.* 100, 1867 **(1996)**.

[58] N. Moumen, M.-P. Pileni, *Chem. Mater.* 8, 1128 **(1996)**.

[59] C. R. Martin, *Science* 266, 1961 **(1994)**.

[60] D Almawlawi, C. Z. Liu, M. Moskovits, *J. Mater. Res.* 9, 1014 **(1994)**.

[61] A. Govindaraj, B. C. Satishkumar, M. Nath, C. N. R. Rao, *Chem. Mater.* 12, 202 **(2000)**.

[62] M. Zheng, L. Zhang, X. Zhang, J. Zhang, G. Li, *Chem. Phys. Lett.* 334, 298 **(2001)**.

[63] J. A. Sioss, C. D. Keating, *Nano Lett.* 5, 1779 **(2005)**.

[64] B. D. Busbee, S. O. Obare, C. J. Murphy, *Adv. Mater.* 15, 414 **(2003)**.

[65] L. Gou, C. J. Murphy, *Chem. Mater.* 17, 3668 (2005).

[66] H.-Y. Wu, H.-C. Chu, T.-J. Kuo, C.-L. Kuo and M. L. H. Huang, *Chem. Mater.* 17, 6447 **(2005)**.

[67] A. Gulati, H. Liao, J. H. Hafner, *J. Phys. Chem. B* 110, 22323 **(2006)**.

[68] A. Gole, C. J. Murphy, *Chem. Mater.* 17, 1325 **(2005)**.

[69] B. Basnar, Y. Weizmann, Z. Cheglakov, I. Willner, *Adv. Mater.* 18, 713 **(2006)**.

[70] C.-K. Tsung, X. Kou, Q. Shi, J. Zhang, M. H. Yeung, J. Wang, G. D. Stucky, *J. Am. Chem. Soc.* 128, 5352 **(2006)**.

[71] A. J. Mieszawska, G.W. Slawinski, F. P. Zamborini, *J. Am. Chem. Soc.* **128**, 5622 **(2006)**.

[72] C. Ni, P. A. Hassan, E. W. Kaler, *Langmuir* 21, 3334 **(2005)**.

[73] Y. Sun, B. Gates, B. Mayers, Y. Xia, *Nano lett.* 2, 165 **(2002)**.

[74] Y. Chen, B. J. Wiley, Y. Xia, *Langmuir* 23, 4120 **(2007)**.

[75] L. Gou, M. Chipara, J. M. Zaleski, *Chem. Mater.* 19,1755 **(2007)**.

[76] D. Ung, G. Viau, C. Ricolleau, F. Warmont, P. Gredin, F. Fievet, *Adv. Mater.* 17, 338 **(2005)**.

[77] W. Z.Wong, B. Poudel, Y.Ma, Z. F. Ren, *J. Phys. Chem. B* 110, 25702 **(2006)**.

[78] Y. Xiong, H. Cai, B. J. Wiley, J.Wang, M. J. Kim, Y. Xia, *J. Am. Chem. Soc.* 129, 3665 **(2007)**.

[79] S. R. C. Vivekchand, G. Gundiah, A. Govindaraj, C. N. R. Rao, *Adv. Mater.* 16, 1842 **(2004)**.

[80] H. Zhang, D. Yang, X.Ma, N. Du, J.Wu, D. Gue, *J. Phys. Chem. B* 110, 827 **(2006)**.

[81] B. Cheng,W. Shi, J.M. R-Tanner, L. Zhang, E. T. Samulski, *Inorg. Chem.* 45, 1208 **(2006)**.

[82] H. Peng, Y. Fangli, B. Liuyang, L. Jinlin, C. Yunfa, *J. Phys. Chem. C* 111, 194 **(2007)**.

[83] L. S. Panchakarla, M. A. Shah, A. Govindaraj, C. N. R. Rao, *J. Solid State Chem.* 180, 3106 **(2007)**.

[84] Z- Gui, J. Liu, Z.Wang, L. Song, Y. Hu,W. Fan, D. Chen, *J. Phys. Chem. B* 109, 1113 **(2005)**.

[85] (a) P. X. Gao, Y. Ding, W. Mai, W. L. Hughes, C. Lao, Z. L. Wang, *Science* 309, 1700 **(2005)**; (b) Z.L. Wang, *Mater. Today* 7, 26 **(2004)**.

[86] Q. Li, V. Kumar, Y. Li, H. Zhang, T. J. Marks, R. P. H. Chang, *Chem. Mater.* 17, 1001 **(2005)**.

[87] Y. Tak, K. Yong, *J. Phys. Chem. B* 109, 19263 **(2005)**.

[88] P. X. Gao, C. S. Lao, W. L. Hughes, Z. L. Wang, *Chem. Phys. Lett.* 408, 174 **(2005)**.

[89] M. Lai, D. J. Riley, *Chem. Mater.* 18, 2233 **(2006)**.

[90] S. Kar, B. N. Pal, S. Chaudhuri, D. Chakravorty, *J. Phys. Chem.B* 110, 4605 **(2006)**.

[91] J. H. He, J.H.Hsu, C.W.Wang, H.N. Lin, L. J. Chen, Z. L.Wang, *J. Phys. Chem. B*, 110, 50 **(2006)**.

[92] L.-X.Yang,Y.-J. Zhu,W.-W.Wang, H. Tong, M.-L.Ruan, *J. Phys. Chem. B* **110**, 6609 **(2006)**.

[93] F. L. Deepak, G. Gundiah, Md. M. Shiekh, A. Govindaraj, C. N. R. Rao, *J. Mater. Res.* 19, 2216 **(2004)**.

[94] P. Chen, S. Xie, N. Ren, Y. Zhang, A. Dong, Y. Chen,Y. Tang, *J. Am. Chem. Soc.* 128, 1470 **(2006)**.

[95] G. Wang, D.-S. Tsai, Y.-S. Huang, A. Korotcov, W.-C. Yeh, D. Susanti, *J. Mater. Chem.* 16, 780 **(2006)**.

[96] A. Magrez, E. Vasco, J. W. Seo, C. Dieker, N. Setter, L. Forro, *J. Phys. Chem. B*, 110, 58 **(2006)**.

[97] K. P. Kalyanikutty, F. L. Deepak, C. Edem, A. Govindaraj, C. N. R. Rao, *Mater. Res. Bull.* 40, 831 **(2005)**.

[98] Y. Hao, G. Meng, C. Ye, X. Zhang, L. Zhang, *J. Phys. Chem. B* 109, 11204 **(2005)**.

[99] G. Gundiah, A. Govindaraj, C. N. R. Rao, *Chem. Phys. Lett.* 351, 189 **(2002)**.

[100] J. Zhang, F. Jiang, Y. Yang, J. Li, *J. Phys. Chem. B* 109,13143 **(2005)**.

[101] J. Zhan, Y. Bando, J. Hu, F. Xu, D. Goldberg, *Small* 1, 883 **(2005)**.

[102] J. Joo, S. G. Kwon, T. Yu, M. Cho, J. Lee, J. Yoon, T. Hyeon, *J. Phys. Chem. B* 109, 15297 **(2005)**.

[103] B. S. Guiton, Q. Gu, A. L. Prieto, M. S. Gudiksen, H. Park, *J. Am. Chem. Soc.* **127**, 498 **(2005)**.

[104] K. P. Kalyanikutty, G. Gundiah, C. Edem, A. Govindaraj, C.N. R. Rao, *Chem. Phys. Lett.* 408, 389 **(2005)**.

[105] Q.Wan, M.Wei,D. Zhi, J. L. MacManus-Driscoll, M.G. Blamire, *Adv. Mater.* 18, 234 **(2006)**.

[106] R.Wang, Y.Chen,Y. Fu,H. Zhang, C. Kisielowski, *J. Phys. Chem. B* 109,12245 **(2005)**.

[107] Y. M. Zhao, Y.-H. Li, R. Z. Ma, M. J. Roe, D. G. McCartney, Y. Q. Zhu, *Small*, 2, 422 **(2006)**.

[108] Y. Li, B. Tan, Y. Wu, *J. Am. Chem. Soc.* 128, 14258 **(2006)**.

[109] J. Zhou, Y. Ding, S. Z. Deng, L. Gong, N. S. Xu and Z. L.Wang, *Adv. Mater.* 17, 2107 **(2005)**.

[110] J.-W. Seo, Y.-W. Jun, S. J. Ko, J. Cheon, *J. Phys. Chem. B* 109, 5389 **(2005)**.

[111] G. Shen, D. Chen, *J. Am. Chem. Soc.* 128, 11762 **(2006)**.

[112] G. Xu, Z. Ren, P. Du, W. Weng, G. Shen, G. Han, *Adv. Mater.* 17, 907 **(2005)**.

[113] S. R. Hall, *Adv. Mater.* 18, 487 **(2006)**.

[114] A.-M. Cao, J.-S. Hu, H.-P. Liang, L.-J. Wan, *Angew. Chem., Int. Ed.* 44, 4391 **(2005)**.

[115] S. Iijima, *Nature* 354, 56 **(1991)**.

[116] S. Iijima, T. Ichihashi, *Nature* 363, 603 **(1993)**.

[117] C. Journet, W. K. Maser, P. Bernier , A. Loiseau, M. Lamy, de la Chappelle, S. Lefrant, P. Deniard, R. Lee, J. E. Fischer, *Nature* 388, 756 **(1997)**.

[118] A. G.Rinzler, J. Liu, H. Dai, P. Nikolaev, C. B. Huffman, F. J. Rodriguez-Macias, P. J. Boul, A. H. Lu, D. Heymann, D. T .Colbert, R. S. Lee, J. E. Fischer, A. M. Rao, P. C. Eklund, R. E. Smalley, *Appl. Phys. A* 67, 29 **(1998)**.

[119] P. Nikolaev, M. J. Bronikowski, R. K. Bradley, F. Rohmund, D. T. Colbert, K. A. Smith, R. E.Smalley, *Chem. Phys. Lett.* 313, 91 **(1999)**.

[120] Z. F. Ren, Z. P. Huang, J.W. Xu, D. Z. Wang, J. G. Wen, J. H.Wang, *Appl. Phys. Lett.* 75, 1086 **(1999)**.

[121] Z. F. Ren, Z. P. Huang, J.W. Xu, J. H. Wang, P. Bush, M. P.Siegal, P. N. Provencio, *Science* 282, 1105 **(1998)**.

[122] Z. P. Huang, J.W. Xu, Z. F. Ren, J. H. Wang, M. P. Siegal, P. N. Provencio, *Appl. Phys. Lett.* 73, 3845 **(1998)**.

[123] D. S. Bethune, C. H. Kiang, M. S. Devries, G. Gorman, R. Savoy, J. Vazquez, *Nature* 363, 605 **(1993)**.

[124] Z. Shi, Y. Lian, F. H. Liao, X. Zhou, Z. Gu, Y Zhang, *J. Phys. Chem. Solids* 61, 1031 **(2000)**.

[125] Y. Saito, K. Nishikubo, K. Kawabata, T. Matsumoto, *J. App. Phys.* 80, 3062 **(1996)**.

[126] A. Thess, R. Lee, P. Nikolaev, H. J. Dai, P. Petit, J. Robert, *Science* 273, 483 **(1996)**.

[127] Y. Zhang, S. Iijima, *Appl. Phys. Lett.* 75, 3087 **(1999)**.

[128] M. Ge, K. Sattler, *Appl. Phys. Lett.* 64, 710 **(1994)**.

[129] G. Che, B. B. Lakshmi, C. R. Martin, E. R. Fisher, R. S. Ruoff, Chem. Mater. 10, 260 **(1998)**.

[130] W. Z. Li, S. S. Xie, L. X. Qian, B. H. Chang, B. S. Zou, W.Y Zho, *Science* 274, 1701 **(1999)**.

[131] X. X. Zhang, Z. Q. Li, G. H. Wen, K. K. Fung, J. Chen, Y. Li, *Chem. Phys. Lett.* 333, 509 **(2001)**.

[132] Z. L. Wang, *Mater. Today* 7, 26 **(2004)**.

[133] Z. W. Pan, Z. R. Dai, Z. L. Wang, *Science* 291, 1947 **(2001)**.

[134 Z. L. Wang, *J. Phys.: Condens. Matter* 16, R829 **(2004)**.

[135] Y. W. Heo, D. P. Norton, L. C. Tien, Y. Kwon, B. S. Kang, F. Ren, S. J. Pearton, J. R. LaRoche, *Mater. Sci. Eng.* R. 47, 1 **(2004)**.

[136] U. Ozgur, Y.I. Alivov, C. Liu, A. Teke, M.A. Reschilkov, S. Dogan, V. Avrutin, S.-J. Cho, H. Morkoc, *J. Appl. Phys.* 98, 041301 **(2005)**.

[137] B.L. Allen, P.D. Kichambare, A. Star, *Adv. Mater.* 19, 1439 **(2007)**.

[138] G.A. Niklasson, C.G. Granqvist, *J. Mater. Chem.* 17, 127 **(2007)**.

[139] L.S. Mende, J.L. Driscoll, *Mater. Today* 10, 40 **(2007)**.

[140] W. Yang, P. Thordarson, J.J. Gooding, S.P. Ringer, F. Braet, *Nanotechnology*, 18, 412001 **(2007)**.

[141] D.V. Bavykin, J.M. Friedrich, F.C. Walsh, *Adv. Mater.* 18, 1 **(2006)**.

[142] G. Hodes, *Adv. Mater*. 19, 639 **(2007)**.

[143] A.K. Wanekaya, W.Chen, N.V. Myung, A. Mulchandani, *Electroanalysis* 18, 533 **(2006)**.

[144] S.J. Pearton, B.S. Kang, S. Kim, F. Ren, B.P. Gilla, C.R. Abernathy, J. Lin, S.N.G. Chu, *J. Phys. Condens. Mater.* 16, R961 **(2004)**.

[145] X. Chen, S.S. Mao, *Chem. Rev.*, 107, 2891 **(2007)**.

[146] M.S. Dreselhaus, G. Dreselhaus, P.C. Eklund, 1996 *Science of Fullerene and Carbon nanotubes*, (New York: Academic).

[147] R. Saito, G. Dreselhaus, M.S. Dreselhaus, 1998 *Physics properties of Carbon nanotubes* (New York: World scientific).

[148] A.C. Dilon, K.M. Jones, T.A. Bekkedahl, C.H. Kiang, D.S. Bethune, M.J. Heben, *Nature* 386, 377 **(1997)**.

[149] P. Chen, X. Wu, J. Lin, K.L. Tan, *Science* 285, 91 **(1999)**.

[150] C. Liu, Y.Y. Fan, M. Liu, H.T. Cong, H.M. Cheng, M.S. Dresselhaus, *Science* 286, 1127 **(1999)**.

[151] K.S. Novoselov, A.K. Geim, S.V. Morozov, D. Jiang, Y. Zhang, S.V. Dubons, I.V. Grigorieva, A.A. Firsov, *Science* 306, 666 **(2004)**.

[152] K.S. Novoselov, A.K. Geim, S.V. Morozov, D. Jiang, M.I. Katsnelson, Y. Zhang, S.V. Dubons, I.V. Grigorieva, A.A. Firsov, *Nature* 438, 197 **(2005)**.

[153] Y. Zhang, Y.W. Tan, H.L. Stormer, P. Kim, *Nature* 201 **(2005)**.

[154] S. Stankovich, D.A. Dikin, G.H.B. Dommett, K.M. Kohlhaas, E.J. Zimney, E.A. Stach, R.D. Piner, S.T. Nguen, R.S. Ruoff, *Nature* 442, 282 **(2006)**.

[155] A.K. Geim, K.S. Novoselov, *Nature Mater.* 6, 183 **(2007)**.

[156] J. Han *et al*., *J. Eur. Ceram. Soc.* 22, 49 **(2002)**.

[157] K.I. Hagemark, *J. Solid State Chem.* 16, 293 **(1976)**.

[158] F.A. Kroger, *The Chemistry of Imperfect Crystals. 2nd Edition, North Holland, Amsterdam* 73, **(1974)**.

[159] M.H. Huang, S. Mao, H. Feick, H. Yan, Y. Wu, H. Kind, E. Weber, R. Russo, P. Yang, *Science* 292, 1897 **(2001)**.

[160] W.I. Park, G.C. Yi, *Adv. Mater.* 16, 87 **(2004)**.

[161] H. Sun, Q.-F. Zhang, J-L. Wu, *Nanotechnology* 17, 2271 **(2006)**.

[162] Z. Zhang, Y. Sun, Y. Zhao, G. Li, T. Wu, *Appl. Phys. Lett.* 92, 103113 **(2008)**.

[163] B. N. Pal, J. Sun, B.J. Jung, E. Choi, A.G. Anreou, H.E. Katz, *Adv. Mater.* 20, 1023 **(2008)**.

[164] R. Konenkamp, R. C. Word, Godinez, *Nanoletters* 5**,** 2005 **(2005)**.

[165] Nadarajah, R.C.Word, J. Meiss, R. Konenkamp, *Nano Letters* 8, 534 **(2008)**.

[166] R. Konenkamp, R.C. Word, C. Schlegel, *Appl. Phys. Lett.* 85, 6004 **(2004)**.

[167] X.W. Sun, J.Z. Huang, J.X. Wang, Z. Xu, *Nano Letters* 8, 1219 **(2008)**.

[168] Y.B. Li, Y. Bando, D. Golberg, *Appl. Phys. Lett.* 84, 3603 **(2004)**.

[169] W.I. Park, J.S. Kim, G.-C. Yi, M.H. Bae, H.-J. Lee, *Appl. Phys. Lett.* 85, 5052 **(2004)**.

[170] Z. Fan, D. Wang, P.-C. Chang, W.-Y. Tseng, J.G. Lu, *Appl. Phys. Lett.* 86, 5923 **(2004)**.

[171] Y.W. Heo, L.C. Tien, D.P. Norton, B.S. Kang, F. Ren, B.P. Gila, S.J. Pearton, *Appl. Phys. Lett.* 85, 2002 **(2004)**.

[172] B.S. Kang, H.T. Wang, F. Ren, S.J. Pearton, T.E. Morey, D.M. Dennis, J.W. Johnson, P. Rajagopal, J.C. Roberts, E.L. Piner, K.J. Linthicum, *Appl. Phys. Lett.* 91, 252103 **(2007)**.

[173] W.-K. Hong, D.-K. Hwang, I.-K. Park, G. Jo, S. Song, S.-J. Park, T. Lee, B.-J. Kim, E.A. Stach, *Appl. Phys. Lett.* 90, 243103 **(2007)**.

[174] Y.-Y. Noh, X. Cheng, H. Sirringhaus, J.I. Sohn, M.E. Welland, D.J. Kang, *Appl. Phys. Lett.* 91, 043109 **(2007)**.

[175] Yoon, W-K. Hong, T. Lee, *J. Nanosci. Nanotechnol.* 7, 4101 **(2007)**.

[176] S.N. Cha, J.E. Jang, Y. Choi, G.A. Amaratunga, G.W. Ho, M.E. Welland, D.G. Hasko, D.-J. Kang, J.M. Kim, *Appl. Phys. Lett.* 89, 263102 **(2006)**.

[177] M.S. Arnold, P. Avouris, Z.W. Pan, Z.L. Wang, *J. Phys. Chem. B* 107, 659 **(2003)**.

[178] Y-F. Lin, W-B. Jian, C.P. Wang, Y-W. Suen, Z-Y. Wu, F-R. Chen, J-J. Kai, J-J. Lin, *Appl. Phys. Lett.* 90, 223117 **(2007)**.

[179] K. Keem, D-Y. Jeong, S. Kim, M-S. Lee, I-S. Yeo, U-I. Chung, J-T. Moon, *Nano Lett.* 6, 1454 **(2006)**.

[180] S. Ju, D.B. Janes, G. Lu, A. Facchetti, T.J. Marks, *Appl. Phys. Lett.* 89, 193506 **(2006)**.

[181] S. Ju, K. Lee, M-h. Yoon, A. Facchetti, T.J. Marks, D.B. Janes, *Nanotechnology* 18, 155201 **(2007)**.

[182] Z-X. Xu, V.A.L. Roy, P. Stallinga, M. Muccini, S. Toffanin, H-F. Xiang, C-M. Che, *Appl. Phys. Lett.* 90, 223509 **(2007)**.

[183] I. Bedga *et al.*, *Langmuir* 13, 2398 **(1997)**.

[184] A. Furube *et al.*, *J. Phys. Chem. B*, 107, 4162 **(2003)**.

[185] B. O'Regan, M. Gratzel, *Nature* 353, 737 **(1991)**.

[186] X. Wang, J. Song, J. Liu, Z. L. Wang, *Science* 316, 102 **(2007)**.

[187] N. Du, H. Zhang, B. Chen, J. Wu, D. Yang, *Nanotechnology* 18, 115619 **(2007)**.

[188] D. Wang, X. Chu, M. Gong, *Nanotechnology* 18, 185601 **(2007)**.

[189] H. Zhang, J. Wu, C. Zhai, N. Du, X. Ma, D. Yang, *Nanotechnology* 18, 455604 **(2007)**.

[190] Z-P. Sun, L. Liu, L. Zhang, D-Z. Jia, *Nanotechnology* 17, 2266 **(2006)**.

[191] L.C. Tien, P.W. Sadik, D.P. Norton, L.F. Voss, S.J. Pearton, H.T. Wang, B.S. Kang, F. Ren, J. Jun, J. Lin, *Appl. Phys. Lett.* 87, 222106 **(2005)**.

[192] H.T. Wang, B.S. Kang, F. Ren, L.C. Tien, P.W. Sadik, D.P. Norton, S.J. Pearton, J. Lin, *Appl. Phys. Lett.* 86, 243503 **(2005)**.

[193] T. Gao, T.H. Wang, *Appl. Phys. A* 80, 1451 **(2005)**.

[194] Y. Dai, Y. Zhang, Q.K. Li, C.W. Nan, *Chem. Phys. Lett.* 358, 83 **(2002)**.

[195] M. Kaur, S. Bhatacharya, M. Roy, S.K. Despande, P. Sharma, S.K. Gupta, J.V. Yakhmi, *Appl. Phys. A* 87, 91 **(2007)**.

[196] S. Kar, B.N. Pal, S. Chaudhari, D. Chakravorty*, J. Phys. Chem. B* 110, 4605 **(2006)**.

[197] E. Comini, G. Fagila, M. Ferroni, G. Sberveglieri, *Appl. Phys. A* 88, 45 **(2007)**.

[198] Y. Qiu, S. Yang, *Adv. Func. Mater.* 17, 1345 **(2007)**.

[199] Q. Wan, Q.H. Li, Y.J. Chen, T.H. Wang, X.L. He, J.P. Li, C.L. Lin, *Appl. Phys. Lett.* 84, 3654 **(2004)**.

[200] T-J. Hsueh, S-J. Chang, C-L. Hsu, Y-R. Lin, I-C. Chen, *Appl. Phys. Lett.* 91, 053111 **(2007)**.

[201] E. Comini, C. Baratto, G. Fagila, M. Ferroni, G. Sberveglieri, *J. Phys. D* 40, 7255 **(2007)**.

[202] P.M. Parthangal, R.E. Cavicchi, M.R. Zachariah, *Nanotechnology* 17, 3786 **(2006)**.

[203] J.X. Wang, X.W. Sun, Y. Yang, H. Huang, Y.C. Lee, O.K. Tan, L. Vayssieres, *Nanotechnology* 17, 4995 **(2006)**.

[204] J.Y. Park, D.E. Song, S.S. Kim, *Nanotechnology* 19, 105503 **(2008)**.

[205] Q. Wan, Q.H. Li, Y.J. Chen, T.H. Wang, X.L. He, X.G. Gao, J.P. Li, *Appl. Phys. Lett.* 84, 3085 **(2004)**.

[206] S.M. Al-Hilli, R.T. Al-Mofarji, P. Klason, M. Willander, *J. Appl. Phys.* 103, 014302 **(2008)**.

[207] S.P. Singh, S.A. Arya, P. Pandey, B.D. Malhotra, S. Saha, K. Sreenivas, V. Gupta, *Appl. Phys. Lett.* 91, 063901 **(2007)**.

[208] F.F. Zhang, X.L. Wang, S.Y. Ai, Z.D. Sun, Q. Wan, Z.Q. Zhu, Y.Z. Xian, L.T. Jin, K. Yamamoto, *Anal. Chim. Acta* 519, 155 **(2004)**.

[209] R. Sheshadri, A. Govindaraj, H. N. Aiyer, R. Sen, G. N. Subbanna, A. R. Raju, C. N. R. Rao, *Current Science 66*, 839 **(1994)**.

[210] R. A. Jishi, L. Venkataraman, M. S. Dresselhaus, G. Dresselhaus, *Chem. Phys. Lett. 220*, 186 **(1994)**.

[211] A. M. Rao, E. Richter, S. Bandow, P.C. Eklund, K. A. Williams, S. Fang, K. R. Subbaswamy, M. Meno, A. Thess, R. E. Smalley, G. Dresselhaus, M. S. Dresselhaus, *Science 275*, 187 **(1997)**.

[212] M. S. Dresselhaus, G. Dresselhaus, A. Jurio, A. G. Souza Filho, M. A. Pimenta, R. Saito, *Acc. Chem. Res. 35*, 1070 **(2002)**.

[213] W.A. de Heer, A. Chatelain, D. Ugarte, *Science* 270, 1179 **(1995)**.

[214] A.G. Rinzel *et al.*, *Science* 269, 1550 **(1995)**.

[215] K.H. An, W.S. Kim, Y.S. Park, J.-M. Moon, D.J. Bae, S.C. Lim, Y.S. Lee, Y.H. Lee, *Adv. Func. Mater.* 11, 387 **(2001)**.

[216] C. Niu, E.K. Sickel, R. Hock, D. Moy, H. Tennent, *Appl. Phys. Lett.* 70, 1480 **(1997)**.

[217] S. Tans *et al.*, *Nature* 393, 49 **(1998)**.

[218] R. Martel, T. Schmidt, H. R. Shea, T. Hertel, Ph. Avouris, *Appl. Phys. Lett.* 73, 2447 **(1998)**.

[219] A. Bachtold, P. Hadley, T. Nakanishi, C. Dekker, *Science* 294, 1317 **(2001)**.

[220] Z. Yao, H. Ch. Postma, L. Balents, C. Dekker, *Nature* 402, 273 **(1999)**.

[221] H. Baughman, A. Anvar. Zakhidov, W. A. de Hee, *Science* 297, 787 **(2002)**.

[222] P. G. Collins, K. Bradley, M. Ishigami, A. Zettl, *Science* 287, 1801 **(2000)**.

[223] J. Kong *et al.*, *Science* 287, 622 **(2000)**.

[224] D.S. Hecht, R.J.A. Ramirez, M. Briman, E. Artukovic, K.S. Chichak, J.F. Stoddart, G. Grunner, *Nano Lett.* 6, 2031 **(2006)**.

[225] K.S. Novoselov, A.K. Geim, S.V. Morozov, D. Jiang, Y. Zhang, S.V. Dubonos, I.V. Grigorieva, A.V. Firsov, *Science* 306, 666 **(2004)**; Y.Q. Wu *et al.*, *Appl. Phys. Lett.* 92, 092102 **(2008)**; S. Gilje, S. Han, M. Wang, K.L. Wang, R.B. Kaner, *Nano Lett.* 7, 3394 **(2007)**; X. Liang, Z. Fu, S. Chou, *Nano Lett.* 7, 3840 **(2007)**; C. G.- Navarro *et al.*, *Nano Lett.* 7, 3499 **(2007)**; G. Gu *et al*., *Appl. Phys. Lett.* 90, 253507 **(2007)**; J.-H. Chen *et al*., *Adv. Mater.* 19, 3623 **(2007)**; N. Staley *et al*., *Appl. Phys. Lett.* 90, 143518 **(2007)**; B. Ozyilmaz *et al.*, *Appl. Phys. Lett.* 91, 192107 **(2007)**.

[226] F. Schedin, A.K. Geim, S.V. Morozov, E.W. Hill, P. Blake, M.I. Katselson, K.S. Novoselov, *Nature. Mater.* 6, 652 **(2007)**.

[227] M. Quazi, T. Vogt, G. Koley, *Appl. Phys. Lett.* 91, 233101 **(2007)**.

[228] A.A. Balandin, S. Ghosh, W. Bao, I. Callizo, D. Teweldebrhan, F. Miao, C.N. Lau, *Nano Lett.* 8, 902 **(2008)**

[229] X. Wang, L. Zhi, K. Mullen, *Nano Lett.* 8, 323 **(2008)**.

Part 2

Gas sensors based on metal oxide nanostructures*

Summary

This part of the thesis deals with the synthesis and characterization of different nanostructures of metal oxides and a detailed study of their gas-sensing characteristics. Nanoparticles, nanowires, nanorods and nanotubes of metal oxides such as ZnO, In_2O_3, V_2O_5, WO_{3-x}, TiO_2 and SnO_2 were prepared by different chemical routes and characterized by transmission electron microscopy, X-ray diffraction, energy dispersive X-ray analysis and Raman spectroscopy. H_2, ethanol, hydrocarbon, H_2S, NH_3 and nitrogen oxides sensing characteristics of these nanostructures have been studied with a locally fabricated experimental set-up. Hydrogen sensing characteristics of single nanowires of ZnO, TiO_2 and $WO_{2.72}$ as well as hydrocarbon sensing characteristics of single $WO_{2.72}$ nanowires have been investigated by contact mode atomic force microscopy.

Hydrogen sensing characteristics of thick films of nanoparticles of ZnO and Co or Mn (1 and 3 at %) doped ZnO with and without impregnation of 1% Pt have been investigated over a wide concentration range. ZnO nanorods prepared by low-

*Papers based on these studies have appeared in Chem. Phys. Lett. (2006); Nanotechnology (2007); J. Nanosci. Nanotech. (2007); Solid State Commun. (2006); J. Mater. Chem. (2006); J. Phys. D: Appl. Phys. (2007); Appl. Phys. A (2006); Sens. Actuators: B (2008).

temperature methods and ZnO nanowires prepared by electrochemical deposition in alumina membranes as well as ZnO nanotubes have been investigated for hydrogen and ethanol sensing characteristics. The sensing characteristics of these nanostructures were also investigated after impregnating them with 1% Pt. The nanowires exhibit excellent hydrogen sensing characteristics at relatively low temperatures (≤ 150° C) specially when impregnated with Pt. Also the effect of humidity on sensitivity has been studied.

Hydrocarbon sensors based on V_2O_5 and $WO_{2.72}$ nanowires have been studied. V_2O_5 nanostructures do not exhibit satisfactory characteristics, while sensors based on $WO_{2.72}$ nanowires show high sensitivity (~1800) for 2000 ppm of LPG at 200 °C as well as relatively short recovery and response times. Impregnation of $WO_{2.72}$ nanowires with Pt in the 0.1-1.0 at% range significantly improves the sensor characteristics, the sensitivity increasing with Pt concentration and reaching a value of ~10^6 for 2000 ppm of LPG in the100–200 °C range with 1 at% Pt.

Nanoparticles and nanoplatelets of WO_3 and nanowires of $WO_{2.72}$ have been investigated for their H_2S-sensing characteristics over the 1-1000 ppm concentration range at 40-250°C. Nanoparticles and nanoplatelets of WO_3 exhibit response values of 757 and 1852 respectively to 1000 ppm H_2S at 250°C, respectively, compared to the response of 3313 of the nanowires of $WO_{2.72}$. Interestingly, the response of the nanowires is satisfactory (121) to 10 ppm H_2S at 250°C, while a large response (240) is observed for 1000 ppm H_2S even at 40°C. $WO_{2.72}$ nanowire emerges as a good candidate for H_2S sensing, with little effect of humidity up to 60% relative humidity as well as satisfactory response and recovery times.

Sensing characteristics of ZnO, In_2O_3 and WO_3 nanowires have been investigated for the three nitrogen oxides, NO_2 , NO and N_2O. In_2O_3 nanowires of ~20 nm diameter prepared by using porous alumina membranes are found to have a sensitivity of about 60 for 10 ppm of all the three gases at a relatively low temperature of 150 °C. The response and recovery times are around 20s. WO_3 nanowires of 5-15 nm diameter prepared by the solvothermal process show a sensitivity of 20-25 for 10 ppm for the three nitrogen oxides at 250 °C. The response and recovery times are 10s and 60s respectively.

Ammonia sensing characteristics of nanoparticles as well as nanorods of ZnO, In_2O_3 and SnO_2 have been investigated over a wide range of concentrations (1-800 ppm) and temperatures (100 −300 °C). The best values of sensitivity are found with ZnO nanoparticles and SnO_2 nanostructures. Considering all the characteristics, the SnO_2 nanostructures appear to be good candidates for sensing ammonia, with sensitivities of 222 and 19 at at 300 °C and 100 °C respectively for 800 ppm of NH_3. The recovery and response times are in the 12-68 sec and 22-120 sec range respectively. The effect of humidity on the performance of the sensors is not marked upto 60% at 300 °C.

2.1 Introduction

Gas sensor elements have been extensively used for many years to detect and monitor a variety of gases and vapors, including toxic or explosive gases, humidity, and odors. The most important fields of applications are:

- Automotive, industrial, and aerospace sector, where gas sensors are needed to detect NO_x, H_2, H_2S, SO_2, O_2, O_3, hydrocarbons or CO_2 in exhaust gases for environment protection [1-5].
- Food industries, where gas sensors are used for control of fermentation processes, for example, N-heterocycles as products of the Maillard reaction or long chain aldehydes from lipid peroxidation [1-2].
- The domestic sector, where CO_2, humidity, and combustible gases have to be detected [3-5].
- The medical sector, where gas and vapor sensors are applied, for example in diagnostics and patient monitoring [6-7].
- The security sector, which requires sensors to detect traces of explosives.

In a laboratory environment, compounds that need to be detected are conventionally measured using techniques such as IR or UV-Vis spectroscopy, Hall measurements, work function and d. c. measurements, impedance measurements or gas chromatography. Although some of these methods are precise and highly selective, and allow the detection of a single compound in a mixture of gases in very low concentrations, their application is limited by cost, instrumentation complexity, and the large physical size of the instrumentation. Thus, for low cost and mobile applications, solid-state gas sensors are most common. Such sensor element has to transform chemical information,

originating from a chemical or physical reaction of the gas molecule to be detected with the gas-sensitive material, into an analytically manageable signal [5, 8]. The different concepts that are applied include calorimetric sensors (pellistors) [9, 10], electrochemical cells, like the lambda probe [11], gas-sensitive field–effect transistors [12], surface and bulk acoustic wave devices [13], quartz microbalances [14,15], and chemiresistors. Among these chemiresistors, or so-called resistive gas-sensing elements are most commonly applied. In chemiresistors, metal oxides are typically used as gas-sensing materials, which change their electrical resistance when interacts with the oxidizing or reducing gas species.

2.1.1 Metal Oxide based gas sensors

Since the demonstration some years ago, by Brattain and Bardeen [16] in the case of Ge and by Heiland [17] in the case of ZnO, that the adsorption of gases on the surface of a semiconductor can bring about a change in the resistance of the material, there has been sustained effort to make use of this change for the purpose of gas detection (Seiyama et al 1962 [18], Taguchi 1970 [19]). Since that time, much technological effort has been made to improve the sensitivity, selectivity, stability, as well as the response and recovery time, which are the key parameters for the performance for a sensor element. The sensing properties are related to the surface reaction between the species to be detected and oxygen ionosorbed. The physical quantity normally measured is the resistance, which depends on the adsorbed species through the height of energy barriers between the grains.

Metal oxide based sensors usually operate between 100 and 500°C in real world condition. The sensor activity is expressed in terms of either *sensor response* (changes in resistance R) or *sensitivity*, S (relative resistance changes, $S=R_{gas}/R_{air}$ or $S=R_{air}/R_{gas}$ for

oxidizing and reducing gases, respectively; R_{gas} and R_{air} denote the sensor resistance in the presence and in the absence, respectively, of the target gas) {Figure 2.1.1}. The *response* or *recovery time* describes the time taken for the sensor output to reach 90% ($\Delta t_{90\%}$) of its saturation after applying or switching off the respective gas in a step function.

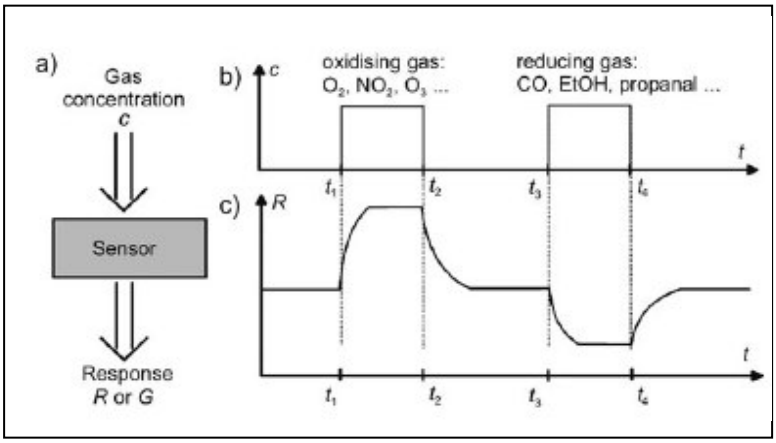

Figure 2.1.1: (a) Metal-oxide-based gas sensor: The changes in the gas concentration (c); (b) the gas is applied at t_1, t_3 and removed at t_2, t_4 lead to changes in the conductance G or resistance R of the sensor; (c) modified from reference [20].

The most-advanced and best-performing metal-oxide based gas sensors have a porous sensing layer based on annealed, nano-scaled oxide powders usually obtained through chemical routes {sol–gel, precipitation, chemical vapor deposition (CVD), FSP (FSP: flame spray pyrolysis)} [21- 24] and functionalized by adding small quantities of noble metals (Pd, Pt, or Au) in the form of surface additives. In a typical metal-oxide based gas sensor, the porous sensing layer is deposited on the transducer surface (e.g. Si_3N_4, Al_2O_3, Si/SiO_x) carrying the electrodes and an integrated heater {Figure 2.1.2 (a), (b)}. The latter helps to achieve the typical sensor operation temperature on the order of 100 to 500°C. Metal electrodes (usually Pt or Au) are fabricated to enable conductance (or resistance) measurement of the sensing material {Figure 2.1.2 (c)}. Hence, for a given type of base material, the sensor property sensitivity depends on the structural features,

the presence of and state of catalytically active surface dopants, and the working temperature.

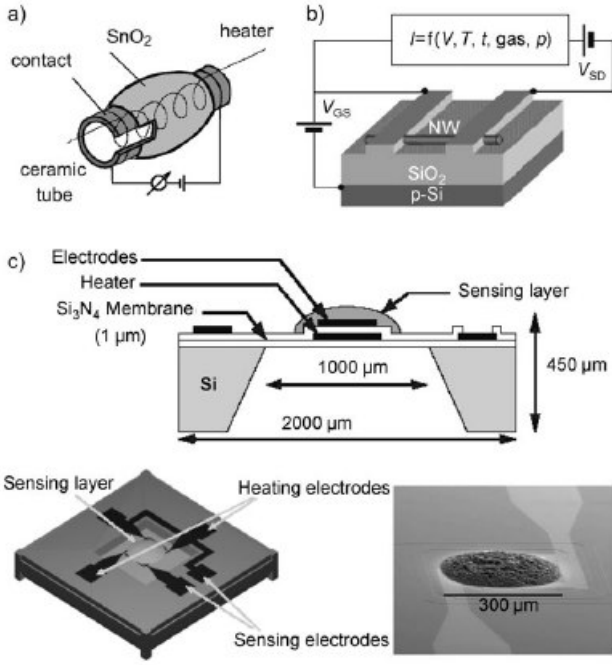

Figure 2.1.2: Typical metal-oxide sensing elements: (a) The Figaro-Taguchi type (TGS) sensor; (b) a SnO_2 nanowire (NW) gas sensor configured as a field-effect transistor (FET) [25] (thickness of SiO_2 layer: 300 nm; p-Si = p-doped silicon, V_{gs}= gate-to-source voltage, V_{sd} = source-to-drain voltage); (c) micromachined sensing element; top: side view, left bottom: 3D view, right bottom: microscopy image of the sensor [26].

2.1.2 Mechanism of gas detection

Two different models currently describe the operation of metal-oxide-based gas sensors. The first considers only the space–charge effects/changes of the electric surface potential that result from the "ionosorption" of gaseous molecules (ionosorption model. The second model explains the sensing effects by changes in the oxygen stoichiometry, that is, by the variation of the amount of the (sub-) surface oxygen vacancies and their ionization (reduction–reoxidation mechanism, Table 2.1.1). It must also be kept in mind

that the mechanism may be influenced significantly by the materials and operating conditions (e.g. temperature, composition of gaseous phase, hydroxylation of the surface).

(a) Ionosorption Model

Key in the mechanistic description of gas sensing is "oxygen ionosorption" and the reaction of reducing gases with ionosorbed oxygen ions. On an n-type semiconductor (e.g. SnO_2), oxygen ions are formed through the transfer of electrons from the conduction band (CB) and are electro-statically stabilized in the vicinity of the surface. The application of these considerations is limited to the temperature range in which diffusion processes do not take place. Accordingly, the operation of SnO_2-based sensors is described as follows: atmospheric oxygen adsorbs on SnO_2 as molecular ($O_2^-{}_{ads}$) and atomic (O^-_{ads}, O^{2-}_{ads}) ions, which trap electrons from the conduction band; reducing gases such as CO react with the oxygen ions (according to either a Eley-Rideal or Langmuir-Hinshelwood mechanism) and release electrons, which return to the conduction band. The nature of the ionized oxygen species is assumed to depend on the adsorption temperature. At low temperature (100-200 °C) oxygen adsorbs on SnO_2 nondissociatively in a molecular form (as charged $O_2^-{}_{ads}$ ions). At high temperature (between 200 and 400 °C, or even higher) it dissociates to atomic oxygen (charged O^-_{ads} or O^{2-}_{ads} ions). O^{2-}_{lat}, are assumed not to play any role in gas sensing. The atomic charged oxygen ion (O^-_{ads}) is assumed to be of particular importance in gas sensing because the O^- ion appears to be more reactive of the two possibilities and thus more sensitive to the presence of organic vapors or reducing and oxidizing agents [27, 28]. Hence, the required electrons for this process originating from donor sites, that is, intrinsic oxygen vacancies, are extracted from conduction band E_c and are trapped at the surface, leading to an electron-depleted

surface region, the so called space-charge layer Λ_{air}. The maximum surface coverage of about 10^{-3} to 10^{-2} cm^{-1} ions is dictated by the Weisz limitation, which describes the equilibrium between the Fermi level and the energy of surface-adsorbed sites [29, 30].

Table 2.1.1: Gas-sensing mechanism on SnO_2 according to the ionosorption and oxygen-vacancy models. [a] [20]

Gas/mixture	Ionosorption model	Oxygen-vacancy model
Oxygen	$O_{2\,(ads)} + e^- (CB) \Leftrightarrow O_{2\,(ads)}^-$ $O_{2\,(ads)}^- + e^- (CB) \Leftrightarrow O_{2\,(ads)}^{2-} \Leftrightarrow 2\,O_{(ads)}^-$	$2V_o^{\bullet} + O_{2\,(gas)} + 2e^- (CB) \Leftrightarrow O_o^x$
CO/presence of oxygen	$CO_{(gas)} + O_{(ads)}^- \Leftrightarrow CO_{2\,(gas)} + e^- (CB)$	$CO_{(gas)} + Oo^x \Leftrightarrow CO_{2\,(gas)} + V_o^x$ $V_o^x \Leftrightarrow V_o^{\bullet} + e^- (CB)$ $V_o^{\bullet} \Leftrightarrow V_o^{\bullet\bullet} + e^- (CB)$
CO/absence of oxygen	$CO_{(gas)} \Leftrightarrow CO_{(ads)}^+ + e^- (CB)$	
NO_2	$NO_{2\,(gas)} + e^- (CB) \Leftrightarrow NO_2^-\,(ads)$	$NO_{2\,(gas)} + V_o^{\bullet} \Leftrightarrow NO_{2\,(ads)}^- + V_o^{\bullet\bullet}$ $2\,NO_{(gas)} + O_{2\,(ads)}^- + V_o^{\bullet} \Leftrightarrow 2NO_{3\,(ads)}^- + V_o^{\bullet\bullet}$
water vapor	$H_2O_{(gas)} + O_{(ads)}^- + 2\,Sn_{Sn}^x \Leftrightarrow 2(Sn_{Sn}^x\text{-}OH) + e^- (CB)$ $H_2O_{(gas)} + Sn_{Sn}^x + O_o^x \Leftrightarrow (Sn_{Sn}^x\text{–}OH) + OH_o^{\bullet} + e^- (CB)$	$H_2O_{(gas)} + 2\,Sn_{Sn}^x + O_o^x \Leftrightarrow 2\,(Sn_{Sn}^x\text{-}OH) + V_o^{\bullet} + e^- (CB)$

[a] CB: conduction band, V_o: oxygen vacancy. The Kroger–Vink notation is used to show the charges of the lattice atoms/species (Sn, O, OH); for adsorbed species and electrons the "real" charges are shown; V_o^x: neutral (i.e., two electrons localized in an oxygen vacancy), $V_o^{\bullet}$: singly ionized oxygen vacancy, $V_o^{\bullet\bullet}$: doubly ionized oxygen vacancy, Sn_{Sn}^x: tin ion (Sn^{4+}) on a tin lattice site, $OH_o^{\bullet}$: hydroxide ion (OH^-) on an oxygen lattice site. Neutral oxygen species, such as physisorbed oxygen, $O_{2,phys}$, and lattice oxygen ions.

The presence of the negative surface charge leads to band bending {Figure. 2.1.3 (b)}, which generates a surface potential barrier $eV_{surface}$ of 0.5 to 1.5 eV. The height ($eV_{surface}$) and depth (Λ_{air}) of the band bending depend on the surface charge, which is determined by the amount and type of adsorbed oxygen. At the same time, layer Λ_{air} depends on the Debye length L_D, which is a characteristic of the semiconductor material for a particular donor concentration.

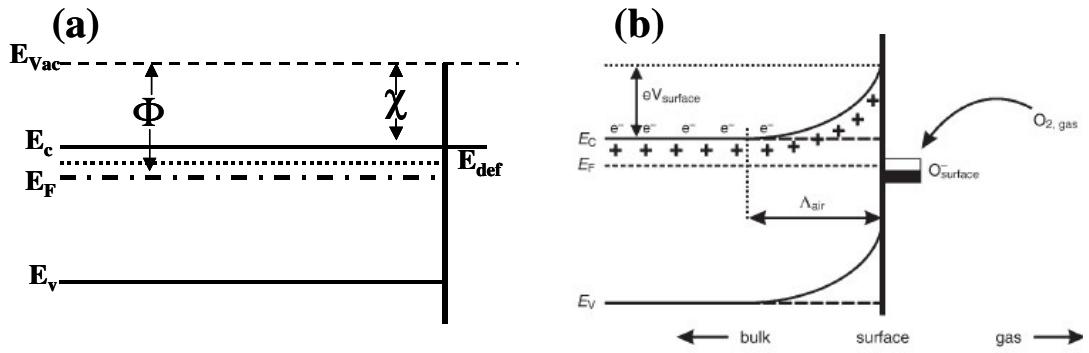

Figure 2.1.3: (a) Schematic representation of flat band in n-type semiconductor, (b) Band bending after chemisorption of charged ion species. (Φ is work function and χ is electron affinity) [21].

$$L_D = (\varepsilon_0 \varepsilon K_B T/q^2 n_c)^{1/2} \qquad (1)$$

Where K_B is Boltzmann's constant, ε the dielectric constant, ε_0 the permitivity of free space, T the operating temperature, e the electron charge, and n_c the carrier concentration, which correspondence to the donor concentration assuming full ionization. As an example, L_D for SnO_2 at 250 °C is about 3 nm, with ε=13.5, ε_0=8.85×10^{-12} F m^{-1} and n_c =3.6×1024 m^{-3} [31].

In case of polycrystalline sensing materials, electronic conductivity occurs along percolation paths via grain-to grain contacts and therefore depends on the value of $eV_{surface}$

of the adjacent grains. $eV_{surface}$ represents the Schottky barrier. The conductance G of the sensing material in this case can be written as [32]:

$$G \cong \exp(-eV_{surface}/K_BT) \qquad (2)$$

Reducing gases such as CO react with the ionosorbed oxygen species via the formation of unidentately and/or bidentately bound carbonate groups and desorb finally as CO_2 [33]. Thus, even traces of reducing gas decrease the amount of adsorbed oxygen significantly and the surface-trapped electrons are released back to the bulk. As a consequence, the height of the Schottky barrier is reduced, which results in an increase of the conductance of the whole sensing layer (Figure 2.1.4).

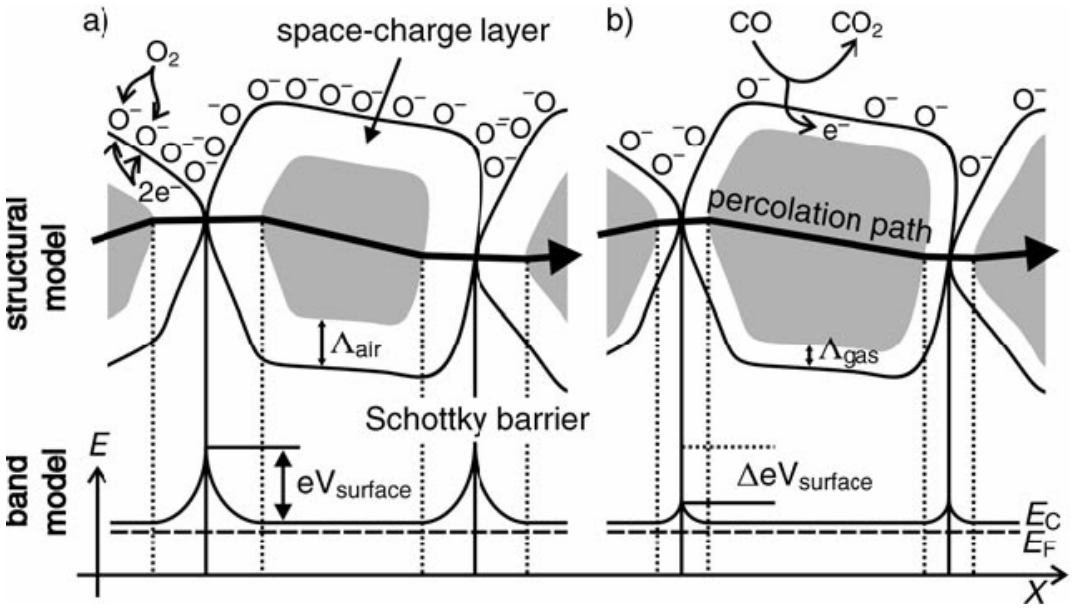

Figure 2.1.4: Structural and band model showing the role of intergranular contact regions in determining the conductance over polycrystalline metal oxide semiconductor: (a) initial state, (b) effect of CO on Λ_{air} and $eV_{surface}$ for large grains [21].

According to Barsan and Weimer, a power law dependence of the conductance on the partial pressure of CO [P_{co}] is given as $G \cong [P_{co}]^n$, where n depends on the morphology of the sensing layer and on the actual bulk properties of the sensing material [23]. In case of oxidizing gases such as NO, O_3 etc, further electrons are extracted from the semiconductor, leading to an increase of the space-charge layer and the height of the space charge layer respectively. Thus the adsorption of oxidizing gases leads to a decreased in conductance of the sensing material.

(b) Effect of grain size on sensitivity

To explain the effect of grain size on the sensitivity of metal-oxide gas sensors, Xu et al. [34] proposed a semi quantitative model, which is shown in figure 2.1.5 schematically. According to the model the sensor consists of partially sintered crystallites that are connected to their neighbors by necks. Those interconnected grains form larger aggregates that are connected to their neighbors by grain boundaries (GB). Three different cases can be distinguished according the relationship between the grain size D and the width of the depletion layer L.

(a) For D >> 2L: When D >> 2L, most of the volume of the crystallites is unaffected by the surface interactions with the gas phase, as shown in figure 2.1.5 (a). In this case the predominant effect of the ambient gas atmosphere on the sensor's conductivity is introduced via the GB barriers for intercrystallite charge transport from one grain (agglomerate) to another. From equation (2), the electrical conductivity is exponential dependent with barrier height and according to the depletion approximation $e|V_B| \propto (N_t^-)^2$, where N_t^- is the trapped charge density at the surface of the crystallites. N_t^- can be modified by charge transfer interactions with reactive gases such as O_2, NO_x, and CO, and

therefore the conductivity is sensitive to the ambient gas composition. Thus, for large grains (D >> 2L) the gas sensing mechanism is controlled by GB barriers. Furthermore, the GB barriers are independent of the grain size and therefore the sensitivity is independent of D.

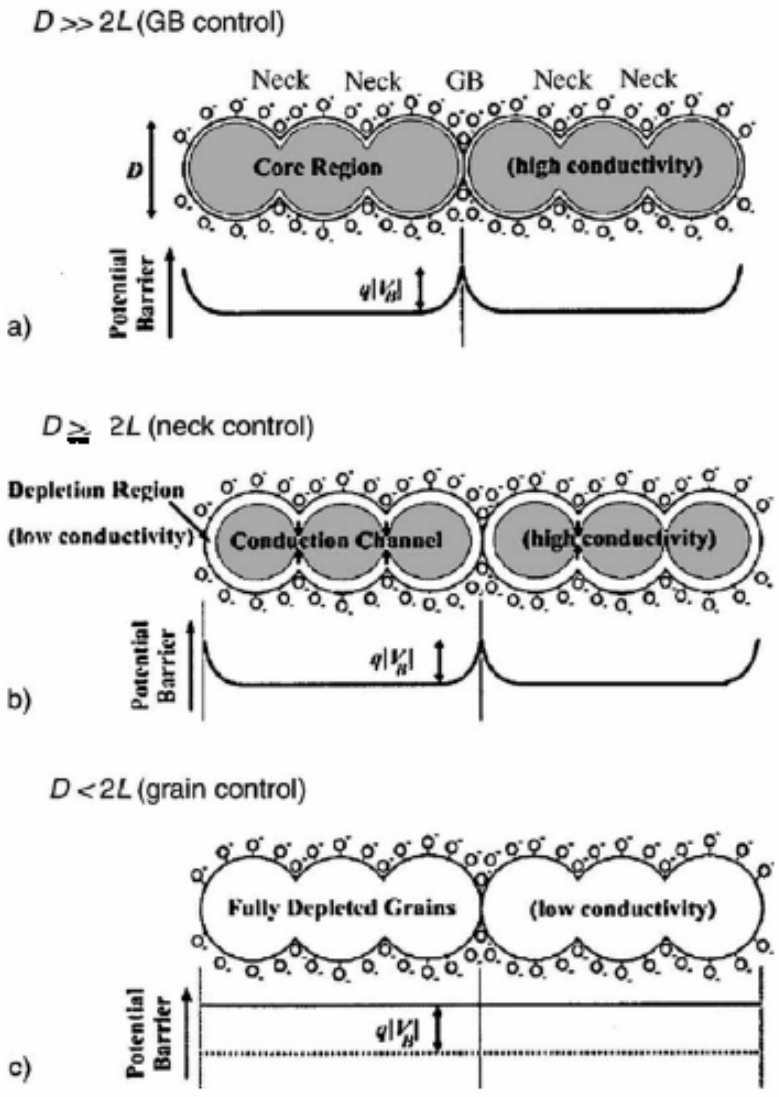

Figure 2.1.5: Schematic model of the effect of the crystallite size on the sensitivity of metal oxide gas sensors: (a) D >> 2L (GB control); (b) D ≥ 2L(neck control); (c) D < 2L (grain control) [35].

(b) For D ≥ 2L: As the grain size decreases the depletion region extends deeper into the grains and consequently the core region, which is relatively conductive with respect to the depletion region adjacent to the surface, becomes smaller. When D approaches but still larger than 2L, i.e., when D ≥ 2L, the depletion region that surrounds each neck forms a constricted conduction channel within each aggregate, as shown in figure 2.1.5(b). Consequently, the conductivity depends not only on the GB barriers but also on the cross section area of those channels. This area is proportional to $(X-L)^2$, where X is the neck diameter, which is proportional to the grain size D (X~0.8D) according to ref. 34). As a result, the conductivity is a function of the ratio X/L (or X/D). Since $L \propto N_t^-$ and N_t^- is modulated by the surface interactions with the gas phase, the effective cross section area of the current path though the grains is sensitive to the ambient gas composition. The current constriction effect adds up to the effect of the GB barriers, and therefore the gas sensitivity is enhanced with respect to the former case {D >> 2L, Figure 2.1.5 (a)}. Furthermore, the sensitivity to gases becomes grain size dependent and it increases when D decreases [35].

(c) For D < 2L: When D < 2L the depletion region extends throughout the whole grain and the crystallites are almost fully depleted of mobile charge carriers, as shown in figure 2.1.5 (c). As a result, the conductivity decreases steeply since the conductions between the grains are vanished. The energy bands are nearly flat throughout the whole structure of the interconnected grains, and since there are no significant barriers for intercrystallite charge transport the conductivity is essentially controlled by the intercrystallite conductivity (grain controlled). Following theoretical evaluation, Rothschild *et al* [35] have shown the effect of particle size between 5-80 nm on the sensitivity of SnO_2. By

their model for particles in which the entire volume is depleted of mobile carriers due to electron trapping at surfaces states, the effect of the gas-induced variations in the surface trapped charge density on the electrical conductivity as a function of the particle size is calculated. As a result, in nanosized particles the gas-induced variations in the surface-trapped charge density are greatly amplified leading to a high sensitivity, which is proportional to 1/D. The experimental data shown in figure 2.1.6 follow similar size dependence [35].

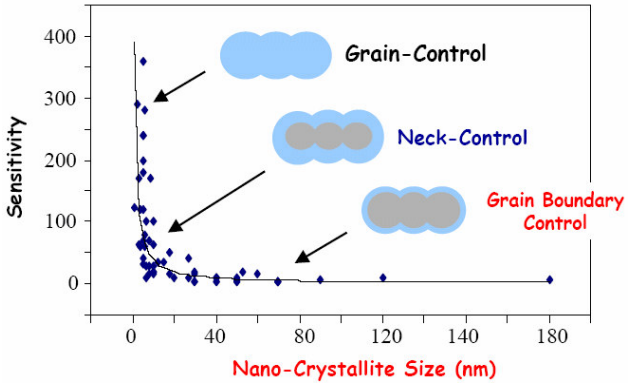

Figure 2.1.6: Influence of SnO_2 particle diameter, D on sensitivity [35].

Besides the particle size, the influence of microstructure, that is, the film thickness and its porosity are critical factors on the response time and the sensitivity. Sensing layers are penetrated by oxygen and analyte molecules so that a concentration gradient is formed, which depends on the equilibrium the diffusion rates of the reactants and their surface reaction. The rate leading to the equilibrium condition determines the response and recovery times. Therefore, a fast diffusion rate of the analyte and oxygen into the sensing body, which depends on its mean pore size and the working temperature, is vital. Furthermore, maximum sensitivity will be achieved if all percolation paths contribute to

the overall change of resistance, that is, that they are all accessible to the analyte molecules in the ambient. Thus a lower film thickness together with a higher porosity contributes to a higher sensitivity and faster response time. By using one-dimensional nanostructures such as wires, rods, belts, tubes and fibers as active sensor materials one can achieve higher diffusion rate and pore volume [36].

(c) Effect of surface doping

To overcome the inherent limitations of the pure base material, doping with metal and/or oxides has a profound impact on the sensor performance. The doping process improves sensor performance by increasing the sensitivity, favoring the selective interaction with the target analyte and thus increasing the selectivity and decreasing response and recovery time, respectively, which is then accompanied by a reduction of the working temperature. Furthermore, surface doping may enhance the thermal and long-term stability.

To explain the influence of surface additives, two different mechanisms, that is, electronic and chemical sensitization, have repeatedly been applied [37-39]. In the case of electronic sensitization, the additive in its oxidized state acts as a strong acceptor for electrons of the host semiconductor. This induces an electron-depleted space-charge layer near the interface. By reacting with a reducing analyte, for example H_2, the additive is reduced releasing the electrons back to the semiconductor {Figure 2.1.7(a)}. This type of sensitization has been observed for AgO/Ag, PdO/Pd, CuO/Cu. Chemical sensitization mechanism involves a catalytic surface reaction. The deposited clusters of noble metals (Pt or Au etc) provide preferred adsorption and activated sites for the target analyte from which activated fragments are spilled over onto the semiconductor to react with the

ionosorbed oxygen {Figure 2.1.7 (b)}. As a result, the surface coverage with oxygen, and therefore $eV_{surface}$ is reduced.

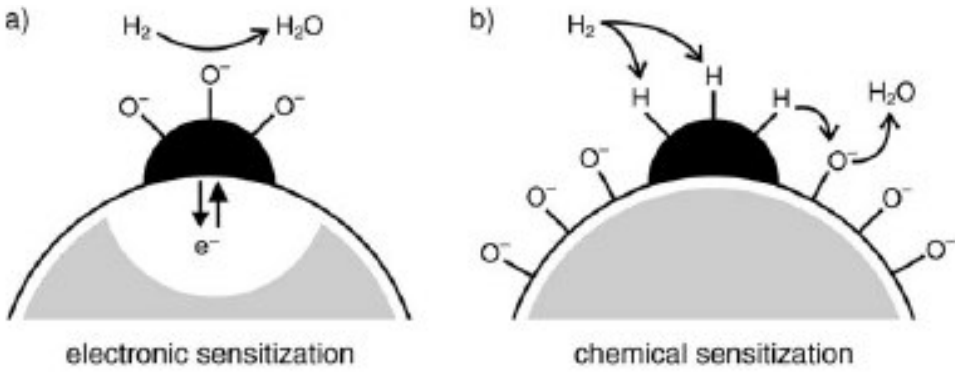

Figure 2.1.7: (a) Electronic sensitization, where the additive is an acceptor for electrons and the redox state/chemical potential is changed by reaction with analyte; (b) chemical sensitization by activation of the analyte (H_2) followed by spill over and change of the surface oxygen concentration [21].

(d) Oxygen-Vacancy Model

This model focuses on oxygen vacancies at the surface, which are considered to be "the determining factor in the chemiresistive behavior"[40]. Tin oxide, the most extensively investigated sensing material, is oxygen deficient and, therefore, an n-type semiconductor, whose oxygen vacancies act as electron donors. Alternate reduction and reoxidation of the surface by gaseous oxygen control the surface conductivity and therefore the overall sensing behavior. In this model, the mechanism of CO detection is represented as follows: 1) CO removes oxygen from the surface of the lattice to give CO_2, thereby producing an oxygen vacancy; 2) the vacancy becomes ionized, thereby introducing electrons into the conduction band and increasing the conductivity; 3) if oxygen is present, it fills the vacancy; in this process one or more electrons are taken from the conduction band, which results in the decrease in conductivity.

2.2 Scope of the present investigations

We have investigated sensing characteristics for H_2, C_2H_5OH, hydrocarbon, H_2S, nitrogen oxides and ammonia of the nanostructures of ZnO, In_2O_3, SnO_2, TiO_2, V_2O_5 and tungsten oxide

2.2.1 H_2 and C_2H_5OH sensors based on pure and doped ZnO nanostructures

ZnO has been recognized as one of the promising materials in a broad range of high-technology applications such as optical, acoustical, electronic, and optoelectronic devices due to their wide band-gap (3.37 eV) and large exciton binding energy (60 meV) [41-43]. ZnO is also a functional material that is sensitive to toxic and combustible gases. ZnO gas sensors with various forms, such as powder, thin films, heterojunctions, nanoparticles, and one-dimensional nanowires, nanorods, nanoflowers have been demonstrated. Among these, nanostructures are particularly useful due to their large surface-to-volume ratio, which lead to higher diffusion rate and pore volume. ZnO nanorods synthesized by low temperature chemical solution route [44], solvothermal method [45, 46], solid-state reaction method [47] have been studied for NH_3, H_2S, ethanol and H_2 sensing characteristics. It is known that the presence of noble metal elements (Pt, Pd, Au etc.) on the surface of metal oxide can enhance the interaction of gas species with the adsorbed oxygen on the surface [48, 49]. One-dimensional ZnO nanostructures such as nanowires [50], nanonails, nanotrees [51], nanocombs [52] and nanotetrapods [53] have been synthesized by oxygen assisted thermal evaporation of zinc metal and by vapor phase techniques at high temperature, and its H_2S, NO_2, CO, H_2, NH_3, ethanol, acetone, humidity sensing characteristics have been studied. Cd-doped ZnO nanowires synthesized by thermal evaporation method, showed a resistance change of more than three orders of

magnitude when it was exposed to a pulse of 95% relative humidity [54]. H_2S sensor using a single ZnO nanowire as a sensing unit has been presented by Liao et al. [55].

We have been exploring the gas sensing properties of pure and ZnO nanostructures impregnated with Pt (1%) to achieve high sensitivity, selectivity and lower response, recovery times. In view of the varied results in the literature, which have generally reported relatively low sensitivities, it seemed desirable to systematically study the sensing properties of nanostructured materials of ZnO for H_2 and ethanol, with a view is to obtain high sensitivity as well as good response and recovery times at relatively low temperatures. For this purpose, we have investigated the characteristics of ZnO nanoparticles; Co/Mn doped (1 and 3%) nanoparticles, nanorods, nanowires and nanotubes prepared by different chemical routes for sensing H_2 and ethanol vapor. The H_2 sensing characteristics were studied over the concentration range of 10-1000 ppm. The ethanol sensing characteristics were examined for 1000 ppm of ethanol. In addition to studying the sensing characteristics of the as-prepared nanostructured materials, we have investigated the effect of impregnating the ZnO nanostructures with 1 at% Pt. Also the effect of humidity on sensing characteristics has been studied. We considered it important to investigate the H_2-sensing characteristics of single nanowires of ZnO at room temperature. We have employed contact mode atomic force microscopy to explore the sensing characteristics of single ZnO and TiO_2 nanowires for sensing H_2 at room temperature.

2.2.2 Hydrocarbon and hydrogen sensors based on tungsten oxide nanowires

Wide-band gap semiconducting oxides such as SnO_2 and ZnO have been studied for making efficient hydrocarbon sensors with noble metal additives such as palladium and platinum [56-59]. The sensitivity of the sensors employing these oxides is well within 100 at 2000 ppm level. Other materials examined for hydrocarbon sensing include WO_3 [60], γ–Fe_2O_3 loaded with PtO [61] and nanocrystalline $Ni_{1-x}Co_xMn_xFe_{2-x}O_4$ [62]. The sensitivity and response times of these sensors are not entirely satisfactory. V_2O_5 supported on ZrO_2 is reported to be a good sensor for n-propane-butane mixtures at 625K [63], but the maximum sensitivity found is around 3 at the 2000 ppm level. Thick films of nano-sized SnO_2 exhibit a sensitivity of 90 for 1000 ppm of liquefied petroleum gas (LPG) [64]. SnO_2 samples sintered at 600 °C show a sensitivity of 100 at 350 °C for 1000 ppm of LPG [65]. In another report, thick-film gas sensors based on pure and Ru-doped nanostructured SnO_2 are found to have a maximum sensitivity of 375 for 1000 ppm of LPG [66] Liu *et al.* [67] have reported a LPG sensor based on multi-walled carbon nanotubes coated with SnO_2 with a sensitivity of ~ 20 at 335 °C for 1000 ppm of LPG.

In the present work we have studied the hydrocarbon sensing characteristics of different nanostructures of V_2O_5 as well as nanowires of tungsten oxide ($WO_{2.72}$) over the concentration range of 50-2000 ppm, after characterizing the nanostructures by X-ray diffraction, electron microscopy and Raman spectroscopy. In addition to studying the sensing characteristics of the as-prepared nanowires of tungsten oxide, we have investigated the effect of impregnating the tungsten oxide nanowires with 0.1, 0.5 and 1 at% Pt. We have found excellent sensing characteristics of $WO_{2.72}$ nanowires towards LPG (propane-butane mixture) at relatively low temperatures in the range of 50-200 °C

with satisfactory response and recovery times. Also the LPG and H_2 sensing characteristics of single nanowires of $WO_{2.72}$ have been studied by conducting atomic force microscopy.

2.2.3 H_2S sensors based on tungsten oxide nanostructures

We were interested in developing sensors for H_2S using metal oxide nanostructures, since H_2S is a toxic gas used in chemical laboratories and industries. H_2S is also liberated in nature due to biological processes and also from mines and petroleum fields. In the literature, there are reports where films of WO_3 have been used for sensing H_2S at ppm level with the response values varying between 3 and 10^4 depending on the temperature and the gas concentration [68-73]. Nanoparticulate WO_3 films show a sensitivity of 3-5 for 1 ppm of H_2S at 200 °C [71]. Active layers of pure and Pt-doped WO_3 films deposited by rf magnetron sputtering were able to sense 100 ppb of H_2S at 200 °C [72]. Rf sputtered WO_3 films and films doped with Pt, Au, Ag, Ti, SnO_2, ZnO and ITO have been examined; sensitivity was improved by Au to H_2S [73]. Tungsten oxide nanocrystalline films [74-76] and nanowire networks [77] have been studied for H_2S sensing. Sensitivities of 9.9 and 9.7 were achieved in 7.7 wt % Pt-doped nanocrystalline WO_3 at 220 °C and 7.2 wt % Pd-doped WO_3 at 170°C respectively for 100 ppm H_2S [74]. Nanocrystalline WO_3 powders annealed at 400 °C and 700 °C have been studied for sensing 20 ppm H_2S in the 200-300 °C range. Samples annealed at 400 °C show higher sensitivity (~10) compared to those annealed at 700 °C [75]. Pure and Al or Au doped nanocrystalline WO_3 films made by advanced reactive gas deposition were investigated for H_2S sensing. WO_3 nanoparticle based sensors were sensitive to H_2S at room temperature, but the response times were of several minutes and recovery times were of

several hours [76]. Three dimensional tungsten oxide nanowire networks show a sensitivity of ~100 for 10 ppm H_2S at a working temperature of 300 °C [77]. Thin films of SnO_2 exhibit a sensitivity ~100 for 5 ppm of H_2S at 200 °C [78], while SnO_2 films impregnated with CuO show a low sensitivity for 10-500 ppm H_2S in the 100-200 °C range [79-82]. $Fe_2(MoO_4)_3$ powders are reported to show a sensitivity ~31 for 10 ppm of H_2S at 250 °C [83]. $LnFeO_3$ (Ln= Eu or Gd) shows a sensitivity ~12 for 50 ppm H_2S at 350° C [84]. We have investigated the sensing characteristics of WO_3 nanoparticles and nanoplatelets and of $WO_{2.72}$ nanowires towards H_2S in the 1-1000 ppm range at a working temperature in the range of 40-250° C. Our study shows that $WO_{2.72}$ nanowires are good candidates for sensing H_2S in the 10-1000 ppm range at 250 °C.

2.2.4 NO_2, NO and N_2O sensors based on In_2O_3 and WO_3 nanowires

Sensing NO_2 in the atmosphere has assumed great importance because of the serious problem of atmospheric air pollution caused by auto-exhaust and other sources. In view of this, there have been attempts to develop sensors for NO_2 based on metal oxides, which have been traditionally used for sensing different gases. Thus, ZnO powder has been found to detect NO_2 at low concentrations at 100 °C, although the sensitivity is not high [85]. Nanobelts and nanowires of SnO_2 are reported to act as NO_2 sensors at 150 °C [86]. Nanocrystalline WO_3 senses low concentrations of NO_2, but the observed sensitivity is low [87, 88]. Single crystalline nanowire bundles of WO_3 seem to exhibit better sensing characteristics for low NO_2 concentrations due to the high surface-to-volume ratio [89], with a sensitivity of ~9 for 50 ppb of NO_2 at 150 °C. Thick and thin films of WO_3 have been shown to sense NO_2 at relatively high temperatures [90-92]. In_2O_3 , which is known to have good sensing characteristics for NH_3 [93], CO, H_2 [94] and O_2 [95], has been

investigated by a few workers to sense NO_2. Thus, nanowire transistors of In_2O_3 act as NO_2 and NH_3 sensors at ppm levels at room temperature [96]. In_2O_3 nanoparticles have been found to sense 2 ppm of NO_2 at 200 °C with a response time of 60s [97]. Thin films of In_2O_3 and of In_2O_3 in mixture with other oxides have also been employed for sensing NO_2 at operating temperatures of 400 °C and 500 °C respectively [98-100]. Besides NO_2 , there is need to find good sensors for NO and N_2O as well. While NO is part of the pollution problem, N_2O is a green-house effect gas which causes ozone-layer depletion. N_2O is also used in medical practice as an anesthetic. SnO_2 loaded with a small amount of SrO, CaO, BaO, Bi_2O_3 and Sm_2O_3 have been studied for N_2O sensing in the concentration range of 10-300 ppm at 500 °C [101].

We were interested in exploring gas sensors for all the three nitrogen oxides, NO_2, NO and N_2O, since they all have detrimental effects on the atmosphere. Since the reduction in grain size of the nanostructured materials allows a high surface-to-volume ratio, thereby providing greater reactivity at the surface and grain boundaries, we have investigated nanowires of ZnO, In_2O_3 and WO_3 for sensing the three nitrogen oxides. The present study reveals that In_2O_3 nanowires of ~20 nm diameter prepared by using porous alumina templates as well as WO_3 nanowires of ~10 nm diameter are ideally suited as sensors for all the three nitrogen oxides, in terms of the high sensitivities as well as the relatively short response and recovery times.

2.2.5 Ammonia sensors based on metal oxide nanostructures

Detection of ammonia in the atmosphere is an extremely important problem with implications to the environment and medical practice as well as the automotive and chemical industries [102]. There have been reports on ammonia sensors, but they do not

make use of nanostructures. Thus, thin films of ZnO and ZnO doped with different metals have been found to sense ammonia with sensitivities varying between 4 and 95 for 1-30 ppm of NH_3 over the temperature 30-300°C range [103, 104]. Surface-ruthenated ZnO films appear to have a sensitivity of ~440 for 1000 ppm of NH_3 at 300°C [105, 106]. Thin films of sol-gel derived SnO_2 are reported to exhibit a linear relationship between the logarithm of sensitivity and NH_3 concentration in the range of 0.05-10 volume% at 350°C [107]. SnO_2 powder modified by Pt or SiO_2 shows sensitivity between 12 and 25 for 200 ppm of NH_3 at 160°C [108]. In_2O_3 ceramics modified by Ti or loaded with Pt, Au show enhanced selectivity for 5-1000 ppm at 145°C [109, 110]. Several other materials have also been tested for sensing ammonia, in particular single-walled nanotubes functionalized with poly-aminobenzene sulfonic acid and N-doped carbon nanotubes [111-113]. The nanotubes exhibit a sensitivity of 2 for 5 ppm of NH_3 at 32°C. Based on the literature, there appears to be a clear need for reliable and satisfactory ammonia sensors.

Our success with the nanostructures of different semiconducting metal oxides for sensing H_2, hydrocarbons and ethanol, suggested that it would be rewarding to explore nanostructures of certain metal oxides for sensing ammonia. Hence, we have studied the NH_3-sensing properties of the nanostructures of ZnO, In_2O_3 and SnO_2, of which those of SnO_2 are particularly satisfactory, with good sensitivity and relatively short response and recovery times.

2.3 Experimental aspects

2.3.1 Synthesis of nanostructures

Nanostructures of different metal oxides have been synthesized by following different chemical routes, which includes sol-gel method, solvothermal method, solid-state reactions, electrophoretic deposition technique, template methods, and carbothermal synthesis etc.

(a) ZnO nanostructures

ZnO nanoparticles were synthesized by the sol-gel technique starting with zinc acetate. An aqueous solution of ammonia was used to hydrolyze the zinc acetate and yield a gel. The gel obtained after 2h, was dried at 100°C for 10h to obtain the xerogel of the material. The xerogel was calcined at 250°C for 3h and ground to form a powder. The powder was slowly heated to 400°C for 30 min to decompose the organic matter completely. The same procedure was used to prepare the powders of ZnO doped with 1 and 3mol% of Co and Mn starting with the acetate solutions. It should be noted that Co and Mn can be doped satisfactorily in ZnO as established by X-ray diffraction as well as optical and EPR spectroscopy and that doping ZnO with 3% Co and Mn lowers the band gap of ZnO [114].

ZnO nanorods were synthesized by two procedures. In the first procedure [115], the nanorods (designated as nanorods-1) were prepared by adding triethanolamine (0.07 mol) to a fine powder of Zn $(CH_3COO)_2$. $2H_2O$ and grinding the mixture with NaOH (0.02 mol) for 30 min. The product was washed several times in an ultrasonic bath with distilled water and alcohol, followed by drying in air at 80 °C for 2 h. The second

procedure was based on oriented attachment of preformed quasi-spherical nanoparticles [116]. These nanorods (designated as nanorods-2) were prepared as follows. Zn $(CH_3COO)_2$. $2H_2O$ was dissolved in methanol under vigorous stirring at 60 °C and 0.03M KOH in methanol added drop wise to this solution. The resulting solution was refluxed for 24 h to obtain the product, which was washed with alcohol and dried. ZnO nanowire arrays were prepared by electrophoretic deposition in anodic alumina membrane (AAM) templates with 20 nm pores [117, 118]. The alumina template was dissolved in 0.6 M NaOH to obtain nanowire bundles. To prepare ZnO nanotubes, Zn nanowires produced by nebulized spray pyrolysis [119], were oxidized by heating in air at 450 °C at a rate of 5 °C / min for 4h.

(b) TiO_2 nanowires

TiO_2 nanowires were synthesized by solvothermal method [120]. For the synthesis of TiO_2 nanowires, 0.15 M $TiCl_3$ (Riedel-de Haen) and 80ml saturated solution of NaCl (Merck, 99% pure) were taken in a Teflon-lined autoclave and heated at 200 °C for 2h. The product obtained after cooling the autoclave to room temperature was washed with deionized water and alcohol several times and dried in vacuum.

(c) V_2O_5 nanostructures

For the synthesis of V_2O_5 nanoparticles, 1g of NH_4VO_3 (Merck, 99.5% pure) was taken in a 100 ml Teflon-lined autoclave containing 80% volume of ethylenediamine (Merck, 99% pure) and heated at 220 °C for 24h. The final product obtained after cooling the autoclave to room temperature was washed with deionized water and then anhydrous alcohol several times and dried at 80 °C for 24h. The powder was then heated slowly at 450 °C for 2h in air.

V_2O_5 nanobelts were prepared by adding 0.01 mol (1.17g) of analytically pure NH_4VO_3 into 50ml (2g l^{-1}) polyethyleneglycol-4000 (Loba Chemie, 99% pure) solution under stirring and the pH of the mixture adjusted to 2-3 by adding HNO_3 (Rankem, 72% pure) dropwise. The solution was transferred into a 100 ml Teflon-lined autoclave. The autoclave was kept at 200 °C for 24h and then allowed to cool. The final product was washed several times with deionized water and ethanol.

In order to prepare V_2O_5 nanowires, an aqueous solution of sodium metavanadate was passed through a cation exchange column (DOWEX) to get vanadic acid. A polycarbonate membrane (Nucleopore Track-Etch membrane, 0.02 μm; Whatman, Kent, UK) was immersed in the vanadic acid solution and kept for 24 hours at 50 ºC. The polycarbonate membrane containing nanowires was slowly heated at 500 ºC for 6h.

(d) Tungsten oxide nanostructures

The procedure for preparing the WO_3 nanoparticles was as follows [121]. 0.2 g of WCl_6 (Aldrich, 98% pure) was taken in 80 ml of a mixture of water and ethanol mixture (3:1 ratio) and kept in an autoclave for 6 h at 150°C. The obtained product was washed with deionized water and ethanol. Then it was heated at 400°C for 1h at a heating rate of 1°C min^{-1}. WO_3 nanoplatelets were obtained by following the method [122]. 0.5 g of WCl_6 and 20 ml of benzyl alcohol were taken in a beaker. After vigorous stirring for 1 h, the solution was transferred to a 25 ml autoclave and kept at 100°C for 48 h. The obtained product was washed with ethanol several times and dried in vacuum at 60°C. To remove water, the product was heated at 400°C for 1 h at a heating rate of 1°C min^{-1}. Tungsten oxide ($WO_{2.72}$) nanowires were prepared by solvothermal synthesis [121]. 1g of WCl_6 was taken in a 25 ml autoclave filled with ethanol up to 90% of its volume. Solvothermal

synthesis was carried out at 200°C for 24 h. The product obtained by centrifugation was washed with ethanol.

(e) In_2O_3 nanostructures

One sample of In_2O_3 nanowires was prepared by the carbothermal process [123]. The detailed experimental procedure is as follows: A thin Au film (~ 30 nm) was deposited on the Si (100) substrate. The In_2O_3 (99.95% purity) and graphite (99.995% purity) powders with a weight ratio of 1:1 were mixed thoroughly. The mixture was then loaded in an alumina boat, which was placed in the quartz tube, placed in a tube furnace. The Au-coated Si substrate in the boat was placed at 5 cm downstream from the powder mixture. The tube was purged with Ar for 10 min at room temperature, followed by a raise of the temperature to 950°C with a heating rate of 3°C/min for the powders Then, a gas mixture of Ar and O_2 (Ar flow rate, ~ 200 sccm; O_2 flow rate, ~ 10 sccm) was introduced to the quartz tube for the reaction to take place. After 2 hrs of growth, the furnace was cooled down to room temperature, and a white-yellowish product was observed on the substrate.

Two other samples of In_2O_3 nanowires were prepared by using anodic alumina membrane (AAM) templates with pore sizes of 200 nm and 20 nm [124] and designated as In_2O_3 –1 and In_2O_3 –2. The method of preparation of these nanowires was as follows. $In(OH)_3$ sol was prepared starting with $InCl_3.4H_2O$ and by adding ethylene diamine dropwise. The sol was taken in 100 ml deionized water and stirred for 6h at room temperature. After getting a light blue hydrated $In(OH)_3$ sol, the alumina template membranes were immersed in the sol for 5h under a pressure of 2 atm. The templates

were then taken out and dried at 60°C and heated under an argon atmosphere at 600°C for 4h. The templates were dissolved in 0.6 M NaOH solution to get the nanowires of In_2O_3.

(f) SnO_2 nanostructures

SnO_2 nanoparticles were prepared by dissolving 1g of $SnCl_4.5H_2O$ (Lobachemie, 98% pure) in 70 ml of H_2O, followed by addition of a few drops of ethylenediamene. The solution was taken in a 100 ml Teflon-lined autoclave and heated at 200°C for 24h. After cooling the autoclave, the product was washed with alcohol and water and dried in air at 60°C overnight. SnO_2 nanorods and flower-like structures were obtained by following methods reported elsewhere [120, 125]. SnO_2 nanorods were prepared starting with a mixture of 1g of $SnCl_4.5H_2O$ in 70 ml of ethanol and water (5:1). After adding 10 M NaOH, the solution was transferred to a 100 ml autoclave and heated at 200°C for 24h. After cooling the autoclave, the product was washed with absolute ethanol several times and then it was dried in vacuum to get the final product. Flower-like structures of SnO_2 were obtained by taking 0.5g of as-prepared SnO_2 nanoparticles and 10 M NaOH in 80 ml ethanol and heating the mixture in an autoclave at 200°C for 36h. The product was washed with dil. HCl and water to remove the byproducts of sodium, and was dried in vacuum at 60°C.

2.3.2 Techniques used for characterization

X-ray diffraction

Powder X-ray diffraction patterns were recorded using Cu-Kα radiation on a Rich-Seifert, XRD-3000-TT and a Rigaku diffractometer.

Scanning electron microscopy

Scanning electron microscopy (SEM) images were obtained on a LEICA S440i scanning electron microscope and a field emission electron scanning electron microscope (FESEM with a NOVA NANOSEM 600). Energy dispersive analysis of X-rays (EDAX) was performed with a Oxford microanalysis group 5526 system attached to the SEM employing Links (ISIS) software and a Si(Li) detector.

Transmission electron microscopy

Transmission electron microscopy (TEM) images were obtained with a JEOL JEM 3010 operating with an accelerating voltage of 300 kV.

Raman Spectroscopy

The Raman experiments were performed in the back scattering geometry (LABRAMAN-HR) using a He-Ne laser at 632.8 nm.

Atomic force microscopy

Contact mode atomic force microscope (CAFM) measurements were made using a digital instrument multimode head attached to a Nanoscope–IV controller and an external multimeter (Kiethley 236) as the source and measurement unit for current-voltage characteristics. Commercial silicon nitride cantilever probes from Olympus (Japan) (spring constant, 0.61N/m) were made conducting by coating them with Ti/Au (10/100 nm) by using a physical vapor deposition (PVD) system. The bias ramp was applied to the conducting probe through the tip holder and the current was measured from a terminal connected through the floating substrate. The conducting nature of the tip was ensured during the experiment by repeatedly measuring the contact resistance (~100-200Ω) after engaging the tip on the substrate. Highly oriented pyrolytic graphite (HOPG) was used as

the conducting substrate on which nanowires of ZnO, TiO_2 or $WO_{2.72}$ were deposited by dispersing them in 2-propanol. An environmental hood was placed enclosing the AFM head for measurements in hydrocarbon or H_2 atmosphere.

Fabrication of gas sensors

To fabricate thick film sensors, an appropriate quantity of diethyleneglycol was added to the powder of the nanostructures and the mixture ground to form a paste. The paste was coated on to an alumina substrate (5 mm x 20 mm, 0.5 mm thick) attached with a comb-type Pt electrode on one side, the other side having a heater. A schematic diagram of the alumina substrate is shown in figure 2.3.1. The films were dried and annealed at 300-600°C for 1h. The oxide films were doped in the solution of chloroplatinic acid to obtain a coating of Pt in the case of some oxide nanostructures.

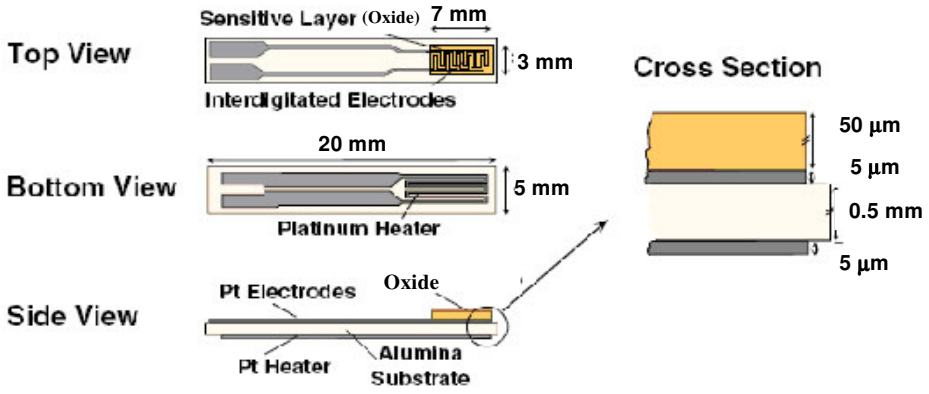

Figure 2.3.1: Schematic diagram of the alumina substrate with Pt electrodes and interdigitated Pt heater on the back side. Sensing oxide layer is coated on top of the interdigitated side and the heater side provides different working temperature.

Gas-sensing measurement set-up

The gas sensing characteristics were measured with a home-built apparatus consisting of a test chamber, sensor holder, a Keithley multimeter-2700, a Keithley

electrometer-6517A, mass flow controllers and a data acquisition system. The test gases were allowed to flow through a pipe network of diameter of 3mm to a test chamber of volume of 8.8 cm^3 via a two-way valve. The valve and the test chamber were connected by a downstream pipe work of length 8 cm. The gas flow was maintained at 200 sccm by using mass flow controllers. The current flowing through the samples was measured using a Keithley multimeter-2700. The working temperature of the sensors was adjusted by changing the voltage across the heater side.

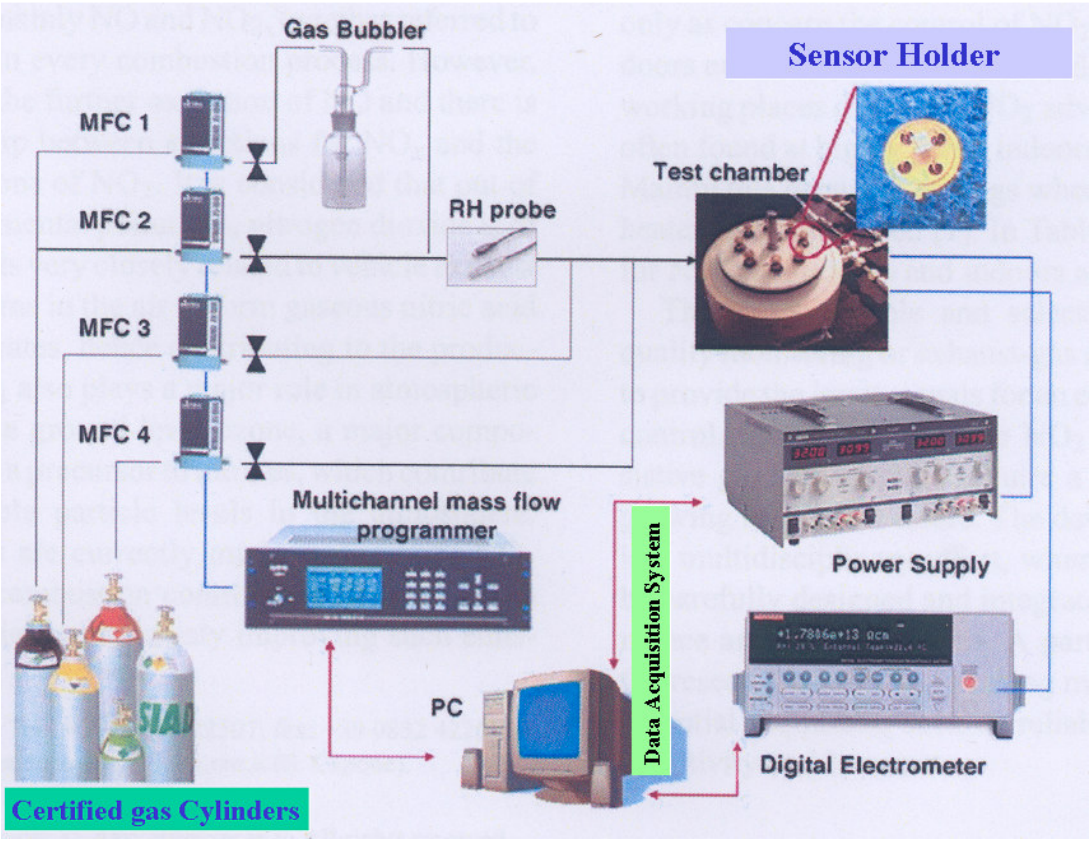

Figure 2.3.2: Schematic diagram of the gas-sensing set-up

By monitoring the output voltage across the sensor, the resistances of the sensor in dry air or in test gas can be measured. A schematic diagram of the experimental set-up is shown in figure 2.3.2. Figure 2.3.3 shows a schematic diagram of the sensor measuring

circuit. The gas sensitivity (response magnitude) of the sensor was determined by the relationship $S=R_{air}/R_{gas}$, for reducing gases and $S=R_{gas}/R_{air}$ for oxidizing gases, where R_{air} is the resistance of the thick film sensor in dry air and R_{gas} is the resistance in the test gas. For resistance measurements, a load resistor R_L was connected in series with the sensor element R_S. The input circuit voltage V was applied across R_L and R_S. The response time was taken as the time required for the variation in conductance to reach 90% of the equilibrium value after the test gas was injected and the recovery time is taken as the time necessary for the sensor to attain a conductance 10% above the original value in air.

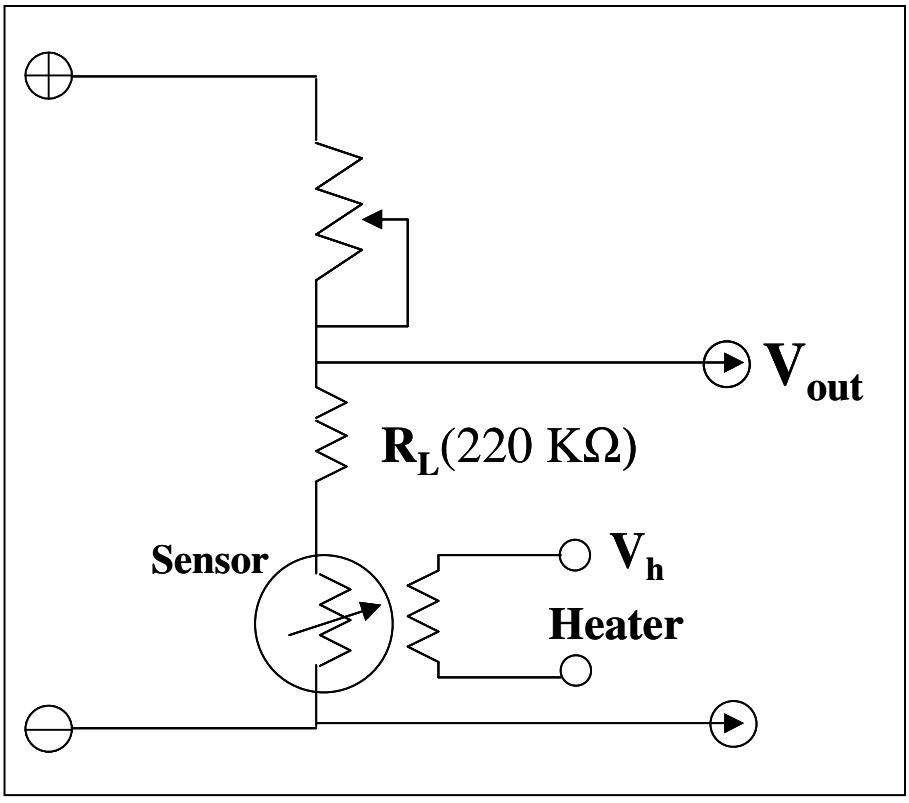

Figure 2.3.3: Schematic diagram of the voltage measuring circuit

2.4 Results and discussion

2.4.1 Hydrogen and ethanol sensors based on ZnO nanostructures

We have investigated the sensing characteristics of thick films of nanoparticles (undoped and doped with Mn and Co), nanorods, nanowires and nanotubes of ZnO for H_2 and ethanol vapor with a view to obtain high sensitivity, selectivity as well as good response and recovery times at relatively low temperatures. We have examined the effect of impregnating pure ZnO naoparticles and nanowires as well as the Mn and Co-doped ZnO nanoparticles with 1% Pt on the sensor characteristics. Effects of humidity on the sensing characteristics and the stability of the sensors have been studied. The resistance of the sensors was of 1.2 - 10 mega-Ohm range in dry air at 30-125 °C.

In figures 2.4.1 (a) and (b), we show typical TEM images of ZnO and 3% Co doped ZnO nanoparticles respectively. The images show nanoparticles along with a few nanorods (~10%). Figure 2.4.1 (c) shows the TEM image of the 3% Co doped ZnO nanoparticles after Pt impregnation. The particle size distribution histograms of all the three types of ZnO nanoparticles are shown in figure 2.4.1 (d). From the TEM studies, the average size of the different types of ZnO nanoparticles is found to be 35 ±15 nm. Similar TEM images were found with the Mn or Co doped ZnO nanoparticle samples and the particle sizes of the Mn doped ZnO were in the similar range.

In figure 2.4.2 (a), we show typical SEM and TEM images of ZnO nanorods-1. The average diameter of the nanorods-1 was in the 30-40 nm range with the length in the 600-800 nm range. The selected area electron diffraction pattern showed the nanorods to

be single crystalline. Figure 2.4.2 (b) shows the SEM image of nanorods-2 with inset showing a TEM image. The XRD pattern of these nanorods gave 002 reflections

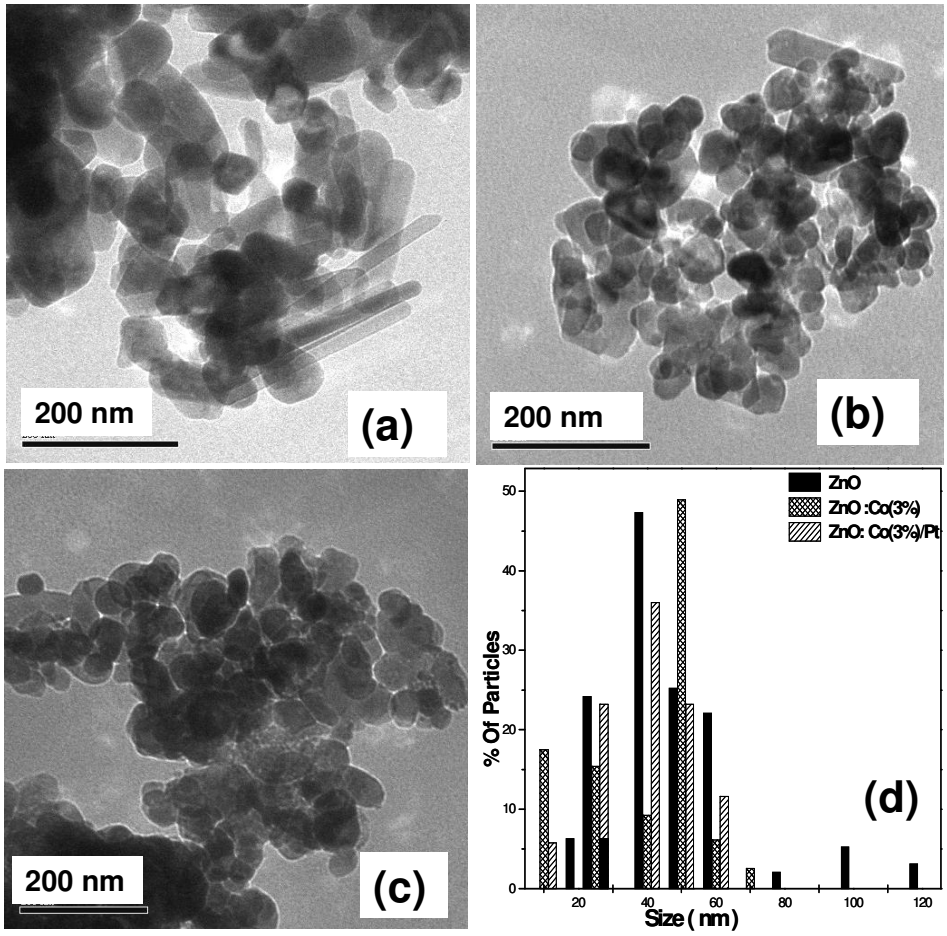

Figure 2.4.1: TEM images of nanoparticles of (a) ZnO, (b) ZnO doped with 3% Co before annealing and (c) ZnO doped with 3% Co and 1% Pt impregnation after annealing at 600° C. (d) Histograms of the particle size distributions of ZnO, ZnO:Co(3%) and ZnO:Co(3%)/Pt nanoparticles.

indicating the formation of the rods along the *c* axis. Figure 2.4.2 (c) shows the SEM image of the nanowires prepared in the AAM templates. The diameter of the nanowires was in the 20-30 nm range and 1-2 micron in length. Figure 2.4.2 (d) shows the SEM image of the ZnO nanotubes. The diameter of the nanotubes was in the range of 60-100 nm.

Hydrogen sensors:

The hydrogen sensing characteristics of the ZnO nanoparticles with and without Pt impregnation are presented in figure 2.4.3 (a) and (b) respectively. The nanoparticles of ZnO show a sensitivity of 48 at 80°C for 1000 ppm of H_2 and the sensitivity increases to 68 at 125°C. On impregnating the ZnO nanoparticles with 1% Pt, we observe a significant improvement in the sensitivity as well as the response and recovery times. On Pt impregnation, the sensitivity reaches 912 at 32°C and 1065 at 125°C, with response and recovery time of 3 and 4 sec respectively.

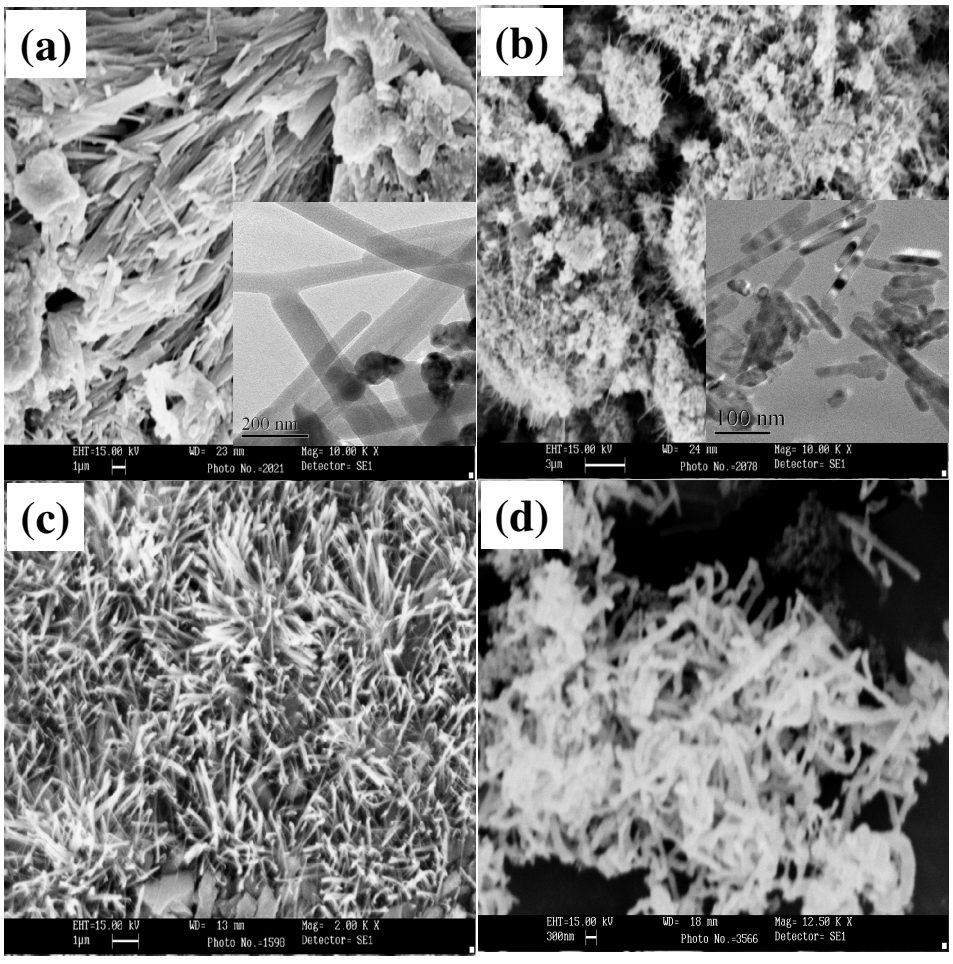

Figure 2.4.2: (a) SEM image of ZnO nanorods-1 with the inset showing a TEM image of the nanorods, (b) SEM image of ZnO nanorods-2 with the inset showing a TEM image. (c) SEM image of ZnO nanowires, (d) SEM image of ZnO nanotubes.

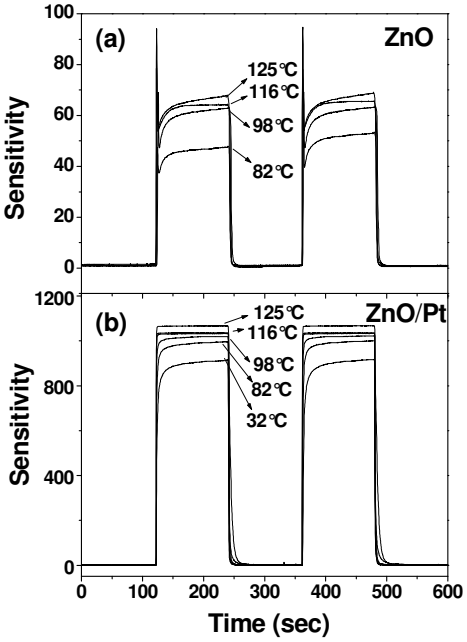

Figure 2.4.3: Gas sensing characteristics of nanoparticles of (a) ZnO and (b) ZnO impregnated with 1% Pt for 1000 ppm of H_2.

In order to ensure that the observed sensitivity is not due to the Pt nanoparticles alone, we examined the gas sensing characteristics of Pt nanoparticles by impregnating 0.08 M chloroplatinic acid on the graphite and silicon powders. We carried out the experiments with 1000 ppm of H_2 and ethanol vapor and obtained low sensitivity towards both these gases. Pt/graphite and Pt/Si show sensitivities of 5 and 3 respectively for 1000 ppm of H_2 at 125 °C. When ZnO was doped with 1% Mn or Co, little change was observed in the sensitivity. For example, ZnO doped with 1% of Mn showed a sensitivity of 20 and 120 at 80°C and 125°C respectively with response and recovery times of 11 and 14 sec {Figure 2.4.4 (a)}. On doping with 3% Mn, however, the sensitivity enhanced considerably giving values of 205 and 350 at 125°C {Figure 2.4.4 (b)}. The 1% and 3% Co doping has a similar beneficial effect as Mn doping for sensing hydrogen {Figure

2.4.4 (c) and (d)}. Doping the ZnO nanoparticles with 3% Co increases the sensitivity to 60-335 in the 80-125°C range.

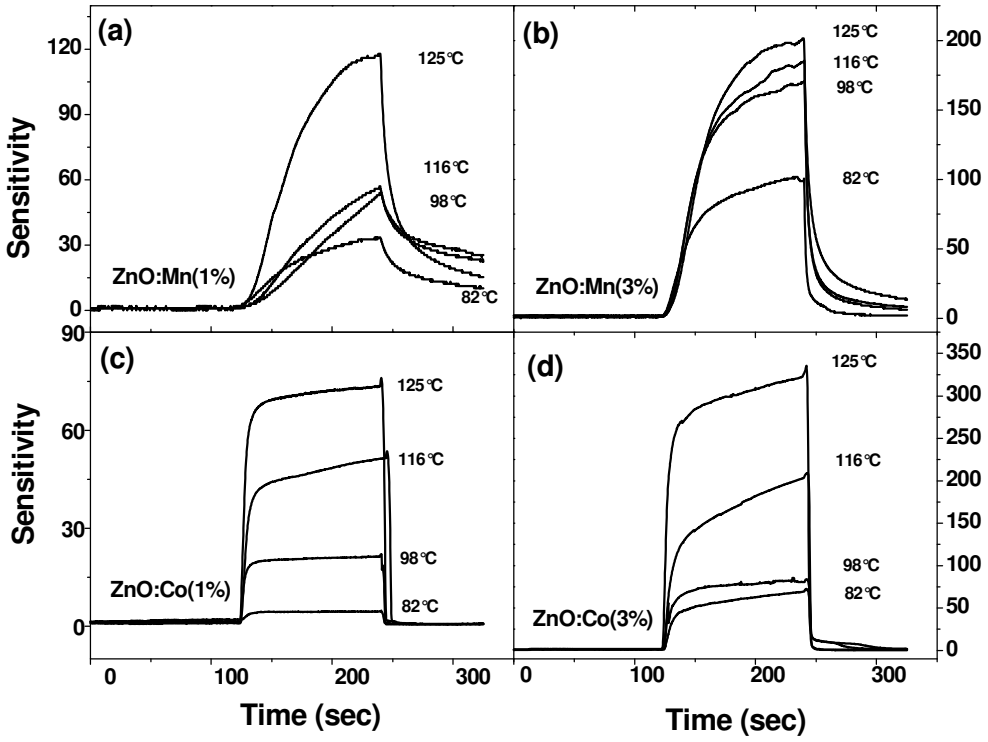

Figure 2.4.4: Gas sensing characteristics of nanoparticles of (a) ZnO:Mn (1%), (b) ZnO:Mn (3%), (c) ZnO:Co (1%) and (d) ZnO:Co (3%) for 1000 ppm H_2.

We have examined the effect of Pt impregnation on the Mn and Co doped samples for sensing H_2. The 1% Mn and 1% Co doped ZnO samples after Pt impregnation showed sensitivities comparable with those of the ZnO/Pt samples, the values of sensitivity being 1030 and 1115 at 125°C {Figures 2.4.5 (a) and (c)}. In figures 2.4.5 (b) and (d) we show the sensor characteristics of 3% Mn and 3% Co doped ZnO samples impregnated with Pt. We observed sensitivities of 1350 and 1720 respectively at125°C for the 3% Mn and Co doped samples. The Pt impregnated samples show good sensitivity even at lower

temperatures. The response and recovery times for ZnO/Pt sample were 4.5 and 7 sec. For ZnO:Co (3%)/Pt sample response and recovery times were 3 and 4 sec respectively.

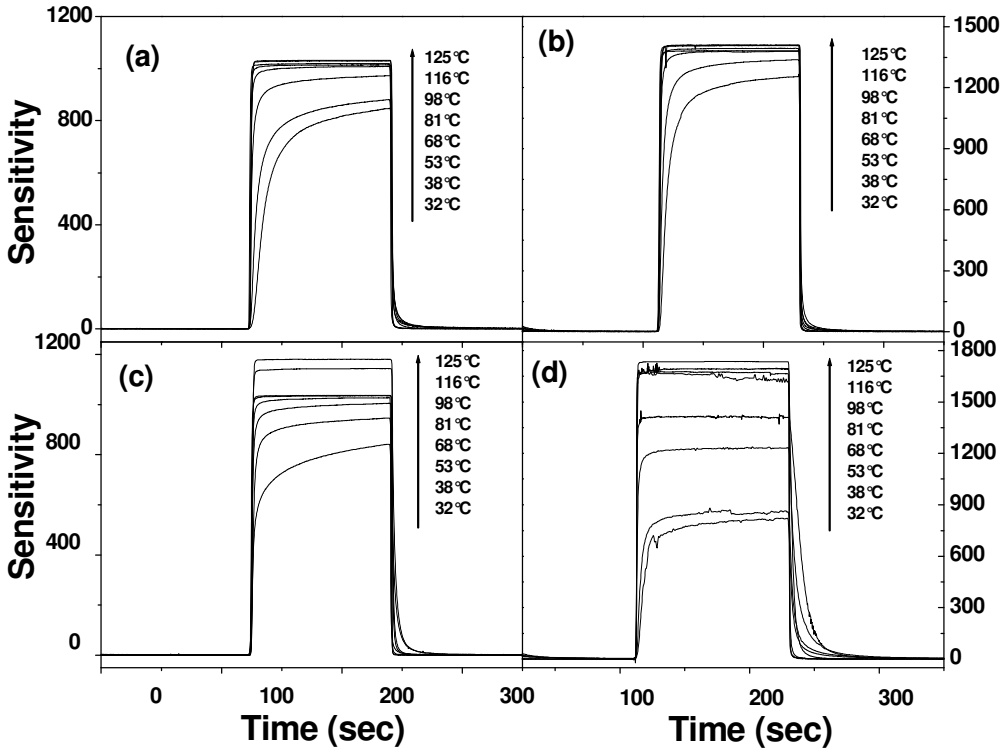

Figure 2.4.5: Gas sensing characteristics of 1% Pt impregnated nanoparticles of (a) ZnO:Mn (1%), (b) ZnO:Mn (3%), (c) ZnO:Co (1%) and (d) ZnO:Co (3%) for 1000 ppm H_2.

In figure 2.4.6 (a), we show the temperature variation of the sensitivity for 1000 ppm of H_2 gas for the doped and undoped samples with and without Pt impregnation. Figure 2.4.6 (b) shows the variation of the sensitivity with the concentration of H_2 at 125°C for ZnO, ZnO/Pt and 3% Co doped ZnO impregnated with Pt. The sensitivity is180 and 150 respectively for ZnO/Pt, ZnO:Co(3%)/Pt at 10 ppm of H_2 while pure ZnO

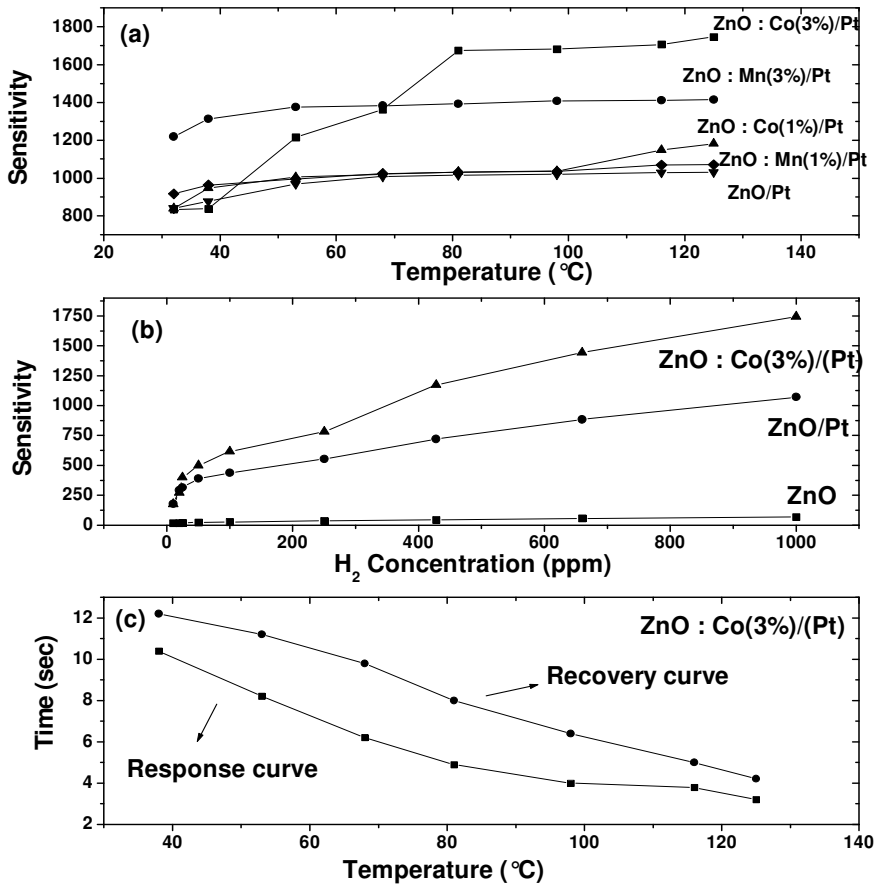

Figure 2.4.6: Variation of sensitivity of ZnO based nanoparticles for H_2 sensing (a) with temperature, (b) with concentration of H_2 and (c) variation of response and recovery times.

(without Pt) shows a sensitivity of 17. Figure 2.4.6 (c) shows the variation of the response and recovery times with temperature for ZnO:Co (3%)/Pt for 1000 ppm of H_2 at 125°C. The recovery times are generally larger than response times. In the figures 2.4.7 (a), (b) and (c), (d), we show the sensing characteristics of nanorods-1 and nanorods-2 for 1000 ppm of H_2 with and without Pt impregnation respectively. The sensitivity is 12 at 125°C and goes upto 32 at 200°C for the as-prepared nanorods. However, Pt-impregnated nanorods-1 exhibit a slightly increased sensitivity of 17 at 125 °C and 56 at 200 °C. The

response time for the as-prepared nanorods-1 is 52 sec at 200 °C while it is 18 sec for the Pt impregnated nanorods. The recovery time was generally less than 10 sec. Nanorods-2 show a sensitivity of 43 at 125°C and 61 at 200°C for 1000 ppm of H_2. On impregnation with Pt, the sensitivity of nanorods-2 increases to 60 at 150°C and 82 at 200°C {Figure 2.4.7 (d)}. The recovery times for both the as-prepared and Pt-impregnated nanorods-2 were less than 10 sec and the response time for the latter was 48 sec.

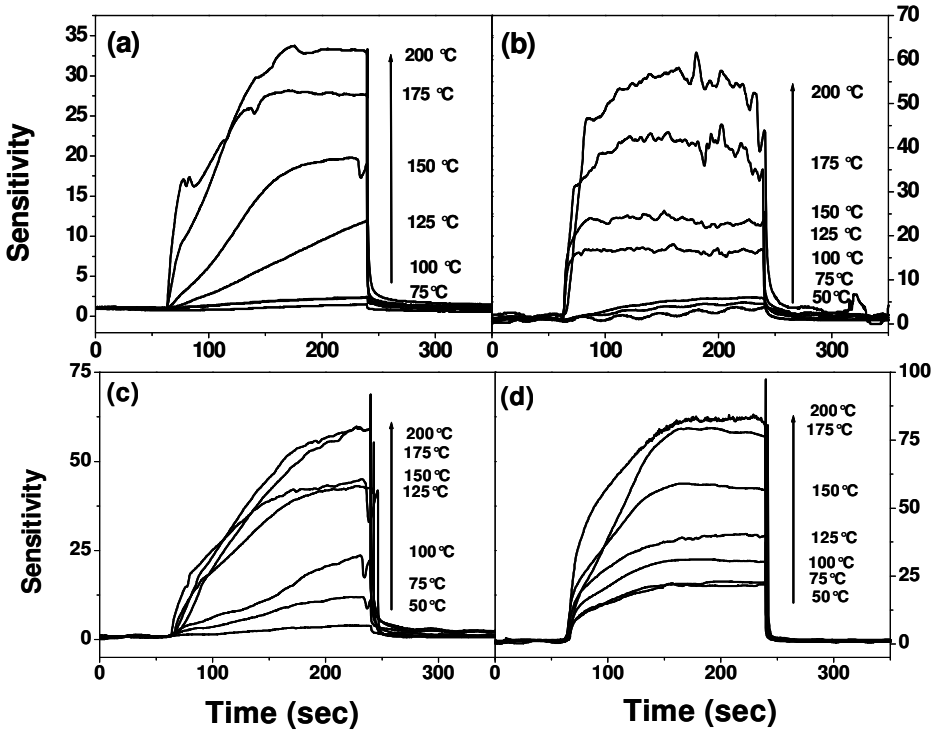

Figure 2.4.7: Hydrogen sensing characteristics of (a) as-prepared and (b) Pt-impregnated ZnO nanorods-1, (c) as-prepared and (d) Pt-impregnated ZnO nanorods-2 for 1000 ppm of H_2.

Compared to the nanorods, the nanowires prepared electrochemically by using AAMs, show much better sensing characteristics towards H_2. In figures 2.4.8 (a) and (b), we show the sensing characteristics of ZnO nanowires without and with Pt impregnation.

The sensitivity for 1000 ppm of H_2 is 43 at 150°C for the as-prepared nanowires and reaches a value of 825 after Pt-impregnation. The sensitivity for the Pt impregnated ZnO nanowires was good (~150) even at 100°C. The response times for the as-prepared and the Pt impregnated ZnO nanowires were however, somewhat high, the values being 54 and 42 sec respectively with the recovery times of 5 and 4 sec. The ZnO nanotubes prepared by us show a sensitivity of 18 at 200°C for 1000 ppm of H_2 while the Pt-

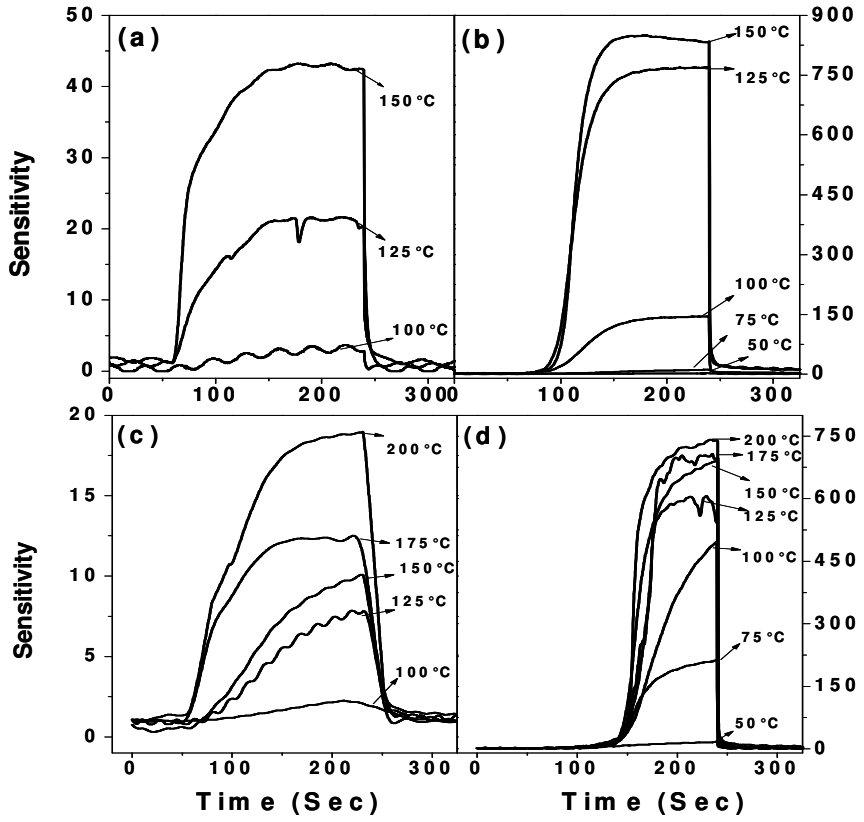

Figure 2.4.8: Hydrogen sensing characteristics of (a) as-prepared and (b) Pt-impregnated ZnO nanowires, (c) as-prepared and (d) Pt-impregnated ZnO nanotubes for 1000 ppm of H_2.

impregnated ZnO nanotubes show a sensitivity of 500 at 100°C and 740 at 200°C {Figures 2.4.8 (c) and (d)}. However, the response time is longer than as one would

desire. From the above data it appears that the ZnO nanowires prepared by using the AAM templates have the best sensing characteristics for 1000 ppm of hydrogen.

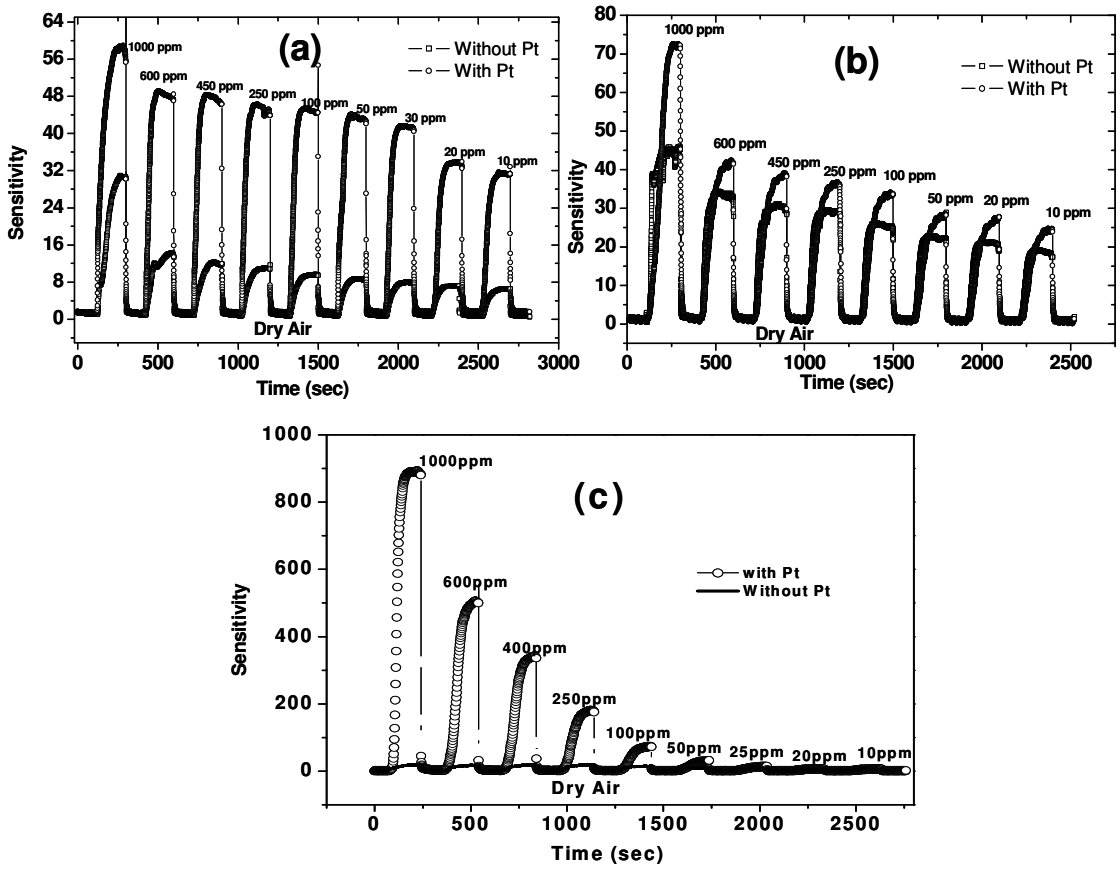

Figure 24.9: Concentration dependence of the sensitivity for sensing H_2 for (a) ZnO nanorods-1 (b) nanorods-2 (with and without Pt impregnation) at 200 °C and (b) ZnO nanowires (with and without Pt impregnation) at 150°C.

In figure 2.4.9 (a)-(c), we show the variation of the sensitivity for the ZnO nanorods-1, nanorods-2 and ZnO nanowires with and without Pt impregnation with the concentration of H_2 over the 10-1000 ppm range at 150°C. The ZnO nanowires with Pt impregnation show a sensitivity of 8 for 10 ppm of H_2 at 150°C. The nanowires show a marked drop in sensitivity on decreasing the H_2 concentration from 1000 ppm to 600 ppm, there being another drop around 100 ppm. For nanorods-1 with Pt, the sensitivity is

36 for 10 ppm of H_2 at 200°C and the sensitivity varies gradually with H_2 concentration over 1000-10 ppm range.

An important question that arises, relates to the effect of humidity on the sensing characteristics of the ZnO sensors described by us. For this purpose, we examined the effect of humidity on several of the thick film sensors prepared by us. We show typical results obtained on the H_2 sensing characteristics of ZnO, ZnO/Pt and ZnO: Co(3%)/Pt sensors in figure 2.4.10. The sensitivity is not affected up to 50% of relative humidity in all the three thick film sensors. In the case of ZnO: Co (3%)/Pt, the sensitivity remains 1100 even at a relative humidity of 90%.

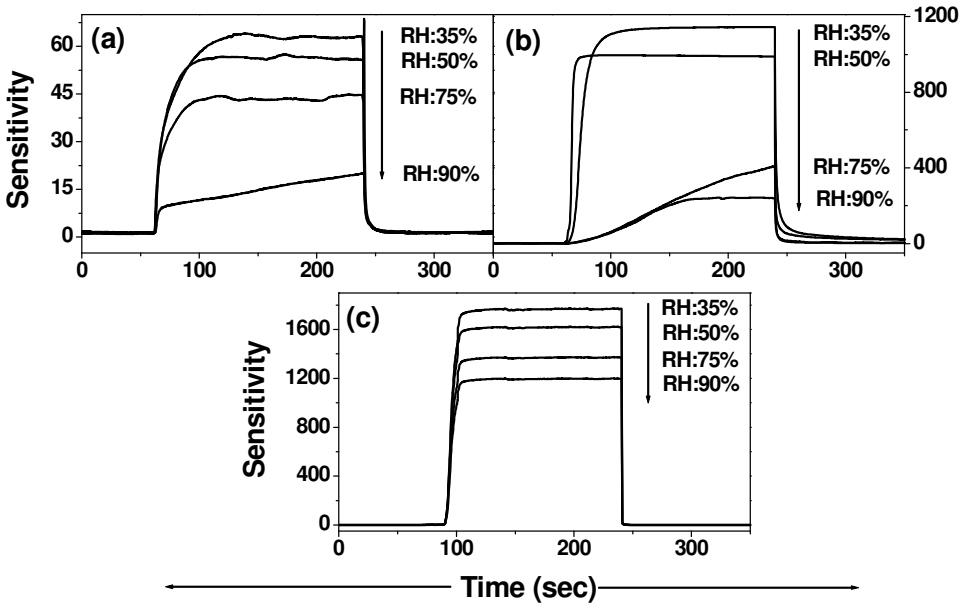

Figure 2.4.10: Effect of humidity on (a) ZnO, (b) ZnO:Co (3%) and (c) ZnO:Co (3%)/Pt nanoparticle sensors for 1000 ppm of H_2 at 125 °C.

We, therefore, conclude that the H_2 sensing characteristics for ZnO: Co (3%)/Pt nanoparticles reported by us are truly excellent even in the presence of moisture. In order

to ensure that the sensors prepared by us are stable, we carried out measurements repetitively by measuring the sensing characteristics several times. In order to ensure that the sensors prepared by us are stable, we carried out measurements repetitively by measuring the sensing characteristics several times. Thus, in case of H_2 sensing, the sensitivity remains the same even after carrying the measurements over 1000 times. We have also tested the practical performance of the H_2 sensors for space applications and found it to be satisfactory.

Ethanol sensors:

The temperature variation of sensitivity of ZnO, ZnO/Pt and ZnO: Co (3%)/Pt nanoparticles for 1000 ppm of ethanol vapor is presented in figures 2.4.11 (a), (b) and (c) respectively. The ZnO nanoparticles show a maximum sensitivity of 220 at 125°C for ethanol, the sensitivity being rather low at 50°C or below. On 1% Pt impregnation, the sensitivity reaches 480 and 2000 at 40°C and 125°C respectively, becoming nearly constant above 75°C. The 3% Co doped ZnO impregnated with Pt shows a sensitivity of 2520 at 125°C, the sensitivity being close to 2500 even at 50°C. It should be noted that the Pt nanoparticles alone deposited on graphite or Si showed a very low sensitivities of ~ 2 at 125°C. We studied the effect of humidity on several thick film ZnO sensors for ethanol sensing. Figures 2.4.11 (d), (e) and (f) show the effect of humidity on the ethanol sensing characteristics of ZnO, ZnO/Pt and ZnO: Co (3%)/Pt nanoparticles. Unlike for H_2, sensor characteristics for ethanol are somewhat reduced when the relative humidity was 50%, even in the case of ZnO: Co (3%)/Pt thick films, but the performance may be considered to be still satisfactory up to 70%.

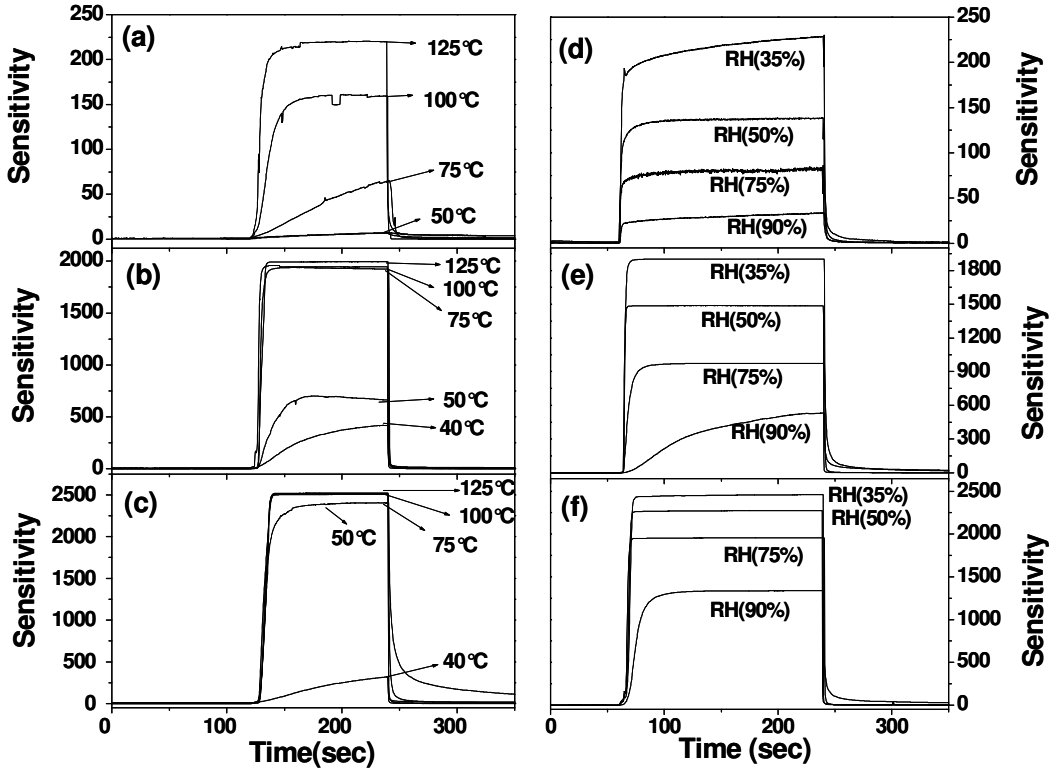

Figure 2.4.11: Ethanol sensing characteristics of (a) ZnO, (b) ZnO/Pt, (c) ZnO:Co (1%)/Pt nanoparticles for 1000 ppm of ethanol and effect of humidity on (d) ZnO, (e) ZnO:Co (3%) and (f) ZnO:Co (3%)/Pt nanoparticle sensors for 1000 ppm of ethanol at 125 °C.

The sensing characteristics of the nanorods-1, nanorods-2, nanowires and nanotubes of ZnO for 1000 ppm of ethanol were studied. The sensing characteristics were quite satisfactory for all the as-prepared nanostructures, with the sensitivity in the 200-300 range at 200 °C. The sensitivity increases to even higher values on impregnation with Pt. The sensitivity is in the range 2200-2500 at 200 °C and 1200 at 100 °C in the case of Pt-impregnated nanorods-1 {Figures 2.4.12 (a) and (b)}. The response times of 5 and 3 s were observed for the as-prepared and Pt impregnated nanorods-1 at 200 °C. The ethanol

sensing characteristics of the nanorod-2 show similar behavior, which is shown in figure 2.4.12 (c) and (d). We show the sensing characteristics of the ZnO nanowires for 1000 300 range at 200 °C. The sensitivity increases to even higher values on impregnation with Pt. The sensitivity is in the range 2200-2500 at 200 °C and 1200 at 100 °C in the case of Pt-impregnated nanorods-1 {Figures 2.4.12 (a) and (b)}. The response times of 5 and 3 s were observed for the as-prepared and Pt impregnated nanorods-1 at 200 °C. The ethanol sensing characteristics of the nanorod-2 show similar behavior, which is shown in figures 2.4.12 (c) and (d).

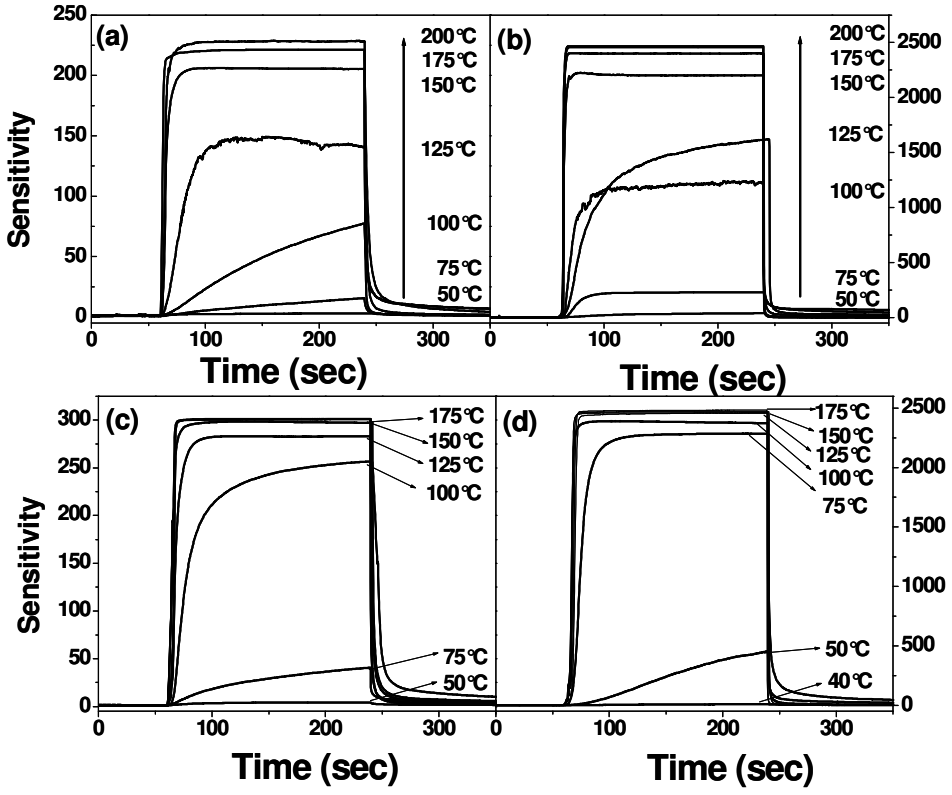

Figure 2.4.12: Ethanol sensing characteristics of (a) as-prepared and (b) Pt-impregnated ZnO nanorods-1, (c) as-prepared and (d) Pt-impregnated ZnO nanorods-2.

We show the sensing characteristics of the ZnO nanowires for 1000 ppm of ethanol in figures 2.4.13 (a) and (b). The sensitivity is 300 and 480 respectively for the as-prepared and Pt-impregnated nanowires at 150 °C, the response times being around 4 and 3 sec. The sensitivity of the ZnO nanotubes was comparable to that of the nanowires, but the response and recovery times were higher {Figures 2.4.13 (c) and (d)}.

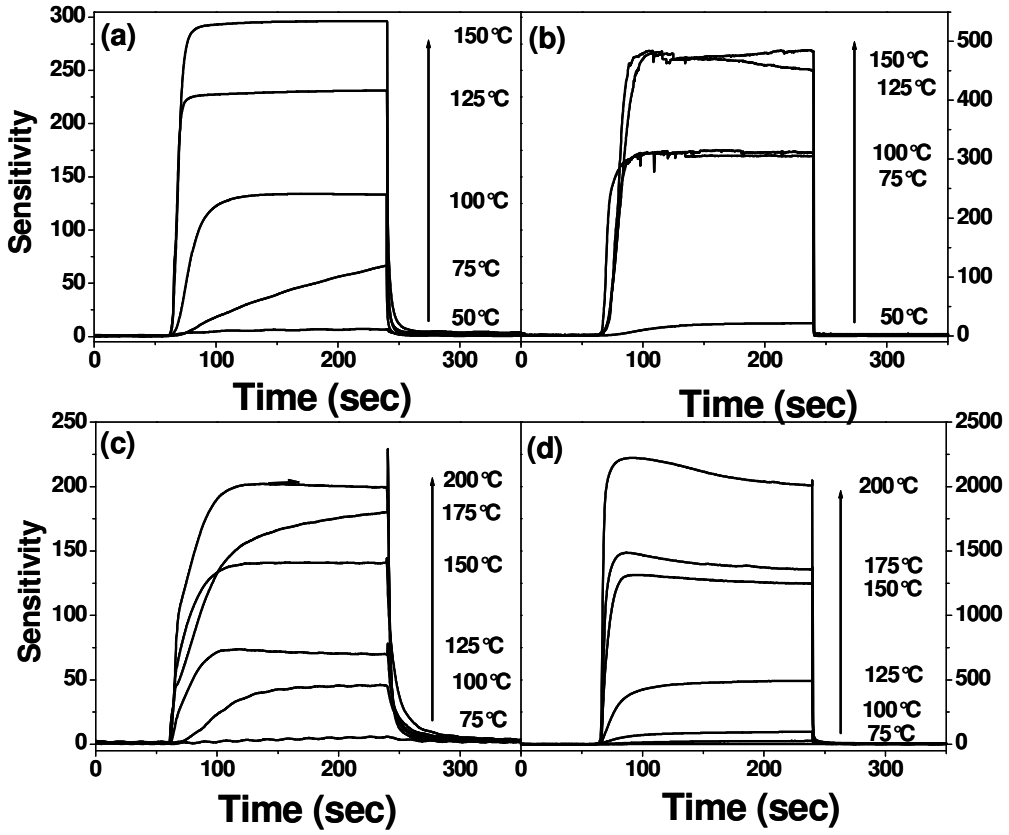

Figure 2.4.13: Ethanol sensing characteristics of: (a) as-prepared and (b) Pt-impregnated ZnO nanowires, (c) as-prepared and (d) Pt-impregnated ZnO nanowires.

It is noteworthy that the Pt-impregnated nanorods-1 and nanowires exhibit good sensitivity for ethanol even at 75 °C, the sensitivity values being higher than the literature

reports. It should be noted that the sensitivity of the ZnO nanorods, nanowires and nanotubes based sensors was not affected significantly upto 50% relative humidity.

Mechanism of sensing

The mechanism by which ZnO acts as a sensor for H_2 and ethanol can be understood based on the well-established characteristics of the oxide semiconductors [132-136]. When a ZnO nanosensor is exposed to air, the surface of the nanoparticles adsorbs oxygen molecules. The adsorbed oxygen captures electrons from the conduction band of the semiconductor to create oxygen ions. When the ZnO nanosensor is exposed to ethanol or H_2 gas, the gas molecules react with the oxygen ions on the surface. The electrons released from the surface reaction go to the conduction band, causing a decrease in the resistivity. A schematic diagram of the change in width of depletion layer is shown in figure 2.4.14 (a), (b), band bending and Fermi-level shift in air and in presence of H_2 or ethanol is shown in figure 2.4.14 (c), (d).

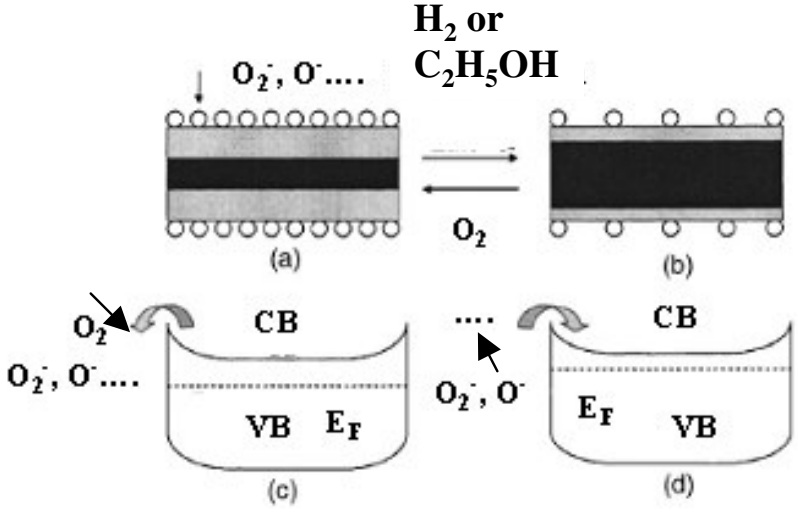

Figure 2.4.14: Change in width of depletion layer (a) in air, (b) in presence of H_2 or ethanol. Band bending diagram (c) in air, (d) in presence of H_2 or ethanol.

The enhancement in gas sensing properties on the ZnO nanostructures coated with Pt can be explained by the chemical sensitization effect, which is explained in section 2.1.5. The Pt nanoparticles catalytically activate the dissociation of molecular oxygen. The obtained oxygen atoms then migrate on to the ZnO surface and capture free electrons from them to form oxygen ions (O_2^-, O^-, O^{2-}) through binding at the oxygen vacancies. The Pt nanoparticles significantly increase the quantity of the oxygen ions. Thus, a deeper depletion layer is induced by Pt nanoparticles compared to bare ZnO nanostructures. Based on the surface depletion controlled sensing mechanism [126], the sensitivity is given by

$$S= R_a/R_g= [1+\Delta V_b/ (r_n)_{air}]^2 \qquad (3)$$

Where ΔV_b is the change of width of the depletion layer and $(r_n)_{air}$ is the width of the conducting layer (core region). $(r_n)_{air}$ further decreases due to the increase of oxygen adsorption. The change of V_b relative to $(r_n)_{air}$ is more remarkable. Surface-depletion controlled sensing is enhanced by Pt nanoparticles, resulting in ultrahigh sensitivity. The substitution effect of 3% Mn or Co, is likely to be due to the decrease in the energy gap of ZnO [114]. For example, 3% doping of Mn and Co brings down energy gap from 3.3 to 3.27 and 3.03 respectively.

Hence, in air: $\frac{1}{2} O_2 + \delta e^- \rightarrow O^{\delta-}(a)$, $\delta = 1, 2$ (4)

Pt helps in dissociation of oxygen,

$$O (Pt) + \delta e^- \rightarrow O^{\delta-}(a) \qquad (5)$$

In presence of H_2: $H_2 + O^-(a) \rightarrow H_2O + e^-$ (6)

In presence of ethanol: $C_2H_5OH + 6O^-(a) \rightarrow 2CO_2 + 3H_2O + 6e^-$ (7)

Room temperature hydrogen sensors based on single nanowires of ZnO and TiO_2

Based on our experience in fabricating high sensitivity gas sensors employing films of nanoparticles and nanowires of metal oxides for various gases and vapors, we considered it important to investigate the gas sensing characteristics of single nanowires of certain metal oxides at room temperature. H_2 sensing characteristics of single ZnO nanowires have been studied by conducting atomic force microscopy. For purpose of comparison we have carried out a similar study on single TiO_2 nanowires.

Figure 2.4.15 (a) and (b) show FESEM and TEM images of the TiO_2 nanowires. The diameters of the nanowires are in the 20-80 nm range and the length varies between100-800 nm range. From the HREM {figure 2.4.15 (c)} and electron diffraction

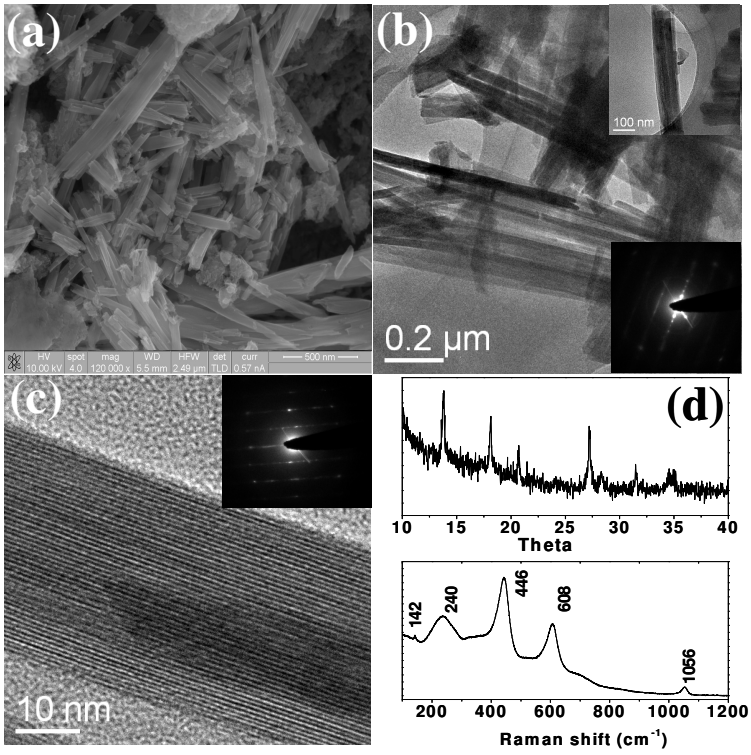

Figure 2.4.15: (a) FESEM image of TiO_2 nanowires, (b) TEM image of TiO_2 nanowires with the inset showing electron diffraction pattern, (c) HREM image of TiO_2 nanowires (d) XRD pattern and Raman spectra of the TiO_2 nanowires.

patterns {insets of figures 2.4.15 (b) and (c)} it is confirmed that the nanowires are single crystalline. TiO_2 nanowires have the rutile structure as found by XRD (a= 4.593 Å and c= 2.959 Å, JCPDS no: 21-1276). Raman bands were observed at 142, 240, 446, 608 and 1056 cm^{-1} {Figure 2.4.15 (d)} in agreement with the literature [128].

We have studied the hydrogen sensing characteristics of the three nanowires by using CAFM. In figure 2.4.16, we show a schematic describing the CAFM measurements. The depletion layer forms on the outer surface of the nanowire by the atmospheric oxygen. This layer is rich in O^- and O^{2-} species and giving rise to high resistance. The core part of the nanowire contains conduction electrons and is more conducting compared to the depletion layer, which helps in the conduction through the nanowire.

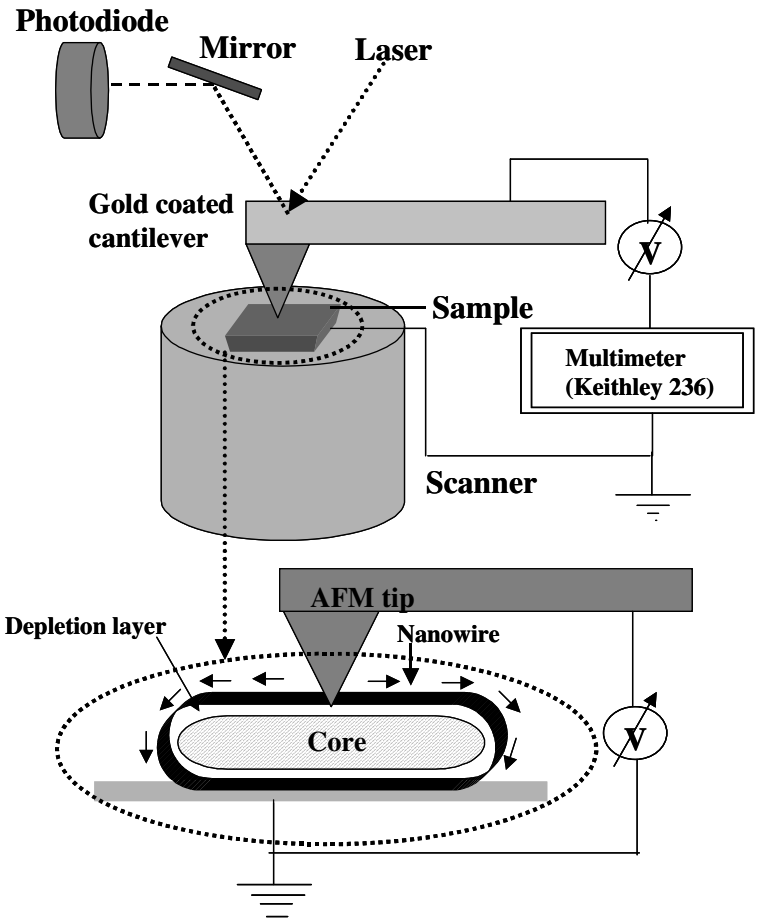

Figure 2.4.16: Schematic diagram of the CAFM measurement. The bias is applied on the tip and the substrate is at ground potential. The core and the depletion layer of the nanowire are represented in cross-section and the current path is indicated.

Highly oriented pyrolytic graphite (HOPG) was used as the conducting substrate on which nanowires of ZnO or TiO_2 were deposited. For this purpose, a dilute dispersion of the nanowire in 2-propanol (Merck, 99.7%) was prepared by sonicating for 30 min. Then, around 10 µl of the dispersed solution was drop-coated and allowed to spread over the HOPG substrate and dried. An environmental hood was placed enclosing the AFM head for measurements in H_2 atmosphere. The test gas was mixed with dry air to achieve the desired concentration (100, 500 and 1000 ppm). Flow rate of the gas flow was maintained at 500 sccm. The current flowing through the nanostructures was measured using the Keithley-236. A computer code was used to measure the variation of current in air and in the test gas with respect to time. The resistance of the oxides decreased on contact with hydrogen.

In figure 2.4.17 (a), we show AFM image of a ZnO nanowire with its profile. The length and diameter of the nanowire are 150 nm and 25 nm respectively. In figure 2.4.17 (b), we show AFM image of a TiO_2 nanowire. From z-profile analysis, we found the nanowire to have a diameter of 60 nm and a length of 125 nm.

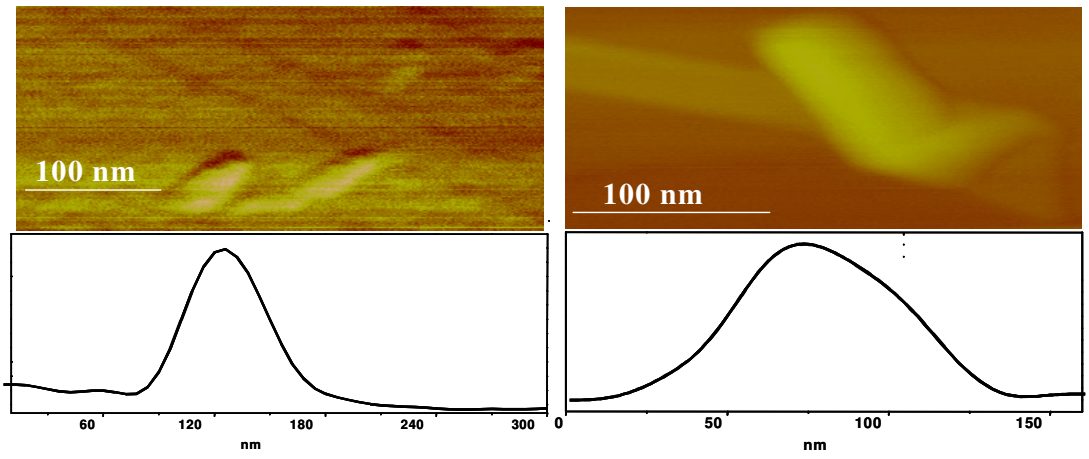

Figure 2.4.17: AFM image of (a) ZnO nanowire, (b) TiO_2 nanowire alongwith the profiles.

In figure 2.4.18, we show the hydrogen sensing characteristics of ZnO and TiO_2 nanowires at 25 °C. I-V characteristics of the ZnO nanowire (Figure 2.4.18 (a)) show a non-linear and asymmetric behavior. This may be contrasted with the linear response from the ohmic contact of the tip with the HOPG surface. The non-linear, rectifying behavior in the I-V characteristics result from Schottky contact formation of the Au-coated tip with the ZnO nanowire [134-136]. The resistance of the ZnO nanowire is in the 1-50 MΩ range at room temperature (25 °C) and the current varies from 1-250 nA in the

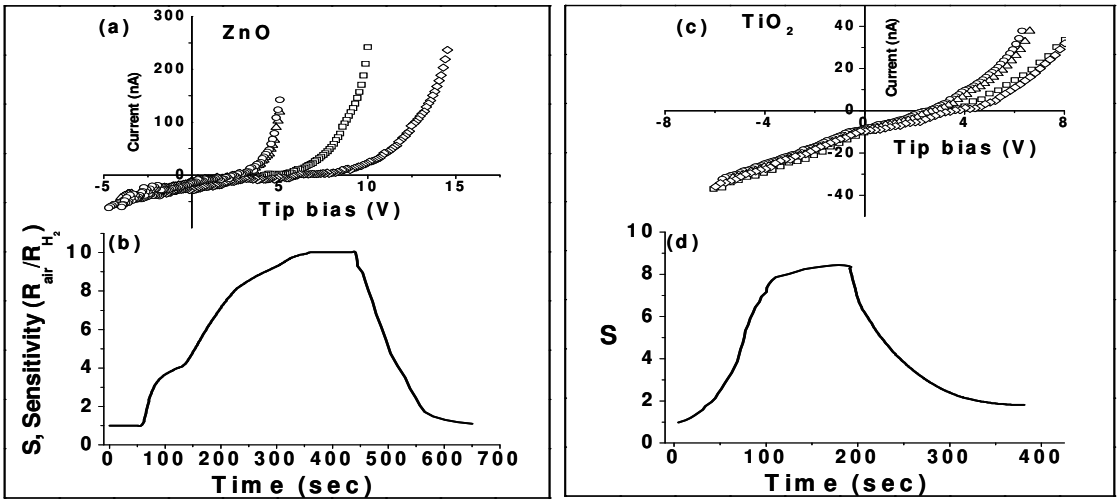

Figure 2.4.18: I-V characteristics of a ZnO nanowire (at 25 °C) in air (diamonds) and in 100 ppm (squares), 500 ppm (triangles) and 1000 ppm (circles) of H_2. (b) Sensitivity vs. time curve for 1000 ppm of hydrogen. (c) I-V characteristics of TiO_2 nanowire in air (diamonds), 100 ppm (squares), 500 ppm (triangles) and 1000 ppm (circles) of H_2. (d) Sensitivity vs. time curve for 1000 ppm of hydrogen.

5-13V range. A typical current-time curve is shown in fig. 2.4.18 (b). The sensitivity of the ZnO nanowire is around 10 for a tip bias of 4V for 1000 ppm of H_2. From the I-V characteristics, the values of sensitivities are calculated to be around 3 and 5 respectively

for 100 and 500 ppm of H_2 at room temperature. The resistance of the TiO_2 nanowire is in the 100-200 MΩ range.

The I-V characteristics of the TiO_2 nanowire in air, for 100, 500 and 1000 ppm of H_2 are shown in figure 2.4.18 (c). The I-V characteristics are similar to those found with the ZnO nanowire. Figure 2.4.18 (d) shows sensing characteristics of the TiO_2 nanowire for 1000 ppm of H_2 at a tip bias of 4V. The sensitivities of the TiO_2 nanowire are around 8, 4 and 2 respectively for 1000, 500 and 100 ppm of H_2 at room temperature.

Since the H_2 sensing characteristics are measured at room temperature, O_2^- species are thereby to be involved in the reaction mechanism.

In air: $O_2\,(g) + e^- \rightarrow O^-_{2\,(ads)}$ (8)

In presence of H_2, the basic reaction is given by:

$H_2 + ½\, O^-_{2\,(ads)} \rightarrow H_2O + e^-$ (9)

2.4.2 Hydrocarbon and hydrogen sensors based on tungsten oxide nanowires

In the present work we have studied the hydrocarbon sensing characteristics of different nanostructures of V_2O_5 as well as nanowires of tungsten oxide ($WO_{2.72}$) over the concentration range of 50-2000 ppm, after characterizing the nanostructures by X-ray diffraction, electron microscopy and Raman spectroscopy. In addition to studying the sensing characteristics of the as-prepared nanowires of tungsten oxide, we have investigated the effect of impregnating the tungsten oxide nanowires with 0.1, 0.5 and 1 at% Pt. We have also examined the sensing characteristics of single WO_{3-x} nanowires for hydrocarbons and hydrogen.

The XRD patterns {Figure 2.4.19 (a)} showed the V_2O_5 nanostructures had the orthorhombic structure (lattice parameters: a=11.52 Å, b=3.5 Å, c=4.3 Å, JCPDS no: 41-1426). The Raman bands observed for V_2O_5 nanoparticles, nanobelts and nanowires {Figure 2.4.19 (b)} showed all the samples are crystalline V_2O_5 and are in line with literature data [137, 138]. The XRD pattern of the tungsten oxide nanowires (Figure 2.4.19 (a)) had the monoclinic structure (lattice parameters: a=18.33 Å, b=3.78 Å, c=14.03 Å, JCPDS no: 36-101) characteristic of $WO_{2.72}$ [139]. The XRD peak intensity of the (010) reflection was relatively higher than that of other reflections. This implies that the nanowires grow along the (010) direction. The four Raman bands at 273, 327, 715 and 807 cm^{-1} {Figure 2.4.19 (b)} observed were in agreement with those of monoclinic $WO_{2.72}$ [140, 141]. Three kinds of vibrations occur in monoclinic WO_3 in three regions of wavenumber, WO_3 vibrations at 900-600 cm^{-1} (stretching modes), 400-200 cm^{-1} (deformation modes) and below 200 cm^{-1} (lattice modes). The band at 137 cm^{-1} belongs to

the W^{6+}-O-W^{6+} bending modes, while the bands situated at 274 and 326 cm^{-1} belong to O-W^{+}-O bending modes of monoclinic WO_3 [142, 143].

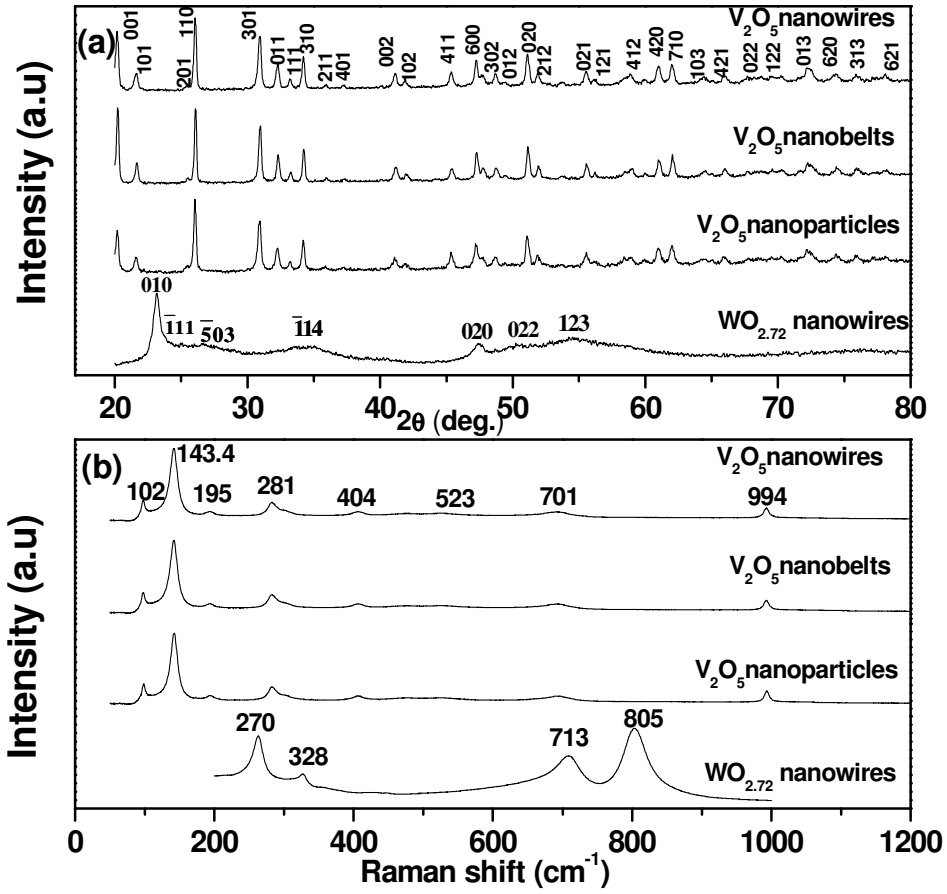

Figure 2.4.19: (a) XRD patterns of V_2O_5 nanowires, nanobelts, nanoparticles and $WO_{2.72}$ nanowires,(b) Raman spectra of V_2O_5 nanowires, nanobelts, nanoparticles and $WO_{2.72}$ nanowires.

The $WO_{2.72}$ films were impregnated with Pt by dipping the metal oxide film in an aqueous solution of H_2PtCl_6 of concentrations 0.01M, 0.05M and 0.1M. The thick films were dried and fired at 350°C for 30 min to promote the decomposition of the platinum precursor into metallic platinum. The extent of impregnation was confirmed by EDAX analysis {see Figure 2.4.20} for a typical EDAX pattern).

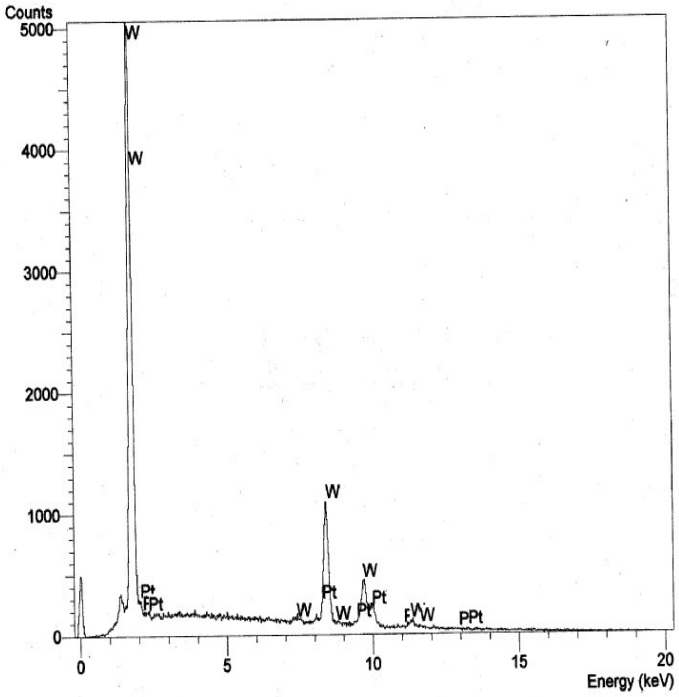

Figure 2.4.20: EDAX pattern of 1 at% Pt impregnated tungsten oxide nanowires.

In figure 2.4.21 (a), we show a typical TEM image of V_2O_5 nanoparticles with the inset showing the selected area electron diffraction (SAED) pattern. The average size of these nanoparticles was in the 30-50 nm range. The SAED pattern indicates the particles to be single crystalline. SEM image of V_2O_5 nanobelts is shown in figure 2.4.21 (b). Figure 2.4.21 (c) shows the TEM image of V_2O_5 nanobelts, with the SAED pattern as the inset. The TEM image reveals that the belts are 500-1000 nm long and 20-50 nm wide. Figure 2.4.21 (d) shows HREM image of a nanobelt. In figure 2.4.21 (e), we have shown SEM image of nanowire bundles of V_2O_5. Figure 2.4.21 (f) shows the SEM image of the V_2O_5 nanowires with the inset showing the SAED pattern and a TEM image. The diameter of the nanowires was in the 20-50 nm range with lengths of several micrometers. The SAED pattern confirms the nanowires to be single crystalline.

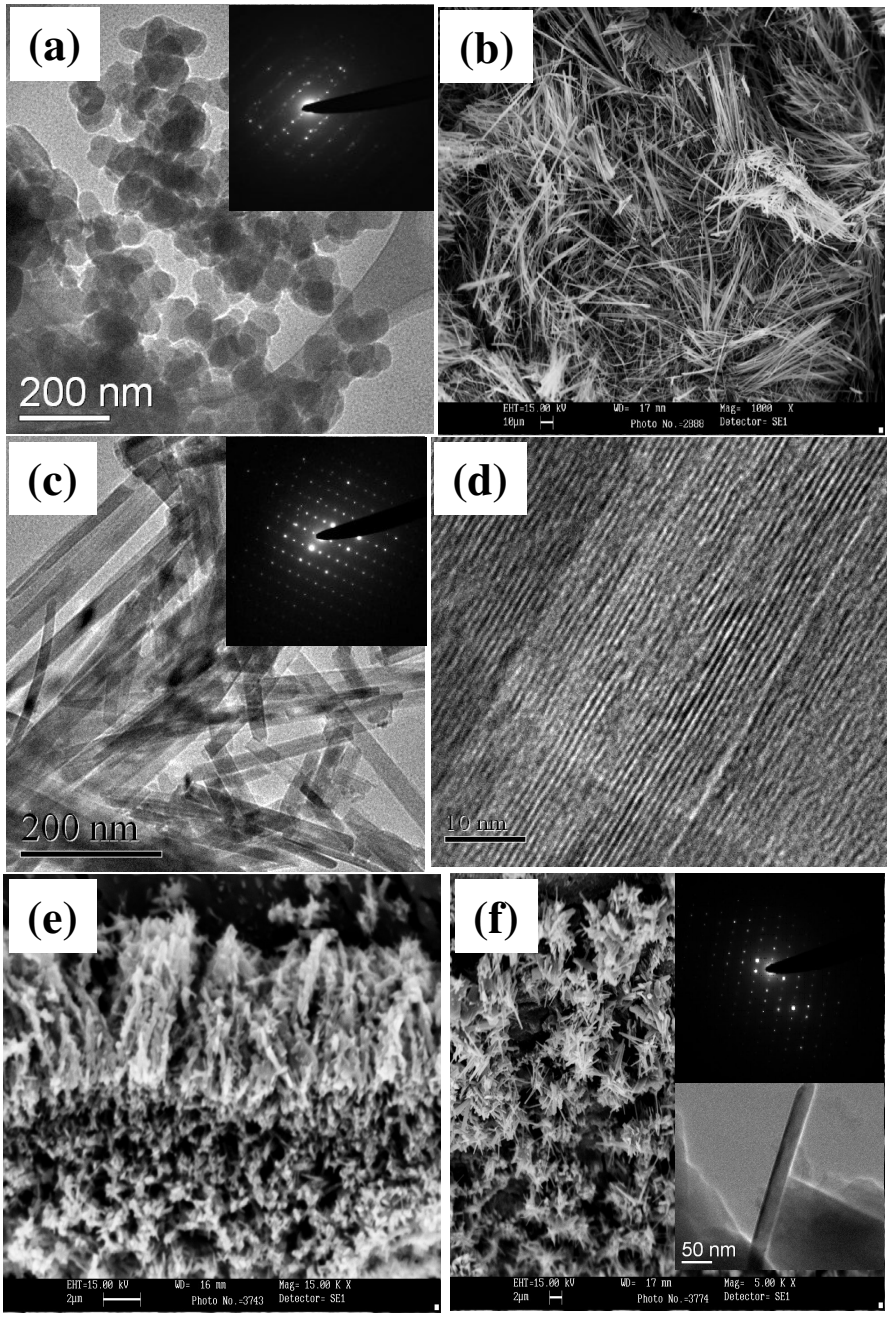

Figure 2.4.21: TEM image of V_2O_5 nanoparticles with the inset showing electron diffraction pattern, (b) SEM image of V_2O_5 nanobelts, (c) TEM image of V_2O_5 nanobelts with the inset showing electron diffraction pattern, (d) HREM image of a V_2O_5 nanobelt, (e) SEM image of V_2O_5 nanowire bundles, and (f) SEM image of V_2O_5 nanowires with the inset showing a TEM image and electron diffraction pattern.

In figure 2.4.22 (a), we show a FESEM image of $WO_{2.72}$ nanowires. TEM images of the $WO_{2.72}$ nanowires are shown in figures 2.4.22 (b) and (c). The average diameter of the nanowires is in the range 5-15 nm and length in the 100-200 nm range. The single crystalline nature of the nanowire is seen from the HREM image given in the inset of figure 2.4.22 (c), with a lattice spacing of 3.81 Å corresponding to the (010) planes. Figure 2.4.22 (d) shows a TEM image of Pt impregnated $WO_{2.72}$ nanowires, from where we can see the presence of Pt nanoparticles in the form of clusters.

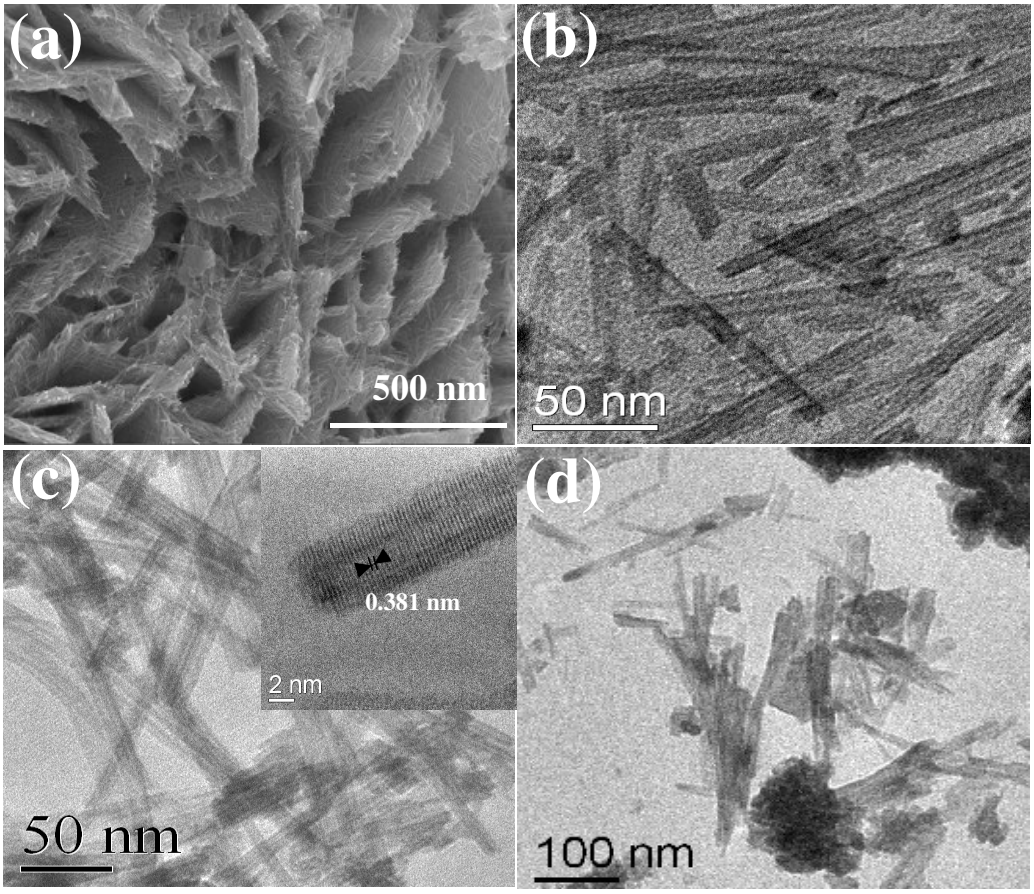

Figure 2.4.22: (a) FESEM image of $WO_{2.72}$ nanowires, (b) and (c) TEM images of $WO_{2.72}$ nanowires with the inset showing HREM image, (d) TEM images of $WO_{2.72}$ nanowires after Pt impregnation.

In figure 2.4.23 (a), we show the sensing characteristics of V_2O_5 nanoparticles towards 2000 ppm of LPG. The highest sensitivity found is 10 at 200 °C and ~7 at 100 °C. The LPG sensing characteristics of the as-prepared V_2O_5 nanobelts and nanowires are shown in figures 2.4.23 (b) and (c) respectively. A maximum sensitivity of 24 was obtained with V_2O_5 nanobelts at 200 °C and the sensitivity at lower temperature decreases drastically. With the nanowires of V_2O_5, the maximum sensitivity at 200 °C is ~11. Thus, the sensitivities found with the V_2O_5 nanostructures are unsatisfactory, with the response and recovery times also being on the high side.

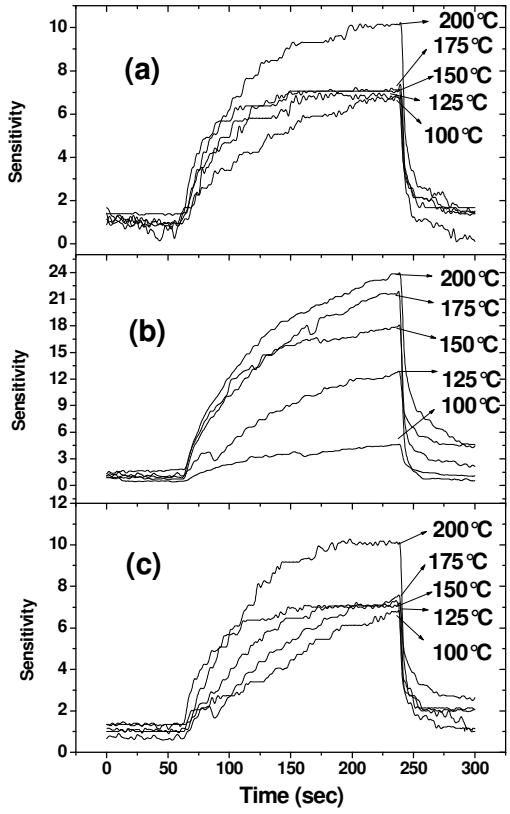

Figure 2.4.23: Gas sensing characteristics of (a) V_2O_5 nanoparticles (b) V_2O_5 nanobelts (c) V_2O_5 nanowires for 2000 ppm of LPG.

In figure 2.4.24 (a), we show the LPG sensing characteristics of the $WO_{2.72}$ nanowires. A maximum sensitivity of 1800 is found with 2000 ppm of LPG at 200 °C

with the as-prepared $WO_{2.72}$ nanowires. Even at 50 °C, the sensitivity is 225 for these nanowires**.** The response as well as recovery times are in the range of 25-80s for 500 ppm of LPG. Variation of the sensitivity of the $WO_{2.72}$ nanowires with the concentration of LPG (50-2000 ppm) at 200 °C is shown in figure 2.4.24 (b). The nanowires show a sensitivity of 13 for 50 ppm of LPG at 200 °C. In figure 2.4.24 (c), we show the variation of the response and recovery times over the temperature range of 50-200 °C. With increasing working temperature, the response and recovery times decrease as expected. The response times vary in the range of 28-65s, and the recovery time in the range of 55-80s.

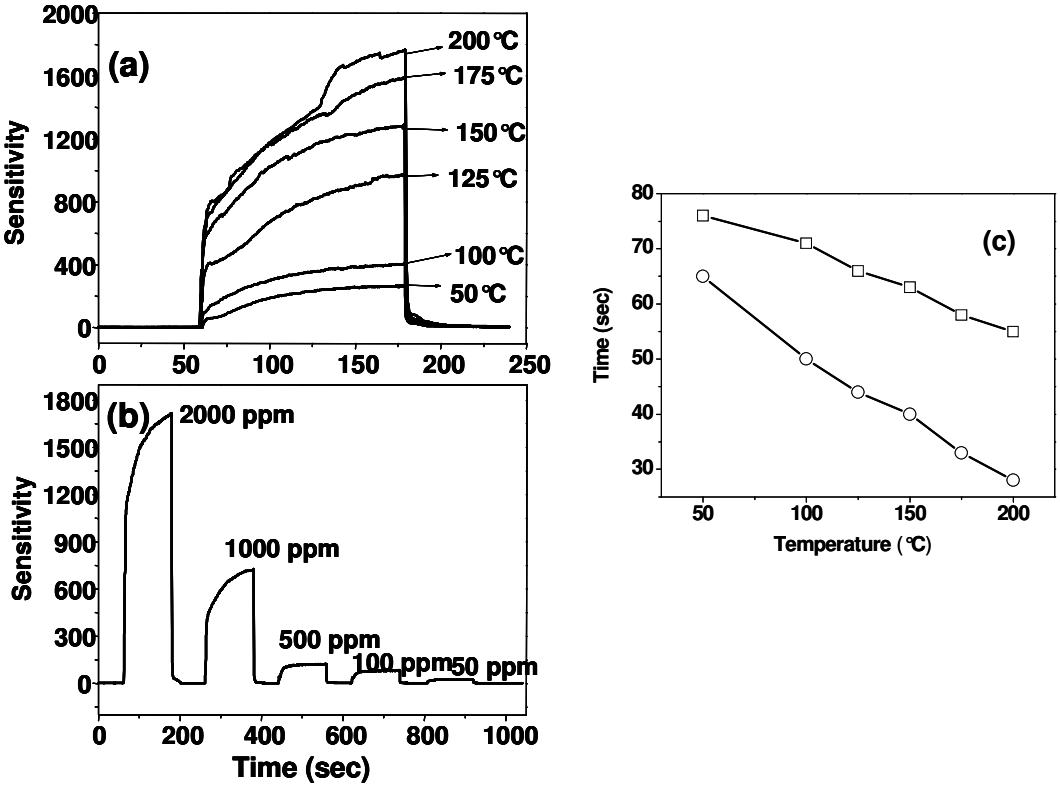

Figure 2.4.24: (a) Gas sensing characteristics of $WO_{2.72}$ nanowires for 2000 ppm of LPG, (b) variation of sensitivity with concentration of LPG at 200°C, (c) Response and recovery curves for the $WO_{2.72}$ nanowires over the temperature range of 50-200 °C.

In order to achieve improved sensing characteristics with the $WO_{2.72}$ nanowires, we carried out studies after impregnating them with 0.1, 0.5 and 1 at% Pt. In figures 2.4.25 (a) and (b) we present the sensing characteristics of 0.1 at% Pt impregnated $WO_{2.72}$ nanowires. We readily notice the very high sensitivity (~2200) for 2000 ppm of LPG at 200 °C. The sensitivity is 110 at 50 °C and goes well above 500 at 125°C. In figure 2.4.25 (b), we show the sensing characteristics of 0.1 at% Pt impregnated $WO_{2.72}$ nanowires for different co concentrations of LPG at 200°C. A sensitivity of 405 is obtained for different for the 50 ppm of LPG. The sensing characteristics of $WO_{2.72}$ nanowires show further improvement on impregnating with 1 at% Pt. We found a

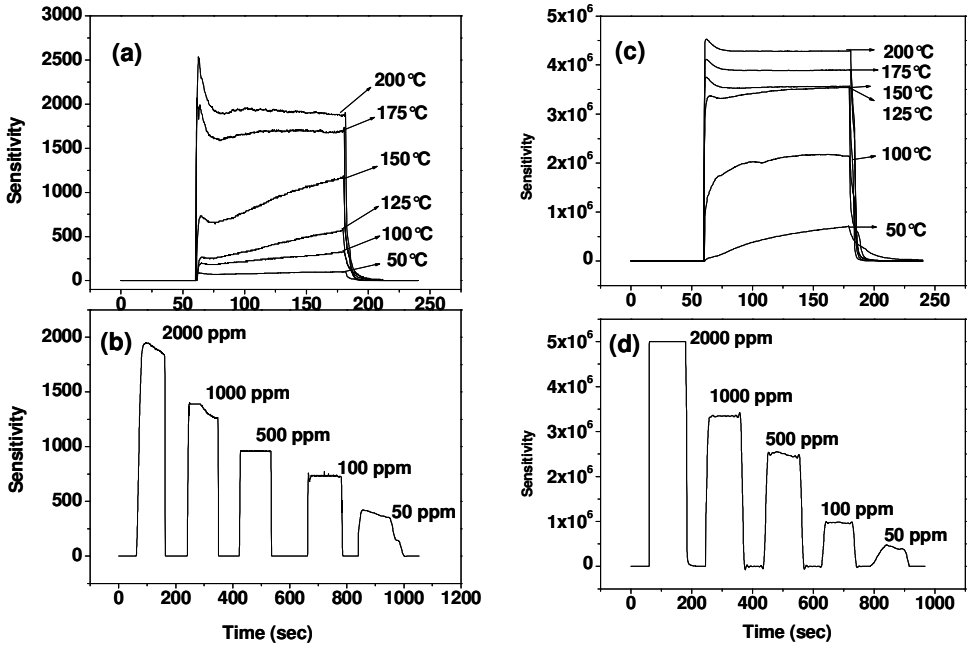

Figure 2.4.25: (a) Gas sensing characteristics of $WO_{2.72}$ nanowires for 2000 ppm of LPG impregnated with 0.1 at% Pt, (b) variation of sensitivity with concentration of LPG at 200°C. (c) Gas sensing characteristics of $WO_{2.72}$ nanowires for 2000 ppm of LPG impregnated with 1 at% Pt, (d) variation of sensitivity with concentration of LPG at 200°C.

maximum sensitivity of ~ 4.3×10^6 for 2000 ppm at 200°C {Figure 2.4.25 (c)}. Even at a temperature of 50°C, the sensitivity is in the 10^5 range. In figure 2.4.25 (d), we show the variation of sensitivity at 200°C with the LPG concentration in the 50-2000 ppm range. In figure 2.4.26 (a), we show the variation of the response and recovery times with temperature in the 50-200°C range for 1 at% Pt impregnated $WO_{2.72}$ nanowires. The response times vary in the 1-40s range and recovery times in the 20-70s range. Above 150°C the response and recovery times are around 1s and 20s respectively.

We have examined the effect of impregnating $WO_{2.72}$ nanowires with 0.5 at% Pt on LPG sensing and found the sensing characteristics of these nanowires to fall in between those for the 0.1 at% and 1 at% Pt impregnated samples. A maximum sensitivity of

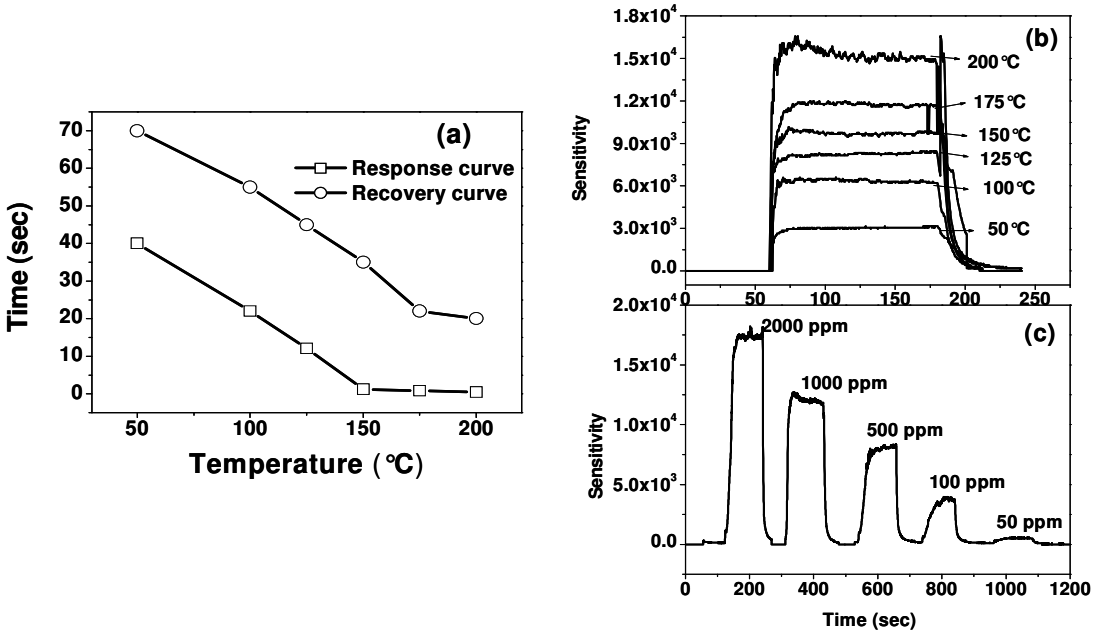

Figure 2.4.26: (a) Response and recovery curves for the 1 at% Pt impregnated $WO_{2.72}$ nanowires for 2000 ppm LPG over the temperature range of 50-200 °C, (c) Gas sensing characteristics of $WO_{2.72}$ nanowires for 2000 ppm of LPG impregnated with 0.5 at% Pt, (d) variation of sensitivity with concentration of LPG at 200°C.

~1.6×10^4 was obtained for 2000 ppm of LPG at 200°C.

We carried LPG sensing with as-prepared and 1 at% Pt impregnated $WO_{2.72}$ nanowires over several cycles over two weeks and found practically no change in the sensitivity as well as the response and recovery times after 200 cycles. We have studied the effect of humidity on the LPG sensing characteristics of the as-prepared and 1 at% Pt impregnated $WO_{2.72}$ nanowires sensors in the range of 35-90% relative humidity. We illustrate the effect of humidity on the sensitivity at 200°C for 2000 ppm of LPG in figures 2.4.27 (a) and (b). There is a slightly decrease in the sensitivity on pure $WO_{2.72}$ nanowires with an increase in the humidity. However, there is not much change in the sensor characteristics of 1at% Pt impregnated $WO_{2.72}$ nanowire sensors even at a relative humidity of 90%.

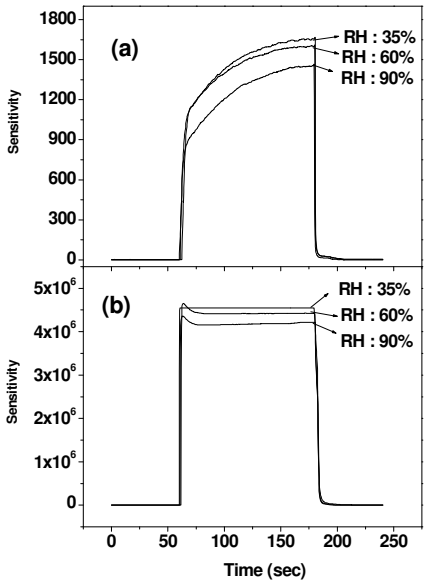

Figure 2.4.27: Effect of humidity on the sensitivity of (a) pure $WO_{2.72}$ nanowires, (b) $WO_{2.72}$ nanowires impregnated with 1 at% Pt at 200°C.

Mechanism

Hydrocarbon sensing by an oxide such as $WO_{2.72}$ involves oxygen species [2, 3] such as O^- and O^{2-} adsorbed on the oxide surface as given by the reaction,

$$\tfrac{1}{2} O_2 + \delta e^- \rightarrow O^{\delta -}(a),\ \delta = 1, 2 \qquad (10)$$

Here, $O^{\delta-}(a)$ is a charged oxygen species adsorbed on the oxide surface. LPG hydrocarbons (HC), first get adsorbed on the oxide to give the HC(a) species which react with $O^{\delta-}(a)$,

$$HC\ (a) + O^{\delta-}(a) \rightarrow HC{:}\ O(a) + \delta\, e^{-} \qquad (11)$$

$$HC{:}\ O(a) + O^{\delta-}(a) \rightarrow CO_2 + H_2O + \delta\, e^{-} \qquad (12)$$

Reactions (2) and (3) release electrons to decrease the resistivity of the oxides. In the presence of Pt, oxygen is dissociatively adsorbed as O (Pt), which spill over to the oxide and forms the charged oxygen species as shown in (4).

$$O\ (Pt) + \delta\, e^{-} \rightarrow O^{\delta-}(a) \qquad (13)$$

Reactions (11) and (12) would follow reaction (13), thereby explaining the increased sensitivity of Pt impregnated $WO_{2.72}$ nanowires.

Room-temperature hydrocarbon and hydrogen sensors based on single nanowires of $WO_{2.72}$

We have studied sensing characteristics of single $WO_{2.72}$ nanowires for hydrocarbons in the form of liquefied petroleum gas as well as hydrogen by CAFM measurements. In figure 2.4.28 (a) and (b), we have shown AFM images of tungsten oxide nanowires (NW1, NW2) with their profiles. From z-profile analysis, NW1 is found to be 40 nm in diameter and 490 nm in length while NW2 is much shorter with a length of 238 nm and with a diameter of 16 nm.

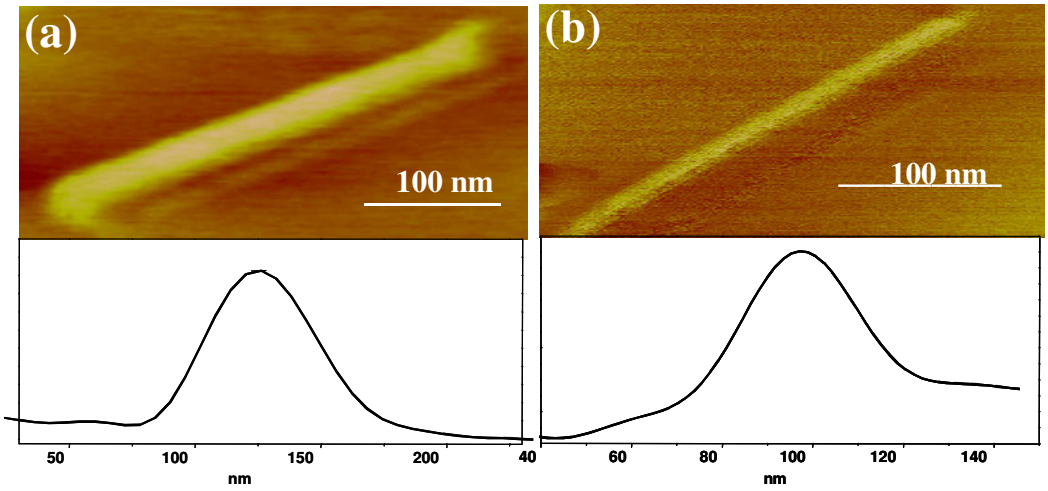

Figure 2.4.28: AFM image (a) $WO_{2.72}$ nanowire (NW1) and (b) $WO_{2.72}$ nanowire (NW2) along with the profiles.

I-V characteristics of the tungsten oxide nanowire NW1 obtained from CAFM measurements are shown for 100, 500 and 1000 ppm of H_2 in figure 2.4.29 (a). The I-V curves are non-linear but symmetric, typical of a metal-insulator-metal junction [144]. The I-V data from the nanowires become steeper with the increasing concentration of H_2. The inset in figure 2.4.29 (a) shows the variation of resistance with the concentration of H_2. The resistance of NW1 in air is ~56 kΩ and changes to ~16 kΩ, 7.7 kΩ and 2.5 kΩ in the presence of 100, 500 and 1000 ppm of H_2 respectively. Assuming a bulk resistivity of $WO_{2.72}$ (1.75×10^{-3} Ωcm) [145], the calculated value of resistance comes to 44.5 kΩ, a value close to the measured value. In figure 2.4.29 (b), we show the hydrogen sensing characteristics of NW1 for 1000 ppm H_2 at a tip bias of 0.05 V. Upon injecting 1000 ppm of hydrogen, the sensitivity increases to around 19 in 38 s and reaches the maximum value of ~22 over the next 40s. On withdrawing the gas, the sensitivity drops off more rapidly (~26 s). Thus, under the given flow conditions (500 sccm), the response time is 38 s while the recovery time is 26 s. In the inset of figure 2.4.29 (b), is shown the

variation in the sensitivity with concentration for hydrogen. The calculated sensitivities are ~7 and 3 for 500 and 100 ppm H_2 respectively at a tip bias of 0.05 V. The resistance of NW2 is 15 kΩ in air and attains a value of 1.65 kΩ in the presence of 1000 ppm of H_2. For NW2 the observed sensitivity is ~9 for 1000 ppm of H_2. From the above studies, we conclude that $WO_{2.72}$ nanowires of the larger diameter are better for sensing H_2 at room temperature compared to ZnO and TiO_2 nanowires. It is to be noted that $WO_{2.72}$ nanowires are also more conducting than ZnO and TiO_2 nanowires.

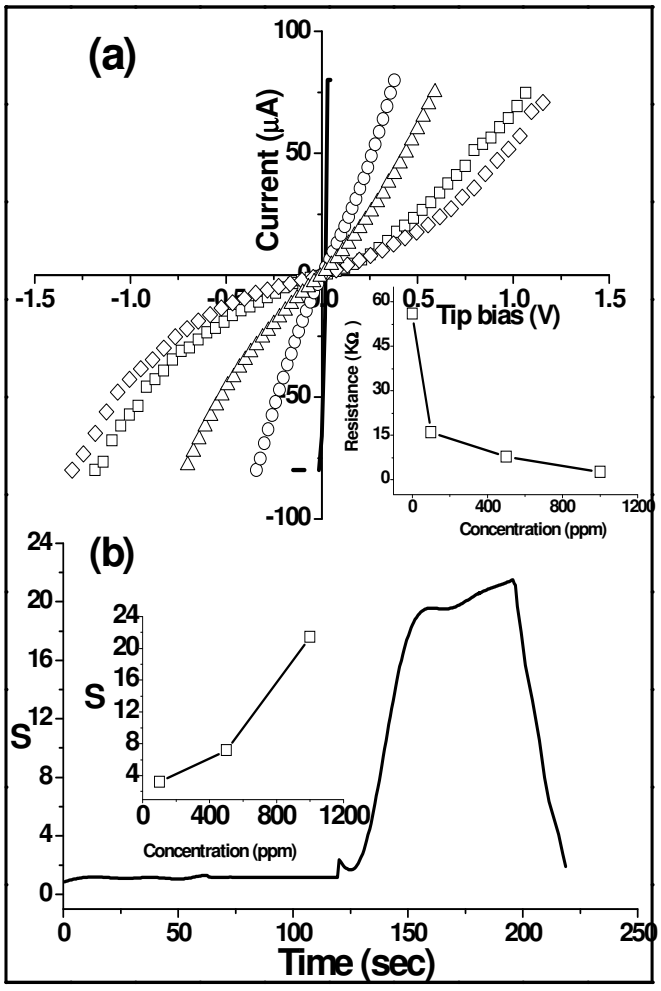

Figure 2.4.29: (a) I-V characteristics of the tungsten oxide nanowire NW1 in air (diamonds), 100 ppm (squares), 500 ppm (triangles), 1000 ppm (circles) hydrogen and on HOPG in air (solid line) at 25°C. Inset shows the variation of resistance in different concentration of hydrogen. (b) Sensitivity vs. time curve for 1000 ppm of hydrogen with the inset showing variation of sensitivity with concentration.

Based on the superior performance of the $WO_{2.72}$ nanowires in sensing hydrogen, we examined the sensing characteristics of $WO_{2.72}$ nanowires for hydrocarbons (LPG). In figure 2.4.30 (a), we show the I-V characteristics of NW1 for 100, 500 and 1000 ppm of LPG at a tip bias of 0.05 V. The nanowire shows a behavior similar to that found for hydrogen. The inset in figure 2.4.30 (a) shows the variation of resistance with the concentration of LPG. The resistance of NW1 drops from ~56 kΩ to ~ 28 kΩ in the presence of 100 ppm of LPG. The drop becomes shallower at higher concentrations and the resistance is 3.7 kΩ at 1000 ppm LPG. In figure 2.4.30 (b), we show the sensing characteristics of $WO_{2.72}$ nanowire for 1000 ppm LPG at a tip bias of 0.05V. From the figure, we see that upon injecting LPG, the sensitivity increases to ~ 15 in 107 s. On withdrawing the gas, the sensitivity drops off rapidly (~36 s). In the inset of figure 2.4.30 (b),we have shown the variation of sensitivity with the concentration of LPG, derived from the data in Fig. 6a. The resistance of NW2 is ~ 15 kΩ in air and attains a value of 1.94 kΩ in the presence of 1000 ppm of LPG. The estimated sensitivity for NW2 is around 8 for 1000 ppm of LPG. Here also NW1 with a bigger diameter is better for sensing LPG at room temperature.

The mechanism of sensing by metal oxide nanosensors deserves some discussion. As it is known from the section 2.1 that, the sensing action by oxide materials such as ZnO, TiO_2, and SnO_2 depends crucially on several factors such as the grain size (available surface area), surface states (electronic contribution) as well as the efficiency with which the test molecules adsorb (chemical affinity). In the ambient atmosphere, oxygen molecules take away electrons from the conduction band of the oxide semiconductor material to form surface O^-_2 and O^- species, thus creating an electron depleted surface

layer with high resistance. Given that the sensors used here are made of active materials such as $WO_{2.72}$,

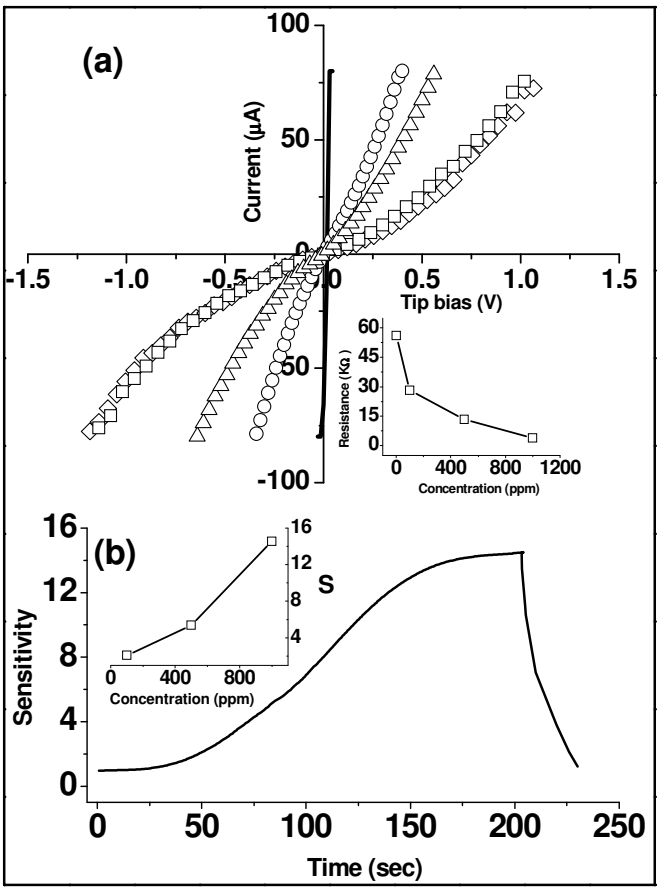

Figure 2.4.30: (a) I-V characteristics of the tungsten oxide nanowire NW1 in air (diamonds), 100 ppm (squares), 500 ppm (triangles), 1000 ppm (circles) LPG and on HOPG in air (solid line) at 25°C. Inset shows the variation of resistance in different concentration of hydrogen. (b) Sensitivity vs. time curve for 1000 ppm of LPG with the inset showing variation of sensitivity with concentration.

the observed differences between NW1 and NW2 must have an electronic origin based on size. The estimated thickness of the depleted layer is ~2.5 nm, assuming a carrier concentration of 1.87×10^{22} cm^{-3} [145].

$O_2\ (g) + e^- \rightarrow O^-_{2\ (ads)}$ (14)

$O^-_{2\ (ads)} + e^- \rightarrow 2O^-_{(ads)}$ (15)

In the presence of a reducing gas such as hydrogen or LPG, there will be back-donation of electrons to the conduction band, resulting in better conduction.

The basic reaction with hydrogen is given by,

$H_2 + ½\ O^-_{2\ (ads)} \rightarrow H_2O + e^-$ (16)

The reaction with hydrocarbon is given by,

$HC + ½\ O^-_{2\ (ads)} \rightarrow HC{:}O_{ads} + e^-$

$HC{:}O_{ads} + ½\ O^-_{2\ (ads)} \rightarrow CO_2 + H_2O + e^-$ (17)

The conducting path for the AFM tip is through the depletion layer, as shown in the schematic diagram in figure 2.4.16. NW1 offers a longer path through the depletion region than NW2 and for this reason; the air-resistance of NW1 is higher than that of NW2. Once the surface layer is reduced by the initial adsorption of H_2 or LPG, the resistance of NW1 drops off sharply (more in the case of H_2 as it is a single step process, see equations 16 and 17). With higher doses (500 and 1000 ppm), perhaps even the deeper layers get reduced but at a slower rate. For NW2, the surface area is relatively small (~1.76×10^4 nm^2 as against ~9.92×10^4 nm^2 of NW1) and this effect is less pronounced. It may be noted that the dimensions of both NW1 and NW2 are well above the thickness of the depleted layer and therefore, confinement effects are not found in our measurements. For smaller oxide nanosensors, such effects have indeed been observed [146, 147].

2.4.5 H_2S sensors based on tungsten oxide nanostructures

Nanoparticles and nanoplatelets of WO_3 and nanowires of $WO_{2.72}$ have been investigated for their H_2S-sensing characteristics over the 1-1000 ppm concentration range at 40-250°C. The resistance of the sensors based on nanostructures of tungsten oxides was in the 200-1 MΩ in dry air in the 40-250 °C range. Resistance of the nanoparticles and nanoplatelets films was higher than that of the nanowires.

The X-ray diffraction patterns of tungsten oxide nanoparticles, nanoplatelets and nanowires are shown in figure 2.4.31. The XRD patterns of the nanoparticles and nanoplatelets correspond to the monoclinic structure of WO_3 (lattice parameters: a=7.285 Å, b=7.517 Å, c=3.835 Å, β=90.15°, JCPDS no: 05-0363). The reflections of WO_3 nanoplatelets are broader than those of the nanoparticles, because of the smaller crystal size. The average diameter of the nanoparticles calculated from the XRD line broadening is ~20 nm. The XRD pattern of the tungsten oxide nanowires corresponds to the monoclinic structure (lattice parameters: a=18.33 Å, b=3.78 Å, c=14.03 Å, β=115.2°, JCPDS no: 36-101) characteristic of $WO_{2.72}$.

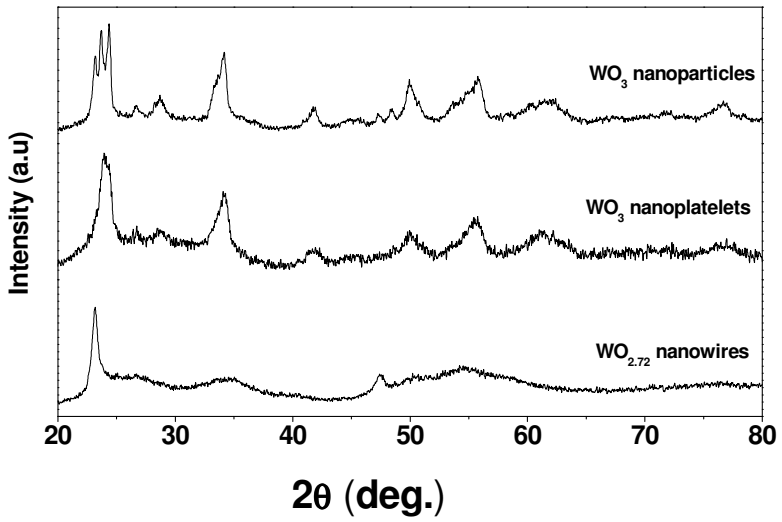

Figure2.4.31: XRD patterns of tungsten oxide nanoparticles, nanoplatelets and nanowires.

In figure 2.4.32 (a), we show a FESEM image of WO_3 nanoparticles, with the inset showing a TEM image and the selected area electron diffraction (SAED) pattern. The SAED pattern indicates the particles to be single crystalline. Figure 2.4.32 (b) shows a FESEM image of WO_3 nanoplatelets with a TEM image as the inset. The TEM image reveals that the platelets are of 60 ± 20 nm long and 1-5 nm thick. Fig 2.4.32 (c) shows TEM image of a single WO_3 nanoplatelet. During TEM analysis it is observed that the thickness of the WO_3 platelets are very thin and it gets destroyed very fast by the electron beam. In figure 2.4.32 (d), we show a TEM image of the $WO_{2.72}$ nanowires. The average diameter of the nanowires is in the 5-15 nm range. The inset in figure 2.4.32 (d) shows a high-resolution image of a nanowire.

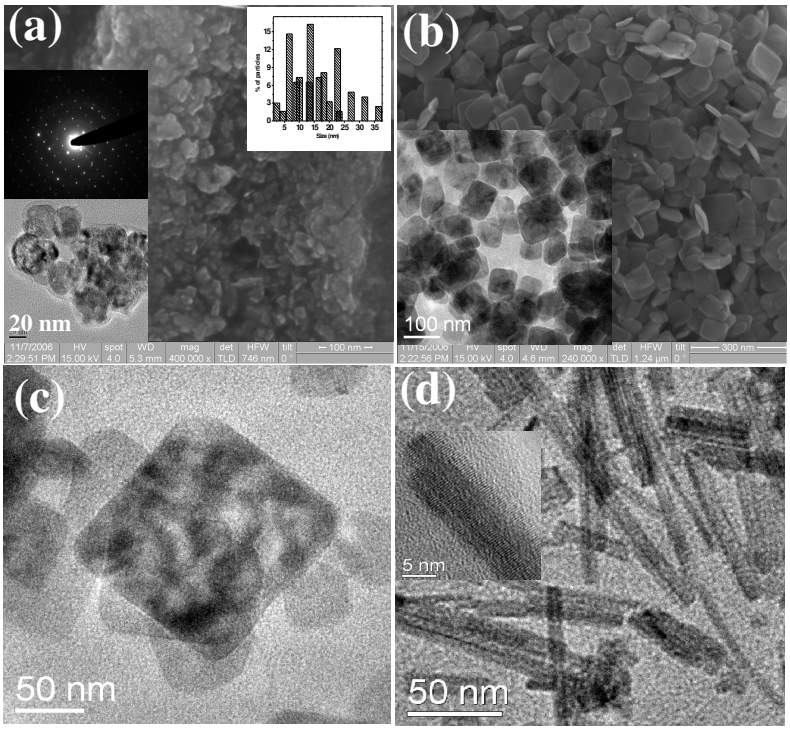

Figure 2.4.32: FESEM images of (a) tungsten oxide nanoparticles with the inset showing a TEM image and electron diffraction and (b) tungsten oxide nanoplatelets with the inset showing a TEM image, (c) TEM image of a WO_3 nanoplatelet and (d) A TEM image of $WO_{2.72}$ nanowires with the inset showing a HREM image.

In figure 2.4.33, we show the Raman spectra of tungsten oxide nanoparticles, nanoplatelets and nanowires. Raman bands occur at 130, 265, 328, 710 and 805 cm^{-1}, which confirm the monoclinic structure of tungsten oxide.

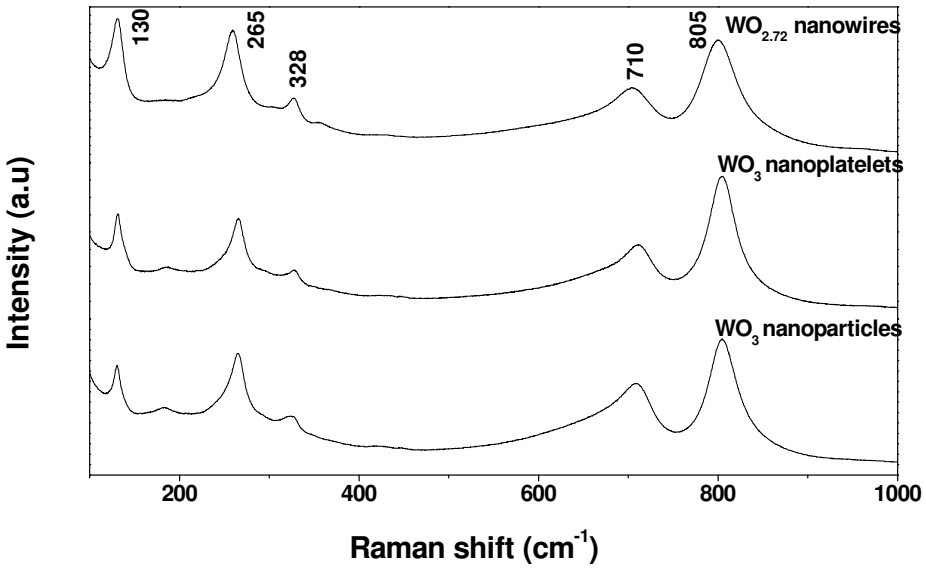

Figure 2.4.33: Raman spectra of tungsten oxide nanoparticles, nanoplatelets and nanowires.

Figure 2.4.34 (a) shows the sensing characteristics of WO_3 nanoparticles towards 1000 ppm of H_2S at working temperatures of 40-250°C. The highest sensitivity found is 757 at 250°C, and 29 at 40°C. The variation in sensitivity of the WO_3 nanoparticles with the concentration (1-1000 ppm) of H_2S at 250°C is shown in figure 2.4.34 (b). The nanoparticles show a sensitivity of 19 to 1 ppm of H_2S at 250 °C. The response and recovery times of the WO_3 nanoparticles are 132 s and 19 s respectively, to 1000 ppm H_2S at 250°C. Figure 2.4.35 (a) shows the sensing characteristics of the WO_3 nanoplatelets. The nanoplatelets show the highest sensitivity of 1852 to 1000 ppm of H_2S

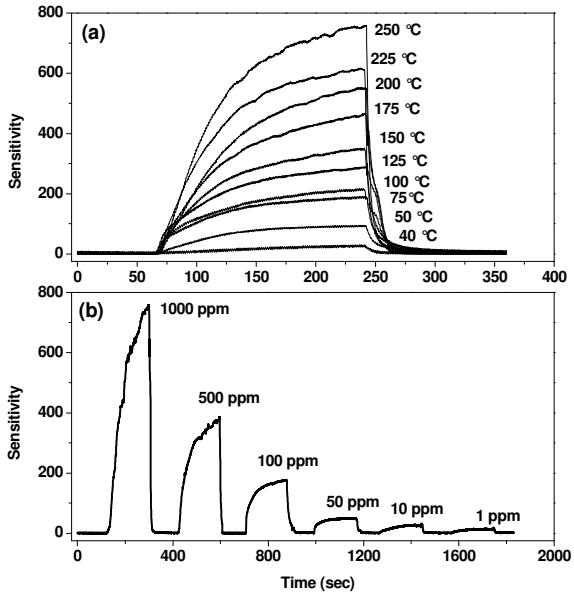

Figure 2.4.34: (a) Gas sensing characteristics of tungsten oxide nanoparticles to 1000 ppm H_2S, and (b) variations in sensitivity with concentration of H_2S at 250°C.

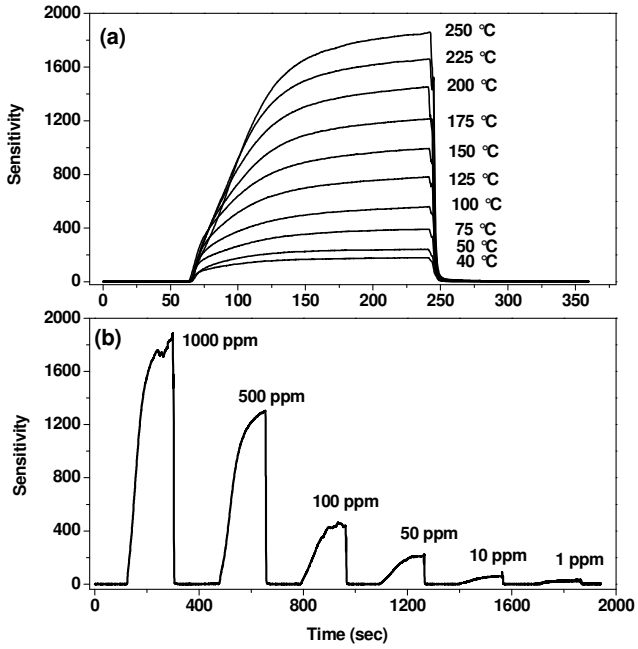

Figure 2.4.35: (a) Gas sensing characteristics of tungsten oxide nanoplatelets to 1000 ppm H_2S, and (b) variations in sensitivity with concentration of H_2S at 250°C.

at 250°C. The sensitivity is ~180 at 40°C. The variation in sensitivity of the WO_3 nanoplatelets with the concentration of H_2S (1-1000 ppm) at 250°C is shown in figure 2.4.35 (b). A sensitivity of 35 is obtained to 1 ppm of H_2S. The response and recovery times of the WO_3 platelets are 91 s and 20 s respectively, to 1000 ppm H_2S at 250°C.

In figure 2.4.36 (a), we show the H_2S-sensing characteristics of $WO_{2.72}$ nanowires, while figure 2.4.36 (b) shows the variation in sensitivity with concentration in the 1-1000 ppm range. The sensitivity of $WO_{2.72}$ nanowires varies between 3313 and 236 to 1000 ppm H_2S over the temperature range of 250-40°C. To 1 ppm of H_2S, a sensitivity of 48 is found at 250°C. The response and recovery times of the $WO_{2.72}$ nanowires are 83 s and 18 s, respectively, to 1000 ppm H_2S at 250 °C.

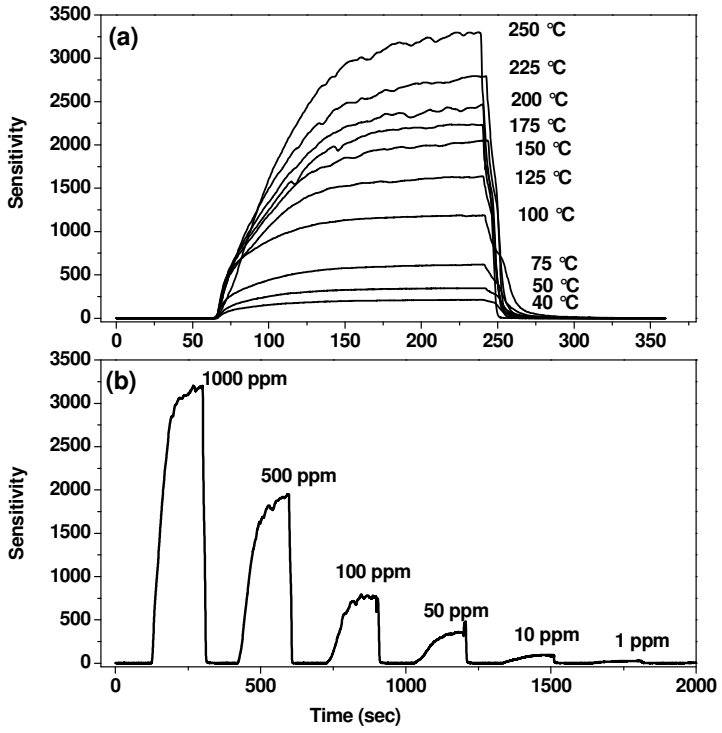

Figure 2.4.36: (a) Gas sensing characteristics of $WO_{2.72}$ nanowires to 1000 ppm H_2S, and (b) variations in sensitivity with concentration of H_2S at 250°C.

Figure 2.4.37 (a) shows the effect of working temperature in the range of 40-250°C, on the sensor response of the tungsten oxide nanostructures towards 1000 ppm H_2S. We see that the $WO_{2.72}$ nanowires show the highest values of sensitivity towards H_2S while the WO_3 nanoparticles show the least response at all the temperatures studied. All the nanostructures, however, show a sensitivity of ~150 at 50°C to 1000 ppm of H_2S, but we found a reasonably good sensitivity value even at 50–100°C. The concentration-variation of sensitivity of the tungsten oxide nanostructures at 250°C is shown in figure 2.4.37 (b). In the 50-100 ppm range, the sensitivity is generally satisfactory. The values of sensitivity are 392, 121 and 50 to 50, 10 and 1 ppm of H_2S at 250°C in the case of the $WO_{2.72}$ nanowires. The sensitivity of 121 of the nanowires to 10 ppm of H_2S is significant since the bad odor of H_2S manifests above this concentration.

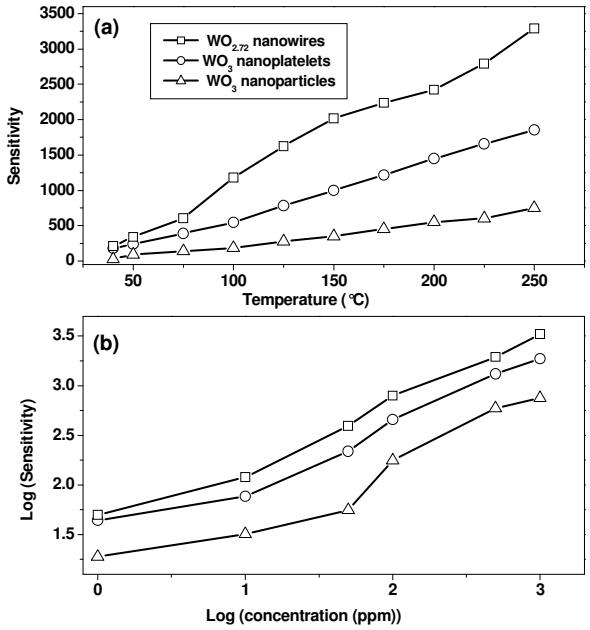

Figure 2.4.37: A comparison of the sensitivity of tungsten oxide nanostructures with (a) temperature (to1000 ppm H_2S) and (b) H_2S concentration (at 250°C).

Figure 2.4.38 shows the response and recovery time curves of the tungsten oxide nanoparticles, nanoplatelets and naowires at 40 – 250°C. The response times vary in the 55-100 s range for the nanoplatelets and nanowires, whereas for the nanoparticles the response time is 80-130 s. Thus, the nanoparticles show slower response compared to the nanowires and platelets. The recovery times of all the nanostructures are in the 18-40 s range depending on the temperature.

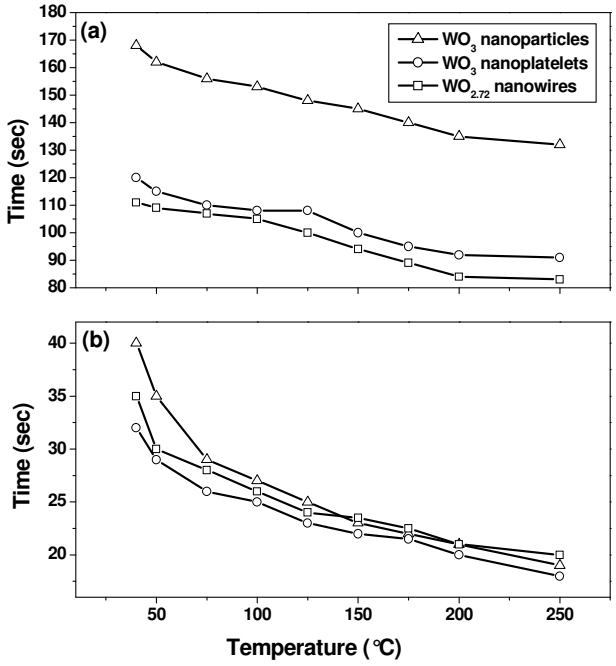

Figure 2.4.38: Temperature variation of (a) response and (b) recovery times (to 1000 ppm H_2S) of tungsten oxide nanoparticles, nanoplatelets and nanowires.

We have studied the effect of humidity on the H_2S-sensing characteristics of the tungsten oxide nanostructure sensors in the range of 35-90% relative humidity. We illustrate the effect of humidity on the sensitivity of the $WO_{2.72}$ nanowires at 250°C to 1000 ppm of H_2S in figure 2.4.39 (a), and of WO_3 nanoplatelets in figure 2.4.39 (b). There

is a slight decrease in the sensitivity with an increase in humidity above a relative humidity of 60%, but there is not much change in the response and recovery times. There was no change in the response as well as the response and recovery times even after 2000 cycles.

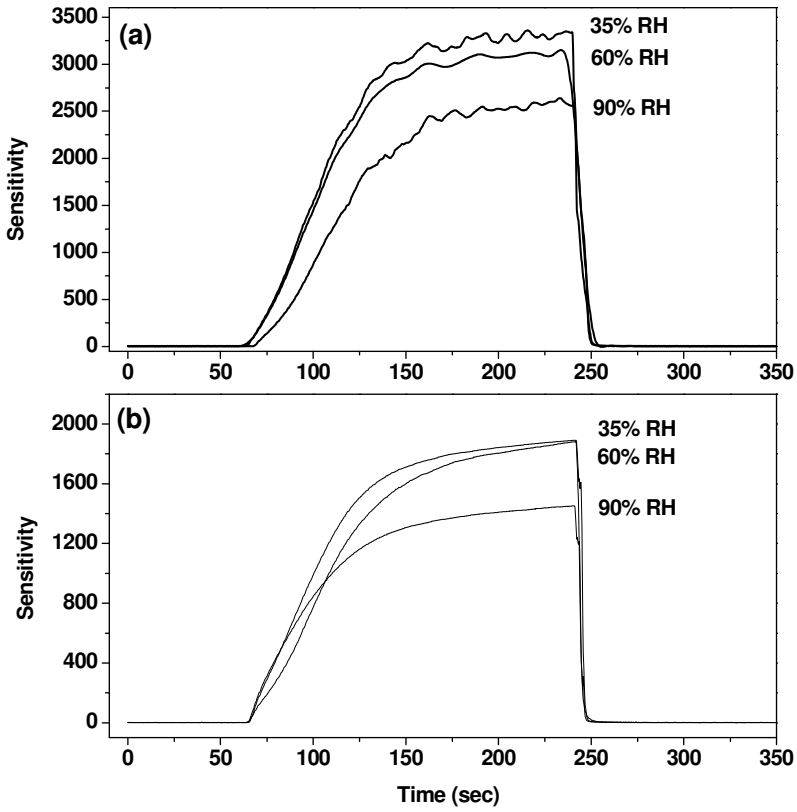

Figure 2.4.39: Effect of humidity on the sensitivity of tungsten oxide (a) nanowires and (b) nanoplatelets at 250°C to 1000 ppm H_2S.

The adsorbed oxygen species play a crucial role in H_2S-sensing. The reaction for H_2S-sensing is given by,

$$H_2S + 3O^-_{(ads)} \rightarrow SO_2 + H_2O + 3e^- \qquad (18)$$

As expected from Eq. (18), the resistance of the nanostructured oxide decreases on contact with H_2S. It is expected that the resistance change upon the exposure to H_2S is mainly due to the resistance change of tungsten oxide. According to Eqs. (14) and (15), oxygen adsorption reaction occurs prior to H_2S-sensing, creating a thin electron-depleted layer at the surface of tungsten oxide. As H_2S is adsorbed, electrons are released into the conduction band according to Eq. (18).

2.4.4 Sensors for the nitrogen oxides, NO_2, NO and N_2O, based on In_2O_3 and WO_3 nanowires

We have investigated ZnO nanorods (nanorods-2, described in section 2.3), In_2O_3 nanowires (In_2O_3 –1 and In_2O_3 –2) and WO_3 nanowires for sensing the three nitrogen oxides. In_2O_3 nanowires were prepared by using PAA membranes and by carbothermal synthesis, which is described in section 2.3. The as-prepared $WO_{2.72}$ nanowires was heated at 450 °C in an oxygen atmosphere for 3h to achieve WO_3 nanowires. The resistance of the ZnO nanorods films was in the range of 0.1-5 MΩ in a temperature range of 100-400°C, whereas for In_2O_3 and WO_3 nanowires it was in the range of 1-65 MΩ for 100-400°C in dry air.

Figure 2.4.40 (a) shows a SEM image of the In_2O_3 nanowires prepared by the carbothermal method, with the inset showing the TEM image of a nanowire. The diameter of the nanowires varies in the 80-100 nm range, with lengths of several micrometers. Figure 2.4.40 (b) shows the SEM images of In_2O_3-1nanowires with the inset showing TEM images. Typical SEM and TEM images of In_2O_3-2 nanowires are shown in figure

2.4.40 (c). The average diameters of the In_2O_3-1 and In_2O_3-2 nanowires were around 200 nm and 20 nm respectively. All the In_2O_3 nanowires had the cubic structure.

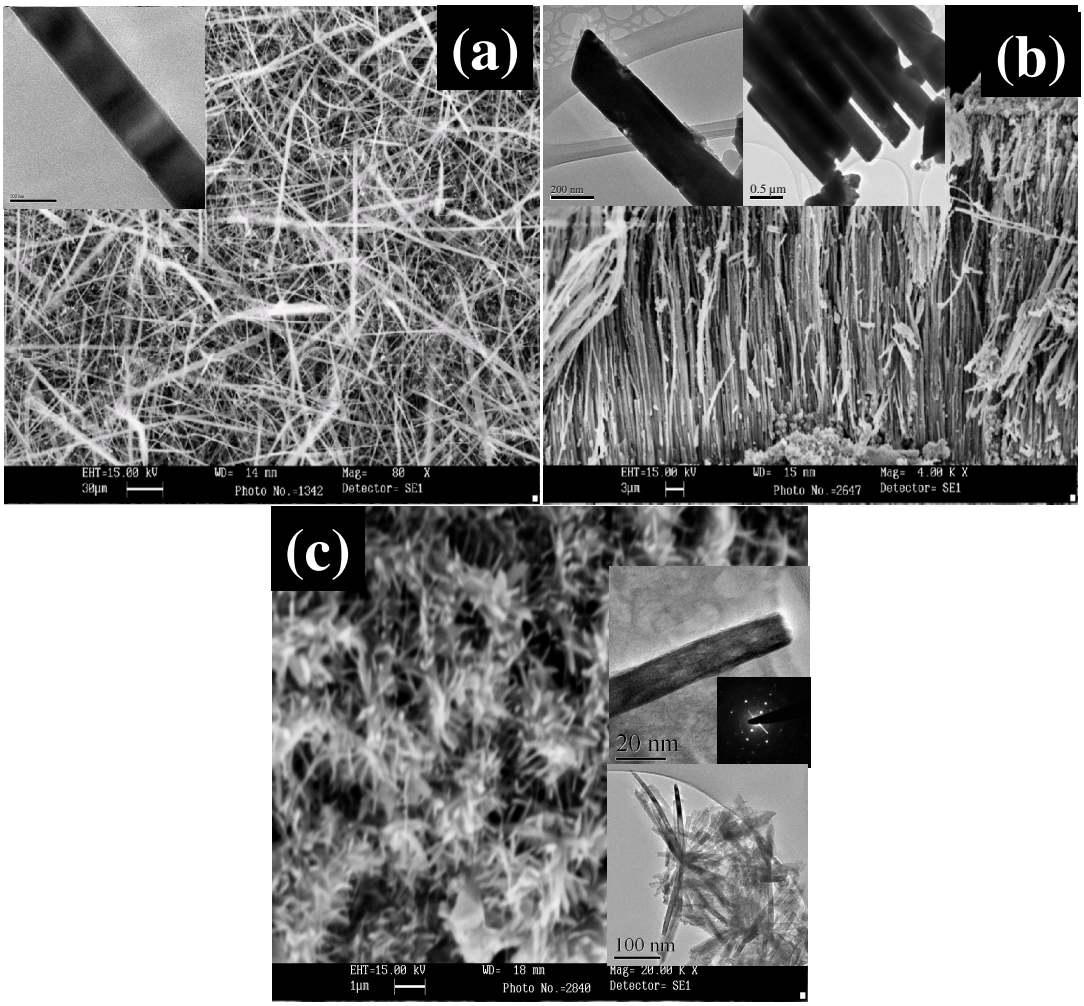

Figure 2.4.40: (a) SEM image of In_2O_3 nanowires prepared by carbothermal synthesis, with inset showing a TEM image, (b) SEM image of In_2O_3 nanowires prepared by using 200 nm AAM membrane with the inset showing TEM images, (c) SEM image of In_2O_3 nanorods with the inset showing TEM image and electron diffraction pattern.

.

The results of our experiments with ZnO nanorods for sensing 10 ppm of NO_2 , NO and N_2O are shown in figure 2.4.41 (a). The sensitivity varied in the range 2 - 5 for all the three gases in the temperature range 125 – 250°C. The response and recovery times

were around 10s and 30s respectively. The sensitivity of the ZnO nanorods found by us was considered to be not high enough for sensing the three nitrogen oxides.

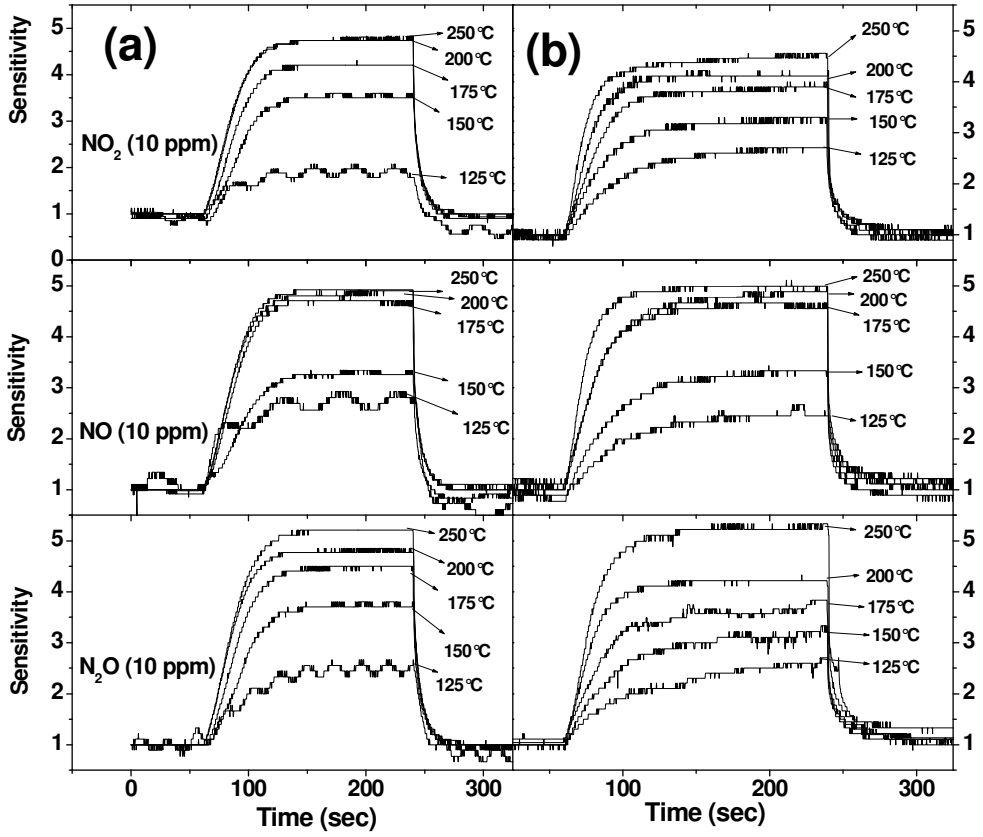

Figure 2.4.41: Gas sensing characteristics of (a) ZnO nanorods, (b) In_2O_3 nanowires prepared by carbothermal synthesis for 10 ppm of NO_2, NO, N_2O respectively.

Our experiments with In_2O_3 nanowires prepared by the carbothermal process were also not encouraging as revealed by the results shown in figure 2.4.41 (b). The sensitivity was in between 2 and 5 in the temperature range 125 – 250°C for 10 ppm of the nitrogen oxides. The response and recovery times were around 30s and 50s, which are also not favorable.

In view of the above results, we investigated the sensing characteristics of the In_2O_3 nanowires prepared by using the AAM templates. In figure 2.4.42, we show the sensor characteristics of the In_2O_3 –1 nanowires (average dia ~200 nm) for 10 ppm of NO_2 , NO and N_2O in the 100 – 250°C range. The sensitivity varies between 2 and 8 for all the three nitrogen oxides. The maximum sensitivity for the three gases is between 7 and 9 at 175°C. Thus, for NO_2 the sensitivity reaches a maximum of 7 at 175°C and decreases on

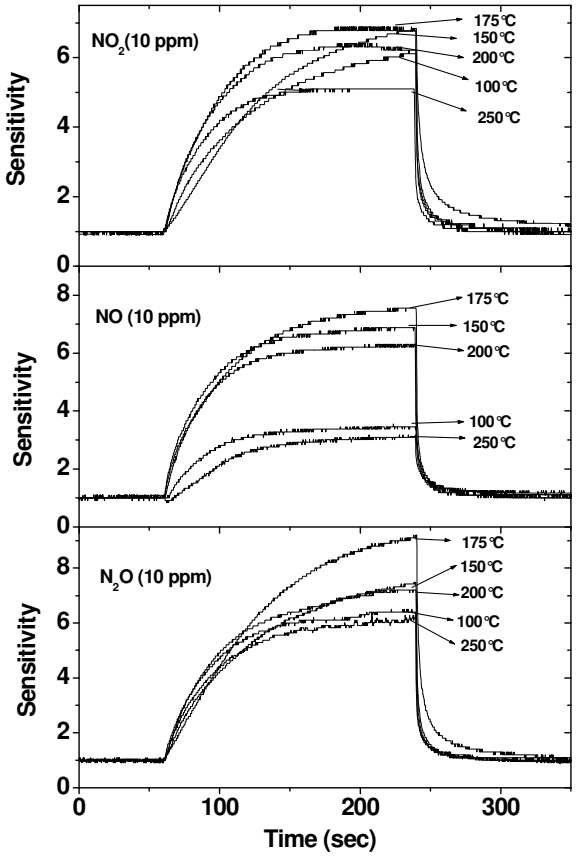

Figure 2.4.42: Gas sensing characteristics of In_2O_3 - 1 nanowires prepared by using 200 nm AAM membrane for 10 ppm of NO_2, NO and N_2O respectively.

further increasing the working temperature. At 250 °C, the sensitivity is around 5. For N_2O, the sensitivity is around 9 at 175°C, whereas it is ~ 6 at 100°C and 250°C. The response and recovery times for the three gases are 20s and 60s respectively. In figure 2.4.43 (a), we show the variation of the sensitivity of In_2O_3 –1 nanowires for the three

nitrogen oxides at 150 °C over the 0.1-100 ppm range. The sensitivities are 6.8, 6 and 7.5 respectively for 0.1 ppm of NO_2 , NO and N_2O. While these sensitivities are satisfactory, we thought to improve the sensitivity by using In_2O_3 nanowires of a smaller diameter.

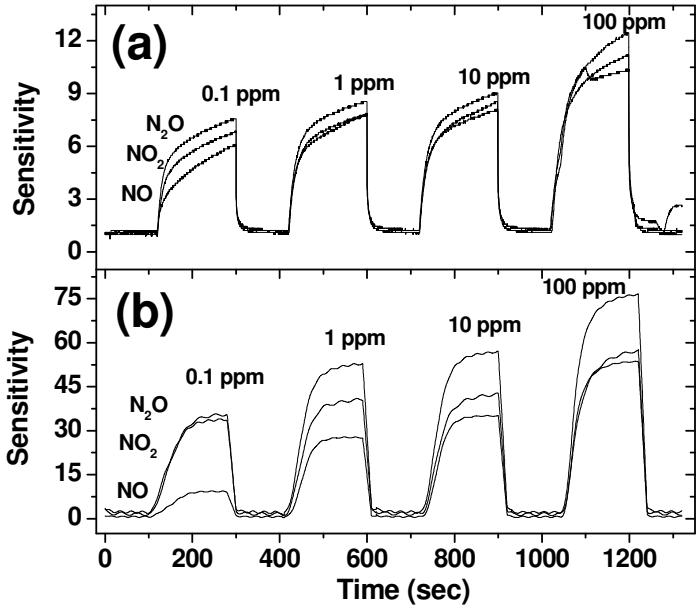

Figure 2.4.43: Variation of sensitivity with concentration of N_2O, NO_2 and NO for (a) In_2O_3 – 1, (b) In_2O_3 – 2 nanowires at 150°C.

In figure 2.4.44, we show the sensing characteristics of the In_2O_3 –2 nanowires (average dia ~20 nm) for 10 ppm of NO_2 , NO and N_2O in the temperature range of 125 – 250°C. A maximum sensitivity of ~ 60 is found for 10 ppm of NO_2 at 150°C. The sensitivity decreases to ~ 10 at 125 °C and to 20 at 175 °C. The highest sensitivities found for NO and N_2O are 50 and 60 respectively at 150 °C. These gases also show a decrease in the sensitivity at temperatures below and above 150°C. The response and recovery times are both in the range of 20s for all the three nitrogen oxides. In figure 2.4.43 (b), we show the variation of the sensitivity for the three gases over the 0.1-100 ppm range at 150

°C. The sensitivity is appreciable for NO_2 and N_2O even at 0.1 ppm, the value being 40 for the two gases. The sensitivity is 10 for 0.1 ppm of NO. From these data, we conclude that the In_2O_3 –2 nanowires are quite suitable for sensing all the three nitrogen oxides, specially NO_2 at 150 °C.

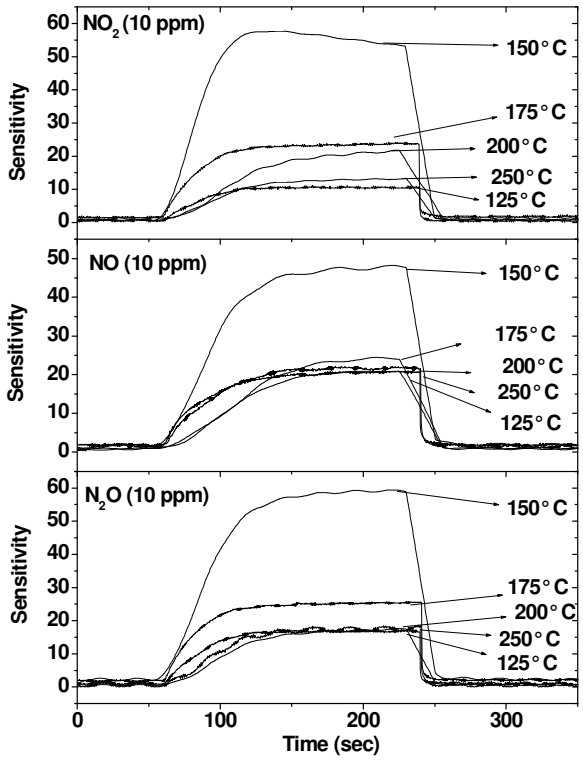

Figure 2.4.44: Gas sensing characteristics of In_2O_3–2 nanowires prepared by using 20 nm AAM for 10 ppm of NO_2, NO and N_2O.

In figure 2.4.45, we show the sensing characteristics of WO_3 nanowires for 10 ppm of NO_2 , NO and N_2O in the temperature range of 150-350°C. A maximum value of sensitivity is obtained at 250°C for all these three gases. The values of sensitivity are 22, 21 and 25 for NO_2 , NO and N_2O respectively. The response and recovery times for the three gases are around 10s and 60s respectively. Figure 2.4.46 shows the variation of sensitivity over the concentration range of 0.1-100 ppm at 250°C. The sensitivity is around 10, 7 and 11 for 0.1 ppm of NO_2 , NO and N_2O respectively at 250°C. While the

values of the sensitivity of the WO_3 nanowires are not as high as with the In_2O_3 –2 nanowires for sensing the nitrogen oxides, they are still in a workable range. The operating temperature for the WO_3 nanowires, however, is much higher than for the In_2O_3 –2 nanowires.

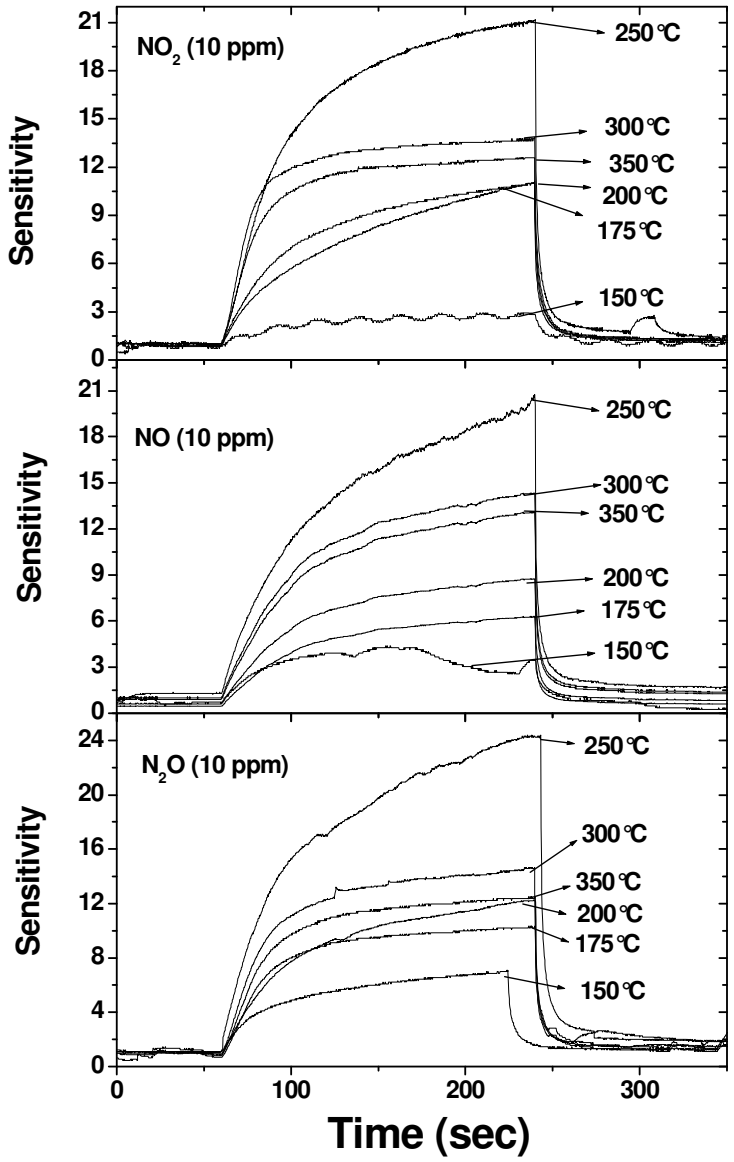

Figure 2.4.45: Gas sensing characteristics of WO_3 nanowires for 10 ppm of NO_2, NO and N_2O.

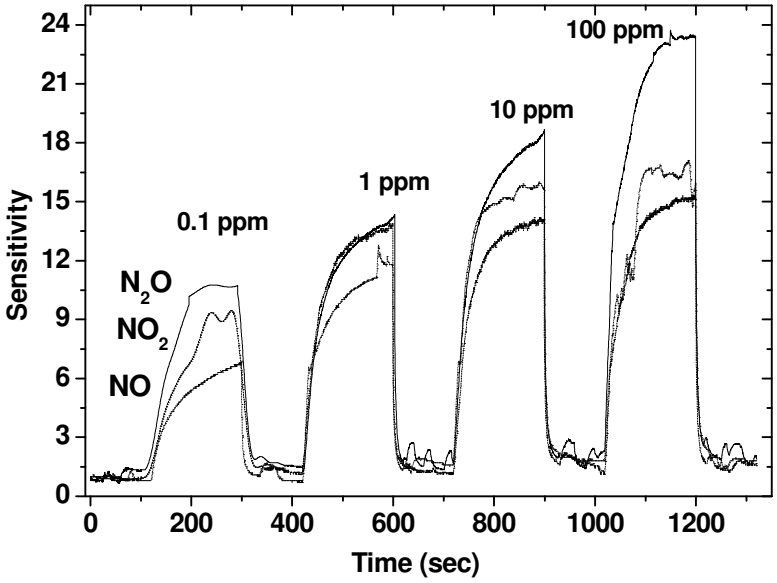

Figure 2.4.46: Variation of the sensitivity of WO_3 nanowires with the concentration of N_2O, NO_2 and NO at 250°C.

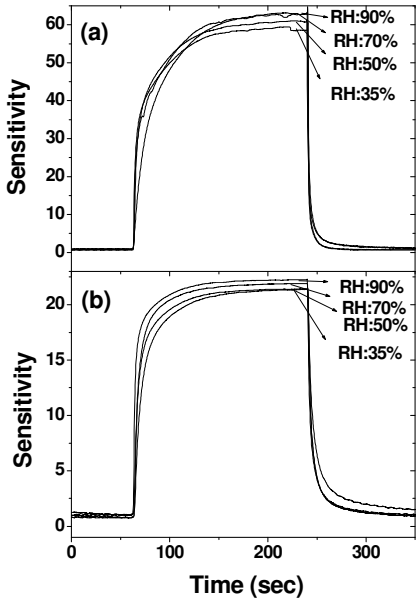

Figure 2.4.47: Effect of humidity on the sensitivity of (a) In_2O_3 –2 at 150°C for 10 ppm of NO_2, and (b) WO_3 nanowires at 250°C for 10 ppm of NO_2.

It is important that metal oxide gas sensors are not affected by humidity. We have, therefore, studied the effect of humidity on the sensing characteristics of In_2O_3 –2 and WO_3 nanowire sensors in the range of 35-90% relative humidity at 150°C and 250°C for

10 ppm of NO_2. Interestingly, there is a little effect of humidity on the sensitivity and other features, as can be inferred from figure 2.4.47. This is somewhat surprising since metal oxides would be expected to sensitive to humidity.

We can understand the sensing action of In_2O_3 based on the following considerations. The electrical conductivity of In_2O_3 is attributed to electron transfer between In^{2+} and In^{3+}, the formation of the In^{2+} occurring through oxygen deficiency.

$$In_2O_3 \rightarrow In_{2-x}^{3+} In_x^{2+} O_{3-x} [V_O]_x + 1/2\ O_2 \qquad (19)$$

The oxygen vacancies (F- centers) are the chemisorptions sites [148-150].

$$NO_2\ (g) + V_O \rightarrow (V_O\text{-}O_{ads}) + NO\ (g) \qquad (20)$$

Oxygen desorption occurs by the reaction,

$$2\ (V_O\text{-}O_{ads}) \rightarrow 2\ (V_O)_s + O_2(g) \qquad (21)\ .$$

Thus, chemisorption of NO_2 on the active surface sites and the eventual desorption of oxygen determine the sensor action. In the case of NO, the first reaction would be,

$$NO\ (g) + V_O \rightarrow (V_O\text{-}O_{ads}) + 1/2\ N_2 \qquad (22)\ .$$

This reaction is followed by reaction (21). In the case of N_2O, the first reaction would be [151],

$$N_2O\ (g) + V_O \rightarrow (V_O\text{-}O_{ads}) + N_2\ (g) \qquad (23)\ .$$

Reaction (23) is followed by reaction (21). The desorption of oxygen as in reaction (21), involving the release of carriers is common to all the three nitrogen oxides. In the case of WO_3 sensors also, NO_2 first gets adsorbed giving out NO, as the first step as in reaction (20).

2.4.5 Ammonia sensors based on metal oxide nanostructures

ZnO nanoparticles, nanorods (nanorods-2), In_2O_3 nanoparticles, nanorods, SnO_2 nanoparticles, nanorods and flowers were prepared by the methods described in section 2.3. The XRD patterns of ZnO nanoparticles and nanorods, In_2O_3 nanoparticles and nanorods, and SnO_2 nanoparticles, nanorods and flowers are shown in figure 2.4.48. The XRD patterns of ZnO correspond to the wurtzite structure (lattice parameters: a=3.25 Å, c=5.2 Å, JCPDS no: 36-1451). In figure 2.4.49 (a), we show a typical TEM image of ZnO nanoparticles with the inset showing the selected area electron diffraction (SAED) pattern. The SAED pattern indicates the particles to be single crystalline. Based on the widths of the reflections in the XRD pattern, the average diameter of the nanoparticle is found to be ~15 nm. The XRD pattern of the ZnO nanorods show sharp 002 reflections, indicating the formation of the rods along the c axis. Figure 2.4.49 (b) shows a FESEM image of ZnO nanorods, with the SAED pattern as the inset. The SAED pattern indicates the single crystalline nature of the nanorods.

In_2O_3 nanoparticles and nanorods have the cubic structure (cell parameters: a=10.11 Å, JCPDS no: 06-0416) as revealed by the XRD patterns (Figure 2.4.31). The average diameter of the nanoparticles estimated to be ~21 nm from the XRD pattern. Figure 2.4.49 (c) shows a TEM image of In_2O_3 nanoparticles, with the inset showing the SAED pattern. The In_2O_3 nanorods are single crystalline as revealed by the SAED pattern and have an average diameter of around 20 nm. XRD patterns of SnO_2 nanoparticles, nanorods and flowers could be indexed on the tetragonal rutile structure (cell parameters: a=4.738 Å, c=3.187 Å, JCPDS no: 41-1445). The average diameter of the nanoparticles estimated from the XRD pattern is ~23 nm. In figure 2.4.50 (a), we show a typical TEM

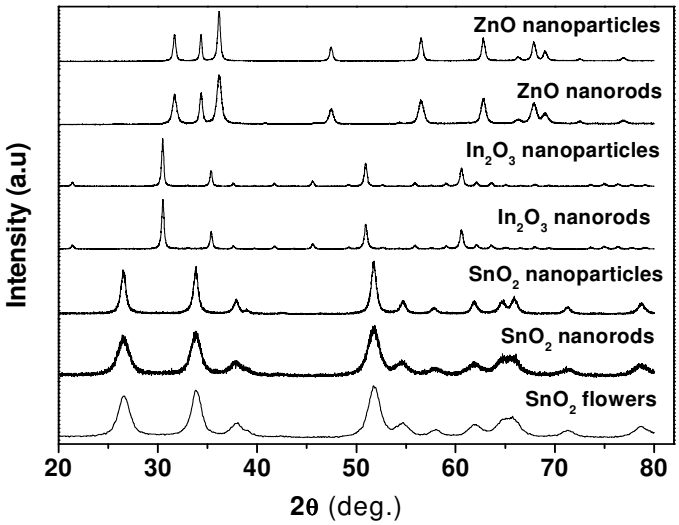

Figure 2.4.48: XRD patterns of nanoparticles and nanorods of ZnO, nanoparticles and nanorods of In_2O_3 and nanoparticles, nanorods and flowers of SnO_2.

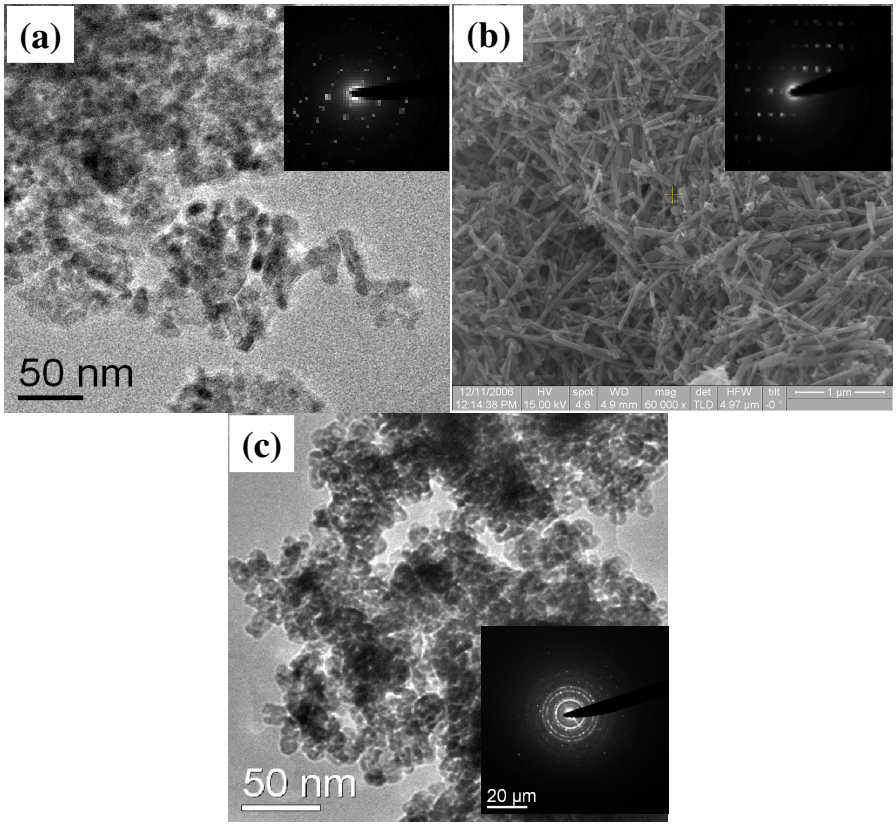

Figure 2.4.49: TEM image of ZnO nanoparticles with the inset showing electron diffraction, (b) FESEM image of ZnO nanorods with the inset showing electron diffraction pattern, (c) TEM image of In_2O_3 nanoparticles with the inset showing electron diffraction pattern.

image of the SnO_2 nanoparticles with the inset showing the electron diffraction pattern and a HREM image, confirming the single crystalline nature of the nanoparticles. In figure 2.4.50 (b), we show a TEM image of SnO_2 nanorods with the inset showing a HREM image and the SAED pattern. The SAED pattern shows the nanorods to be single crystalline nature. The average diameter of the nanorods is ~25 nm. FESEM images of flower-like structures of SnO_2 is shown in figure 2.4.50 (c) and (d). The inset of figure 2.4.50 (c) shows a high-resolution picture of SnO_2 flower. The flowers consist of fine rod-like or fiber-like structures with diameters around 25 nm.

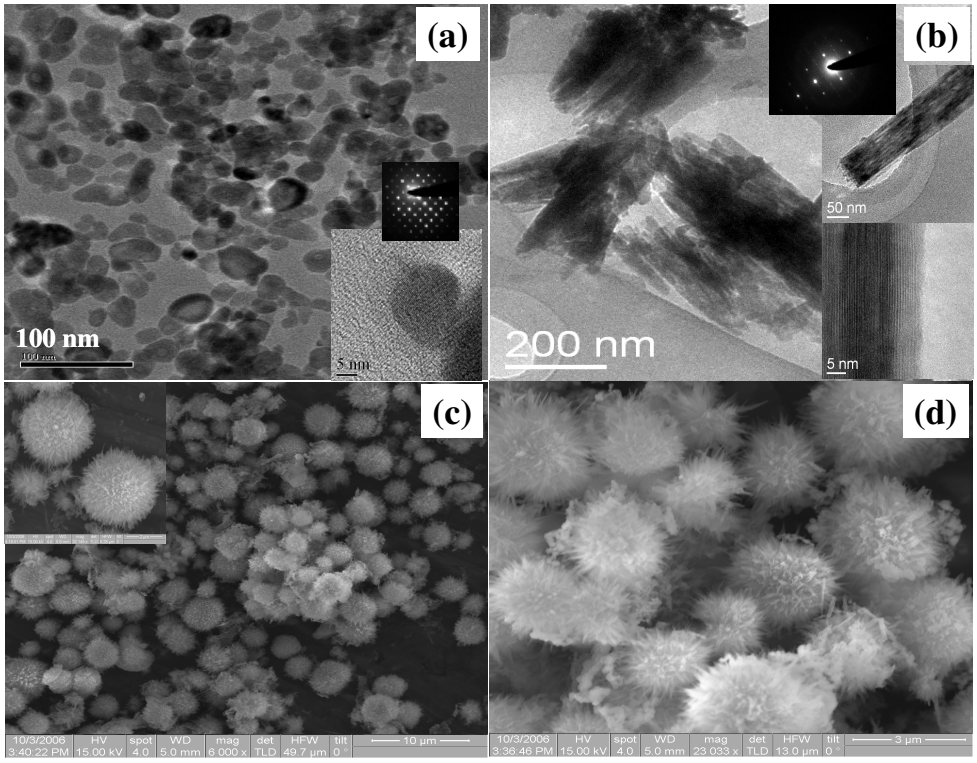

Figure 2.4.50: (a) TEM image of SnO_2 nanoparticles with the inset showing electron diffraction pattern, HREM image, (b) TEM image of SnO_2 nanorods with the inset showing electron diffraction pattern and HREM image, (c) and (d) FESEM image of SnO_2 flowers.

In figure 2.4.51 we show the Raman spectra of the various metal oxide nanostructures studied by us. Raman bands are found at 332, 441, 1076 cm^{-1} for the ZnO nanoparticles and nanorods [152]. Bulk ZnO shows Raman bands at 330, 439 cm^{-1} [152, 153]. The nanoparticles and nanorods of In_2O_3 show Raman bands at 305, 364, 495 and 630 cm^{-1}. For bulk In_2O_3, the Raman bands are at 306, 366, 495 and 630 cm^{-1} [154]. Raman bands of SnO_2 nanostructures are observed at 315, 472, 578, 632 and 773 cm^{-1}, in agreement with the literature [146]. Bulk SnO_2 exhibits Raman bands at 472, 632 and 773 cm^{-1}[155], where as for nanostructures two extra bands are found at 315 and 578 cm^{-1}. The Raman band positions of the nanostructures do not differ significantly from those of the bulk samples. This is not expected since phonon confinement occurs at much smaller sizes.

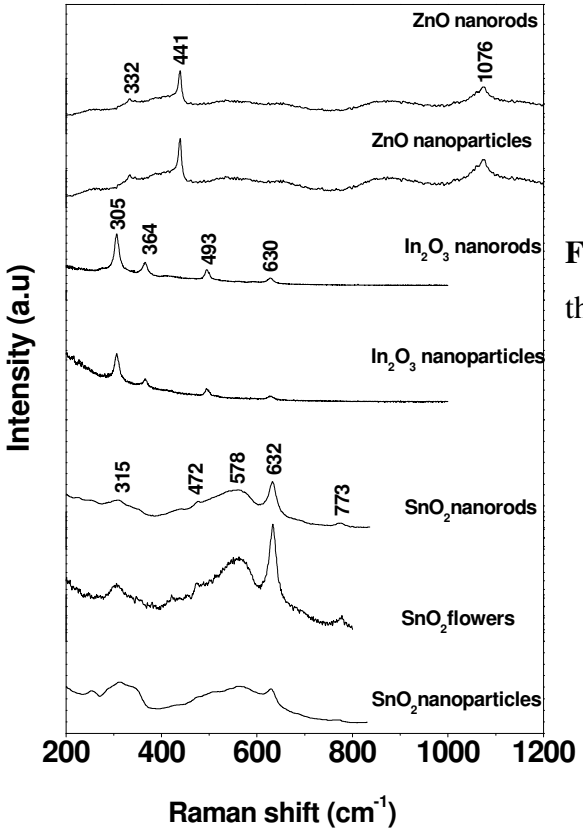

Figure 2.4.51: Raman spectra of the various oxide nanostructures.

In figures 2.4.52 (a) and (b), we show the sensing characteristics of In_2O_3 nanoparticles and nanorods respectively for 800 ppm of ammonia. The highest sensitivity is 77 for nanoparticles and 71 for nanorods at 300 °C. At 100 °C the sensitivities become 32 for nanoparticles and nanorods. The variation of sensitivity of the In_2O_3 nanorods with the concentration of NH_3 (1-800 ppm) at 300 °C is shown in figure 2.4.52 (c). The nanorods show a sensitivity of 4 for 1 ppm of NH_3 at 300 °C. The inset of the figure

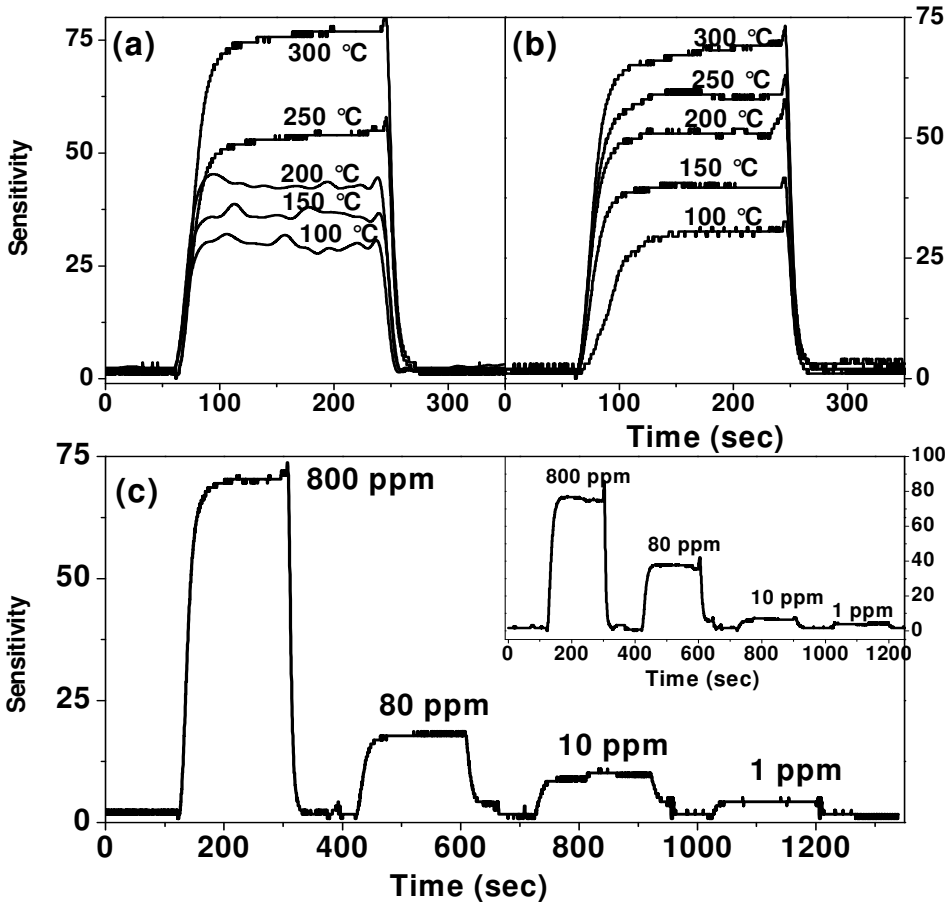

Figure 2.4.52: Gas sensing characteristics of (a) In_2O_3 nanoparticles, (b) In_2O_3 nanorods for 800 ppm of ammonia, (c) variation of sensitivity with concentration of ammonia for In_2O_3 nanorods, the inset showing variation of sensitivity with concentration of ammonia for the nanoparticles at 300°C.

2.4.52 (c) shows the variation of sensitivity of the In_2O_3 nanoparticles with the concentration of NH_3 at 300 °C (1-800 ppm). The response time for In_2O_3 nanoparticles and nanorods are 12s, 18s respectively for 800 ppm NH_3 at 300 °C; the recovery times are 9 and 15s respectively for In_2O_3 nanoparticles and nanorods.

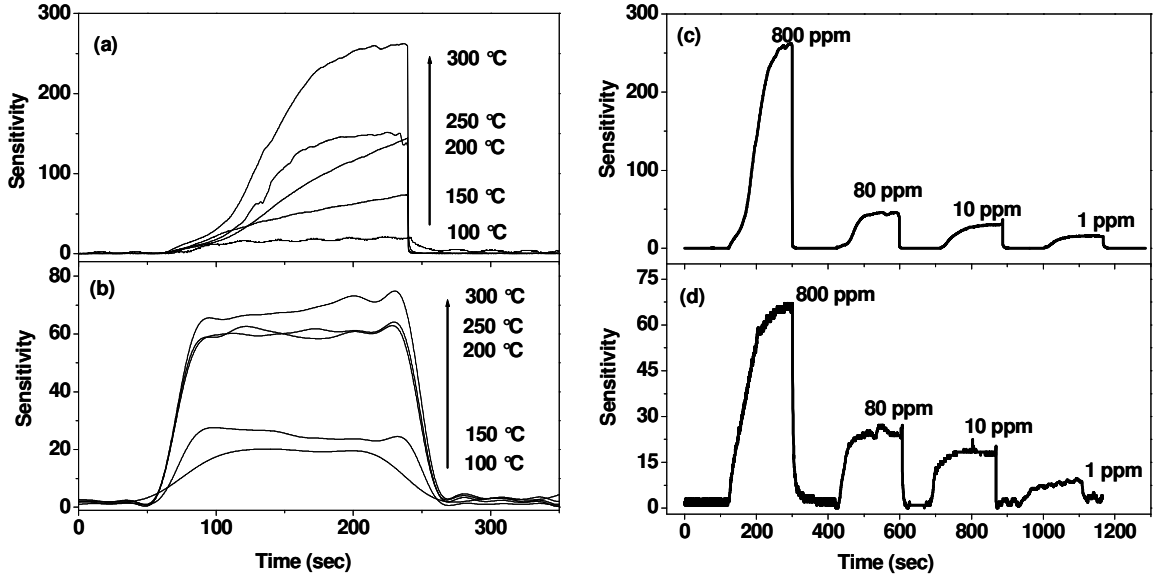

Figure 2.4.53: Gas sensing characteristics of (a) ZnO nanoparticles and, (b) ZnO nanorods for 800 ppm of ammonia, Variation of sensitivity with concentration of ammonia for (c) ZnO nanoparticles and (d) ZnO nanorods at 300°C.

Figures 2.4.53 (a) and (b) show the sensing characteristics of the ZnO nanoparticles and nanorods. ZnO nanoparticles show a highest sensitivity of ~260 for 800 ppm of NH_3 at 300 °C and at 100 °C the sensitivity becomes ~19. For ZnO nanorods, the observed values of sensitivity are 80 and 18 for 800 ppm of ammonia at 300 °C and 100 °C respectively. The variation of sensitivity with the concentration of NH_3 (1-800 ppm) at 300 °C is shown in figures 2.4.53 (c) and (d) respectively for ZnO nanoparticles and nanorods. The sensitivity values are 16 and 9 for 1 ppm of NH_3 for the nanoparticles

and nanorods respectively. The response and recovery times for the ZnO nanoparticles are 48s and 10s respectively for 800 ppm NH_3 at 300 °C. For ZnO nanorods, the response and recovery times are 26s and 7s at 300 °C.

The results of our experiments with the SnO_2 nanoparticles for sensing ammonia are shown in figure 2.4.54 (a). Conductance of the SnO_2 nanoparticles does not show saturation behavior for first few cycles. It is due to the availability of more number of adsorbed oxygen species during initial measurements and after several cycles the sensitivity saturates at a particular value. We did not find any change in sensitivity after 20 cycles.

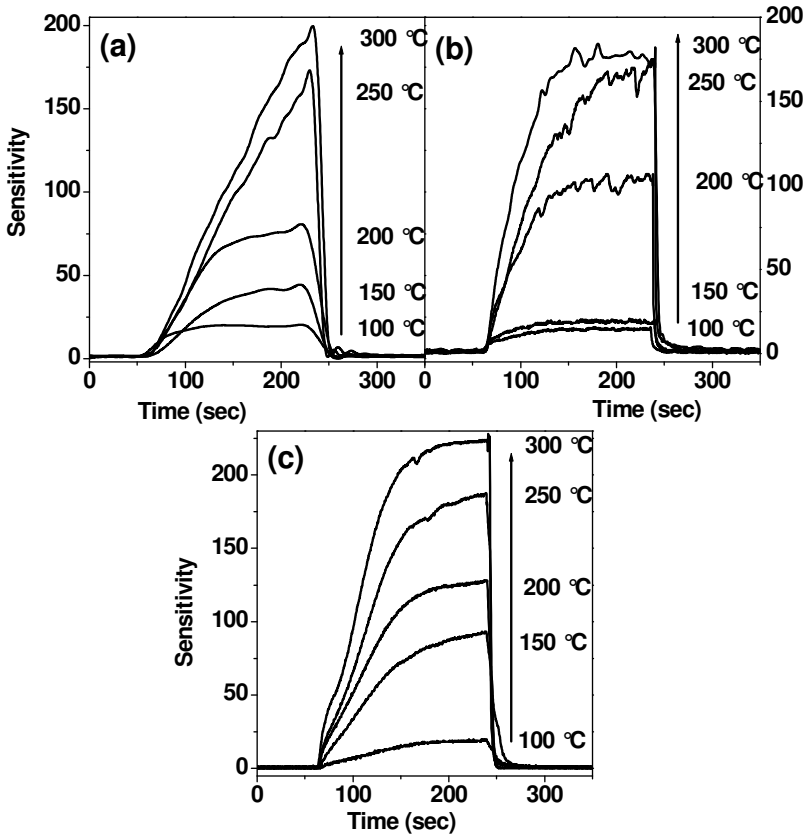

Figure 2.4.54: Gas sensing characteristics of (a) SnO_2 nanoparticles, (b) SnO_2 nanorods, (c) SnO_2 flowers for 800 ppm of ammonia.

The sensitivity varies in the range 20 - 200 for 800 ppm of ammonia in the temperature range 100 – 300°C. In figure 2.4.54 (b), we show ammonia-sensing characteristics of SnO_2 nanorods while figure 2.4.54 (c) shows ammonia-sensing characteristics of SnO_2 flowers for 800 ppm ammonia. The sensitivity of SnO_2 nanorods varies between 180-20 for 800 ppm of ammonia. SnO_2 flowers show a sensitivity of 220 at 300°C for 800 ppm of ammonia.

The variation of sensitivity with the concentration of ammonia for SnO_2 nanoparticles at 300°C is shown in figure 2.4.55 (a). For 1 ppm of ammonia a sensitivity of 18 is found at 300°C. The response and recovery times for the SnO_2 nanoparticles are

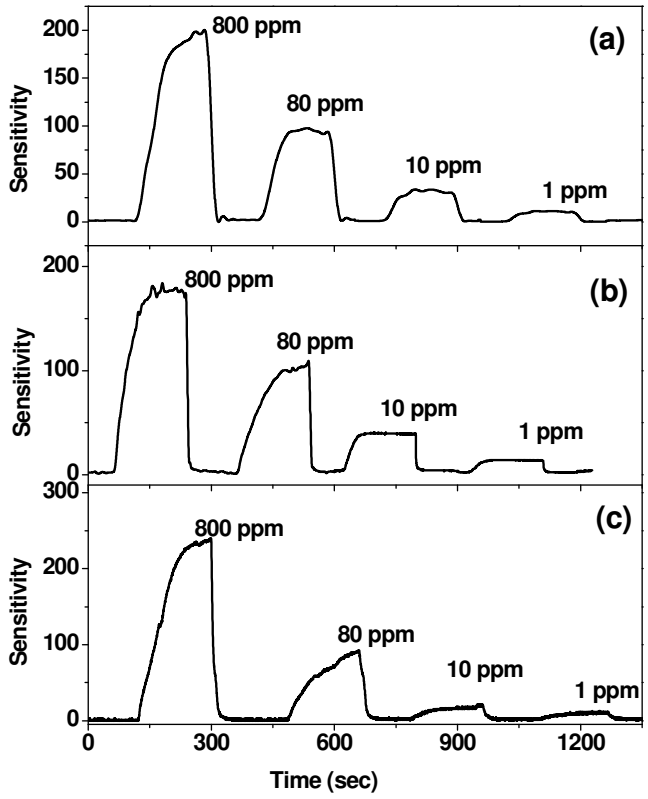

Figure 2.4.55: Variation of sensitivity with concentration of ammonia for (a) SnO_2 nanoparticles, (b) SnO_2 nanorods and (c) SnO_2 flowers at 300°C.

22s and 10s respectively for 800 ppm NH_3 at 300 °C. Figure 2.4.55 (b) shows the variation of sensitivity with concentration for SnO_2 nanorods, whereas figure 2.4.55 (c) shows variation of sensitivity with the concentration of ammonia for SnO_2 flowers at 300°C. For the nanorods and flowers, the response times are 36s and 25s respectively, whereas recovery times are 20s and 12s.

In figure 2.4.56, we compare the temperature variation of sensitivity in the 100-300°C range for ZnO, In_2O_3 and SnO_2 nanostructures. We see that ZnO nanoparticles show the highest values of sensitivity towards ammonia at 300°C. SnO_2 nanoparticles, nanorods and flowers also show satisfactory values of sensitivity. The sensitivity is lowest with the In_2O_3 nanoparticles and nanowires. The nanostructures of all the oxides show similar behavior at low temperatures (<150°C).

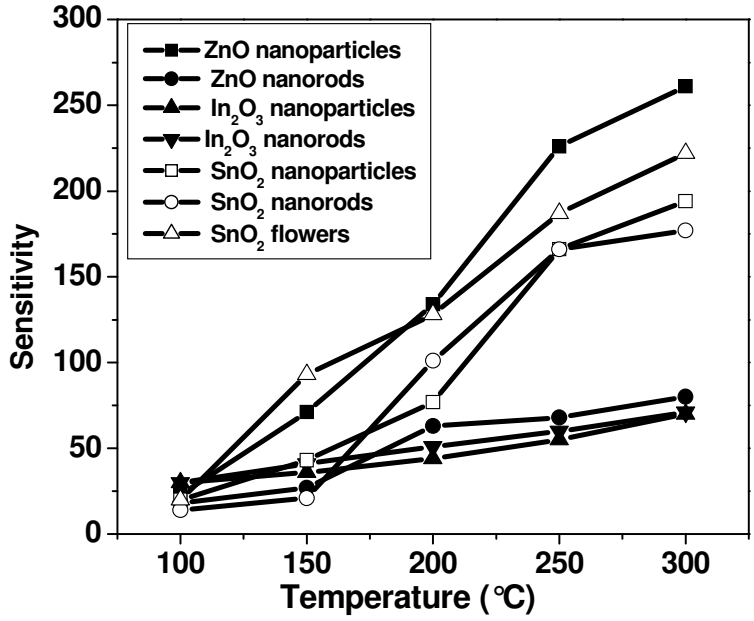

Figure 2.4.56: Temperature variation of sensitivity of ZnO, In_2O_3 and SnO_2 nanostructures.

The temperature variations of the response and recovery times of the ammonia sensors based on the nanostructures of ZnO, In_2O_3 and SnO_2 are shown in figure 2.4.57 (a) and b respectively. The response times vary in the range of 20s - 120s for all the materials. In_2O_3 nanowires and nanoparticles show fast response, but the sensitivity of these nanostructures is rather low compared to SnO_2 and ZnO nanostructures. At 300°C, the recovery times for the sensors are in the 8-30s range. At low temperatures, the recovery times are high, but below 70s at 100°C.

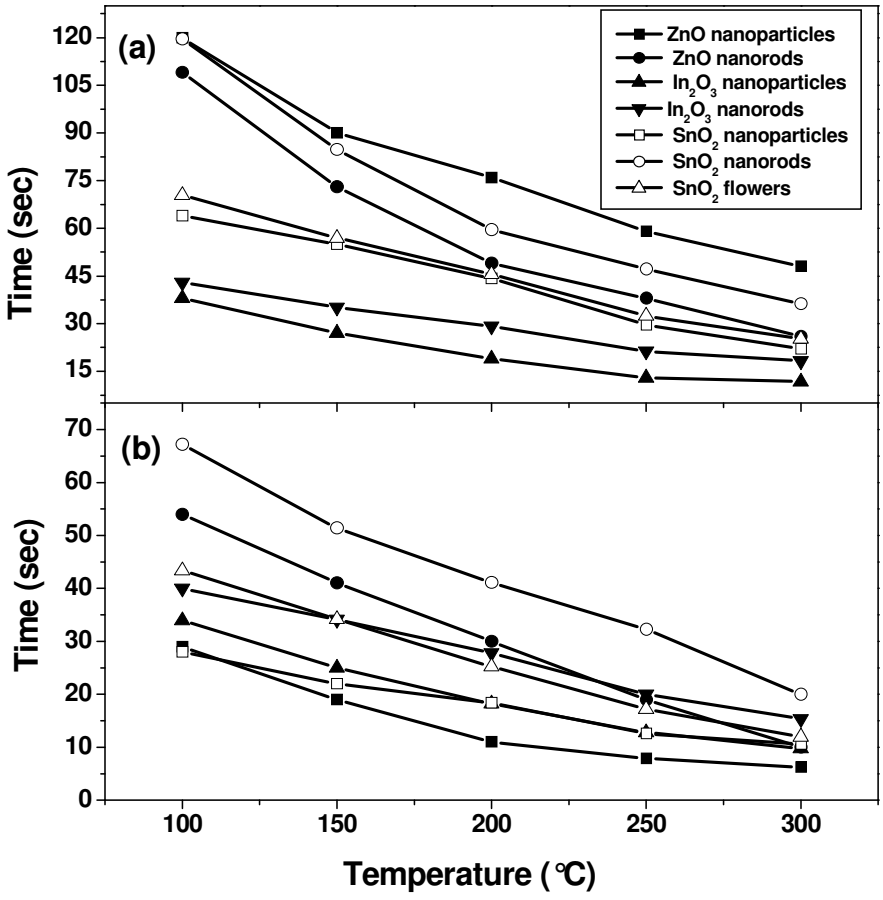

Figure 2.4.57: Temperature variation of (a) response and (b) recovery times for ZnO nanoparticles and nanorods, In_2O_3 nanoparticles and nanorods and SnO_2 nanoparticles, nanorods and flowers.

We have studied the effect of humidity on the ammonia sensing characteristics of the ZnO, In_2O_3 and SnO_2 nanostructure sensors in the range of 35-90% relative humidity. We illustrate the effect of humidity on the sensitivity for the In_2O_3 nanowires at 300°C for 800 ppm of NH_3 in figure 2.4.58 (a), and for ZnO nanoparticles in figure 2.4.58 (b). The humidity effect on the sensing characteristics of SnO_2 nanoparticles and nanorods is shown in figure 2.4.58 (c) and (d) respectively. There is a slight decrease in the sensitivity of the sensors with the increase in humidity upto a relative humidity of 60%, but the sensitivities as well as the response and recovery times are still in the acceptable range. The sensing characteristics deteriorate when the relative humidity is 90%. There was no change in the sensitivity as well as the response and recovery times after 200 cycles for the ZnO and SnO_2 nanostructures. We must also point out that we found no changes in the Raman spectra or XRD patterns of the oxide nanostructures after exposure to NH_3 repeatedly.

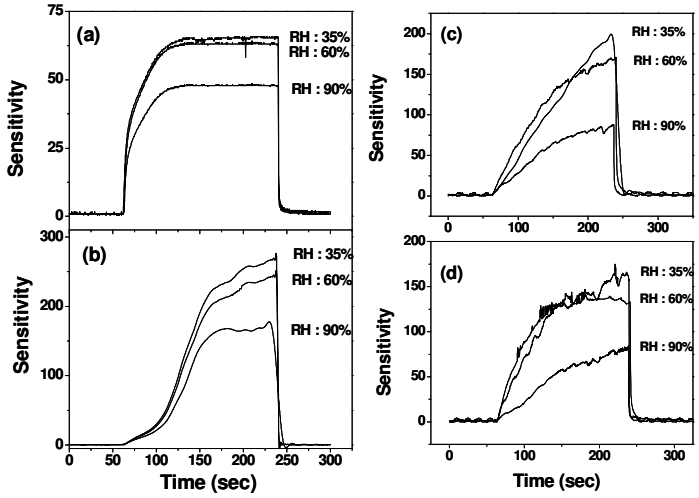

Figure 2.4.58: Effect of humidity on the sensitivity of (a) In_2O_3 nanorods, (b) ZnO nanoparticles, (c) SnO_2 nanoparticles, and (d) SnO_2 nanorods at 300°C for 800 ppm of NH_3.

In order to check the selectivity for sensing ammonia, we have studied the sensing characteristics of ZnO, In_2O_3 and SnO_2 nanostructures for NO_2, NO, N_2O, H_2, CO, H_2S and SO_2. The ZnO nanoparticles and nanorods showed a maximum sensitivity of 2-5 for the nitrogen oxides in the temperature range of 100 −300 °C. Maximum sensitivity values of 62, 8 and 17 were observed for 1000 ppm of H_2, CO and H_2S respectively in the case of ZnO nanoparticles. We did not find In_2O_3 to have good sensing characteristics for H_2, CO and H_2S, whereas it sensed nitrogen oxides at the ppm level. The SnO_2 nanostructures showed maximum sensitivity values of 43, 11 and 18 for 1000 ppm of H_2, CO and H_2S, which are considerably low as compared to the sensitivity obtained in the case of ammonia. The nanostructures of ZnO, In_2O_3 and SnO_2 do not sense SO_2.

The sensing action by metal oxides depends on several factors such as grain size (available surface area), surface states as well as the efficiency with which the test gas molecules adsorb on the surface. The sensing mechanism of n-type semiconducting metal oxides involves the formation of a charge depletion layer (L_D) on the surface of the oxides due to electron trapping on adsorbed oxygen species O^- and O_2^-. The adsorbed oxygens are present on the surface of the metal oxides, which is described in section 2.1.

The adsorbed oxygen species play a crucial role in sensing ammonia. The reaction for sensing ammonia is given by,

$$2NH_3 + 3O^-_{(ads)} \longrightarrow N_2 + 3H_2O + 3e^- \qquad (24)$$

As expected from equation (24), the resistance of the nanostructured material decreases on contact with ammonia. The thickness of the depletion layers of ZnO, In_2O_3 and SnO_2 is around 5 nm [146, 156, 157]. If the grain size is closer to $2L_D$, electrons in the nanostructures get depleted due to oxygen adsorption from air. Electrons are released

when the nanostructures are exposed to ammonia, leading to an increase in the conductance according to equation (24) [146, 158]. In the present study, ZnO nanoparticles show a linear dependence of sensitivity on NH_3 concentration and show higher sensitivity compared to the nanorods (Figure 2.4.59). Metal oxide nanostructures are known to show non-linear behavior with respect to the test gas concentration when the particles have an average diameter larger than 20 nm [159].

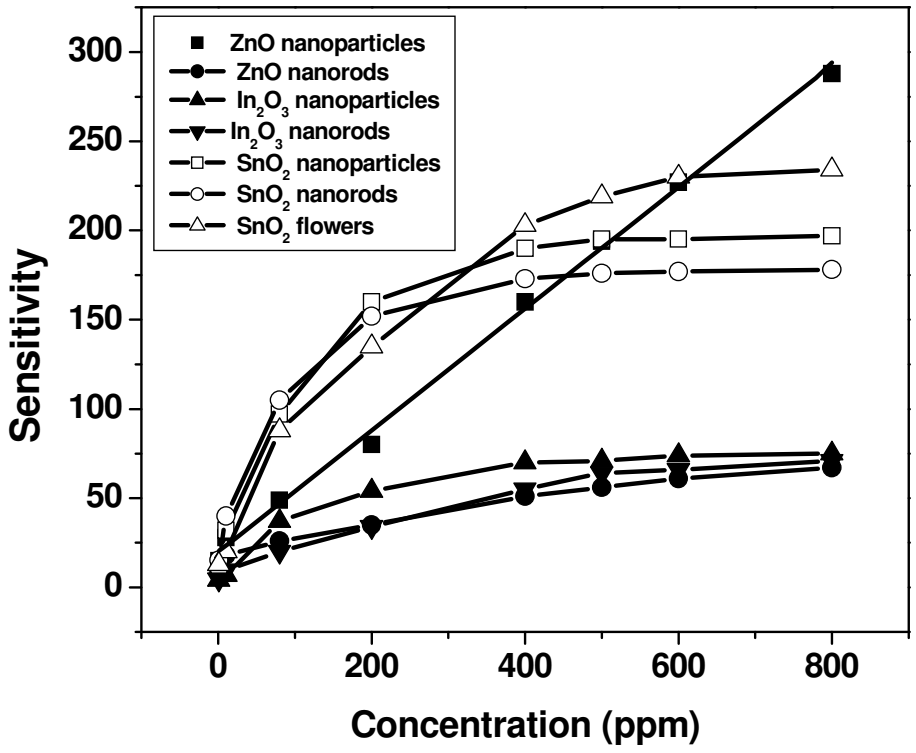

Figure 2.4.59: Comparison of the sensitivities of the different oxide nanostructures for sensing NH_3.

The nanostructures of SnO_2, however, show nearly equal values of sensitivity over a concentration range of 1-800 ppm, and they also have comparable sizes. SnO_2 nanostructures also show high sensitivities and a non-linear dependence with respect to

the NH_3 concentration. This may be due to the higher carrier concentration of SnO_2 [21, 160-163]. At higher concentrations of ammonia, the sensitivity of the SnO_2 nanostructures seems to saturate. Such a saturation behavior is related to the relative size of the nanostructures, as reported in the literature for flower-like structures of ZnO [156, 157]. The conductivity of the nanostructures varies according to the relation $\sigma = A\,[C]^N$, where A is a constant and C is the concentration of the test gas and N varies between 0.5 and 1.0 depending on the grain size (D), which is nearly equal to $2L_D$ [159]. For the particles of very small size ($D << 2L_D$), the depletion region extends throughout the whole grain and crystallites are almost fully depleted of mobile charge carriers. As a result the conductivity decreases steeply since the conduction channels between the grains are vanished. When $D >> 2L_D$, the gas sensing mechanism is controlled by the grain boundary barriers. The grain boundary barriers are independent of the grain size and the sensitivity is independent of D. In the case, $D \geq 2L_D$, the depletion region that surrounds each neck forms a constricted conduction channel within each aggregate. Hence the ammonia sensing characteristics using different nanostructures of ZnO, In_2O_3 and SnO_2 follow the space-charge model.

2.5 Conclusions

Thick films of nanoparticles of ZnO impregnated with Pt and/or doped with Mn or Co show good sensitivity for H_2 and ethanol at relatively low temperatures. Thus, the sensitivity for 1000 ppm H_2 reaches values of over 1000 and 1500 for 1% Pt impregnated ZnO and 3% Co doped ZnO at 125°C or lower. The sensitivities of these nanoparticles for ethanol are also high. The response and recovery times are generally well within 10 sec in

the regime of high sensitivity. The ZnO nanoparticle sensors are stable over several cycles for several weeks, thereby demonstrating their practical utility. Furthermore, the performance is not affected even by 50% relative humidity or greater.

The comparative study of the hydrogen and ethanol sensing characteristics of the different types of ZnO nanostructures with and without impregnation of Pt has revealed that, by and large, nanorods-1 and the nanowires prepared in alumina membranes are both good hydrogen sensors at or below 150° C, specially when impregnated with Pt. The sensitivities and other features of these H_2 sensors are superior to those reported in the literature. Nanorods-1 and nanowires also exhibit good sensing characteristics for 1000 ppm of ethanol at or below 150° C. The Sensitivity of the nanostructures for H_2 and ethanol was not affected significantly upto 50 % relative humidity. Furthermore, the sensitivity remained essentially the same upto 1000 cycles. These factors make the sensors based on the ZnO nanostructures to the potentially useful for practical applications. Gas sensing characteristics of single nanowires of metal oxides can be conveniently studied by conducting atomic force microscopy. Single nanowires of ZnO (25 nm dia), TiO_2 (60 nm dia) and $WO_{2.72}$ (40 and 16 nm dia) act as sensors for 100, 500 and 1000 ppm of hydrogen at room temperature, the values of sensitivities being 10, 8 and 22 respectively for 1000 ppm hydrogen at 298K. The sensitivity is higher with a $WO_{2.72}$ nanowire of 40 nm diameter as compared to a nanowire of 16 nm diameter.

We have successfully demonstrated that $WO_{2.72}$ nanowires are good for hydrocarbon (LPG) sensing with a sensitivity of the order of 10^3 or more at 200 °C for 2000 ppm of LPG. The response and recovery times are in the 25-80s range. Impregnation of the $WO_{2.72}$ nanowires with Pt has profound effect on the sensor characteristics, the

sensitivity increasing from 2200 for 0.1 at% Pt to 4.3×10^6 for 1 at% Pt at 200 °C for 2000 ppm of LPG. The sensitivity is 405 and 4.5×10^5 for 50 ppm of LPG with 0.1 and 1 at% Pt impregnation. It is remarkable that even 90% relative humidity has negligible effect on the sensor characteristics of the Pt impregnated $WO_{2.72}$ nanowires. The results can be understood on the basis of the interaction of charged surface oxygen species and the hydrocarbons. Single nanowires of $WO_{2.72}$ are also good sensors for liquefied petroleum gas at room temperature. The values of sensitivities are around 15, 5 and 2 for 1000, 500 and 100 ppm LPG with a nanowire of 40 nm diameter, while the sensitivity is 8 for 1000 ppm LPG in the case of the nanowire of 16 nm diameter. The recovery and response times for both the $WO_{2.72}$ nanowires are satisfactory.

Tungsten oxide nanostructures also exhibit good sensing characteristics for H_2S in the concentration range of 1-1000 ppm over the temperature range 40-250°C. The best results are obtained with the $WO_{2.72}$ nanowires at 250 °C where the sensitivity value reaches 3313 to 1000 ppm of H_2S and 121 for 10 ppm of H_2S. The sensitivity is satisfactory at 40 °C. The recovery and response times are generally satisfactory. It is noteworthy that the sensitivity is not affected significantly by humidity up to 60% relative humidity.

The study on the sensing characteristics of In_2O_3 (200 nm and 20 nm) and WO_3 (~10 nm) nanowires for the three nitrogen oxides, reveal the following general features.
(a) All the three nitrogen oxides, NO_2 , NO and N_2O can be sensed satisfactorily by In_2O_3 and WO_3 nanowires. (b) In_2O_3 nanowires with a diameter of ~20 nm (In_2O_3 –2) give the best performance in terms of the sensitivity and the operating temperature. The operating temperature of 150°C found by us is lower than many of the results reported in the

literature. This is specifically true for N_2O. The WO_3 nanowires can be useful even though the sensitivity is somewhat lower than that with In_2O_3-2. (c) The sensitivity values for 1000 ppm of the three nitrogen oxides show minor variations with both In_2O_3-2 and WO_3 nanowires. There is, however, some change in the sensitivity at lower concentrations of the gases. (d) Since the N_2O sensors are likely to be used for medical purposes, no contamination is expected from NO_2 or NO. In_2O_3 and WO_3 nanowires can be used satisfactorily for N_2O sensing. Both NO_2 and NO can be sensed by the In_2O_3 and WO_3 nanowires. This should not matter since both are atmospheric pollutants and NO_2 transforms to NO before it is sensed. (e) The mechanism of sensing proposed here suggests that the desorption of oxygen is a common step in sensing all the three nitrogen oxides.

Zinc and tin oxide nanostructures exhibit good sensing characteristics for ammonia. Although ZnO nanoparticles show higher sensitivity, the different nanostructures of SnO_2 seem to have a slight edge. The sensitivities and other characteristics are very good at 300°C, but are quite acceptable even at 200°C or at a somewhat lower temperature. It is also to be noted that the sensitivity values as well as recovery and response times of the SnO_2 nanostructures are generally better than those reported in the literature. Furthermore, the characteristics found by us are in the absence of any noble or transition metal additive. Since humidity does not have a marked effect on the sensitivity upto 60% relative humidity, and the sensing characteristics do not deteriorate on repeated cycling, SnO_2 nanostructures emerge as good ammonia sensors.

From the above studies the best sensitivities are found with nanostructures of ZnO (~1720 at 125 °C, H_2), (~2500 at 125 °C, Ethanol), $WO_{2.72}$ (~10^6 at 200 °C, aliphatic

hydrocarbon), WO_3 (~ 3300 at 250 °C, H_2S), In_2O_3 (~ 60 at 150 °C, NO, NO_2 and N_2O) and SnO_2 (~ 250 at 300 °C, NH_3).

References

[1] D. Kohl, *J. Phys. D* 34, R125 **(2001)**.

[2] S. Ampuero, J.O. Bosset, *Sens. Actuators B* 94, 1 **(2003)**.

[3] N. Docqier, S. Candel, *Progr. Energy Combust. Sci.* 28, 107 **(2002)**.

[4] J. Riegel, H. Neumann, H.M. Wiedenmann, *Solid State Ionics* 152/153, 783 (2002).

[5] G. Tschulena, A. Lahrmann, *Sensors in Household Applications in Sensors Applications*, Vol. 5 (Eds.: J. Hess, J. Gardner, W. Gopel), Wiley-VCH, Weinheim **(2004)**.

[6] P.A. Oberg, T. Togawa, F.A. Spelman, *Sensors in Medicine and Health Care in Sensor Application*, Vol. 3 (Eds.: J. Hess, J. Gardner, W. Gopel), Wiley-VCH, Weinheim **(2004)**.

[7] B. Timmer, W. Othuis, A. Berg, *Sens. Actuators B* 107, 666 **(2005)**.

[8] N. Yamazoe, G. Sakai, K. Shimanoe, *Catal. Surv. Asia* 7, 63 **(2003)**.

[9] N. Barsan, D. Koziej, U. Weimer, *Sens. Actuators B* 121, 18 **(2007)**.

[10] H. Debeda, D. Rebiere, J. Pistre, J. Menil, *Sens. Actuators B* 1995, 27, 297–300.

[11] A. D. Brailsford, M. Yussouff, E. M. Logothetis, *Technical Digest of the 4th International Meeting on Chemical Sensors* (Ed.: N. Yamazoe), Japan Association of Chemical Sensors, Tokyo, **(1992)**.

[12] B. Ostrik, M. Fleischer, H. Meixner, D. Kohl, *Sens. Actuators B* 68, 197 **(2000)**.

[13] R. Lucklum, P. Hauptmann, *Sens. Actuators B* 70, 30 **(2000)**.

[14] S. M. Chang, Y. H. Kim, J. M. Kim, Y. K. Chang, J. D. Kim, *Mol. Cryst. Liq. Cryst.* 267, 405 **(1995)**.

[15] U. Schramm, D. Meinhold, S. Winter, C. Heil, J. Muller-Albrecht, L. Wachter, Hoff, C. E. O. Roesky, T. Rechenbach, P. Boeker, P. S. Lammers, E. Weber, J. Bargon, *Sens Actuators B* 67, 219 **(2000)**.

[16] W. H. Brattein, J. Bardeen, *Bell Syst. Tech.* J. 32, 1 **(1953)**.

[17] G. Heiland, J. *Phys.* 138, 549 **(1954)**.

[18] T. Seiyama, A. Kato, K. Fujiishi, M. Nagatami, *Anal. Chem.* 34, 1502 (1962,); T. Seiyama, S. Kagawa, *Anal. Chem.* 38, 1069 **(1966)**.

[19] N. Taguchi, *Patent* 45–38200, **(1962)**.

[20] A. Gurlo, R. Riedel, *Angew. Chem. Int. Ed.* 46, 2 **(2007)**.

[21] M. E. Franke, T. J. Koplin, U. Simon, *Small* 2, 36 **(2006)**.

[22] G. Eranna, B. C. Joshi, D. P. Runthala, R. P. Gupta, *Crit. Rev. Solid State Mater. Sci*. 29, 111 **(2004)**.

[23] M. Graf, A. Gurlo, N. Barsan, U. Weimar, A. Hierlemann, *J. Nanoparticle Res.*, 8, 823 **(2006)**.

[24] L. M. Tdler, A. Roessler, S. E. Pratsinis, T. Sahm, A. Gurlo, N. Barsan, U. Weimar, *Sens. Actuators B* 114, 283 **(2006)**.

[25] Y. Zhang, A. Kolmakov, S. Chretien, H. Metiu, M. Moskovits, *Nano Lett*. 4, 403 **(2004)**.

[26] M. Blaschke, T. Tille, P. Robertson, S. Mair, U. Weimar, H. Ulmer, *IEEE Sens. J.*, 8, 1298 **(2006)**.

[27] M.J. Madou, S.R. Morison, *Chemical Sensing with Solid State Devices,* Academic Press, San Diego, **(1989)**.

[28] D.E. Williams in *Solid State Gas Sensors* (Eds.: P.T. Moseley, B.C. Tot-field), Adam Hilger, Philadelphia, pp. 71-123 **(1987)**.

[29] P. B. Weisz, *J. Chem. Phys*. 21 1531 **(1953)**.

[30] U. Lampe, M. Fleischer, N. Reitmeier, H. Meixner, J. B. McMonagle, A. Marsch, *New Metal Oxide Sensors: Materials and Properties in Sensors*, Vol. 2 (Eds.: W. Gçpel, J. Hesse, J. N. Zemel) VCH, Weinheim, 29–30 **(1997)**.

[31] H. Ogawa, M. Nishikawa, A. Abe, *J. Appl. Phys.* 53, 4448 **(1982)**.

[32] M.J. Madou, S.R. Morrison, *Chemical Sensing with Solid State Devices, Academic Press, New York* **(1989)**.

[33] S. Lenaerts, M. Honore, G. Huyberechts, J. Roggen, G. Maes, *Sens. Actuators B* 18, 478 **(1994)**; M. I. Baraton, L. Merhari, H. Ferkerl, J. F. Castagnet, *Mater. Sci. Eng. C* 19, 315 **(2002)**.

[34] C. Xu, J. Tamaki, N. Miura, N. Yamazoe, *J. Electrochem. Soc. Jpn.* 58, 1143 **(1990)**; *Sens. Actuators B* 6, 239 **(1992)**.

[35] A. Rothschild, Y. Komem, *J. Appl. Phys.* 95, 6374 **(2004)**.

[36] X.-J. Huang, Y.-K. Choi, *Sens. Actuators B* 122, 659**(2007)**.

[37] S.R. Morrison, *Sens. Actuators* 12, 425 **(1987)**.

[38] D. Kohl, *Sens. Actuators B* 1, 158 **(1990)**.

[39] N. Yamazoe, *Sens. Actuators B* 5, 7 **(1991)**.

[40] J.N. Zemel, *Thin Solid Films* 163, 189 **(1988)**.

[41] U. Ozgur, Y.I. Alivov, C. Liu, A. Teke, M.A. Reschilkov, S. Dogan, V. Avrutin, S.-J. Cho, H. Morkoc, *J. Appl. Phys.* 98, 041301 **(2005)**.

[42] X. Wang, J. Song, Z.L. Wang, *J. Mater. Chem.* 17, 711 **(2007)**.

[43] C. Klingshirn, *ChemPhysChem.* 8, 782 **(2007)**.

[44] N. Du, H. Zhang, B. Chen, J. Wu, D. Yang, *Nanotechnology* 18, 115619 **(2007)**.

[45] D. Wang, X. Chu, M. Gong, *Nanotechnology* 18, 185601 **(2007)**.

[46] H. Zhang, J. Wu, C. Zhai, N. Du, X. Ma, D. Yang, *Nanotechnology* 18, 455604 **(2007)**.

[47] Z-P. Sun, L. Liu, L. Zhang, D-Z. Jia, *Nanotechnology* 17, 2266 **(2006)**.

[48] L.C. Tien, P.W. Sadik, D.P. Norton, L.F. Voss, S.J. Pearton, H.T. Wang, B.S. Kang, F. Ren, J. Jun, J. Lin, *Appl. Phys. Lett.* 87, 222106 **(2005)**.

[49] H.T. Wang, B.S. Kang, F. Ren, L.C. Tien, P.W. Sadik, D.P. Norton, S.J. Pearton, J. Lin, *Appl. Phys. Lett.* 86, 243503 **(2005)**.

[50] M. Kaur, S. Bhatacharya, M. Roy, S.K. Despande, P. Sharma, S.K. Gupta, J.V. Yakhmi, *Appl. Phys. A* 87, 91 **(2007)**.

[51] S. Kar, B.N. Pal, S. Chaudhari, D. Chakravorty*, J. Phys. Chem. B* 110, 4605 **(2006)**.

[52] E. Comini, G. Fagila, M. Ferroni, G. Sberveglieri, *Appl. Phys. A* 88, 45 **(2007)**.

[53] Y. Qiu, S. Yang, *Adv. Func. Mater.* 17, 1345 **(2007)**.

[54] Q. Wan, Q.H. Li, Y.J. Chen, T.H. Wang, X.L. He, X.G. Gao, J.P. Li, *Appl. Phys. Lett.* 84, 3085 **(2004)**.

[55] L. Lio, H.B. Lu, J.C. Li, C. Liu, D.J. Fu, *Appl. Phys. Lett.* 91,173110 **(2007)**.

[56] P. Mitra, H.S. Maiti, *Sens. Actuators B* 84**,** 49 **(2004)**.

[57] B. Baruwati, D.K. Kumar, S.V. Manorama, *Sens. Actuators B* 119, 676 **(2006)**.

[58] S. Saito, M. Miyama, K. Koumoto, H. Yanagida, *J. Am. Ceram. Soc.* 68, 40 **(1985)**.

[59] J.G. Duh, J.W. Jou, B.S. Chiou, *J. Electrochem. Soc.* 136, 2740 **(1989)**.

[60] G.N. Choudhari, A.M. Bende, A.B. Bodade, S.S. Patil, S.V. Manorama, *Talanta* 69, 187 **(2006)**.

[61] J. Wang, M. Tong, X. Wang, Y. Ma, D. Liu, J. Wu, D. Gao, G. Du, *Sens. Actuators B* 84, 95 **(2002)**.

[62] L. Satyanaranyana, K.M. Reddy, S.V. Manorama, *Sens. Actuators B* 89, 62 (2003).

[63] A.R. Raju, C.N.R. Rao, *Chem. Commun.* 18, 1260 **(1991)**.

[64] A. Srivastava, K. Jain, Rashmi, A.K. Srivastava, S.T. Lakshmikumar, *Materials Chem. Phys.* 97, 85 **(2006)**.

[65] F. Pourfayaz, A. Khodadadi, Y. Mortazavi, S.S. Mohajerzadeh, *Sens. Actuators B* 108, 172 **(2005)**.

[66] R.N. Niranjan, Y.K. Hwang, D.-K. Kim, S.H. Jhung, J.-S. Chang, I.S. Mulla, *Mater. Chem. Phys.* 92, 384 **(2005)**.

[67] Y.-L. Liu, H.-F. Yang, Y. Yang, Z.-M. Liu, G.-L. Shen, R.-Q. Yu, *Thin solid films* 497, 355 **(2006)**.

[68] J.L. Solis, A. Hoel, L.B. Kish, C.G. Granqvist, *J. Am. Ceram. Soc.* 84, 1504 **(2001)**.

[69] M.D. Antonik, J.E. Schneider, E.L. Witttman, K. Snow, J.F. Vetelino, R.J. Lad, *Thin Solid Films* 256, 247 **(1995)**.

[70] J.L. Solis, S. Saukko, C.G. Granqvist, V. Lantto, *Thin Solid Films* 391, 255 **(2001)**.

[71] R. Ionescu, A. Hoel, C.G. Granqvist, E. Llobet, P. Heszler, *Sens. Actuators B* 104, 132 **(2005)**.

[72] M. Stankova, X. Vilanova, J. Calderer, E. Llobet, P. Ivanov, I. Gracia, C. Cane, X.Correig, *Sens. Actuators B* 102, 219 **(2004)**.

[73] M. Stankova, X. Vilanova, J. Calderer, E. Llobet, J. Brezmes, I. Gracia, C. Cane, X.Correig, *Sens. Actuators B* 113, 241 **(2006)**.

[74] H-M. Lin, C-M. Hsu, H-Y. Yang, P-Y. Lee, C-C. Yang, *Sens. Actuators B* 22, 63 **(1994)**.

[75] J. Jimenez, J. Arbiol, G. Dezanneau, A. Cornet, J.R. Morante, *Sens. Actuators B* 93, 475 **(2003)**.

[76] L.F. Reyes, A. Hoel, S. Saukko, P. Heszler, V. Lantto, C.G. Granqvist, *Sens. Actuators B* 117, 128 **(2006)**.

[77] A. Ponzoni, E. Comini, G. Sberveglieri, J. Zhou, S. Z. Deng, N. S. Xu, Y. Ding, Z. L. Wang, *Appl. Phys. Lett.* 88, 203101 **(2006)**.

[78] M. Ando, S. Suto, T. Suzuki, T. Tsuchida, C. Nakayama, N. Miura, N. Yamazoe, *J. Mater. Chem.* 4, 631 **(1994)**.

[79] S. Manorama, G.S. Devi, V.J. Rao, *Appl. Phys. Lett.* 64, 3163 **(1994)**.

[80] A. Khanna, R.Kumar, S.S.Bhatti, *Appl. Phys. Lett.* 82, 4388 **(2003)**.

[81] G.S. Devi, S. Manorama, V.J. Rao, *Sens. Actuators B* 28, 31**(1995)**.

[82] V.R. Katti, A.K. Debnath, K.P. Muthe, M. Kaur, A.K. Dua, S.C. Gadkari, S.K.Gupta, V.C. Sahni, *Sens. Actuators B* 96, 245 **(2003)**.

[83] G. Kersen, L. Holappa, *Appl. Phys. A.* 85, 431 **(2006)**.

[84] X. Niu, W. Du, W. Du, *Sens. Actuators B* 99, 399 **(2004)**.

[85] C. Baatto, G. Sberveglieri, A. Onischuk, B. Caruso, S. di Stasio, *Sens. Actuators B* 100, 261 **(2004)**.

[86] C. Baatto, E. Comini, G. Sberveglieri, M.Jha, A. Zappettini, *Sens. Actuators B* 109, 2 **(2005)**.

[87] S. H. Wang, T. C. Chou, C. C. Liu, *Sens. Actuators B* 94, 343 **(2003)**.

[88] D-S. Lee, S-D. Han, J-S. Huh, D-D. Lee, *Sens. Actuators B* 60, 57 **(1999)**.

[89] J. Polleux, A. Gurlo, N. Barsan, U. Weimar, M. Antonietti, M. Niederberger, *Angew. Chem. Int. Ed.* 45, 261 **(2005)**.

[90] Y-K. Chung, M-H. Kim, W-S. Um, H-S. Lee, J-K. Song, S-C. Choi, K-M. Yi, M-J. Lee, K-W. Chung, *Sens. Actuators B* 60, 49 **(1999)**.

[91] L. G. Teoh, Y. M. Hon, J. Shieh, W.H. Lai, M. H. Hon, *Sens. Actuators B* 96, 219 **(2003)**.

[92] C. Cantalini, H. T. Sun, M. Pelino, S. Santucci, L. Lozzi, M. Passacantando, *Sens. Actuators B* 31, 81 **(1996)**.

[93] D. Zhang, C. Li, X. Liu, S. Han, T. Tang, C. Zhou, *Appl. Phys. Lett.* 83, 1845 **(2003)**.

[94] G. Korotcenkov, V. Brinzari, A. Cerneavschi, M. Ivanov, A. Cornet, J. Morante, A. Cabot, J. Arbiol, *Sens. Actuators B* 98, 122 **(2004)**.

[95] G. Neri, A. Bonavita, G. Micali, G.Rizzo, S. Galvagno, M. Niederberger, N. Pinna, *Chem. Comm.* 48, 6032 **(2005)**.

[96] D. Zhang, Z. Liu, C. Li, T. Tang, X. Liu, S. Han, B. Lei, C. Zhou, *Nano Lett.* 4, 1919 **(2004)**.

[97] N. Pinna, G. Neri, M. Antonietti, M. Niederberger, *Angew. Chem. Int. Ed.* 43, 4345 **(2004)**.

[98] A. Gurlo, N. Barsan, M. Ivanovskaya, U. Weimar, W. Gopel, *Sens. Actuators B* 47, 92 **(1998)**.

[99] M. Ivanovskaya, P. Bogdanov, G. Fagila, G. Sberveglieri, *Sens. Actuators B* 68, 344 **(2000)**.

[100] L. Francioso, A. Forleo, S. Capone, M. Epifani, A. M. Taurino, P. Siciliano, *Sens. Actuators B* 114, 646 **(2006)**.

[101] E. Kanazawa, G. Sakai, K. Shimanoe, Y. Kanmura, Y. Teraoka, N. Miura, N. Yamazoe, *Sens. Actuators B* 77, 72 **(2001)**.

[102] B. Timmer, W. Olthuis, A. Berg, *Sens. Actuators B* 107, 666 **(2005)**.

[103] H. Nanto, T. Minami, S. Takata, *J. Appl. Phys*. 60, 482 **(1986)**.

[104] G. Sberveglieri, S. Groppelli, P. Nelli, A. Tintinelli, G. Giunta *Sens. Actuators B* 24, 588 **(1995)**.

[105] M. Aslam, V.A. Chaudhary, I.S. Mulla, S.R. Sainkar, A. B. Mandale, A. A. Belhekar, K. Vijayamohanan, *Sens. Actuators A* 75, 162 **(1999)**.

[106] M. S. Wagh, G. H. Jain, D. R. Patil, S. A. Patil, A. L. Patil, *Sens. Actuators B* 115, 128 **(2006)**.

[107] A. Teeramongkonrasmee, M. Sriyudhsak, *Sens. Actuators B* 66, 256 **(2000)**.

[108] Y. Wang, X. Wu, Q. Su, Y, Li, Z Zhou, *Solid State Electron.* 45, 347 **(2001)**.

[109] P. Guo, H. Pan, *Sens. Actuators B* 114, 762 **(2006)**.

[110] V. Romanovskaya, M. Ivanovskaya, P. Bogdanov, *Sens.Actuators B* 56, 31 **(1999)**.

[111] E. Bekyarova, M. Davis, T. Burch, M. E. Itkis, B. Zhao, S. Sushine, R. C. Haddon, *J. Phys. Chem. B* 108, 19717 **(2004)**.

[112] N. H. Quang, M. V. Trinh, B. Lee, J. Huh, *Sens. Actuators B* 113, 341 **(2006)**.

[113] F. V. Paez, A. H. Romero, E. M. Sandoval, L. M. Martinez, H. Terrones, M. Terrones, *Chem. Phys. Lett.* 386, 137 **(2004)**.

[114] C.N.R. Rao, and F.L. Deepak, *J. Mat. Chem*., 15, 573 **(2005)**; Also see S. V. Bhat, F. L. Deepak, *Solid State Comm*.135, 345 **(2005)**.

[115] C. Jin, X. Yuan, W. Ge, J. Hong, X. Xin, *Nanotechnology* 14, 667 **(2003)**.

[116] C. Pacholski, A. Kornowski and H. Weller, *Angew. Chem. Int. Ed.* 41, 1188 **(2002)**.

[117] Y. C. Wang, I. C. Leu and M. H.Hon, *J. Mater. Chem.* 12, 2439 **(2002)**.

[118] H. Morikawa, N.Tsuihiji, T. Mitsui and K. Kanamura, *J. Electro Chem. Soc.* 151, A1733 **(2004)**.

[119] S. R. C. Vivekchand, G. Gundiah, A.Govindraj and C.N.R.Rao, *Adv. Mater.* 16, 1842 **(2004)**.

[120] X. Chen, S.S. Mao, *J. Nanosc. Nanotech*. 6, 906 **(2006)**.

[121] H.G. Choi, Y.H. Jung, D.K. Kim, *J. Am. Ceram. Soc.* 88, 1684 **(2005)**.

[122] M. Niederberger, M.H. Bartl, G.D. Stucky, *J. Am. Chem. Soc.*124,13642 **(2002)**.

[123] K. C. Kam, F. L. Deepak, A. K. Cheetam, C. N. R. Rao, *Chem. Phys. Lett.* 397, 329 **(2004)**.

[124] H. Cao, X. Qiu, Y. Liang, Q. Zhu, M. Zhao, *Appl. Phys. Lett.* 83, 761 **(2003)**.

[125] Y.J. Chen, X.Y. Xue, Y.G. Wang, T.H. Wang, *Appl. Phys. Lett.* 87, 233503 **(2005)**.

[126] P. Romppainen and V. Lantto, *J. Appl. Phys*. 63, 5159 **(1988)**.

[127] C. Xu, J. Tamaki, N. Miura and N. Yamazoe, *Sens. Actuators B* 3, 147 **(1991)**.

[128] N. Yamazoe and N. Miura, *Chemical Sensor Technology* 4**,** 19 **(1992)**.

[129] X. Wang, S. S. Yee and W. P. Carey, *Sens. Actuators B* 24-25, 454 **(1995)**.

[130] S. Shukla, S. Seal, L. Ludwig, C. Parish, *Sens. Actuators B* 97, 256 **(2004)**.

[131] X. Y. Xue, Y. J. Chen, Y. G. Wang and T. H. Wang, *Appl. Phys. Lett*. 86, 233101 **(2005)**.

[132] C. Li, L. Li, Z. Du, H. Yu, Y. Xiang, Y. Li, Y. Cai, T. Wang, *Nanotechnology* 19, 035501 **(2008)**.

[133] H. Cheng, J. Ma, Z. Zhao, L. Qi, *Chem. Mater.* 7, 663 **(1995)**.

[134] J. Xu, N. Wu, C. Jiang, M. Zhao, J. Li, Y. Wei, S. X. Mao *Small* 2, 1458 **(2006)**.

[135] Y. W. Heo, L. C. Tien, D. P. Norton, B. S. Kang, F. Ren, B. P. Gila, S. J. Pearton *Appl. Phys. Lett.* 85, 2002 **(2004)**.

[136] W. I. Park, G. –C. Yi, J –W. Kim, S –M. Park, *Appl. Phys. Lett.* 82, 4358 **(2003)**.

[137] S.-H. Lee, H.M. Cheong, M.J. Seong, P. Liv, C.E. Tracy, A. Mascarenhas, J.R. Pitts, S.K. Deb, *J. Appl. Phys.* 92, 1893 **(2002)**.

[138] M. Gotic, S. Popovic, M. Ivanda, S. Music, *Mat. Lett.* 57, 3186 **(2003)**.

[139] J. Polleux, A. Gurlo, N. Barsan, U. Weimar, M. Antonietti, M. Niederberger, *Angew. Chem. Int. Ed.* 45, 261 **(2005)**.

[140] J.A. Horsley, I.E. Watchs, J.M. Brown, G.H. Via, F.D. Hardcastle, *J. Phys. Chem*. 91, 4014 **(1987)**.

[141] Z. Xiao, L. Zhang, X. Tian, X. Fang, *Nanotechnology* 16, 2647 **(2005)**.

[142] D. Y. Lu, J. Chen, J. zhu, S. Z. Deng, N.S. Xu, J.B. Xu, *J. Raman Spectrosc.* 38, 176 **(2007)**.

[143] L. Zhixiang, S. M. Kanan, C.P. Tripp, *J. Mater. Chem.* 12, 983 **(2002)**.

[144] A. Dutta, S. Basu, *J. Mater. Sci: Mater. Electron*. 6, 415 **(1995)**.

[145] K. Viswanathan, K. Brandt, E. Salje, *J. Solid. State. Chem.* 36, 45 **(1981)**.

[146] Y.J. Chen, L. Nie, X.Y. Xue, Y.G. Wang, T.H. Wang, *Appl. Phys. Lett.* 88, 083105 **(2006)**.

[147] M. Paulose, O.K. Varghese, G.K. Mor, C.A. Grimes, K.G. Ong, Nanotechnology 17,398 **(2006)**.

[148] M. Ivanovskaya, P. Bogdanov, G. Fagila, G. Sberveglieri, *Sens. Act: B* 68, 344 **(2000)**.

[149] L. Francioso, A. Forleo, S. Capone, M. Epifani, A. M. Taurino, P. Siciliano, *Sens. Act: B* 114, 646 **(2006)**.

[150] Ivanovskaya, A. Gurlo, P. Bogdanov, *Sens. Act: B* 77, 264 **(2001)**.

[151] E. Kanazawa, G. Sakai, K. Shimanoe, Y. Kanmura, Y. Teraoka, N. Miura, N. Yamazoe, *Sens. Act: B* 77, 72 **(2001)**.

[152] K.A. Alim, V.A. Fonoberov, M. Shamsa, A.A. Babandin, *J. Appl. Phys.* 97, 124313 **(2005)**.

[153] H. Zhou, H. Alves, D.M. Hofmann, W. Kriegseis, B.K. Meyer, G. Kaczmarczyk, A. Hoffmann, *Appl. Phys. Lett.* 80, 210 **(2002)**.

[154] G. Korotcenkov, V. Brinzari, M. Ivanov, A. Cerneavschi, J. Rodriguez, A. Cirea, A. Cornet, J. Morante, *Thin solid films* 479, 38 **(2005)**.

[155] Z.W. Chen, J.K.L. Lai, C.H. Shek, *Phys. Review B* 70, 165314 **(2004)**.

[156] Y. Chen, C.L. Zhu, G. Xiao, *Nanotechnology* 17, 4537 **(2006)**.

[157] V.V. Sysoev, K. Bradly, B.K. Button, K. Wepsie, S. Dmitriev, A. Kolmakov *Nano Lett.* 6, 1584 **(2006)**.

[158] P.Feng, T.H. Wang *Appl. Phys. Lett.* 87, 213111 **(2005)**.

[159] H. Ogawa, M. Nishikawa, A. Abe, *J. Appl. Phys.* 53, 4448 **(1982)**.

[160] H.S.Yang, D.P. Norton, S.J. Pearto, F. Ren, *Appl. Phys. Lett*. 87, 212106 **(2005)**.

[161] M.W. Allen, M.M. Alkaisi, S. M. Durbin, *Appl. Phys. Lett*. 89, 103520 **(2006)**.

[162] C. Li, D. Zhang, S. Han, X. Liu, T. Tang, C. Zhou, *Adv. Mater.* 15,143 **(2003)**.

[163] A. Rothschild, Y. Komem, *J. Appl. Phys.* 95, 6374 **(2004)**.

Part 3

Properties of field effect transistors and heterojunction light emitting diodes based on metal oxide nanorods*

Summary

This part of the thesis contains studies on electrical properties and hydrogen-sensing characteristics of field effect transistors (FETs) based on nanorods of ZnO and $WO_{2.72}$. Electroluminescence and rectifying properties of heterojunction light emitting diodes (LEDs) based on ZnO nanorods have also been investigated.

Top-gated field effect transistors (FETs) using Au-gap (5 μm) electrodes on glass substrate and SiO_2/Si as gate have been fabricated with undoped and doped nanorods of ZnO as well as with $WO_{2.72}$ nanorods as active semiconductor elements. The I-V characteristics at different gate voltages show that the nanorods are n-type semiconductors and the derived transfer characteristics show that the FET devices function in the depletion mode. Al-doping (3 at%) enhances the carrier mobility of ZnO nanorods to 128.6 cm^2/ V.s as against to 0.009 cm^2/ V.s estimated in the case of the undoped nanorods. Doping with Cd and Mg (3 at%) as well as N (~1 at%) similarly increases the mobility although to a smaller extent. The Cd-doped ZnO nanorods exhibit the high sensitivity (20) for 1000 ppm of hydrogen. Application of gate voltage decreases

* A paper based on these studies has appeared in Nanotechnology (2008) and another has been communicated to J. Nanosci. Nanotech.

the response and recovery times of the nanorod sensors. FETs based on $WO_{2.72}$ nanorods also show the depletion mode type characteristics and a carrier mobility of 8.38 $cm^2/V.s$ is obtained. The $WO_{2.72}$ based FETs exhibit good sensitivity (~10) for 1000 ppm hydrogen.

n-ZnO NR/p-Si and n-ZnO NR/p-PEDOT/PSS heterojunction light emitting diodes have been fabricated with ZnO nanorods (NRs) grown by a low-temperature method as well as by employing pulsed laser deposition (PLD). The low-temp method involves growth of the ZnO nanorods by the reaction of water with zinc metal. The I-V characteristics of the heterojunctions show good rectifying diode characteristics. Electroluminescence (EL) spectra of the nanorods show an emission band around 390 nm and defect-related bands in the 400-550 nm region. Room-temperature electroluminescence is detected under forward bias for both the heterostructures. With the low-temperature grown nanorods, defect-related bands in the 400-550 nm range are more intense in the EL spectra whereas with the PLD grown nanorods, only the 390 nm band is prominent.

3.1 Introduction

3.1.1 About FETs

A transistor is a three-terminal electronic device composed of a layer of semiconductor materials, which regulates current or voltage flow and acts as a switch or gate for an electronic circuit. In 1947, William Shockley, John Bardeen and Walter Brattain, working at Bell Telephone Laboratories, were trying to understand the nature of the electrons at the interface between a metal and a semiconductor. They realized that by making two point contacts very close to one another, they could make a three terminal device, the first "point contact" transistor [1]. Modern transistors are divided into two main categories: bipolar junction transistor (BJTs) and field effect transistors (FETs). Applying current in BJTs and voltage in FETs between the input and common terminals increases the conductivity between the common and output terminals, thereby controlling current flow between them. The characteristics of a transistor depend on its type.

Bipolar transistors are so named because they conduct by using both majority and minority carriers. The three terminals of the BJT are named emitter, base and collector. Two p-n junctions exist inside a BJT: the base/emitter junction and base/collector junction. The BJT is useful in amplifiers because the currents at the emitter and collector are controllable by the relatively small base current. By controlling the number of electrons that can leave the base, the number of electrons entering the collector can be controlled. The field-effect transistor (FET), sometimes called a unipolar transistor, uses either electrons (in n-channel FET) or holes (in p-channel FET) for conduction. The four

terminals of the FET are named source, gate, drain, and body (substrate). Most commonly used FETs are of three types.

(a) The **MOSFET** (Metal–Oxide–Semiconductor Field-Effect Transistor) utilizes an insulator (typically SiO_2) between the gate and the body .

(b) The **JFET** (Junction Field-Effect Transistor) uses a reverse biased p-n junction to separate the gate from the body.

(c) The **MESFET** (Metal–Semiconductor Field-Effect Transistor) substitutes the p-n junction of the JFET with a Schottky barrier; used in GaAs and other III-V semiconductor materials.

Figure 3.1.1 shows a schematic diagram of an n-channel metal-oxide semiconductor field effect transistor (MOSFET).

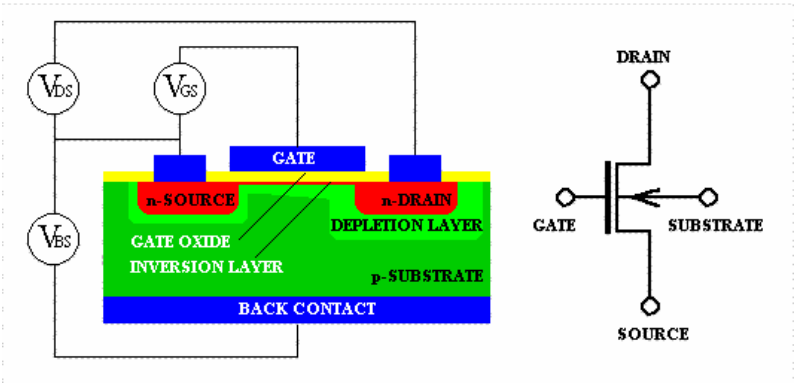

Figure 3.1.1: Cross-section and circuit symbol of an *n*-channel Metal-Oxide-Semiconductor-Field-Effect-Transistor (MOSFET) [2].

3.1.2 About LEDs

A Light Emitting Diode is a semiconductor device that emits light when it is connected to forward bias of the p-n junction. It consists of an n-type (electron majority) and p-type (hole majority) semiconductor materials, which form the p-n junction. Figure 3.1.2 shows a schematic diagram of p-n junction with a forward bias. Upon applying voltage to the p-n junction through respective electrodes, a positive charge (hole) from anode recombines with a negative charge (electron) from cathode in the junction and falls into the lower energy state and emits light in the form of photon. This process is called electroluminescence {Figure 3.1.3 (a)}. Hence, electroluminescence is the result of radiatve recombination of electrons and holes in a material (usually a semiconductor). There is another way of exciting a chemical compound or a substance into a higher electronic energy level by photoluminescence {Figure 3.1.3 (b)}, in which light is absorbed by the substance, which excites an electron into the higher electronic energy level and then radiates light when it falls back to the lower energy state. The wavelength of light coming out from the LED depends on the material being used and their band gap energy.

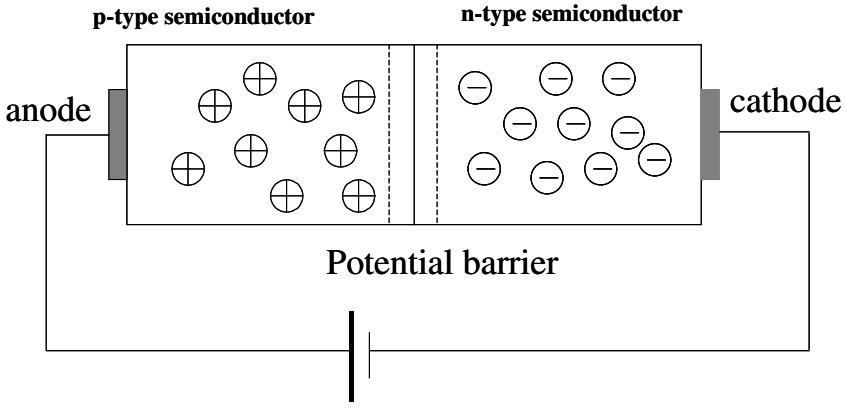

Figure 3.1.2: Schematic diagram of a LED.

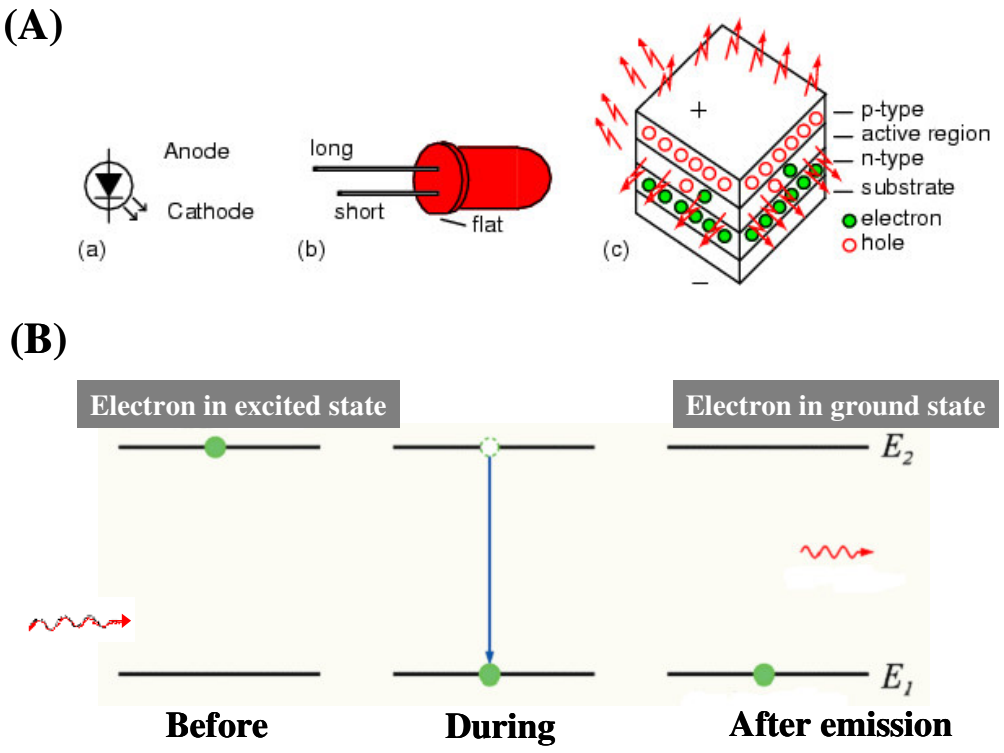

Figure 3.1.3: Schematic diagram of the (A) electroluminescence and (B) Photoluminescence [3].

Starting early in the twentieth century, light emission from SiC was first observed by Captain Henry Joseph Round [4]. Round reported that a yellow light was produced when a current was passed through a silicon carbide detector [5]. B. Gudden and R.W. Pohl conducted experiments in Germany in the late 1920s with phosphors made from zinc sulfide doped with copper (ZnS:Cu) [6]. Infrared (870-980 nm) LEDs and lasers based on GaAs were first reported in 1962 by groups working at RCA, GE, IBM and MIT (Hall *et al*., 1962; Nathan *et al*., 1962; Pankove and Berkeyheiser, 1962; Pankove and Massoulie, 1962; Quist *et al*., 1962). The first generation of bright LED (red, yellow and green) was produced in the mid 1980. A major breakthrough in LED's history was fabrication of blue LEDs using GaN in the early 1990, which paved the way to create virtually any color of

light. To date, white light is produced by mounting red, green, blue LEDs on single chip or by coating blue LED chip with fluorescent phosphors.

As it has been mentioned earlier, to get light emission from material or substance electron has to be excited into higher energy states to make an electron-hole pair (exciton) either by photon of light or by voltage. In metal, there is no possibility of creating exciton since it has no energy gap in between conduction and valence band. So they are used as metallic contacts to the devices and as an interconnect in the electronic circuits. On the other hand, both semiconductor and insulator have certain energy gap; can be used to make opto-electronic devices. But insulator has been in use for insulating or non-conducting material for different applications due its large band gap until 1970s. A major breakthrough in polymer field was the discovery of the increase of electrical conductivity of the polymer polyacetylene over some orders of magnitude upon chemical doping by iodine ion by A. Heeger and co-workers. After this, the unique properties of polymers have been employed for the fabrication of different electronic devices such as LED, FET and solar cell to make it thin, flexible, lightweight and low cost.

3.2 Scope of the present investigations

Semiconducting metal oxide nanowires have attracted increasing attention due to their optoelectronic properties important in device applications [7-9]. Among them, ZnO nanostructures have secured popularity due to their non-toxic and low cost, suitable optical band gap and electrical characteristics besides being simple to prepare at low costs [10-12].

3.2.1 Electrical and hydrogen-sensing characteristics of FETs based on nanorods of ZnO and $WO_{2.72}$

There have been recent reports on field effect transistors (FETs) based on ZnO nanostructures using different electrode configurations and gate dielectrics [13-17]. Single crystalline ZnO nanowires with a circular cross section and omega-shaped gate FET have been utilized to fabricate nanowire devices by bottom gate configuration [13, 14]. ZnO nanowire FETs using a self-assembled nanodielectric organic gate insulator have been demonstrated [15, 16]. The field effect behavior of nanocomposite FET containing ZnO nanowires dispersed in a polymer matrix of MEH-PPV has been studied [17].

In a previous study in part 2, we presented the electrical and gas-sensing characteristics of single nanowires of $WO_{2.72}$ and ZnO using conducting AFM measurements [18]. In the present investigation, we have deposited the nanorods between Au paired electrodes by dielectrophoresis for FET fabrication. We have fabricated FETs using a simple top-gate approach with doped and undoped ZnO nanorods. The dopants employed are Mg, Cd and Al (all ~3-4 at%) and nitrogen (~1 at%). Besides obtaining the electrical characteristics, we have studied the hydrogen sensing characteristics of the FETs based on ZnO nanorods. FETs of $WO_{2.72}$ nanorods prepared by solvothermal synthesis have also examined for H_2-sensing characteristics at room temperature.

3.2.2 Electroluminescence and rectifying properties of heterojunction LEDs based on ZnO nanorods

ZnO has emerged to become one of the prime materials for use in different optical devices because of its wide band gap and large exciton binding energy [9, 19-21]. Thus, light emitting diodes (LEDs) based on ZnO p-n junctions have been of much interest for

optoelectronic applications [22-24], and p-n heterojunctions based on thin films of ZnO, have been deposited on p-type materials such as Si [25-30], p-AlGaN [31], p-GaN [32], $SrCuO_2$ [33], NiO [34]. Also, p-type polymers have been employed to fabricate p-n heterojunctions on ITO substrates [35-38]. Vertical p-n junction diodes based on n-ZnO/p-pentacene have been fabricated on ITO coated glass substrates [35]. Konenkamp *et al.* have reported ZnO nanowire heterojunctions prepared on ITO substrate by the electrodeposition technique [36-38]. We have constructed electrically-driven light-emitting devices employing p-n heterojunctions based on ZnO nanorods (NRs) prepared by two methods and studied the electrical, room-temperature photoluminescence (PL) and electroluminescence (EL).

Since Si has considerable merit in making the driving voltage of LEDs lower and the cost of the device less expensive compared to ITO, we have employed p-Si (111) substrates with ZnO nanorods grown by a low-temperature procedure wherein Zn metal was converted to ZnO nanorods by reaction with water. We have also employed pulsed laser deposition (PLD) to obtain the nanorods on n-Si (100) substrates. For the low-temperature grown ZnO nanorods, the Si substrate acts as the p-type semiconductor for the hole injection. For the growth of ZnO nanorods by PLD, we have used the Au layer on n-Si (100), which acts as catalyst. Since at the interface of the PLD grown ZnO nanorods and n-Si (100), there is an Au layer, we have used a strongly p-doped layer of PEDOT/PSS (poly (3,4-ethylene-dioxythiophene)/poly (styrenesulfonate)) as the hole injector on top of the nanorod layer.

3.3 Experimental and related aspects

3.3.1 Synthesis of ZnO and $WO_{2.72}$ nanorods

Undoped and doped ZnO nanorods and $WO_{2.72}$ nanorods were synthesized by solvothermal synthesis for the FET fabrication. ZnO nanorods have been grown on Si substrates by a simple low-temperature method and also by PLD, for the fabrication of the n-ZnO NR/p-Si and n-ZnO NR/p-PEDOT/PSS heterojunction devices.

(a) Solvothermal synthesis of nanorods

ZnO nanorods were synthesized by the solvothermal synthesis [39]. 600 mg of zinc acetate (Qualigens, 99%) was dissolved in 40 ml of water and ethanol mixture (1:1 ratio). The mixture of the above solution and 20:1 molar ratio of NaOH and Zn^{2+} were taken in a Teflon-lined autoclave. The solution mixture was pretreated under an ultrasonic water bath for 20-40 min. The solvothermal synthesis was conducted at 200°C for 24h. After the reaction, the white products were washed with deionized water and alcohol and dried at 60°C for 24h. For Cd, Al, Mg doped ZnO nanorods, 3 % (molar ratio) of cadmium acetate (Rolex, 98.5%), aluminum nitrate (Merck, 95%) and magnesium nitrate (Ranbaxy, 99%) were added to the above zinc acetate solution and solvothermal synthesis were carried out at 230°C for 24h. N-doped (~1%) ZnO nanorods were prepared by following the procedure reported elsewhere [40]. Tungsten oxide ($WO_{2.72}$) nanorods were prepared by solvothermal synthesis [41]. 1 g of WCl_6 was taken in a 25 ml autoclave filled with ethanol up to 90% of its volume. Solvothermal synthesis was carried out at 200°C for 24h. The product obtained by centrifugation was washed with ethanol.

(b) Synthesis of ZnO nanorods by a low-temperature method and by pulsed laser deposition (PLD)

ZnO nanorod forests as well as islands were grown on heavily p-doped Si (111) substrates by a simple, low-temperature procedure, developed in this laboratory [42]. For this purpose, Zn metal (~100 nm thick) was deposited on p-Si (111) substrates using a physical vapor deposition system. The Zn-coated Si substrates were kept in a vial containing 20 ml of double distilled water (pH =6.5). The reaction with double distilled water was carried out at 25°C for 72h. At 50 and 75°C, the reaction mixture was kept for 24h. After the reaction, the substrates were dried and heated at 350°C for 4h in air.

ZnO nanorods were also grown on Au-coated Si (100) substrates by high pressure PLD. A KrF excimer laser with a repetition rate of 10 Hz was used for ablating the ZnO target prepared using a standard sol-gel route. The pellets were pressed and sintered at 1000°C for 4h in air before ablation. A 30 nm thick of gold was coated on Si (100) substrates by using a sputtering system. The PLD chamber was evacuated by a turbo molecular pump yielding typical base pressure of ~1 $\times 10^{-6}$ Torr. The output of the KrF excimer laser (Lambda-physik) was focused on the rotating target with the incident laser energy of 250 mJ. The substrates were arranged off-axis and situated at a target to substrate distance of 5 cm. All samples were grown in a low background pressure of oxygen (> 99.9 % purity, p (O_2) = 2×10^{-1} bar), flow rate of 20 sccm and at different substrate temperature. Depositions run typically involved 108, 00 pulses for 1h. After each deposition, the samples were kept for 3h under the same O_2 partial pressure and growth temperature as during the deposition before cooling down to room temperature. A schematic diagram of the PLD set-up is shown in figure 3.3.1.

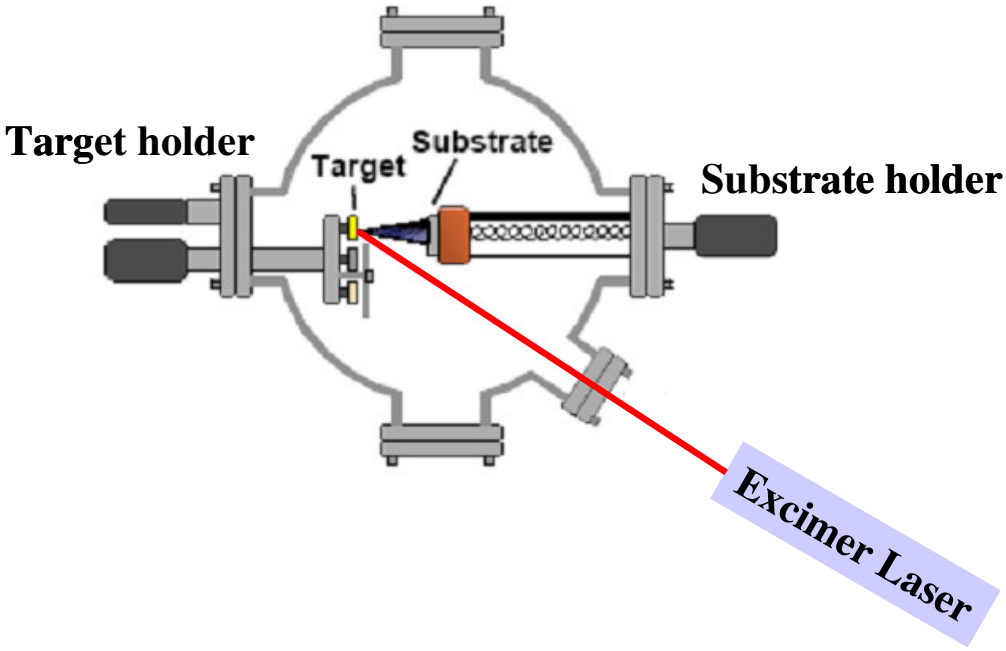

Figure 3.3.1: Schematic diagram of the PLD set-up.

3.3.2 Characterization techniques

The as-grown ZnO nanorods were characterized with a field emission scanning electron microscope (FESEM) using a FEI NOVA NANOSEM 600, as well as a LEICA S440i instrument, X-ray diffraction (SEIFERT, XRD 3000TT), micro-Raman spectroscopy (LABRAMAN-HR) using a He-Ne laser (632.81 nm) in the back scattering geometry. The composition of the nanorods was analysed with energy dispersive X-ray spectrometer (EDAX) attached to the FESEM. UV-vis absorption spectra were recorded with a Perkin-Elmer Lamda 900 UV/vis/NIR spectrometer. PL and EL spectra were recorded with a Perkin-Elmer model LS55 and a Horiba Jobin Yvon iHR-320 luminescence spectrometer. A Keithley-236 multimeter was used to measure the I-V characteristics of the devices. All the measurements were performed at room temperature.

3.3.3 Fabrication of FETs and gas-sensing measurements

ZnO nanorods synthesized by solvothermal method were well dispersed in 10 ml ethanol by sonication for 10 min to get 0.01 M solution. They were then assembled across pre-patterned electrodes on glass substrates employing the dielectrophoresis (DEP) technique [43, 44]. Dielectrophoresis is a technique where a non-uniform electric field is used to selectively move neutral particles in a liquid dielectric medium. The dielectrophoretic force (F_{DEP}), generated due to the induced dipole moment is given by,

$$F_{DEP}(t) = [p(t).\nabla] E(t) \qquad (3.1)$$

The pre-patterned source and drain electrodes with a gap of 5 μm were made by evaporating Au (~50 nm thick) on glass substrates. In order to form an assembly of nanorods, 100 μl ethanol solution containing dispersed ZnO nanorods was dropped onto the gap between the electrodes using a micropipette. An A.C. voltage signal (5 V_{pp} at 1 MHz) was applied between the electrodes; this signal condition has been found to be suitable in optimizing the alignment of ZnO nanorods [45]. Following a similar procedure, $WO_{2.72}$ nanorods were deposited between the Au electodes. The A.C signal generates an alternating electrostatic force on the nanorods in the solution. By DEP force effect, the nanorods tend to align to the electrodes.

For the top gate configuration, we have used highly doped Si substrates, which were thermally oxidized to have ~300 nm thick SiO_2 layer. The Si substrates were subjected to the RCA cleaning procedure, prior to oxidation [46]. A schematic diagram for the fabrication of the field effect transistors is shown in figure 3.3.2.

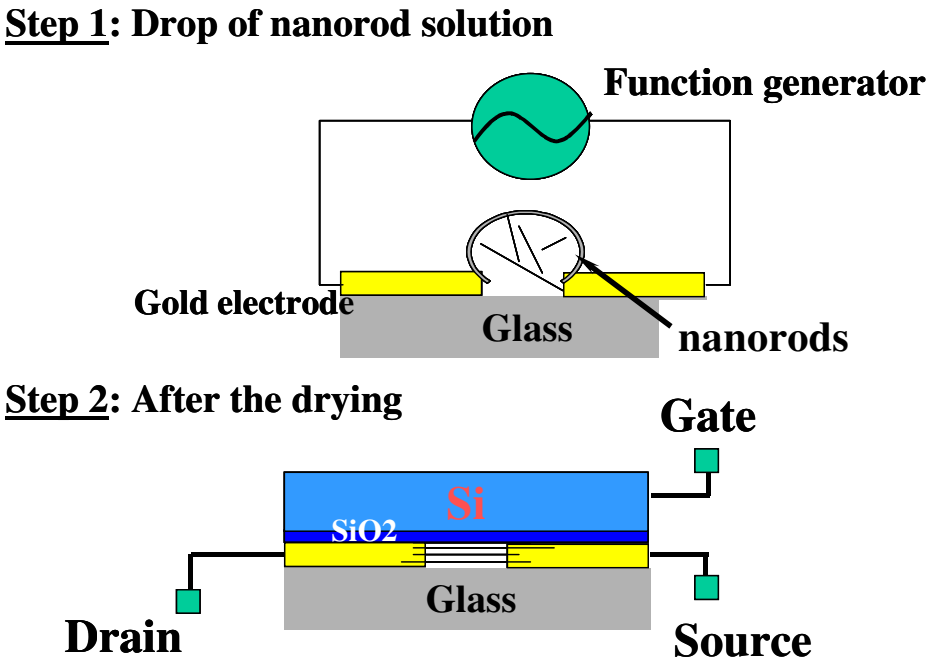

Figure.3.3.2: Schematic diagram of the FET fabrication procedure.

H_2-sensing properties were measured using a home-built computer-controlled characterization system consisting of a test chamber, a Keithley multimeter-2700, a Keithley electrometer-6517A, mass flow controllers and a data acquisition system. By monitoring the output voltage across the device, the resistance of the nanostructures in dry air or in H_2 can be measured. The sensitivity, S, was determined as the ratio R_{air}/R_{H2}, where R_{air} is the resistance of the nanostructure in dry air and R_{H2} is the resistance in the presence of H_2. Details of the experimental set-up and gas-sensing measurements are described in part 2.

3.3.4 Fabrication of heterojunction LEDs

We have followed two different procedures for the fabrication of p-n junctions based on the ZnO nanorods. It is known that unintentionally doped ZnO is typically n-type due to oxygen vacancies and/or zinc interstitials [47-49]. Figure 3.3.3 (a) shows a schematic diagram of the n-ZnO NR/p-Si heterojunctions light-emitting device for the nanorods grown by the reaction of Zn metal with water. After the growth of the nanorods

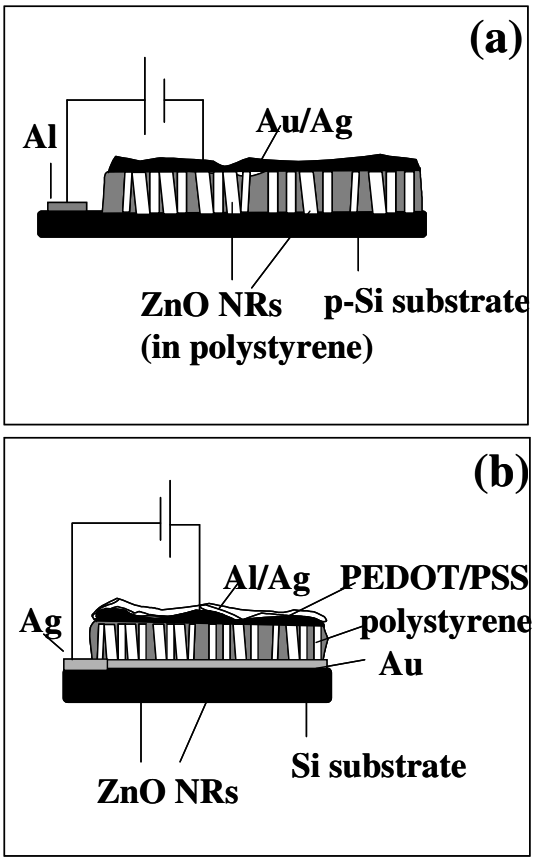

Figure 3.3.3: Schematic diagram of EL devices with (a) n-ZnO NR/p-Si, (b) n-ZnO NR/p-PEDOT/PSS heterojunctions.

on p-Si (111) substrate, the free space between the individual nanorods were filled with high molecular weight polymers, such as polystyrene by spin coating with a spin speed of 3000 rpm. Polystyrene of molecular weight 1.7×10^6 g/mol in a concentration of 50 gl^{-1} dissolved in toluene was used. The films were UV cured for 1h and soaked in toluene for

10 min and rinsed by pipette with toluene to remove the excess polystyrene from the nanorod surface. Finally a layer of Al was deposited on the p-Si to form ohmic contact and contacts were taken from the top of the nanorods by depositing Au/Ag layers. In figure 3.3.3 (b), we show the schematic diagram of the p-n junction fabricated from the PLD grown ZnO nanorods. After coating a thin layer of polystyrene as mentioned above, a strongly p-doped layer of PEDOT/PSS was deposited which serve as a hole injecting contact. Finally an Al/Ag layer was deposited on PEDOT/PSS for the top contact and bottom contact was taken from the gold layer by depositing Ag.

3.4 Results and discussion

3.4.1 Electrical and hydrogen-sensing characteristics of FETs based on nanorods of ZnO and $WO_{2.72}$

Figure 3.4.1 shows FESEM images of undoped and doped ZnO nanorods. The undoped nanorods have diameters in the 30-100 nm range, with lengths 5-10 μm {Figure 3.4.1(a)}. The XRD pattern showed that the rods possess the wurtzite structure (a=3.25 Å and c=5.2 Å, JCPDS no: 36-1451) {Figure 3.4.2}. Raman bands of the ZnO nanorods were found at 328, 378 and 438 cm^{-1} in agreement with the literature [50]. In case of ZnO:N nanorods, we observed four additional bands at 275, 507, 579 and 642 cm^{-1}, which correspond to the silent modes arising from the breakdown of the translational crystal symmetry induced by defect [8, 40]. For ZnO:Cd nanorods, the diameter is in the range of 20-60 nm and the length, 5-10 μm {Figure 3.4.1 (b)}. The diameter of ZnO:Al nanorods {Figure 3.4.1(c)} varies between 10-50 nm while that of ZnO:Mg in the 30-80 nm range {Figure 3.4.1(d)}. ZnO:N nanorods possess diameters in the 70-200 nm range with lengths between 5-10 μm {Figure 3.4.1(e)}. The extent of doping was confirmed by EDS

analysis and the doping was between 3 and 4 at% for Cd, Al, Mg and ~ 1 at% for N-doped ZnO nanorods {see Figure 3.4.1(f)}.

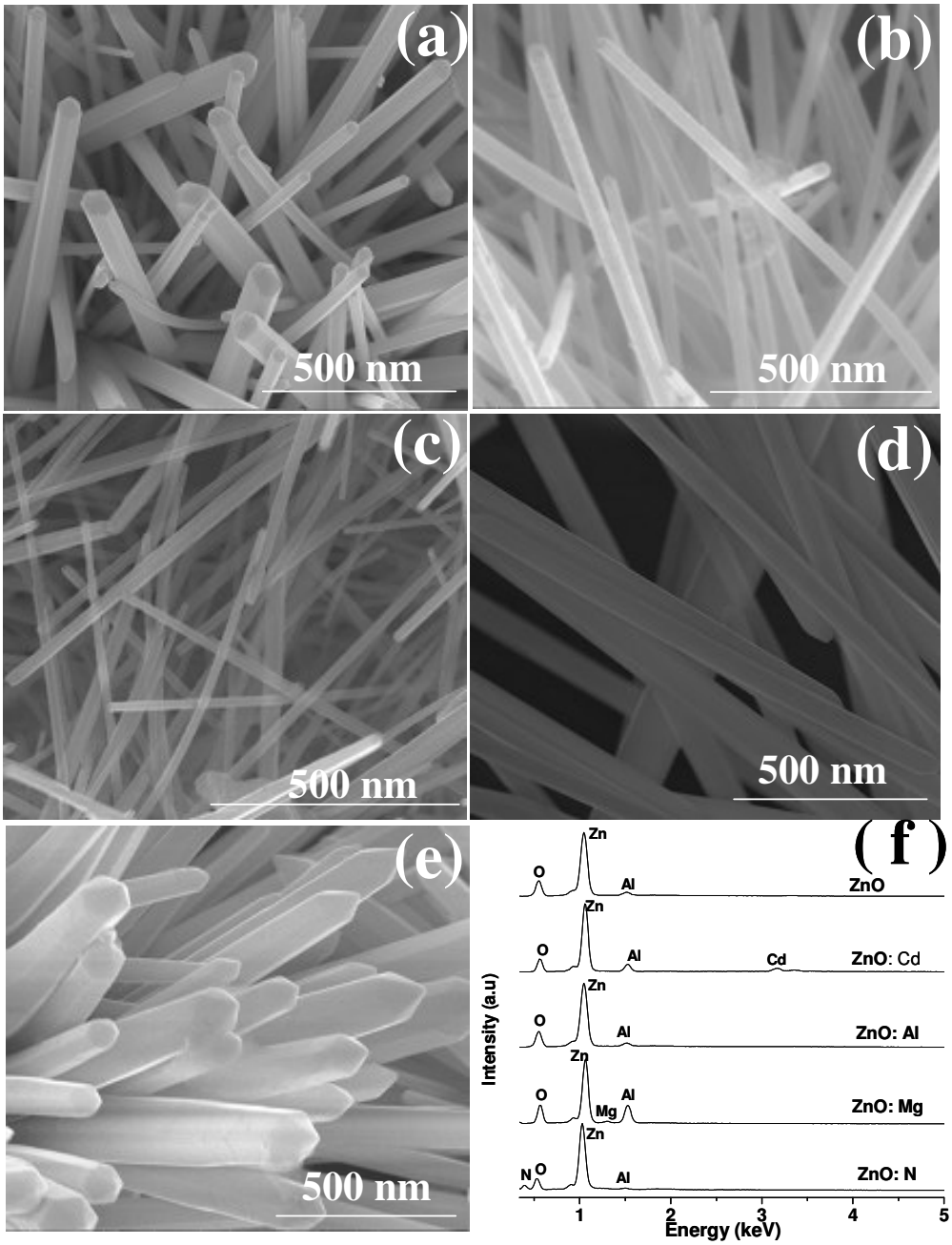

Figure 3.4.1: FESEM image of (a) undoped ZnO nanorods, (b) ZnO:Cd nanorods, (c) ZnO:Al nanorods, (d) ZnO:Mg nanorods, (e) ZnO:N nanorods and (f) EDS spectra of undoped and doped ZnO.

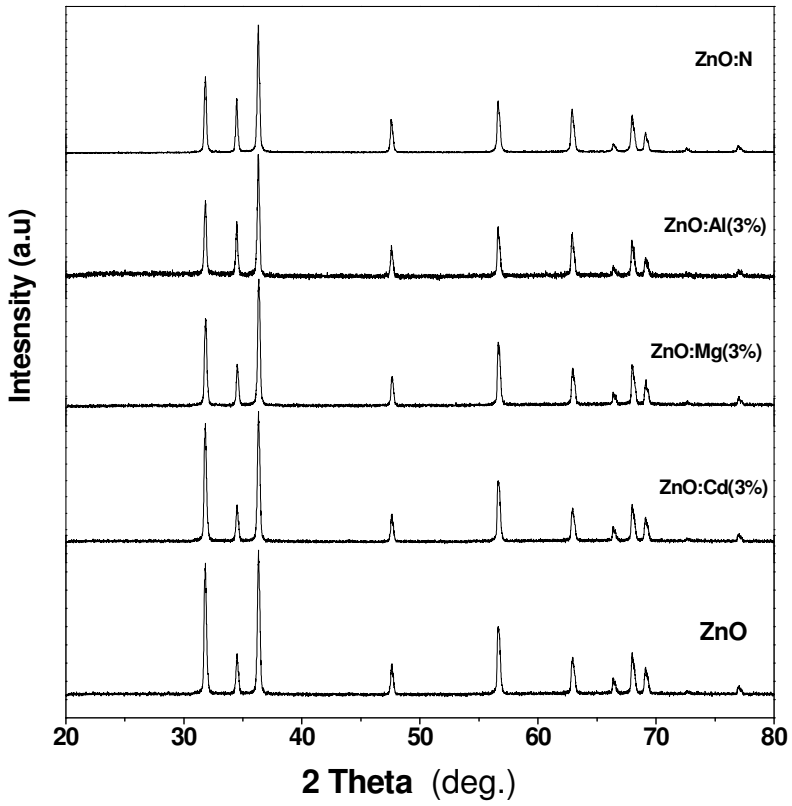

Figure 3.4.2: XRD patterns of ZnO, ZnO:Cd, ZnO:Mg, ZnO:Al and ZnO:N nanorods.

Figure 3.4.3 shows a FESEM image of ZnO nanorods assembled across the source and drain electrodes. The inset shows a low magnification image of the gap electrodes. The transistor characteristics of the top-gate ZnO nanorod FET were obtained as shown in figure 3.4.4. Figure 3.4.4 (a) is the source-drain current versus voltage (I_d - V_{ds}) curve at different gate voltages in the range, –50 to + 50 V. The inset of Figure 3.4.4 (a) is source-drain current versus gate voltage (I_d - V_g) at a source-drain voltage of 1 V. Since the current increases with increasing positive gate voltages and decreases with increasing negative gate voltage, this is typical n-type semiconducting behavior. It is also observed that this transistor is a depletion mode device [51, 52]. It may be noted that our N-doped

nanorods are not completely p-type, as expected. This remains still a challenging problem in the literature [53-55].

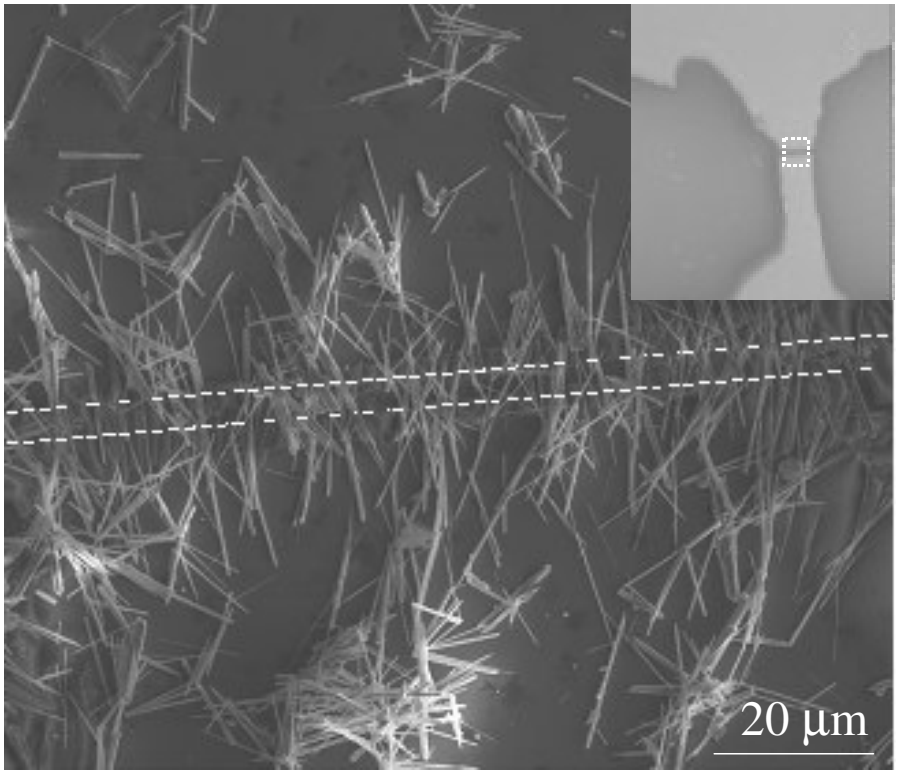

Figure 3.4.3: FESEM image of assembled ZnO nanorods on the patterned gold electrodes on glass substrate with the inset showing a low magnification image of the gap electrodes. The dashed lines are drawn to indicate the gap.

The carrier mobility is calculated by the equation,

$$\mu = (L^2/C_g V_{ds})(dI_{ds}/dV_{gs}) \qquad (3.2)$$

where L is channel length of the nanorod (5 μm), C_g is the total gate capacitance of the device. The gate capacitance was calculated following Dattoli et al [56], $C_g = C_0 \times (W \times L)$. Here C_0 is the capacitance per unit area using a parallel plate model $C_0 = \varepsilon_r \varepsilon_0/d$ and W is the channel width = 150 μm. ε_0 is the vacuum dielectric constant and ε_r is the relative dielectric constant which was chosen to be 2.5 (average of air, 1 and SiO_2, 3.9). Based on

the estimated C_g value and measured device parameters, the carrier mobility (μ) was estimated to be 0.009 cm^2/V.s for ZnO nanorods, which is comparable with the literature values of mobility 0.01-7 cm^2/V.s obtained by the thin film based ZnO FET [57-59].

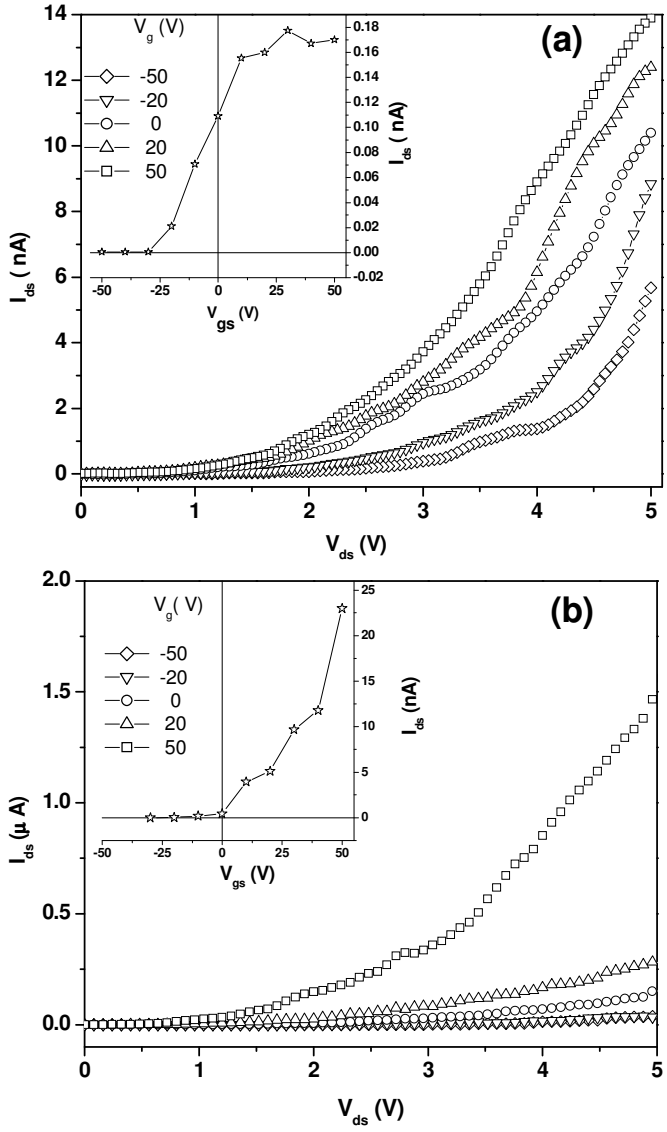

Figure 3.4.4: I_d – V_{ds} characteristics of (a) undoped ZnO, (b) ZnO:Cd nanorods with the insets showing I_d –V_g characteristics. (The lines connecting the data points are only guide to the eye).

In Figure 3.4.4 (b), we show the I_d - V_{ds} curve of ZnO:Cd nanorods at different gate voltages with the inset showing I_d - V_g curve at a source-drain voltage of 1 V. In figure 3.4.5 we have shown I_d – V_{ds} characteristics of ZnO:Mg, ZnO:N and ZnO:Al nanorods with the insets showing I_d –V_g characteristics. Following equation (3.2), the carrier mobility of the ZnO:Cd, ZnO:Mg and ZnO:N nanorods are 1.023, 0.845 and 2.208 cm^2/ V.s respectively. The calculated carrier mobility for the ZnO:Al is 128.6 cm^2/ V.s, which shows that Al doping enhances the conductivity of nanorods more compared to Cd, Mg or N doping. Al doping is reported to give a mobility of 65.6 cm^2/ V.s, by Hall measurements [60, 61].

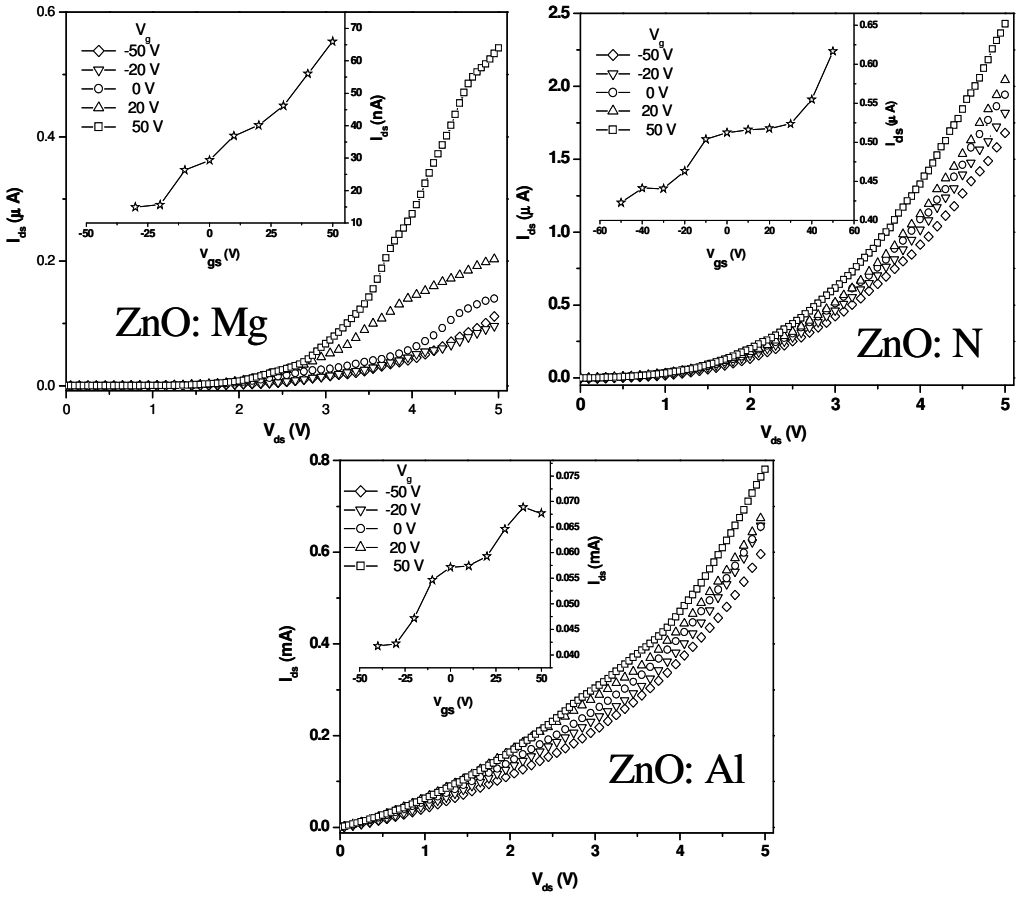

Figure 3.4.5: I_d – V_{ds} characteristics of ZnO:Mg, ZnO:N and ZnO:Al nanorods with the insets showing I_d –V_g characteristics.

We have studied the hydrogen sensing characteristics using the FETs based on undoped and doped ZnO nanorods at V_{ds} = 3 V for V_g = 0 V and 50 V. In figure 3.4.6 (a), we show the hydrogen sensing characteristics at V_g = 0 V at room temperature. The sensitivity of undoped ZnO is 3 for 1000 ppm of H_2 with a response and recovery times of 150 and 178 s respectively. For Al, Mg and N doped ZnO nanorods, a sensitivity of 7, 3 and 6 respectively were obtained for 1000 ppm of H_2. In case of ZnO:Cd nanorods, a maximum sensitivity of 20 is observed but the response and recovery times extend to several minutes. These observations suggest that the electron transfer process is not reaching the saturation during adsorption and desorption at room temperature. H_2-sensing characteristics of undoped and doped ZnO at a gate voltage of 50 V is shown in figure 3.4.6 (b). It is observed that the response and recovery times are lower at V_g =50 V as compared to the values at V_g = 0 V.

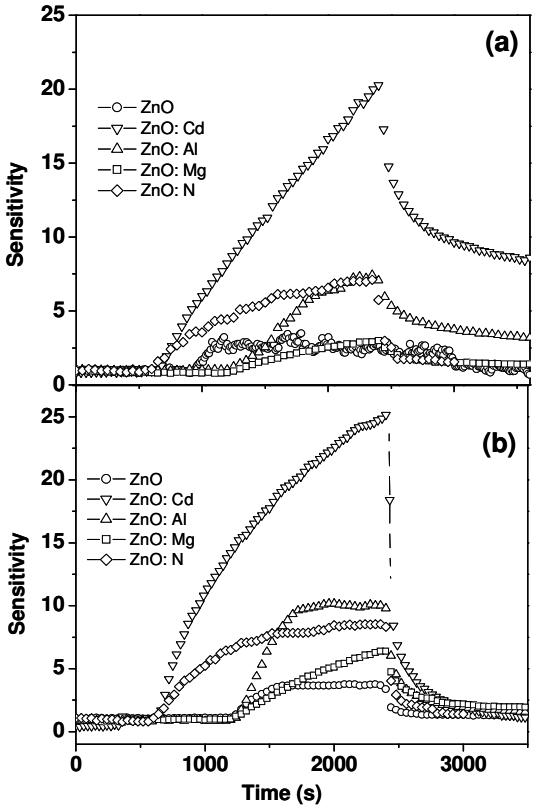

Figure 3.4.6: H_2 sensing characteristics of undoped and doped ZnO nanorods (a) at V_g=0 V and (b) at V_g=50 V.

In figure 3.4.7, we show FESEM images of the $WO_{2.72}$ nanorods FESEM images show that the $WO_{2.72}$ nanorods have diameters in the 5-30 nm range and length in the 100-500 nm range. The XRD pattern showed that the tungsten oxide nanowires possess a monoclinic structure (a=18.33 Å, b=3.78 Å, c=14.03 Å, JCPDS no: 36-101) characteristic of $WO_{2.72}$. Raman bands were observed at 270, 328, 713 and 805 cm^{-1} in agreement with those of monoclinic $WO_{2.72}$ [62].

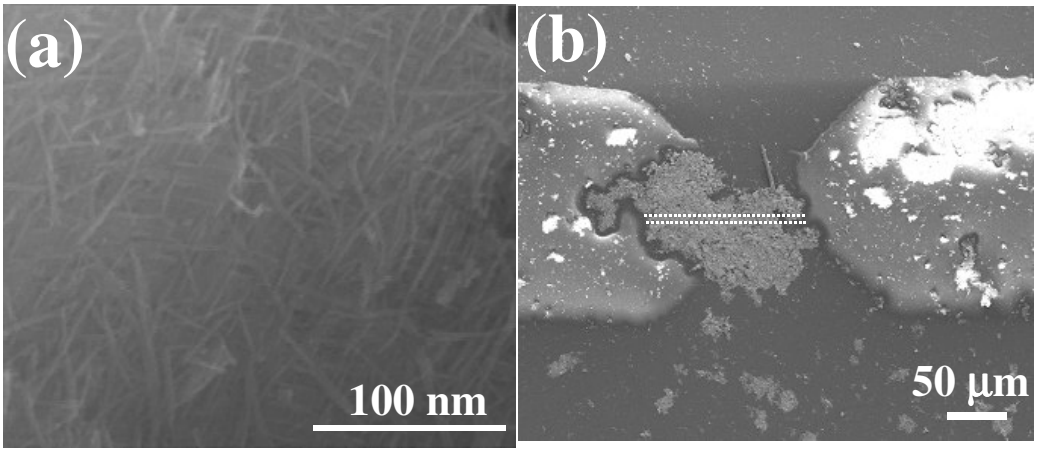

Figure 3.4.7: FESEM images of (a) $WO_{2.72}$ nanorods, (b) $WO_{2.72}$ nanorods on the patterned gold electrodes on glass substrate and the dashed lines are drawn to indicate the gap position.

In figure 3.4.8 (a), we show the $I_d - V_{ds}$ characteristics at different gate voltages in the range from –50 to 50 V. The characteristics showed that the $WO_{2.72}$ nanorods are n-type and the FET device works in the depletion mode. The inset of figure 3.4.8 (a) shows $I_d - V_g$ characteristics at V_{ds}=1 V. By using the slope of the $I_d - V_g$ curve, we find the carrier mobility to be 8.38 cm^2/V.s. Figure 3.4.8 (b) shows the H_2-sensing characteristics of the $WO_{2.72}$ nanorods at a drain-source voltage of 3 V and at V_g=0 and 50 V. At V_g=0 V, the sensitivity is 7 with recovery and response times of 1200 ± 20 s. By applying a gate

voltage of 50 V, the sensitivity is enhanced to 10 with recovery and response times of 770 ± 5 s.

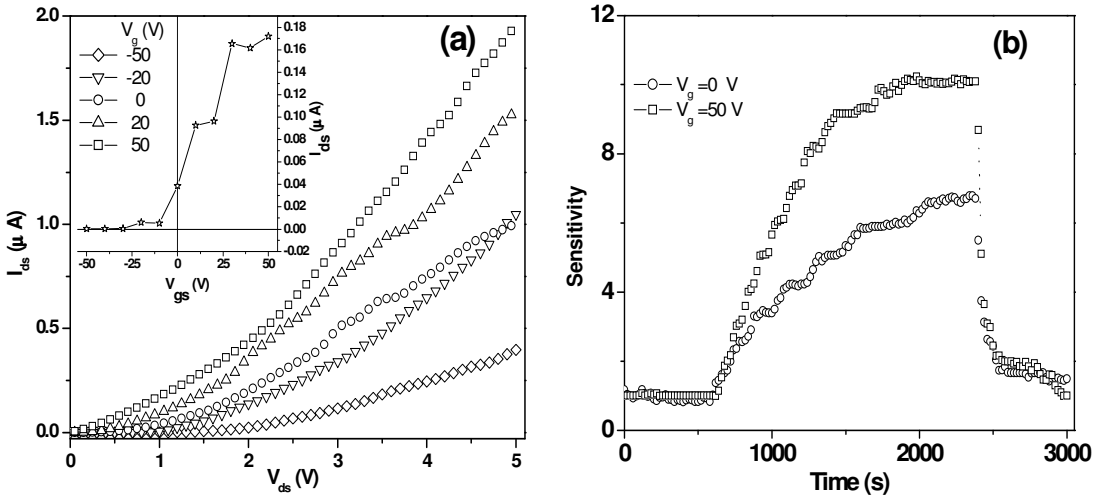

Figure 3.4.8: (a) $I_d - V_{ds}$ characteristics of $WO_{2.72}$ nanorods with the inset showing $I_d - V_g$ characteristics, (b) H_2 sensing characteristics of $WO_{2.72}$ nanorods at V_g=0 V and 50 V.

The mechanism of H_2-sensing using ZnO and $WO_{2.72}$ is based on the adsorption and desorption phenomena on the oxide surface, which is described in chapter 2 [63, 64]. It is widely accepted that upon exposure to reductive gases, chemisorbed oxygen on the semiconductor surface reacts with the reductive gas species and the electrons trapped by oxygen are released into the semiconductor, changing the resistance [65]. From our report on single nanowire sensors [18], a maximum sensitivity of ~10 and 22 were observed for nanorods of ZnO and $WO_{2.72}$ for 1000 ppm of H_2 at room temperature. Hence, the sensitivity (3 and 7) obtained for the multiple ZnO and $WO_{2.72}$ nanorod-based sensors are comparable with the single nanorod H_2 sensors. The contact resistance of the single nanorods of ZnO and $WO_{2.72}$ were ~50 MΩ and 60 KΩ [18], whereas for circuits containing multiple nanorods, the resistances are ~500 MΩ and 5 MΩ (at a bias of 5 V)

respectively. Since our FETs are of depletion mode type, by applying positive gate voltage, electrons in the nanorods become more mobile and excess electrons contribute in the adsorption-desorption mechanism where charge transfer processes involved for sensing H_2. Hence we observe the improvement in recovery and response times by applying higher gate voltage. A comparison of sensitivity for undoped and doped ZnO nanorods and $WO_{2.72}$ nanorods is shown in table 3.4.1.

Nanorods	Sensitivity (At V_g= 0 V)	Sensitivity (At V_g= 50 V)
ZnO	2	4
ZnO:Cd	20	25
ZnO:Mg	3	6
ZnO:N	7	9
ZnO:Al	7	10
$WO_{2.72}$	6	10

Table 3.4.1: Comparison of sensitivity for undoped and doped ZnO nanorods and $WO_{2.72}$ nanorods.

3.4.2 Electroluminescence and rectifying properties of heterojunction LEDs based on ZnO nanorods

In figure 3.4.9, we show FESEM images of the nanorods grown on Si substrates by the low temperature method involving the reaction of Zn metal with water. Figure 3.4.9 (a) shows the FESEM image of the nanorods grown at 25°C. The diameter of the aligned nanorods is in the 50-70 nm range and lengths are in the 100-150 nm range. The FESEM images of the nanorods grown by this method at 50°C and 75°C are shown in figures 3.4.9 (b) and (c) respectively. The diameter of the nanorods grown at 50°C is in the 30-50 nm range and the length varies between 150-200 nm range. At 75 °C, we can observe that the nanorods start growing randomly and form web type of structures. This may be due to the uncontrolled growth of the nanorods at higher temperatures. An island of ZnO nanorods grown by this method is shown in figure 3.4.9 (d).

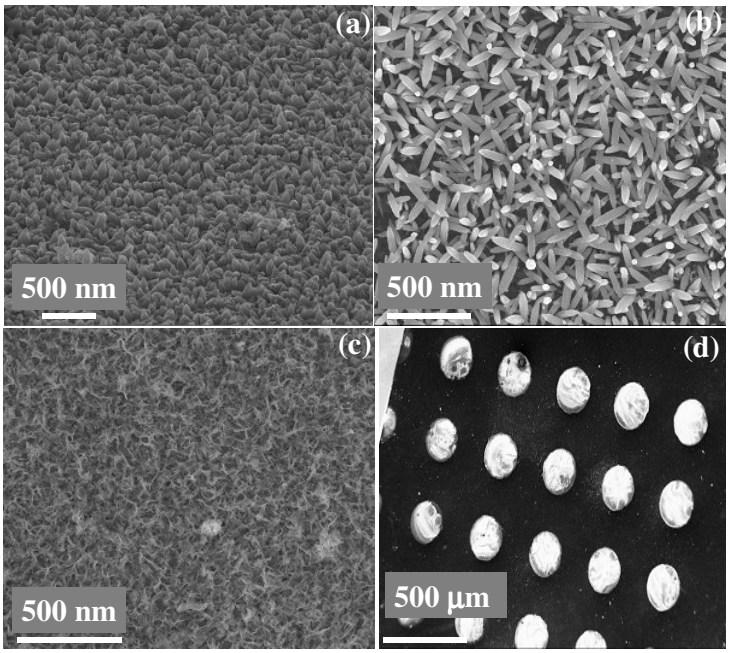

Figure 3.4.9: (a-c) FESEM images of the ZnO nanorods grown by the reaction of Zn metal with water at 25°C, 50°C and 75°C respectively, (d) islands of ZnO nanorods grown on the Si (111) substrate.

Figure 3.4.10 shows the FESEM images of the nanorods grown on sapphire substrate by PLD. Figure 3.4.10 (a) and (b) show the nanorods grown at 600°C, whereas nanorods grown at 700°C are shown in figure 3.4.10 (c) and (d). Figure 3.4.10 (e) and (f) show the nanorods grown at 800°C. The diameters of the nanorods varied between 20-100 nm depending on the growth temperature. Figure 3.4.11 shows the FESEM images of the nanorods grown on Si (100) substrate by PLD. The diameter of the nanorods was in

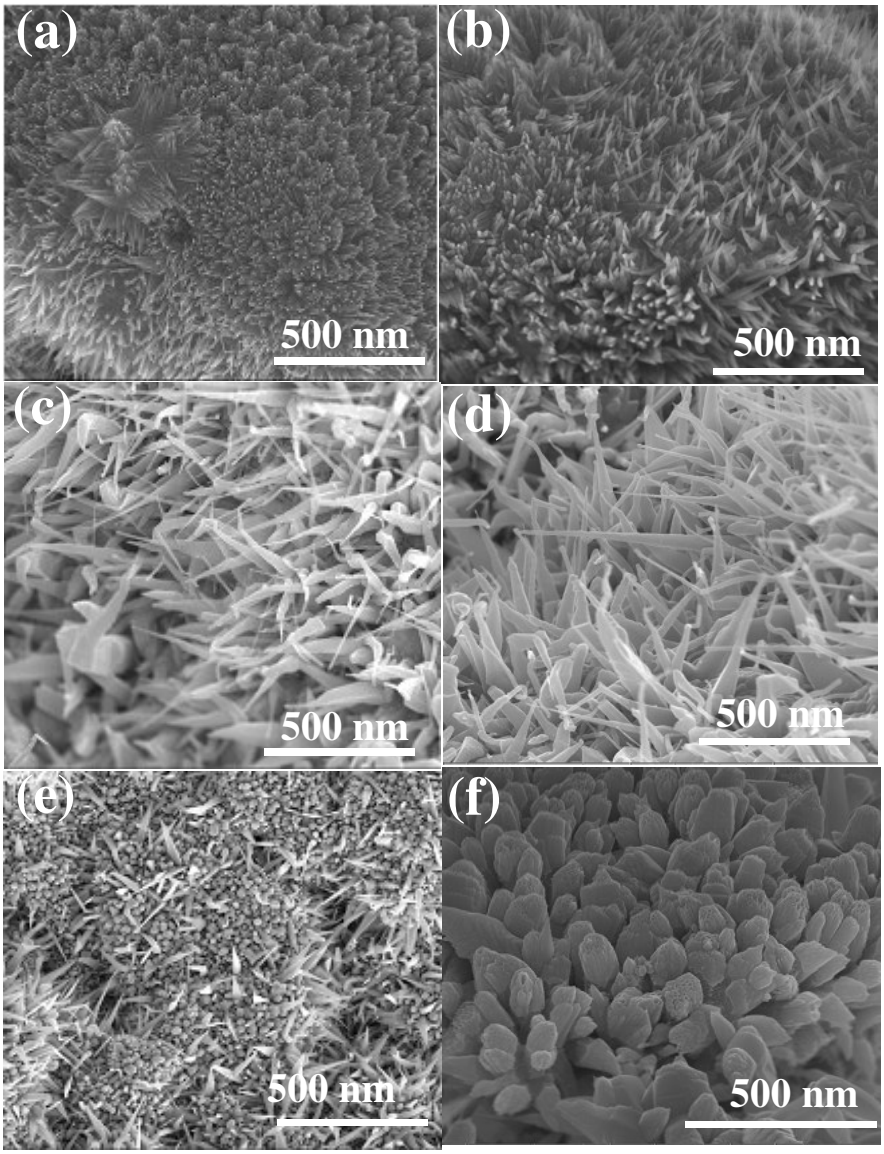

Figure 3.4.10: FESEM images of the ZnO nanorods grown by PLD on saphire substrates at (a, b) 600°C, (c, d) 700°C and (e, f) 800°C respectively.

the 30-70 nm range depending on the substrate temperature which was generally between 600 and 800°C. Figure 3.4.11 (a) shows the nanorods grown at 600°C and the diameter of the nanorods are in the 30-50 nm range and length varies between 100-300 nm. The nanorods grown at 700°C have the diameter in the 40-60 nm range and lengths in the 200-400 nm range as can be seen from figure 3.4.11 (b). Figure 3.4.11 (c) shows FESEM image of the nanorods grown at 800°C and the diameter varies in the 30-70 nm range, with the length of the nanorods in the 200-400 nm range. The XRD patterns of the as-grown ZnO nanorods {Figure 3. 4.12 (a)} obtained by the reaction of Zn metal with water and by PLD method show a strong (002) peak, indicating that the nanorods are

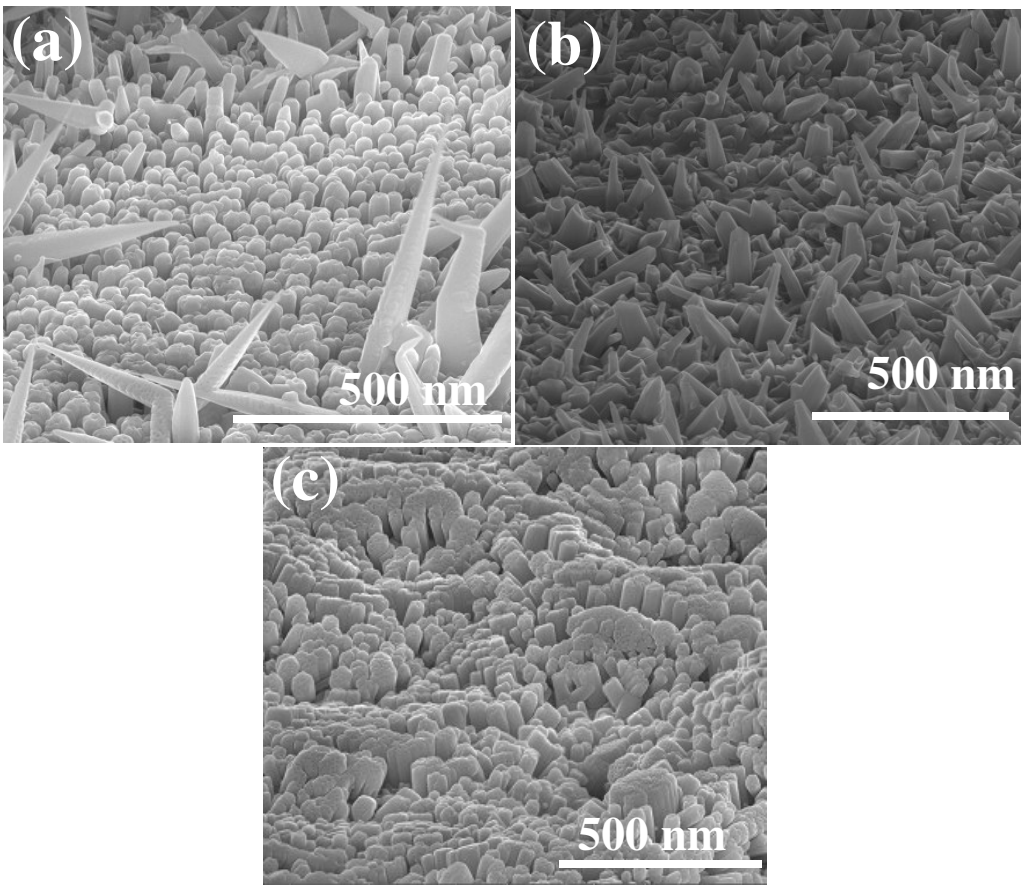

Figure 3.4.11: 45° tilted angle FESEM images of the ZnO nanorods grown by PLD on Si (100) substrates at (a) 600°C, (b) 700°C and (c) 800°C respectively.

oriented preferentially along the c-axis. The XRD patterns of the nanorods could be indexed on the hexagonal wurtzite structure (a=0.3249 nm, c=0.5206 nm, JCPDS card no: 36:1451). Thus, the ZnO nanorods prepared by both the methods have good crystallinity. EDAX analysis confirms the zinc and oxygen are with an atomic ratio of about 1:1.

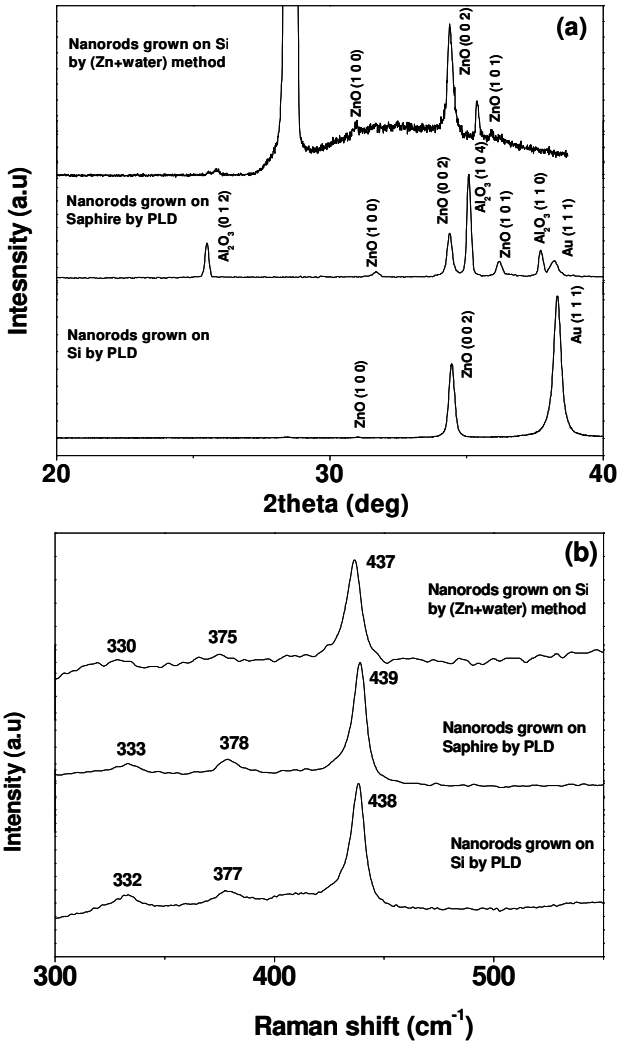

Figure 3.4.12: (a) XRD patterns of the ZnO nanorods prepared by the low-temp method on Si (111) and by PLD on sapphire and on Si (100), (b) Raman spectra of the ZnO nanorods grown by the low-temp method and by PLD.

ZnO nanorods prepared by the reaction of Zn metal with water exhibit Raman bands at 330, 375, 437 cm^{-1} and those prepared by PLD on Si substrate exhibit bands at 332, 377, 438 cm^{-1}, whereas for the nanorods grown on sapphire exhibit Raman bands at 333, 378 and 439 cm^{-1} {Figure 3.4.12 (b)}. The bands near 437 and 377 cm^{-1} attributed to

E_2 (high) mode and A_1 (TO) mode respectively and the band at 332 cm^{-1} could arise from a multiphonon process [50]. For bulk ZnO, the Raman bands are expected at about 330, 379 and 439 cm^{-1} [50, 66]. From the shifts of the Raman bands, we concluded that there is optical phonon confinement by the grains or phonon localization by defects (oxygen deficiencies, zinc excess and surface impurities etc) [66-68]. The shift of the E_2 (high) phonon mode is due to the presence of intrinsic defects in the ZnO nanorods [67, 68]. The UV-absorption spectra of the ZnO nanorods show a strong exciton absorption edge around 372 nm (Figure 3.4.13). Stronger exciton effect is an important characteristic of quantum confinement in nano-semiconductors, the reason being that the carriers are confined in a very small region that makes the electrons and holes move only in a potential well [69].

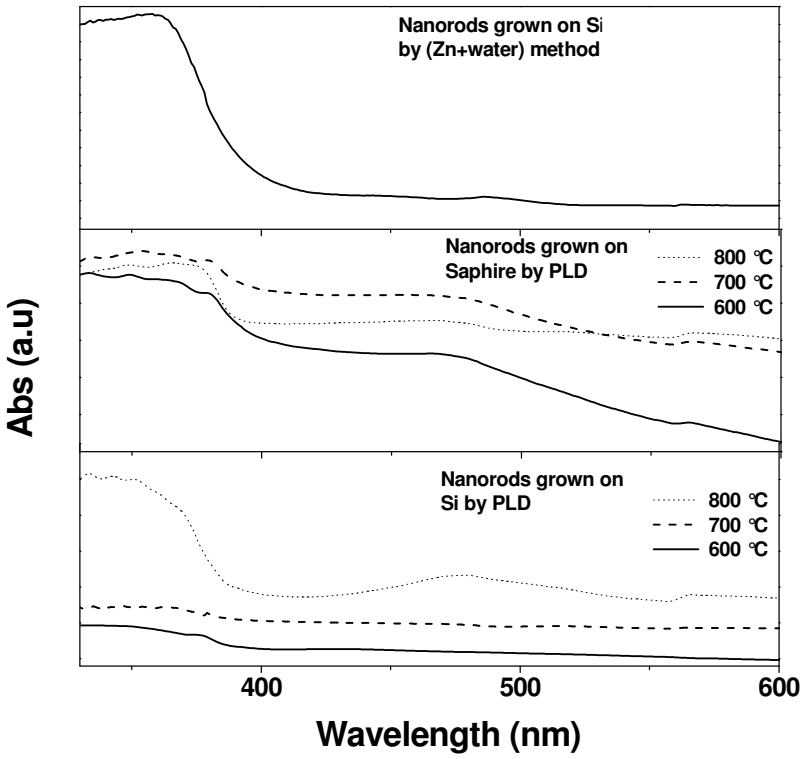

Figure 3.4.13: UV-Vis spectra of the nanorods grown by low temperature method and by PLD.

Photoluminescence spectra of the ZnO nanorods show a UV emission peak at 390 nm and defect related bands in the 400-550 nm regions. UV emission is attributed to band-edge luminescence and the exciton related recombination [70]. ZnO nanorods prepared by the low-temp method show a weak 390 nm band, while the PLD nanorods give an intense 390 nm band. We observe peaks in the 400-530 nm region due to the defect states of the nanorods [40] and these are considered weaker compared to the 390 nm band in the case of the PLD ZnO nanorods (Figure 3.4.14). We observed the oxygen

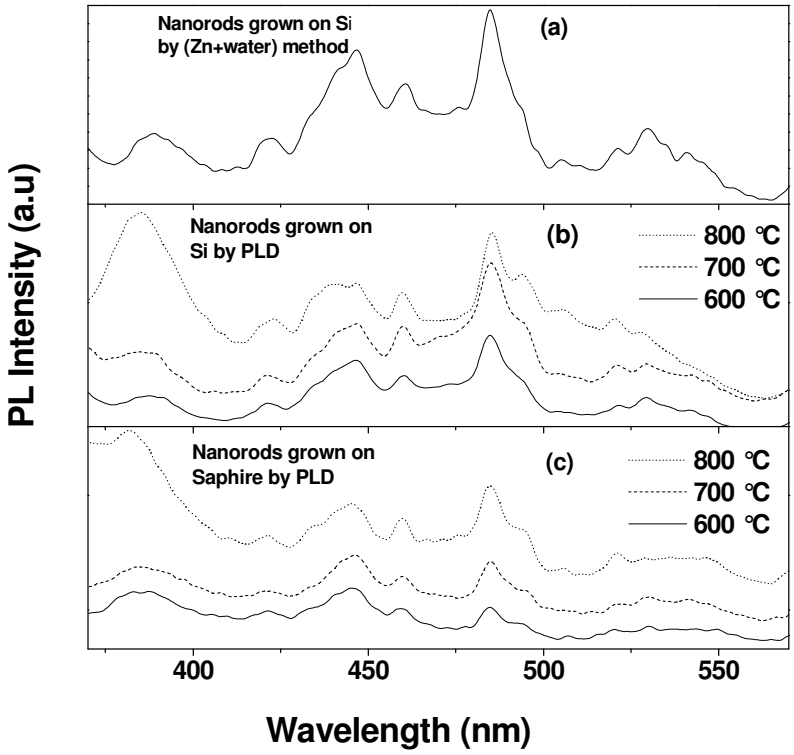

Figure 3.4.14: Photoluminescence spectra of ZnO nanorods grown (a) by the low-temp method, (b) and (c) by PLD.

vacancies and defect related PL bands around 430, 444, 461, 485 and 530 nm for the nanorods grown by both methods, which we had observed in our earlier studies as well

[40]. From theoretical and EPR studies [71, 72], it is known that oxygen vacancies in ZnO can occur in different charge states: the V_{ϕ} state which is neutral relative to the lattice, the singly ionized $V_o^{\bullet}$ state and the $V_o^{\bullet\bullet}$ which did not trap any electron and is doubly positively charged with respect to the lattice. The mechanism responsible for green emission (around ~530 nm band) is recombination of $V_o^{\bullet}$ electrons with the excited holes in the valence band. The bands around ~500 nm can be attributed to the isolated $V_o^{\bullet}$ cenetrs. The possible explanation, why the $V_o^{\bullet}$ complex would cause green emission at a slightly longer wavelength could be that the defect energies lie lower in the band gap than those of the isolated $V_o^{\bullet}$ center [71].

In figure 3.4.15, we show the I-V characteristics of the ohmic contacts between p-Si and Al, ZnO and Ag/Au and the inset shows the contacts of Ag/Al and PEDOT/PSS. Typical I-V curves of the n-ZnO NR/p-Si heterojunctions in linear and semilog form

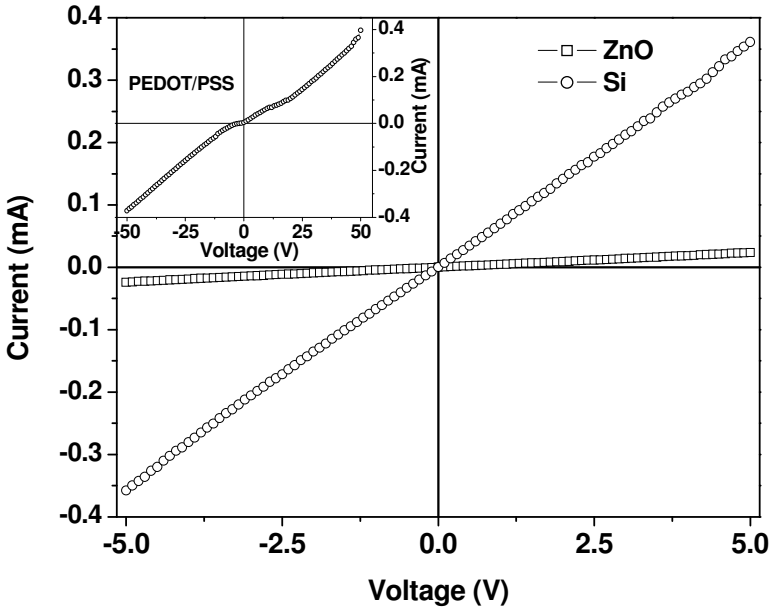

Figure 3.4.15: I-V characteristics of Al contacts on p-Si and Ag/Au contacts on ZnO. The inset shows the Ag/Al contacts on PEDOT/PSS.

made from the nanorods grown by the reaction of Zn metal with water are shown in figure 3.4.16 (a) and (b) respectively. The heterojunctions exhibit good rectification characteristics in the I-V curves. The turn-on voltage of the p-n junction is around 0.7 V under forward bias. The leakage current is only 3.6 μA at a reverse bias of 5 V and the rectification ratio of the forward-to-reverse bias current is 243 at a bias voltage of ±5 V.

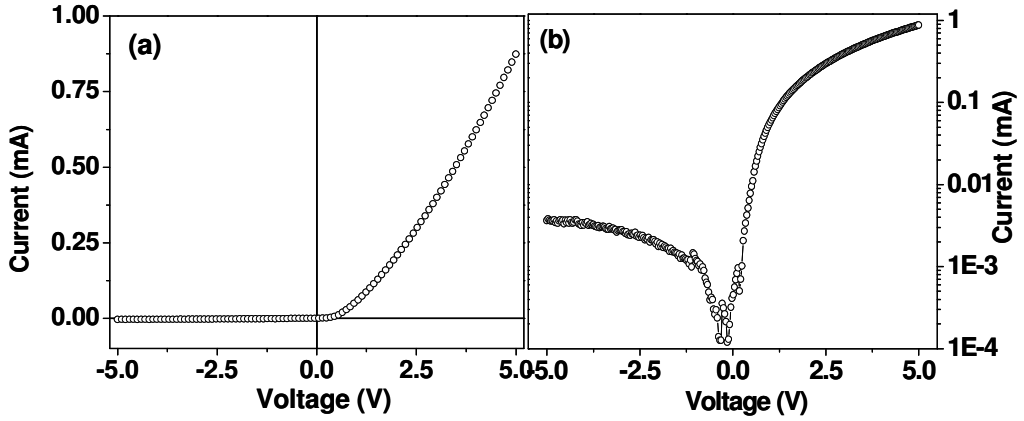

Figure 3.4.16: I-V characteristics of the EL device of n-ZnO NR/p-Si in (a) linear and (b) semilog form.

A schematic energy diagram of n-ZnO NR/p-Si heterojunction without bias is shown in figure 3.4.17. According to Anderson model, energy barrier for an electron (the conduction band offset) for the ZnO/p-Si heterojunction is:

$\Delta E_c = E_c\,(ZnO) - E_c\,(Si) = 0.3$ eV

and energy barrier for a hole (the valence band offset) is:

$\Delta E_v = E_v\,(ZnO) - E_v\,(Si) = E_g\,(ZnO) + \Delta E_c - E_g\,(Si) = 2.55$ eV.

Since $\Delta E_v >> \Delta E_c$, thus favoring the electron injection from ZnO to p-Si below 2.8V [24]. The carrier concentration of ZnO nanorods is found in the range of ~10^{17}-10^{18} cm^{-3} and for the highly doped p-Si the carrier concentration is in the 5.8×10^{18} cm^{-3} range [29, 30].

These values are both in a similar range. Hence, we expect some of the minority carriers from the p-Si side can diffuse and recombine in the depletion region at higher voltage (~10V), resulting in recombination process.

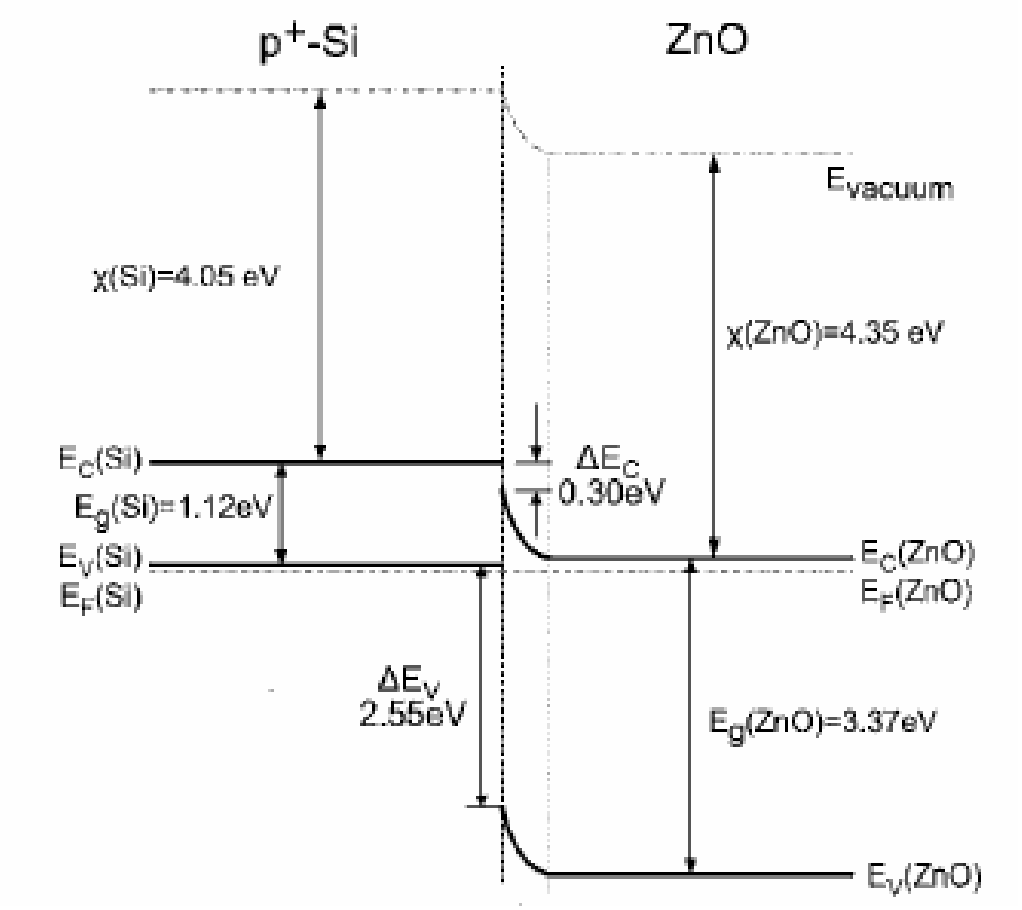

Figure 3.4.17: A schematic energy diagram of n-ZnO NR/p-Si heterojunction at zero bias [26]. (χ denotes electron affinity).

Figure 3.4.18 (a) shows the I-V characteristics of the n-ZnO NR/p-PEDOT/PSS heterostructure prepared with PLD ZnO nanorods on Si (100) substrate. In figure 3.4.18 (b), we have shown the semilog I-V plot of the n-ZnO NR/p-PEDOT/PSS heterojunction. The I-V characteristics show excellent rectification behavior. The rectification ratio of the forward-to-reverse bias current is 3.8 and 4574 at ±5 and ±50 V respectively. For the n-

ZnO/p-PEDOT/PSS structure, Ag/Au and Ag/Al are chosen as bottom and top electrodes respectively.

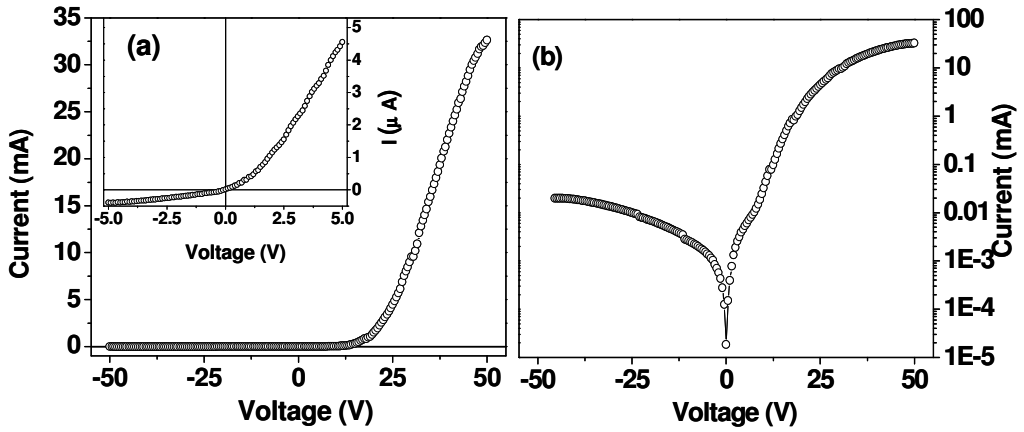

Figure 3.4.18: I-V characteristics of n-ZnO NR/p-PEDOT/PSS heterojunction in (a) linear and (b) semilog form.

The work functions of Ag, Au and Al are 4.26, 5.1 and 4.28 eV respectively. The electron injection barrier at the Ag/ZnO is 0.06 eV and the hole injection barrier at PEDOT/PSS/Ag is 0.96 eV. There is a 0.9 eV barrier for electron injection from ZnO conduction band to PEDOT/PSS LUMO (lowest unoccupied molecular orbit) and a 2.3 eV barrier for hole injection from PEDOT/PSS HOMO (highest occupied molecular orbit) to ZnO valence band edge. Hence at least a forward potential of 2.36 V is required for hole injection from PEDOT/PSS to ZnO. A schematic energy diagram of n-ZnO NR//p-PEDOT/PSS heterojunction without bias is shown in figure 3.4.19. Since the contacts are ohmic, the rectification shown in figures 16 and 18 are from n-ZnO NR/p-Si and n-ZnO NR/p-PEDOT/PSS heterojunctions.

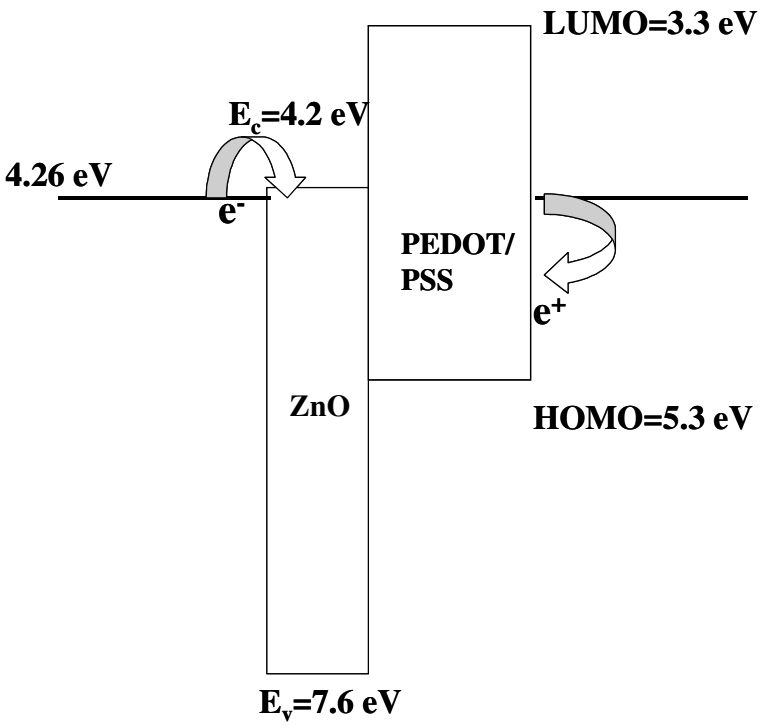

Figure 3.4.19: A schematic energy diagram of n-ZnO NR/PEDOT/PSS heterojunction at zero bias.

In figure 3.4.20 (a) we show the EL spectra of the n-ZnO NR/p-Si heterojunctions formed with the nanorods prepared at low-temp at a forward bias of 10 V. There is no emission at 0 V and under reverse bias, while visible light peaks due to defect states of ZnO are observed under forward biases. The EL bands arising from the defect states are observed at 407, 440, 460, 485 and 530 nm respectively. The 390 nm band and the defect related bands have comparable intensity. For reverse bias, not sufficient holes from the p-Si substrate get injected into the ZnO side, and therefore no EL is observed. A broad EL band in the 700-800 nm range is observed at 10 V bias voltage, probably may be due to the formation of some small silicon oxide on p-Si wafers [29, 73]. It should be noted that the intensity of the EL spectra is low in comparison to the current. The deep-level emission band around 430-500 nm range arises from the radiative recombination through

the deep level defects [74]. As the forward bias is applied, electrons in the conduction band of ZnO may first fall into deep-level defects, dislocations caused by large lattice mismatch as well as diffused Si impurity from Si substrate, which act as the empty traps.

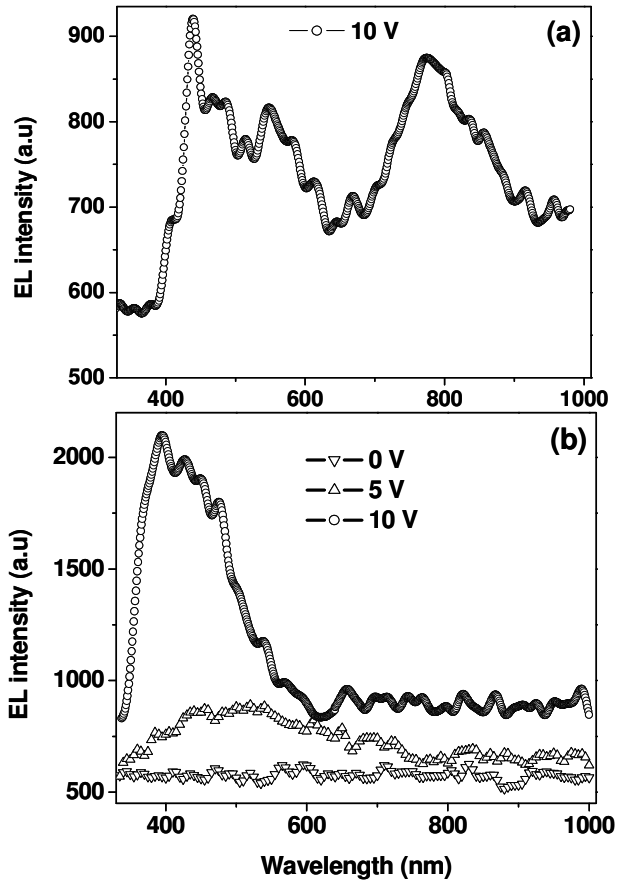

Figure 3.4.20: Electroluminescence spectra of (a) n-ZnO NR/p-Si, (b) n-ZnO NR/p-PEDOT/PSS heterojunctions.

Subsequently these electrons recombine with the holes injected from the p-Si side giving the emission ~430-500 nm [75]. Since low temp grown ZnO nanorods are expected to show more defects compared to high temp (PLD) grown nanorods, this effect is prominent in case of the n-ZnO NR/p-Si heterojunction. Yet, the origin of the bands around 430-500 nm is not clear although similar emissions are attributed to oxygen

vacancies or Zn interstitials in other reports [76, 77]. Also we observe the intensity of the UV peak to be low compared with deep level emission, probably due to low raditive efficiency and self-absorption effect induced by deep levels [78].

Figure 3.4.20 (b) shows the EL spectra of the n-ZnO NR/p-PEDOT/PSS heterojunctions prepared with PLD grown ZnO nanorods at 0, 5 and 10 V respectively. The UV emission band at 390 nm is intense and we hardly observe defect related bands at a bias voltage of 10 V. A broad peak in the range of 400-550 nm is observed at a bias voltage of 5 V. For reverse bias and 0 V bias, there was no emission. In the case of n-ZnO NR/p-Si heterojunctions, we observe the intensity of the UV peak to be low compared with deep level emissions. For n-ZnO NR/p-PEDOT/PSS heterojunctions, the UV EL dominates over visible EL and the defect related bands are observed marginally.

From the above results, we notice that there is a remarkable difference between PL and EL of the two samples studied by us. This may be because EL and PL involve different excitation processes. PL belongs to selective stimulation, and only a thin near layer surface region can be investigated. It is not a bulk characterization process and there is hardly any carrier transport process. In the EL process, injecting electrons and holes under an electric field in the bulk generates non-equilibrium carriers and there is always a barrier impeding the injection of electrons and holes from one to other side. In addition, the injected electrons and holes are easily captured by defect states in the bulk and interface depending on the fabrication process of the p-n junction [27]. Since we have fabricated p-n heterojunctions of different geometries, we observe more defects in the case of n-ZnO NR/p-Si heterojunctions compared to n-ZnO NR/p-PEDOT/PSS heterojunctions.

3.5 Conclusions

We have employed dielectrophoresis to directly assemble ZnO and $WO_{2.72}$ nanorods between Au gap (5 μm) electrodes on glass subtrate. Top-gated FETs using SiO_2 (~300 nm)/Si as gate dielectric were fabricated and the transistor characteristics were studied. Undoped and doped ZnO nanorods show n-type behavior and the fabricated FETs are of depletion mode type. The carrier mobility of the ZnO nanorods (0.009 cm^2/ V.s) is improved to 0.845, 1.0023, 2.208 and 128.6 cm^2/ V.s by Mg, Cd, N and Al doping respectively. Cd-doped ZnO nanorods show higher sensitivity (~20) to 1000 ppm of H_2 at room temperature compared to undoped and Mg, N, Al-doped nanorods. Response and recovery times are minimized by applying a gate voltage, V_g=50 V. Also FET-characteristics of the $WO_{2.72}$ nanorods have been studied which show the depletion mode type characteristics with the carrier mobility of 8.38 cm^2/ V.s. The sensitivity for 1000 ppm of H_2 at room temperature is enhanced from 7 to 10 by applying a gate voltage, V_g=50 V.

ZnO nanorods have been grown on Si substrates by a simple low-temperature method and also by PLD. The n-ZnO NR/p-Si and n-ZnO NR/p-PEDOT/PSS heterojunction devices have good diode characteristics. For n-ZnO NR/p-Si heterojunctions, the leakage current is only 3.6 μA at a reverse bias of 5 V and the ratio of the forward-to-reverse bias current is 243 at a bias voltage of ±5 V. For the n-ZnO/p-PEDOT/PSS structure, the rectification ratio of the forward-to-reverse bias current is 3.8 and 4574 at ±5 and ±50 V respectively. The EL spectra of n-ZnO NR/p-Si show intense defect-related bands in the 400-550 nm relative to the 390 nm band, under sufficient forward bias. The n-ZnO NR/p-

PEDOT/PSS LED device shows a broad ultraviolet EL band at 390 nm at room temperature and negligible defect emission. We believe that this system can have promising LED applications.

References

[1] http://nobelprize.org/nobel_prizes/physics/laureates/1956/index.html

[2] http://ece.colorado.edu/~bart/book/

[3] http://www.indiana.edu/~hightech/fpd/papers/ELDs.html

[4] http://nina.ecse.rpi.edu/shur/SiC/tsld011.htm, *Electrical World*, Vol. 19, p. 309, (**1907**).

[5] C.H. Gooch, Injection electroluminescent devices, (Newyork, Wieley 1973) p.2.

[6] B. Gudden and R.W. Pohl, *Zeitschrift fhr Physik*, vol. 2, 192, (**1929**); B. Gudden and R.W. Pohl, *Zeitschrift fhr Physik*, vol. 2, 181 (**1930**).

[7] C.M. Lieber, *MRS Bull.* 28, 486 **(2003)**.

[8] C. Thelander, P. Agarwal, S. Brongersma, J. Eymery, L.F. Feiner, A. Forchel, M. Scheffler, W. Riess, B.J. Ohlsson, U. Gosele, L. Samuelson, *Mater. Today* 9, 28 **(2006)**.

[9] Z.L. Wang, *Mater. Today* 7, 26 **(2004)**.

[10] Z. Fan, D. Wang, P. Chang, W. Tseng, J.G. Lu, *Appl. Phys. Lett.* 85, 5923 **(2004)**.

[11] Q.H. Li, T. Gao, Y.G. Wang, T.H. Wang, *Appl. Phys. Lett.* 86, 123117**(2005)**.

[12] P. Yang, H. Yan, S. Mao, R. Russo, J. Johnson, R. Saykally, N. Morris, J. Pham, R. He, H. Choi, *Adv. Func. Mater.* 12, 323 **(2002)**.

[13] Y-F. Lin, W-B. Jian, C.P. Wang, Y-W. Suen, Z-Y. Wu, F-R. Chen, J-J. Kai, J-J. Lin, *Appl. Phys. Lett.* 90, 223117 **(2007)**.

[14] K. Keem, D-Y. Jeong, S. Kim, M-S. Lee, I-S. Yeo, U-I. Chung, J-T. Moon, *Nano Lett.* 6, 1454 **(2006)**.

[15] S. Ju, D.B. Janes, G. Lu, A. Facchetti, T.J. Marks, *Appl. Phys. Lett.* 89, 193506 **(2006)**.

[16] S. Ju, K. Lee, M-h. Yoon, A. Facchetti, T.J. Marks, D.B. Janes, *Nanotechnology* 18, 155201 **(2007)**.

[17] Z-X. Xu, V.A.L. Roy, P. Stallinga, M. Muccini, S. Toffanin, H-F. Xiang, C-M. Che, *Appl. Phys. Lett.* 90, 223509 **(2007)**.

[18] C.S. Rout, G.U. Kulkarni, C.N.R. Rao, *J. Phys, D: Appl. Phys.* 40, 2777 **(2007)**.

[19] M.H. Huang, S. Mao, H. Feick, H. Yan, Y. Wu, H. Kind, E. Weber, R. Russo, P. Yang, *Science* 292, 1897 **(2001)**

[20] S. Singh, P. Thiyagarajan, K.M Kant, D. Anita, S. Thirupathiah, N. Rama, B. Tiwari, M. Kottaisamy, M.S.R. Rao, *J. Phys. D: Appl. Phys.* 40, 6312 **(2007)**.

[21] G.-C. Yi, C. Wang, W. Park, *Semicond. Sci. Technol.* 20, S22 **(2005)**.

[22] Y.R. Ryo, T.S. Lee, J.H. Leem, H.W. White, *Appl. Phys. Lett.* 83, 4032 **(2003)**.

[23] A. Allenic, W. Guo, Y.B. Chen, Y. Che, Z.D. Hu, B. Liu, X.Q. Pan, *J. Phys. D: Appl. Phys.* 41, 025103 **(2008)**.

[24] M. Sun, Q.-F. Zhang, J.-L. Wu, *J. Phys. D: Appl. Phys.* 40, 3798 **(2007)**.

[25] J.D. Ye, S.L. Gu, S.M. Zhu, W. Liu, S.M. Liu, R. Zhang, Y. Shi, Y.D. Zheng, *Appl. Phys. Lett.* 88, 182112 **(2006)**.

[26] P. Chen, X. Ma, D. Yang, *J. Appl. Phys.* 101, 053103 **(2007)**.

[27] X. Li, B. Zhang, H. Zhu, X. Dong, X. Xia, Y. Cui, Y. Ma, G. Du, *J. Phys. D: Appl. Phys.* 41, 035101 **(2008)**.

[28] R. Konenkamp, R.C. Word, M. Dosmailov, J. Meiss, A. Nadarajah, *J. Appl. Phys.* 102, 056103 **(2007)**.

[29] H. Sun, Q-F. Zhang, J-L. Wu, *Nanotechnology* 17, 2271 **(2006)**.

[30] W.Q. Yang, H.B. Huo, L. Dai, R.M. Ma, S.F. Liu, G.Z. Ran, B. Shen, C.L. Lin, G.G. Qin, *Nanotechnology* 17, 4868 **(2006)**.

[31] Y.I. Alivov, E.V. Kalinina, A.E. Cherenkov, D.C. Look, B.M. Ataev, A.K. Omaev, M.V. Chukichev, D.M. Bagnall, *Appl. Phys. Lett.* 83, 4719 **(2003)**.

[32] Y.I. Alivov, J.E.V. Nostrand, D.C. Look, M.V. Chukichev, B.M. Ataev, *Appl. Phys. Lett.* 83, 2943 **(2003)**.

[33] H. Ohta, M. Orita, M. Hirano, H. Hosono, *J. Appl. Phys.* 89, 5720 **(2001)**.

[34] H. Ohta, M. Hirano, K. Nakahara, H. Maruta, T. Tanabe, M. Kamiya, T. Kamiya, H. Hosono, *Appl. Phys. Lett.* 83, 1029 **(2003)**.

[35] B.N. Pal, J. Sun, B.J. Jung, E. Choi, A.G. Anreou, H.E. Katz, *Adv. Mater.* 20, 1023 **(2008)**.

[36] R. Konenkamp, R.C. Word, M. Godinez, *Nano Lett.* 5, 2005 **(2005)**.

[37] A. Nadarajah, R.C. Word, J. Meiss, R. Konenkamp, *Nano Lett.* 8, 534 **(2008)**.

[38] R. Konenkamp, R.C. Word, C. Schlegel, *Appl. Phys. Lett.* 85, 6004 **(2004)**.

[39] B. Liu, H. C. Zeng, *J. Am. Chem. Soc.* 125, 4430 **(2003)**.

[40] N. Varghese, L.S. Panchakarla, M. Hanapi, A. Govindaraj, C.N.R. Rao, *Mater. Res. Bull.* 42, 2117 **(2007)**.

[41] H.G. Choi, Y.H. Jung, D.K. Kim, *J. Am. Ceram. Soc.* 88, 1684 **(2005)**.

[42] L.S. Panchakarla, M.A. Shah, A. Govindaraj, C.N.R. Rao, *J. Solid State Chem.* 180, 3106 **(2007)**.

[43] L. Shi, Q. Hao, V.H. Yu, D. Kim, N. Mingo, X.Y. Kong, Z.L. Wang, *Appl. Phys. Lett.* 84, 2638 **(2004)**.

[44] A. Yoon, W-K. Hong, T. Lee, *J. Nanosci. Nanotechnol.* 7, 4101 **(2007)**.

[45] S.L. Chang, L. Jin, G. Puxian, Z. Lyuan, D. Dragomir, T. Rao, Z.L. Wang, *Nano Lett.* 6, 263 **(2006)**.

[46] H. Iwasaki, T. Yoshinobu and K. Sudoh, *Nanotechnology* 14, R55 **(2003)**.

[47] S.B. Zhang, S-H. Wei, A. Zunger, *Phys. Rev. B* 63, 075205 **(2001)**.

[48] W. Gopel, L.J. Brillson, C.F. Brucker, *J. Vac. Sci. Technol.* 17, 894 **(1980)**.

[49] F. Tuomisto, V. Ranki, K. Saarinen, D.C. Look, *Phys. Rev. Lett.* 91, 205502 **(2003)**.

[50] K.A. Alim, V.A. Fonoberov, M. Shamsa, A.A. Balandin, *J. Appl. Phys.* 97 124313 **(2005)**.

[51] W-K. Hong, D-K. Hwang, I-K Park, G. Jo, S. Song, S-J. Park, T. Lee, B-J. Kim, E.A. Stach, *Appl. Phys. Lett.* 90, 243103 **(2007)**.

[52] Y.W. Heo, L.C. Tien, Y. Kwon, D.P. Norton, S.J. Pearton, B.S. Kang, F. Ren, *Appl. Phys. Lett.*85, 2274 **(2004)**.

[53] U. Ozgur, Y.I. Alivov, C. Liu, A. Teke, M.A. Reshchikov, S. Dogan, V. Avrutin, S.-J. Cho, H. Morkoc, *J. Appl. Phys.* 98, 041301 **(2005)**.

[54] G.D. Yuan, Z.Z. Ye, L.P. Zhu, Q. Qian, B.H. Zhao, R.X. Fan, C.L. Perkins, S.B. Zhang, *Appl. Phys. Lett.* 86, 202106 **(2005)**.

[55] S. Yamauchi, Y. Goto, T. Hariu, *J. Cryst. Growth* 1, 260 **(2004)**.

[56] E.C. Dattoli, Q. Wan, W. Guo, Y. Chen, X. Pan, W. Lu, *Nano Lett.* 7, 2463 **(2007)**.

[57] E.M.C. Fortunato, P.M.C. Barquinsha, A.C.M.B.G. Pimentel, A.M.F. Goncalves, A.J.S. Marques, L.M.N. Perira, R.F.P. Martins, *Adv. Mater.* 17, 590 **(2005)**.

[58] H.S. Bae, S. Im, *J. Vac. Sci. Technol. B*, 22, 1191 **(2004)**.

[59] S.H. Noh, W.Choi, M.S. Oh, D.K. Hwang, K. Lee, S. Im, S. Jang, E. Kim, *Appl. Phys. Lett.* 90, 253504 **(2007)**.

[60] K-K. Kim, S. Niki, J-Y. Oh, J-O Song, T-Y. Seong, S-J. Park, S. Fujita, S-W. Kim, *J. Appl. Phys.* 97, 066103 **(2005)**.

[61] J.G. Lu, Z.Z. Ye, Y.J. Zeng, L.P. Zhu, L. Wang, J. Yuan, B.H. Zhao, Q.L. Liang, *J. Appl. Phys.* 100, 073714 **(2006)**.

[62] Z. Xiao, L. Zhang, X. Tian, X. Fang, *Nanotechnology* 16, 2647 **(2005)**.

[63] C.S. Rout, K. Ganesh, A. Govindaraj, C.N.R. Rao, *Appl. Phys. A: Mater. Sci. Process.* 40, 2777 **(2007)**.

[64] C.S. Rout, M. Hegde, A. Govindaraj, C.N.R. Rao, *Nanotechnology*, 18, 205504 **(2007)**.

[65] S.M. Sze, Semiconductor Sensors, 1st ed. (Wiley, New York, 1994) p. 383

[66] A.K. Alim, V.A. Fonoberov, A.A. Balandin, *Appl. Phys. Lett.* 86, 053103 **(2005)**.

[67] N. Ashkenov, B.N. Mbenkum, C. Bundesmann, V. Riede, M. Lorenz, D. Spemann, E.M. Kaidashev, A. Kasic, M. Schubert, M. Grundmann, G. Wagner, H. Neumann, V. Darakchieva, H. Arwin, B. Monemar, *J. Appl. Phys.* 93, 126 **(2003)**.

[68] J. Serrano, F.J. Manjon, A.H. Romero, F. Widulle, R. Lauck, M. Cardona, *Phys. Rev. Lett.* 90, 055510 **(2003)**.

[69] P. Huh, F. Yan, M. Kim, R. Mosurkal, L.A. Samuelson, J. Kumar, *J. Mater. Chem* 18, 637 **(2008)**.

[70] A. Dev, S. Kar, S. Chakrabati, S. Chaudhari, *Nanotechnology* 17, 1533 **(2006)**.

[71] K. Vanheusden, W.L. Warren, C.H. Seager, D.R. Tallant, J.A. Voigt, B.E. Gnade, *J. Appl. Phys.* 79, 7983 **(1996)**.

[72] A. Zeuner, H. Alves, D.M. Hofmann, B.K. Meyer, M. Heuken, J. Bla¨sing, A. Krost, *Appl. Phys. Lett.* 80, 2078 **(2002)**.

[73] G.G. Qin, Y.M. Huang, J. Lin, L.Z. Zhang, B.Q. Zong, B.R. Zhang *Solid State Commun.* 94, 607 **(1995)**.

[74] A.B. Djurisic, W.C.H. Choy, V.A.L. Roy, Y.H. Leung, C.Y. Kwong, K.W. Cheah, T.K.G. Rav, W.K. Chan, H.F. Lui, C. Surya, *Adv Func. Mater.* 14, 856 **(2004)**.

[75] J.D. Ye, S.L. Gu, S.M. Zhu, W. Liu, S.M. Liu, Zhang R, Y. Shi, Y.D. Zheng, *Appl. Phys. Lett.* 88,182112 **(2006)**.

[76] J.C. Sun, J.Z. Zhao, H.W. Liang, J.M. Bian, L.Z. Hu, H.Q. Zhang, X.P. Liang, W. F. Liu, G.T. Du, *Appl Phys Lett.* 90, 121128 **(2007)**.

[77] L.J. Mandalapu, Z. Yang, S. Chu, J.L. Liu, *Appl Phys Lett.* 92, 122101 **(2008).**

[78] A. Tsukazaki, M. Kubota, A. Ohtomo, T. Onuma, K. Ohtani, H. Ohno, S.F. Chichibu, M. Kawasaki, *Jpn. J. Appl. Phys.* Part 2 44, L643 **(2005)**.

Part 4

Other investigations*

(Some studies based on carbon nanostructures)

Summary

This part of the thesis deals with the supercapacitive behavior of RuO_2 and IrO_2 functionalized mesoporous carbon and exfoliated graphene. The capacitance of the mesoporous carbon can be increased from 140 to 378 F/g in aq. H_2SO_4 by RuO_2 loading and to 152 F/g by IrO_2 loading. The nanographene prepared by exfoliation of graphitic oxide exhibit high specific capacitance in aq. H_2SO_4, the value reaching upto 117 F/g.

Interaction of single-walled carbon nanotubes (SWNTs) with electron donor and acceptor aromatic molecules has been studied by electrical measurements. Vertical SWNT devices were fabricated in a porous anodic alumina (PAA) template by microwave plasma chemical vapor deposition (MPCVD). I-V characteristics of the SWNTs in air and in the presence of aniline, anisole, chlorobenzene and nitrobenzene have been studied. The resistance decreases markedly in the presence of electron withdrawing molecules such as nitrobenzene and chlorobenzene, whereas it increases in the presence of electron donating molecules such as aniline and anisole.

---

* A paper based on these studies has appeared in J. Chem. Sci. (2008) and another paper has been communicated.

4.1 Supercapacitors

4.1.1 Introduction

Supercapacitors based on nanoporous carbon materials, commonly called electric double-layer capacitors (EDLCs), have recently attracted considerable attention [1, 2]. Carbon supercapacitors bridge the gap between batteries and conventional dielectric capacitors and are ideal for the rapid storage and release of energy. The first patent on supercapacitor was granted to Becker at General Electric Corp. in 1957 [3], in which he proposed a capacitor based on porous carbon material with high surface area. In 1969, Sohio first attempted to market such energy storage device using high surface area carbon materials with tetraalkylammonium salt electrolyte [4]. In late 70's and 80's, Conway and coworkers made a great contribution to the capacitor research work based on RuO_2, which has high specific capacitance and low internal resistance [5]. In the 90's, supercapacitors received much attention in the context of hybrid electric vehicles [1, 2]. A comparison of the properties and performance between battery, capacitor, and supercapacitor is given in Table 4.1.1.

Supercapacitors have two electrodes immersed in an electrolyte solution, with one separator between them, and two current collectors. The process of energy storage is associated with buildup and separation of electrical charge accumulated on two conducting plates spaced some distance apart as shown in figure 4.1.1. Even if their technology is close to that of the batteries, their particularity is to involve only electrostatic phenomenon (non-faradaic). This is a first difference between batteries and supercapacitors: their power density is higher because there are no chemical reactions

during charging and discharging. Thus, the constant time for loading and unloading is reduced, and their lifetime is increased. The amount of stored energy is a function of the available electrode surface, the size of the ions, and the level of the electrolyte decomposition voltage.

Parameters	Capacitor	Supercapacitor	Battery
Charge Time	10^{-6} ~ 10^{-3} sec	1 ~ 30 sec	0.3 ~ 3 hrs
Discharge Time	10^{-6} ~ 10^{-3} sec	1 ~ 30 sec	1 ~ 5 hrs
Energy Density	< 0.1	1 ~ 10	20 ~ 100
Power Density	> 10,000	1,000 ~ 2,000	50 ~ 200
Cycle Life	> 500,000	> 100,000	500 ~ 2,000
Charge/Discharge efficiency	~ 1.0	0.90 ~ 0.95	0.7 ~ 0.85

Table 4.1.1: Comparison of Capacitor, Supercapacitor and Battery [6].

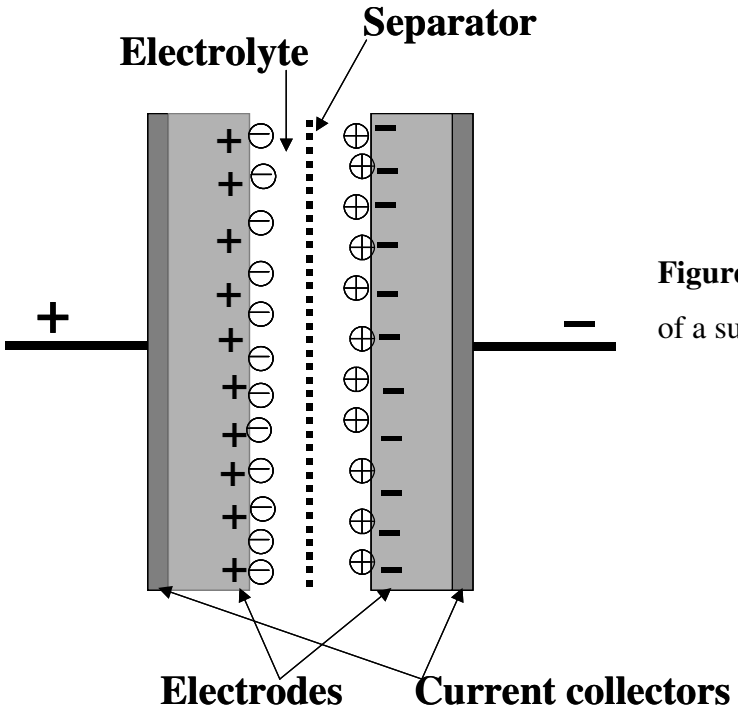

Figure 4.1.1: Schematic diagram of a supercapacitor

The membrane, which separates two electrodes, allows the mobility of the charged ions and forbids the electronic contact. The electrolyte supplies and conducts the ions from one electrode to the other. As the dissociation voltage of the electrolytes generally used is less than 3 volts, this limits the maximum voltage that can be reached for a supercapacitor. To develop supercapacitors as an alternative to batteries, currently intense research efforts aim at increasing the energy density by optimizing the pore size distribution of nanoporous carbon materials, which act as electrodes.

A different kind of capacitance can arise at electrodes of certain kinds, for example RuO_2, when the extent of faradaically admitted charge depends linearly, or approximately linearly, on the applied voltage. This capacitance can be large but it is faradaic and not electrostatic (i.e. non-faradaic) in origin. This is hence an important difference from the nature of double-layer capacitance, so it is called "pseudocapacitance". Most of the oxides like ruthenium oxide, and conducting polymers show pseudocapacitance behavior.

In a plane capacitor with a pair of plates of equal area, A, in parallel configuration and separated by a distance, d, in vacuum, the capacitance, C, is given by equation (4.1).

$$C = A/4\pi d \qquad (4.1)$$

If the plates are separated by a dielectric medium, ε, the capacitance is given by equation (4.2).

$$C = A\varepsilon/4\pi d \qquad (4.2)$$

Electrical double layer capacitor stores energy in the similar way, but the charge does not accumulate on two conductors separated by a dielectric. Instead, the charge accumulates

in the electric double layer at the interface between the surface of a conductor and an electrolyte solution. When charged, the negative ions in the electrolytes will diffuse to the positive electrode, while the positive ions will diffuse to the negative electrodes. In this case, it creates two separate layers of capacitive storage, so the maximum energy density, W, stored in the capacitor is given by equation (4.3).

$W = 1/2\ CV^2$ (4.3)

where C is the specific capacitance, and V is voltage. The double layer capacitor does not involve chemical reactions, thus supercapacitors have long life cycles of charge and discharge. Besides the capacitance contribution from the separation of charge in the double layer, capacitance associated with reactions on the surface of the electrode, are also important. During these reactions, electron transfer does take place across the double layer, with consequence of oxidation state change. Thus the capacitance from the faradaic process is referred to as pseudocapacitance.

4.1.2 Scope of the present investigations

Supercapacitors based on exfoliated graphene, RuO_2 and IrO_2 functionalized mesoporous carbon have been studied. Porous carbon materials such as activated carbon [7, 8], xerogels [9] carbon nanotubes [10-13], mesoporous carbon [14] and carbide-derived carbons [15] have been investigated for use as electrodes in EDLCs. The supercapacitive behavior of several transition metal oxides such as RuO_2 [16], IrO_2 [17], NiO [18] have been reported. These oxides can store charges by reversibly accepting or donating protons from an aqueous electrolyte. In view of their electrical double-layer capacitance, which can be as high as 100-200 F/g, templated carbons have received much attention in recent years [19-21]. The electrochemical performance of mesoporous carbon

prepared by a templating procedure using SBA-15 or MCM-48 have been studied [19]. Due to the presence of secondary micropores, capacitance values of 200 and 110 F/g were obtained in aqueous and organic media respectively. Using SBA-16 as the template materials and polyfurfuryl alcohol as the carbon source, mesoporous carbon of pore size 3-8 nm have been synthesized and a maximum capacitance of 150 F/g was found [20]. Ordered carbon materials were prepared by using MCM-41, SBA-15 and MSV-1 as templates and its electrochemical performance showed a capacitance in the 50-200 F/g range depending on the aqueous or organic electrolytes [21]. Capacitance of 243 F/g has been achieved by ruthenium loading, whereas unloaded mesoporous carbon delivers a specific capacitance of 100 F/g [22]. An in situ reduction method has been employed to synthesize a novel structured MnO_2/mesoporous carbon composite and a maximum specific capacitance of 200 F/g for the composite was observed [23]. In the present study we report the supercapacitive behaviour of RuO_2 and IrO_2 functionalized mesoporous carbon. Using cyclic voltametry we have found that the capacitance of the mesoporous carbon can be increased from 140 to 378 F/g in aq. H_2SO_4 by RuO_2 loading and to 152 by IrO_2 loading.

In the last few years, there has been great interest in nanographene, which constitutes an entirely new class of carbon. Electrical characterization of single-layer nanographene has been reported [24, 25]. We have investigated the use of nanographene as electrode material in electrochemical supercapacitors. For this purpose, we have employed nanographene prepared by exfoliation of graphitic oxide and supercapacitor behavior with aq. H_2SO_4 as the electrolyte has been studied.

4.1.3 Experimental

For the synthesis of the mesoporous carbon two methods were followed. The first method involves the polymerization via enhanced hydrogen bonding interaction which is described elsewhere [26]. To prepare the mesoporous carbon, a composition range of weight ratios of phloroglucinol: pluronic F127: formaldehyde: ethanol: water: HCl ≅ 1: 1:0.3:150:90:0.03 were taken. As the reaction proceeded, the reaction mixture separated into two layers within 30 min. The upper layer consisted of water/ethanol, while the lower layer was a polymer-rich containing phloroglucinol/formaldehyde oligomers, F217 and small amount of water/ethanol. After removing the upper layer, the polymer solution was stirred for overnight and it forms elastic, but non-sticky monolith. Then, the monolith was dried at 100°C for 20h and then calcined at 850°C for 2h in N_2 atmosphere. In the second method, SBA-15 is used as the template, which is described in ref. [27]. 1g of SBA-15 was added to a solution obtained by dissolving 1.25g of sucrose and 0.14g H_2SO_4 in 5g of H_2O. The mixture was placed in a drying oven for 6h at 100°C and subsequently the oven temperature was raised to 150°C and maintained for 6h. Again 0.8g of sucrose, 0.09g of H_2SO_4 and 5g of H_2O were added and kept at 150°C for 6h. The carbonization was completed by pyrolysis with heating to 900°C in N_2 atmosphere. Then the carbon-silica composite obtained was washed with 1M NaOH solution to remove the silica templates. Then the template-free carbon products was filtered, washed with ethanol and dried at 100°C.

The mesoporous carbon samples prepared by in situ polymerization was referred as MC1 and the samples prepared by using SBA-15 as templates was referred as MC2. The MC2 samples with different ruthenium and iridium contents were prepared by using

$RuCl_3$ and $IrCl_3$ aqueous solution with conc. of 0.005, 0.01, 0.03,0.05 M [28]. In a typical loading procedure, 0.1g of mesoporous carbon (MC2) was dispersed into 50 ml aqueous solution of $RuCl_3$ or $IrCl_3$ and NaOH and stirred for 48h. The obtained sample was washed with distilled water and dried in vacuum at 100°C for 6h. These samples were referred as 0.005RuMC, 0.01RuMC, 0.03RuMC, 0.05RuMC, 0.03IrMC and 0.05IrMC respectively.

Graphene was prepared by thermal exfoliation of graphitic oxide [29]. In this method, graphitic oxide was prepared by reacting graphite (Alfa Aesar, 2-15 μm) with concentrated nitric acid and sulphuric acid with potassium chlorate at room temperature for 5 days. Thermal exfoliation of graphitic oxide was carried out in a long quartz tube at 1050°C.

The mesoporous carbon and graphene electrodes and supercapacitor cells were fabricated following Conway[1] and the measurements were carried out with a two-electrode configuration, the mass of each electrode being 5 mg. Electrochemical measurements were performed using a PG262A potentiostat/galovanostat, (Technoscience Ltd, Bangalore, India). We have performed cyclic voltammetry as well as constant current charging and discharging to characterize the two-electrode supercapacitor cells with the graphene and different mesoporous carbon samples, the RuO_2 and IrO_2 loaded samples and aqueous H_2SO_4 was used as the electrolyte. Specific capacitance (Fg^{-1}) was calculated using the following formulae:

In cyclic voltammetry,

$$C_{CV} = 2(i_+ - i_-)/(m \times \text{scan rate}), \qquad (4.4)$$

where i_+ and i_- are maximum current in the positive scan and negative scan respectively and m is the mass of electrode.

As we know C=Q/V, the cell capacitance can be deduced from the slope of the discharge curve: C = i/(dV/dt), i is the constant current applied and dV/dt is the slope of the discharge curve. Hence, in constant current charging and discharging,

C_{CD}= 2(i)/(s x m), (4.5)

s is the slope of the discharge curve.

4.1.4 Results and discussion

In figures 4.1.2 (a) and (b), we show the FESEM images of mesoporous carbons MC1 and MC2 respectively. The Brunauer-Emmett-Teller (BET) surface area of MC1 and MC2 were 750 and 903 m^2/g respectively. The average pore size was 2.4 and 2 nm for the MC1 and MC2 samples. In figures 4.1.2 (c) and (d), we show the TEM images of MC2 and 0.03RuMC samples. The EDAX results confirmed the deposition of RuO_2 and IrO_2 on the mesoporous carbon. The peak around 2.5 kV and 2 kV showed the presence of ruthenium or Iridium. The XRD patterns of the mesoporous carbon shows broad diffraction peaks at 2θ=24° and 43° that are related to the (002) and (100) reflections of microcrystalline carbon [30]. After loading of RuO_2 and IrO_2 the intensity of the diffraction peaks decreased. For the more loaded samples (0.05RuMC and 0.05IrMC) only the weak peak at 2θ=24° existed in the XRD patterns (Figure 4.1.3). So the structural order decreased after the loading. From the XRD pattern it is revealed that RuO_2 and IrO_2 in those composites were all amorphous and no Ru metal or crystalline RuO_2 or IrO_2 formed.

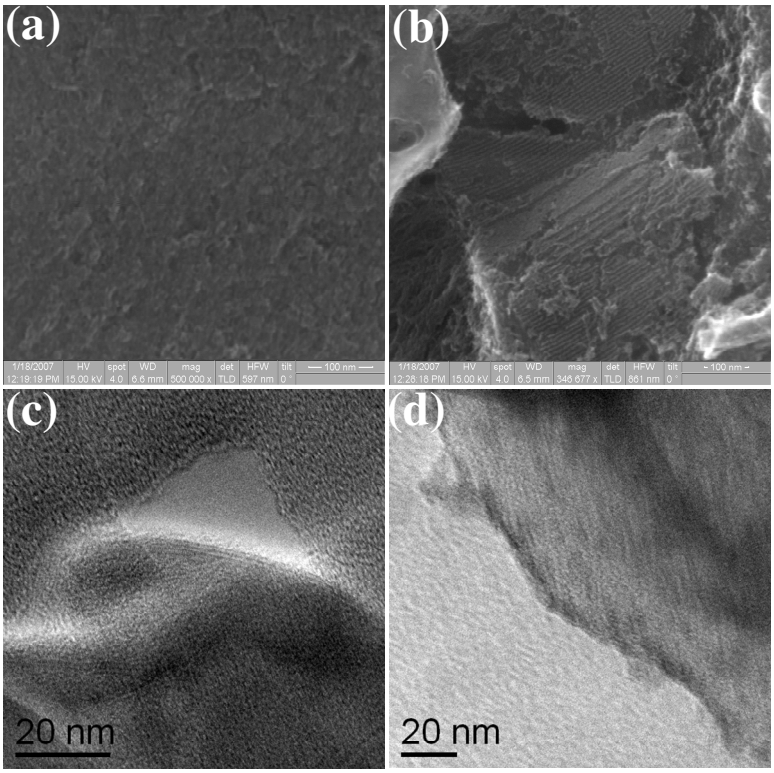

Figure 4.1.2: FESEM images of mesoporous carbons (a) MC1 and (b) MC2, TEM images of (c) MC2 and (d) 0.03RuMC sample.

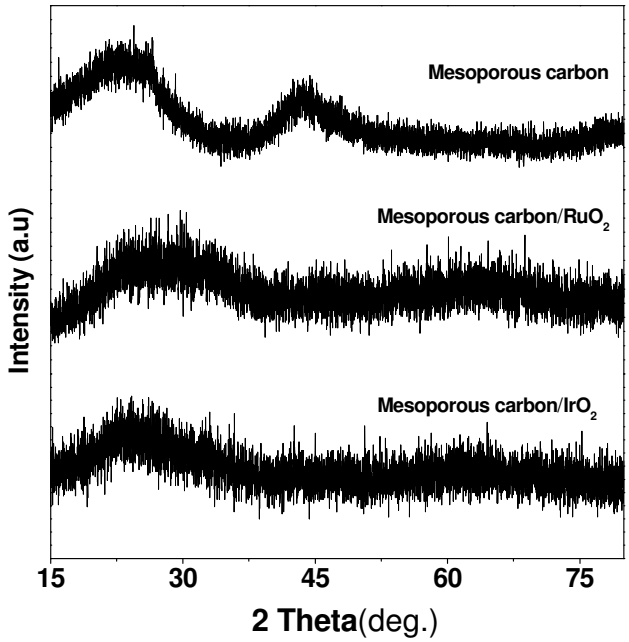

Figure 4.1.3: XRD patterns of mesoporous carbon, and RuO_2, IrO_2 coated mesoporous carbon.

In figure 4.1.4 (a), we show cyclic voltamograms (CVs) under a potential in the range of 0 to 1.0 V with a scan rate of 5 mV/s for capacitors built using mesoporous carbon and the RuO_2, IrO_2 loaded samples as electrodes and 1M H_2SO_4 as electrolyte. All the supercapacitors exhibit good box-like CVs with 0.05RuMC exhibiting the highest specific capacitance of 377 F/g and MC1, MC2 shows a capacitance of 86 and 136 F/g respectively. Capacitance of 173, 192 and 250 F/g is observed for the 0.005RuMC, 0.01RuMC and 0.03RuMC based supercapacitors. Supercpacitors based on 0.03IrMC and 0.05IrMC shows a specific capacitance of 140 and 151 respectively. Figure 4.1.4 (b) shows the CVs of the supercapacitors based on different samples with a scan rate of 100 mV/s. Good box like CVs are observed for the samples, which are loaded with less quantities of RuO_2 or IrO_2. As the loading increases it is observed that the CVs are not nearly rectangles, which indicates that the ohmic resistance for electrolyte motion in the carbon pores has affected the double-layer formation mechanism. The surface of the loaded mesoporous carbon is involved in the pseudocapacitive behavior of RuO_2 and IrO_2. The loaded carbon walls can provide large surface area and good electric conductivity, which contributes for the enlarged electrochemical capacitance.

In figure 4.1.5, we show typical charge-discharge curves at 10 mA current for supercapacitors built using MC1, MC2, 0.005RuMC, 0.01RuMC, 0.03RuMC and 0.05RuMC. The charging and discharging curves are nearly linear. Figure 4.1.6 (a) shows variation of specific capacitance with respect to scan rate. It is observed that at a scan rate below 100 mV/s, the capacitance increases drastically compared to higher scan rates. In figure 4.1.6 (b) we show variation of specific capacitance with respect to discharge current.

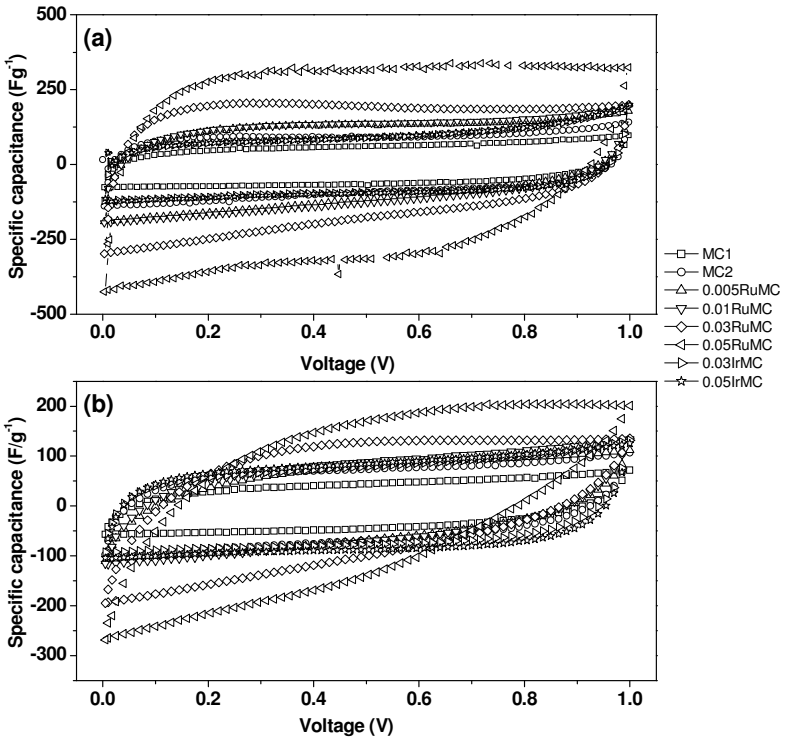

Figure 4.1.4: Cyclic voltamograms (CVs) with a scan rate of (a) 5 mV/s, (b) 100 mV/s for capacitors built using mesoporous carbon (MC1 and MC2) and RuO_2 (0.005 M, 0.01 M, 0.03 M and 0.05 M), IrO_2 (0.03 M and 0.05 M) loaded samples as electrodes.

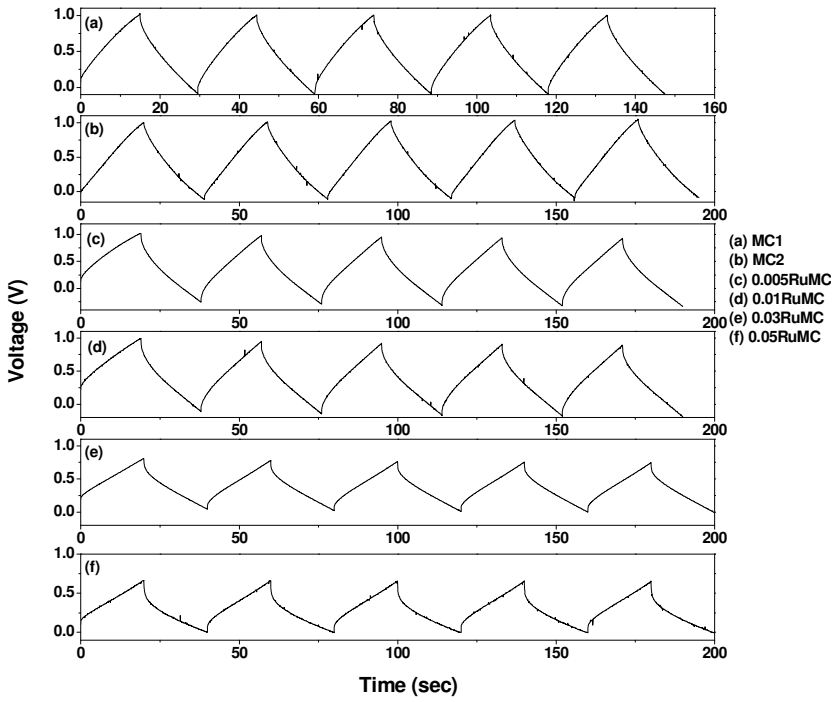

Figure 4.1.5: Typical charging and discharging curve at 10 mA for supercapacitors based on MC1, MC2, 0.005RuMC, 0.01RuMC, 0.03RuMC and 0.05RuMC

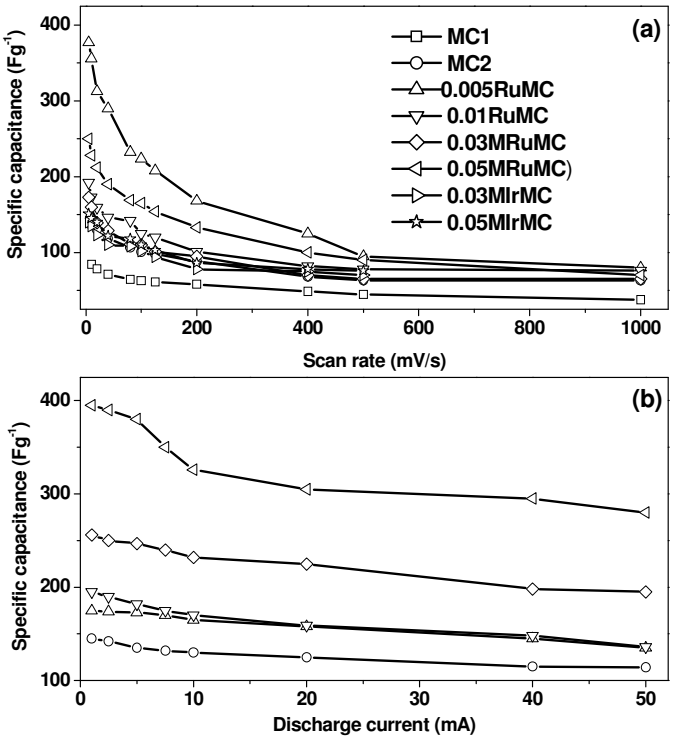

Figure 4.1.6: (a) Specific capacitance as a function of scan rate, (b) Specific capacitance as a function of discharge current for MC1, MC2, 0.005RuMC, 0.01RuMC, 0.03RuMC, 0.05RuMC, 0.03IrMC and 0.05IrMC.

In figure 4.1.7, we show AFM images of exfoliated graphene with image profiles. There is some disorder in the graphene sheets. In figure 4.1.8 (a), we show cyclic voltamogram (CV) at a scan rate of 100 mV/s for a capacitor built using nanographene as electrodes and 1M H_2SO_4 as electrolyte. The supercapacitor exhibits good box-like CV exhibiting the highest specific capacitance of 117 F/g. The specific capacitance decreases slightly as the scan rate is increased as shown in figure 4.1.8 (b), but the capacitance remains at 100 F/g at a scan rate of 1000 mV/s, retaining the box-like characteristics. The results obtained from cyclic voltammetry were confirmed by charge-discharge experiments. In figure 4.1.8 (c), we show typical charge-discharge curves at 5 mA current for a supercapacitor built using graphene. The charging and discharging curves are linear with no loss due to series resistance. The specific capacitance decreases slightly as the discharge current is increased from 1 mA to 50 mA {Figure 4.1.8 (d)}.

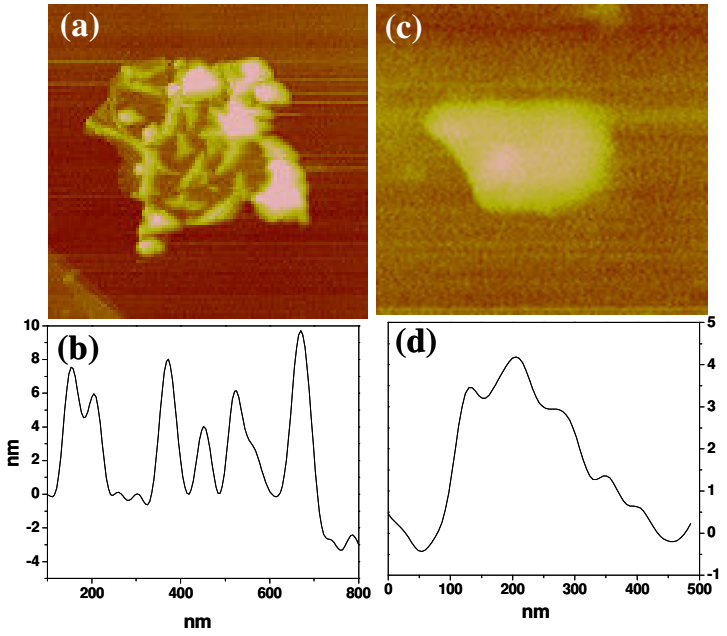

Figure 4.1.7: AFM height profiles of graphene.

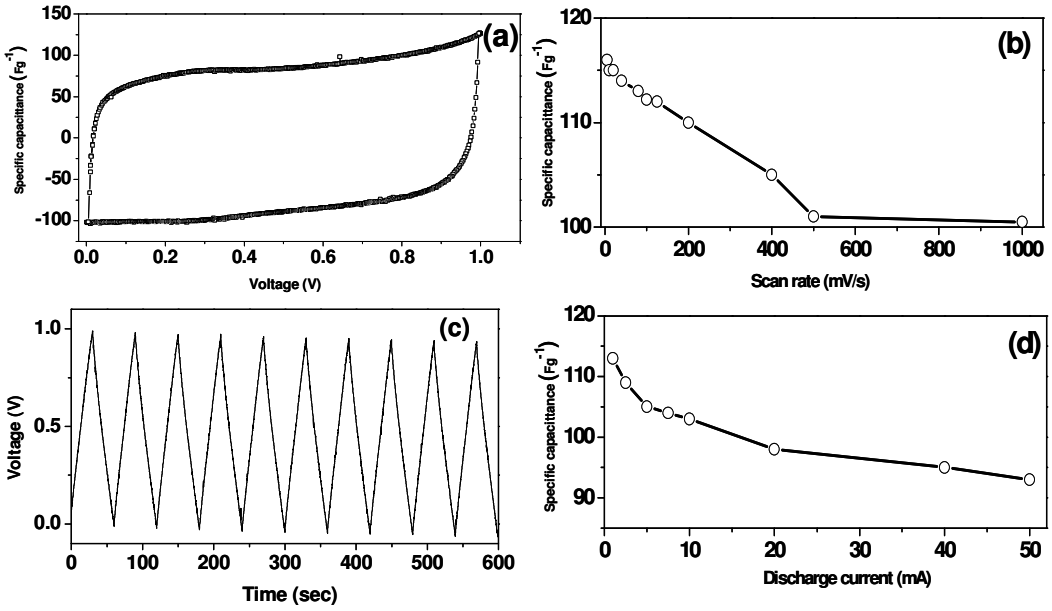

Figure 4.1.8: (a) Voltammetry characteristics of a capacitor built from graphene electrodes (5 mg each) at a scan rate of 100 mV/s using aqueous H_2SO_4 (1 M) as electrolyte, (b) Specific capacitance as a function of scan rate, (c) Typical charging and discharging curve at 5 mA and (d) specific capacitance as a function of discharge current.

4.2 Electrical properties of SWNTs

4.2.1 Introduction

Single-walled carbon nanotubes (SWNTs) exhibit diverse electronic structure and properties arising from the quantization of electron wave vector of the 1D system [31-33]. Thus, SWNTs exhibit significant changes in the electronic structure and chemical reactivity depending on the geometry, doping, chemical environment and solvent. Electron or hole doping influences the electronic structure of SWNTs and thereby their Raman spectra [34] and electrochemical doping also causes similar effects [35]. Interaction of SWNTs with gold and platinum nanoparticles can give rise to a semiconductor to metal transition [36]. More interestingly, aromatic solvents containing electron donating and electron withdrawing groups have been shown to modify the electronic structure of the nanotubes giving rise to changes in the electrical properties [37]. Clearly, the electron transfer caused by the interaction of SWNTs with other molecules depends on the density of states near the Fermi level [38]. We have investigated the interactions of electron-withdrawing and electron-donating molecules with SWNTs to determine the sensitivity of their electronic structure and properties to molecular charge-transfer.

4.2.2 Experimental

In order to carry out electrical resistivity measurements, vertical SWNT devices were fabricated in a porous anodic alumina (PAA) template [39-42]. The process involves the deposition of a thin Ti layer on the surface of the wafer to serve as an electrical back-contact. Three subsequent metal layers, 100 nm Al, 1 nm Fe, and 500 nm Al, are then deposited onto the wafer. The Al layers are used to create a nanoporous template, while

the thin middle layer (Fe) ultimately serves as the catalyst. The metal films and substrate are then submerged in an acid and anodized using a standard two-step technique. The anodization process forms self-assembled nanopores in the Al layer as it oxidizes and turns to PAA. After anodization, a microwave plasma chemical vapor deposition (MPCVD) system is used to create hydrogen plasma at a microwave power of 300 W and substrate temperature of 900°C. The substrate is exposed to this plasma for 10 minutes to reductively open the bottom of the oxide layer. Methane gas is then introduced into the MPCVD chamber to provide a carbon source for growth of the nanotubes from the Fe catalyst on the pore wall. During this process, SWNTs grow with a typical density of one per pore. Subsequently, Pd is electrodeposited into the pore bottoms. Continued Pd electrodeposition past the establishment of bottom contacts to SWNTs results in the formation of Pd nanoclusters that concentrically surround SWNTs on the top PAA surface [43]. Many of the clusters exhibited cubic or a combination of cubic and pyramidal geometries. A thin layer consisting of Ti (~20 nm) and Au (~50nm) was deposited by physical vapor deposition on top of the PAA membrane to achieve the top contact for the electrical resistivity measurements. Bottom contacts were taken from the Ti-coated Si substrates. The I-V characteristics of the SWNT bundle prepared as above and soaked in the liquids of electron-withdrawing and electron-donating molecules were measured using a Keithley 236 multimeter.

4.2.3 Results and discussion

Figure 4.2.1 shows the schematic diagram of the vertically aligned SWNTs grown on Si substrate, as by Fisher and coworkers.

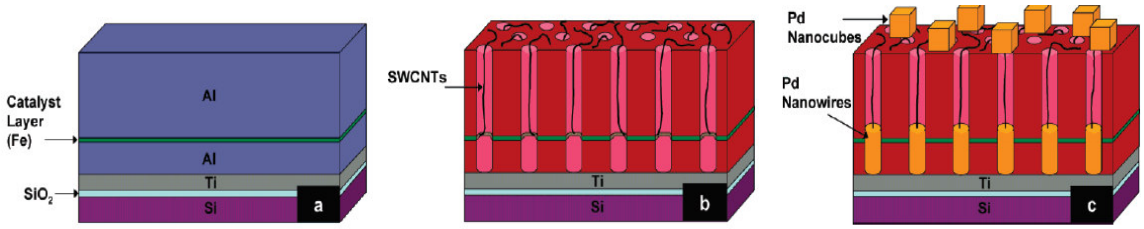

Figure 4.2.1: Tilted cross-sectional schematic of the growth of the SWNTs (a) an evaporated metal film stack prior to anodization, (b) SWNTs emerging from PAA pores after undergoing anodization and PECVD synthesis, and (c) electrodeposited Pd nanowires contacting the bottom of SWNTs and Pd nanocubes forming on SWNTs located on the top of PAA surface (From Fisher and coworkers [42]).

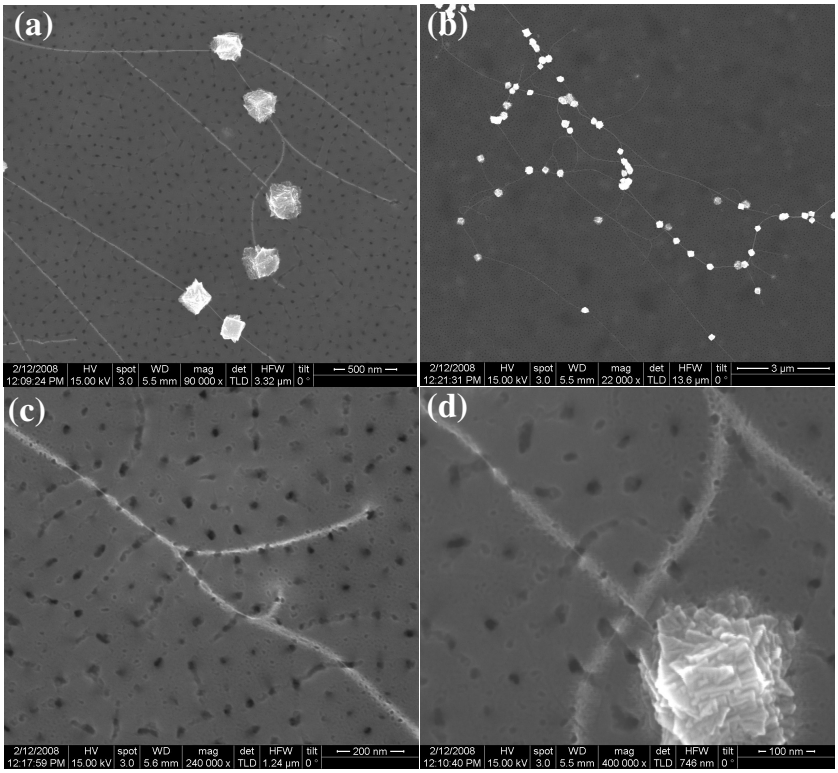

Figure 4.2.2: FESEM images of the SWNTs with Pd cubes on the PAA surface (From Fisher and coworkers).

In figure 4.2.2 we show FESEM images of SWNTs with Pd cubes on the PAA surface. It is observed that only nanotube grows from a pore. The I-V characteristics of this SWNT obtained by conducting AFM measurements exhibit a nearly linear behavior, establishing that the electrical contacts were well established (Figure 4.2.3). Inset of figure 4.2.3 shows an AFM image of Pd cubes connected to SWNTs.

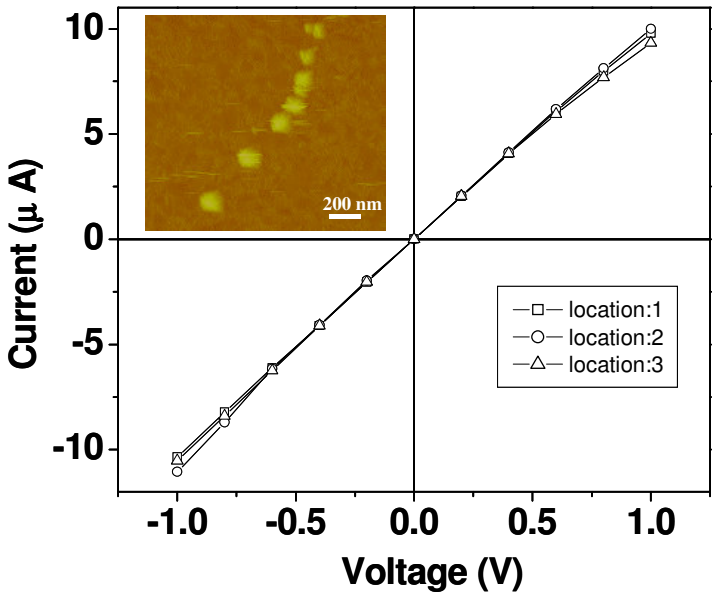

Figure 4.2.3: I-V characteristics obtained by CAFM measurements, with the inset showing the AFM image of the Pd cubes on which the I-V characteristics were obtained by contacting the CAFM tip.

Figure 4.2.4 presents the I-V characteristics of the SWNTs in air and in the presence of aniline, anisole, chlorobenzene and nitrobenzene, with the inset showing the calculated resistance at a bias voltage of 0.05 V. The resistance of the SWNTs is 492 Ω in air at a bias voltage of 1 V. At a forward bias, the resistance decreases markedly in the presence of electron withdrawing molecules such as nitrobenzene and chlorobenzene, whereas it increases in the presence of electron donating molecules such as aniline and

anisole. Thus, the resistance of the SWNTs was 2.5 kΩ and 725 Ω in the presence of aniline and anisole respectively at 1 V, the corresponding values in the presence of the chlorobenzene and nitrobenzene being 297 Ω and 217 Ω respectively. At a bias voltage of 0.05 V, the resistance of the SWNTs is 1.0 kΩ in air. In the presence of aniline, anisole,

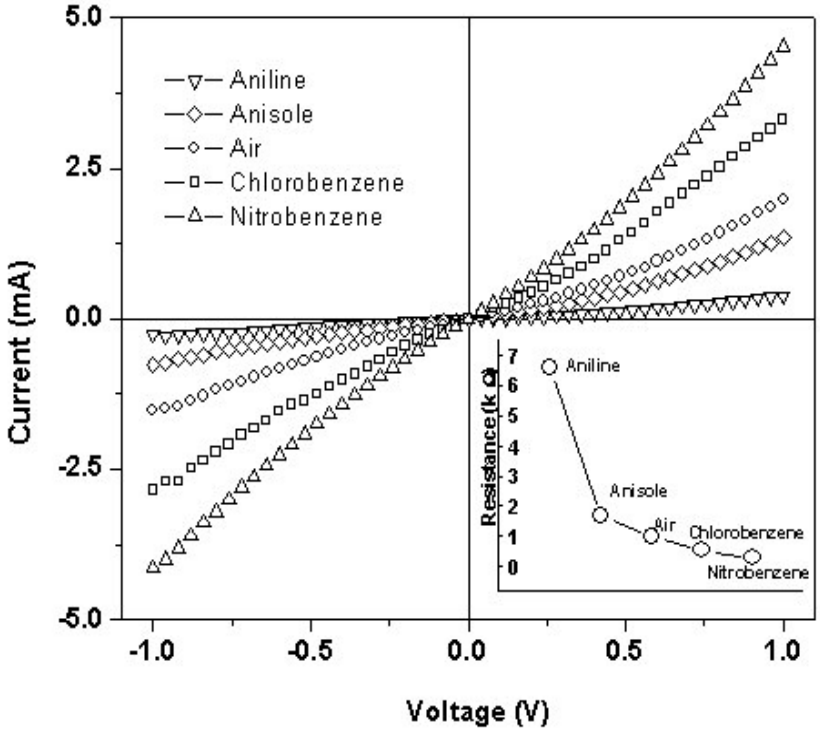

Figure 4.2.4: I-V characteristics of the SWNTs in air and in the presence of different aromatic molecules attached with electron-withdrawing and electron-donating groups.

chlorobenzene and nitrobenzene, the resistance values are 6.6, 1.7, 0.5 and 0.3 kΩ respectively. SWNTs under ambient conditions usually show p-type behavior [37]. It is possible that in the presence of electron-donating molecules, the number of hole carriers is reduced, causing an increase in the resistance. In the presence of electron-withdrawing molecules more holes are generated in semiconducting SWNTs. Interestingly, that the resistance varies proportionally with the Hammett substituent constants, the order being

NH_2 > OCH_3 > Cl > NO_2. This trend reflects the changes in the nature and the concentration of carriers as well as their mobilities brought about by interaction with electron donor and acceptor molecules. The I-V curves become more nonlinear as one goes from aniline to nitrobenzene. The slope of the I-V curve also increases going from nitrobenzene to aniline, due to the presence of a higher proportion of metallic like nanotubes in the presence of aniline.

4.3 Conclusions

In conclusion, we have shown that mesoporous carbon and nanographenes act as good electrode materials for application in supercapacitors. Supercapacitive behavior of RuO_2 and IrO_2 functionalized mesoporous carbon is studied using cyclic voltametry. We have found that the capacitance of the mesoporous carbon can be increased from 140 to 378 F/g in aq. H_2SO_4 by RuO_2 loading and to 152 F/g by IrO_2 loading. The specific capacitance of the exfoliated nanographene in the aqueous electrolyte is comparable to that obtained with activated carbon [8] while value of the energy density of the nanographene capacitors is one of the highest known to date. The supercapacitor characteristics are directly related to the quality of the nanographene, specifically the number of layers and the associated surface area.

Vertical SWNT devices were fabricated in a porous anodic alumina (PAA) template by microwave plasma chemical vapor deposition technique. The interactions of electron-withdrawing and electron-donating molecules with SWNTs were investigated. The present study establishes the high sensitivity of SWNTs to molecular charge-transfer. This feature of SWNTs may be useful in many of the applications such as sensors and nanoelectronics.

References

[1] (a) B.E. Conway, Electrochemical supercapacitors: scientific fundamentals and technological applications, Kluwer Academic/Plenum, New York, **(1999)**, (b) New carbon based materials for electrochemical energy storage systems: Batteries, supercapacitors and fuel cells (Eds: I.V. Barsukov, C.S. Johnson, J.E. Doninger, V.Z. Barsukov), Springer Dordrecht, The Netherlands, **(2006)**.

[2] Reviews: (a) E. Frackowiak, *Phys. Chem. Chem. Phys.* 9, 1774 **(2007)**; (b) A.S. Arico, P. Bruce, B. Scrosati, J.-M. Tarascon, W. Schalwijk, *Nat. Mater.* 4, 366 **(2005)**; (c) A.G. Pandolfo, A.F. Hollenkamp, *J. Power Sources* 157, 11 **(2006)**; (d) M. Winter, R.J. Brodd, *Chem. Rev.* 104, 4245 **(2004)**; (e) A. Bruke, *J. Power Sources* 91, 37 **(2000)**; (f) R. Kotz, M. Carlen, *Electrochim. Acta* 45, 2483 **(2000)**; (g) S. Sarangapani, B.V. Tilak, C.-P. Chen, *J. Electrochem. Soc.* 143, 3791 **(1996)**.

[3] H. E. Becker. U.S. Patent 2 800 616 (**1957**).

[4] D. I. Boos. U.S. Patent 3 536 963 (**1970**).

[5] B. E. Conway. *J. Electrochem. Soc.* 138, 1539 **(1991)**.

[6] http://www.nuin.co.kr/html/pro6.html.

[7] Frackowiak, F. Beguin, *Carbon* 39, 937 **(2001)**.

[8] D. Qu, H. Shi, *J. Power. Sources* 74, 99 **(1998)**.

[9] S. T. Meyer, R. W. Pekala, J. L. Kaschmitter, *J. Electrochem. Soc.* 140, 446 **(1993)**.

[10] C. M. Niu, E. K. Sichel, R. Hoch, D. Moy, H. Tennent, *Appl. Phys. Lett.* 70, 1480 **(1997)**.

[11] E. Frackowiak, K. Metenier, V. Bartagna, V. Beguin, *Appl. Phys. Lett.* 77, 2421 **(2000)**.

[12] K. H. An, W. S. Kim, Y. S. Park, Y. S. Park, Y. C. Choi, S. M. Lee, D. Chung, D. J. Bae, S. C. Lim, Y. Lee, *Adv. Mater.* 13, 497 **(2001)**.

[13] C. Du, J. Yeh, N. Pan, *Nanotechnology* 16, 350 **(2005)**.

[14] S. Yoon, J. Lee, T. Hyeon, S. M. Oh, *J. Electrochem. Soc.* 147, 2507 **(2000)**.

[15] J. Chimola, G. Yushin, Y. Gogotsi, C. Portet, P. Simon, P. L. Taberna, *Science* 313, 1760 **(2006)**.

[16] C.C. Hu, K.H. Chang, M-C. Lin, Y-T. Wu, *Nano Lett.* 6, 2690 **(2006)**.

[17] C.C. Hu, Y.H Huang, K.H. Chang, *J. Power sources* 108, 117 **(2002)**.

[18] K.W. Nam, K.B. Kim, *J. Electrochem. Soc.* 149, A346 **(2002)**.

[19] K. Jurewicz, C.V. Guterl, E. Frackwiak, S. Saadallah, M. Reda, J. Parmentier, J. Patarin, F. Beguin, *J. Phys. Chem. Solids* 65, 287, **(2004)**.

[20] A.B. Fuertes, G. Lota, T.A. Centeno, E. Frackowiak, *Electrochim. Acta* 50, 2799 **(2005)**.

[21] C. V-Guterl, E. Frackowiak, K. Jurewicz, M. Friebe, J. Parmentier, F. Beguin, *Carbon* 43, 1293 **(2005)**.

[22] J.H. Jang, S. Han, T. Hyeon, S.M. Oh, *J. Power sources* 123, 79 **(2003)**.

[23] X. Dong, W. Shen, J. Gu, L. Xiong, Y. Zhu, H. Li, J. Shi, *J. Phys. Chem. B* 110, 6015 **(2006)**.

[24] K. S. Novosolev, A. K. Geim, S. V. Morozov, D. Jiang, Y. Zhang, S. V. Dubonos, I. V. Grigorieva, A. A. Firsov, *Science* 306, 666 **(2004)**.

[25] A. K. Geim, K. S. Novosolev, *Nat. Mater.* 6, 183 **(2007)**.

[26] C. Liang, S. Dai, *J. Am. Chem. Soc*. 128, 5316 **(2006)**.

[27] S. Jun, S.H. Joo, R. Ryoo, M. Kruk, M. Jaroniec, Z. Liu, T. Ohsuna, O. Terasaki, *J. Am. Chem. Soc.* 122, 10712 **(2000)**.

[28] B.C. Satishkumar, A. Govindaraj, M. Nath, C.N.R. Rao, *J. Mater. Chem.* 10, 2115 **(2000)**.

[29] H. C. Schniepp, J.-L. Li, M.J. McAllister, H. Sai, M. Herrera-Alonso, D.H. Adamson, R.K. Prud'homme, R. Car, D. A. Saville, I. A. Aksay, *J. Phys. Chem. B* 110, 8535 **(2006)**.

[30] T. Zheng, Q. Zhong, J.R. Dahn, *J. Electrochem. Soc.* 142, L211 (**1995)**.

[31] R. Saito, G. Dresselhaus and M. S. Dresselhaus, *Physical Properties of Carbon Nanotubes* (Imperial College Press, London), (**1998**).

[32] P. Avouris, *Acc. Chem. Res.* 35, 1026 **(2002)**.

[33] C. N. R. Rao, A. Govindaraj *Nanotubes and Nanowires* RSC Nanoscience & Nanotechnology series, *Royal Society of Chemistry, Cambridge* (**2005**).

[34] A. Das, A. K. Sood, A. Govindaraj, M. Saitta, M. Lazzeri , F. Mauri and C N R Rao, *Phys. Rev. Lett*. 99, 136803 **(2007)**.

[35] M. Scolari, A. Mews, N. Fu, A. Myalitsin, T. Assmus, K. Balasubramanian, M. Burghard and K. Kern, *J. Phys. Chem. C* 112, 391 **(2008)**.

[36] R. Voggu, S. Pal, S. K. Pati and C. N. R Rao, *J. Phys.: Condens. Matter* 20**,** 215211 **(2008)**.

[37] H. J. Shin, S. M. Kim, S. M. Yoon, A. Benayad, K. K. Kim, S. J. Kim, H. K. Park, J. Y. Choi and Y. H. Lee, *J. Am. Chem. Soc.* 130**,** 2062 **(2008)**

[38] M. S. Strano, C. A. Dyke, M. L. Usrey, P. W. Barone, M. J. Allen, H. Shan, C. Kittrell, R. H. Hauge, J. M. Tour, R. E. Smalley, *Science* 301, 1519 **(2003)**.

[39] A. D. Franklin, M. R. Maschmann, M. DaSilva, D. B. Janes, T. S. Fisher, T. D. Sands, *J. Vacuum Sci. Tech. B* 25, 343 **(2007)**.

[40] M.R. Maschmann, A.D. Franklin, P.B. Amama, D.N. Zakharov, E.A. Stach, T.D. Sands and T.S. Fisher, *Nanotechnology* 17, 3925 **(2006)**.

[41] M.R. Maschmann, A.D. Franklin, A. Scott, D.B. Janes, T.D. Sands, T.S. Fisher, *Nano Lett.* 6, 2712 **(2006)**.

[42] M. R. Maschmann, A. D. Franklin, T. D. Sands, T. S. Fisher, *Carbon* 45, 2290 **(2007)**.

[43] A.D. Franklin, J.T. Smith, T. Sands, T.S. Fisher, K-S. Choi and D.B. Janes*, J. Phys. Chem.* 111, 13756 **(2007)**.